



HAL
open science

Numerical simulation of boiling for industrial quenching processes

Nadine El Kosseifi

► **To cite this version:**

Nadine El Kosseifi. Numerical simulation of boiling for industrial quenching processes. Other. Ecole Nationale Supérieure des Mines de Paris, 2012. English. NNT : 2012ENMP0019 . pastel-00734601

HAL Id: pastel-00734601

<https://pastel.hal.science/pastel-00734601>

Submitted on 24 Sep 2012

HAL is a multi-disciplinary open access archive for the deposit and dissemination of scientific research documents, whether they are published or not. The documents may come from teaching and research institutions in France or abroad, or from public or private research centers.

L'archive ouverte pluridisciplinaire **HAL**, est destinée au dépôt et à la diffusion de documents scientifiques de niveau recherche, publiés ou non, émanant des établissements d'enseignement et de recherche français ou étrangers, des laboratoires publics ou privés.

Ecole doctorale n°364 : Sciences Fondamentales et Appliquées

Doctorat ParisTech

T H È S E

pour obtenir le grade de docteur délivré par

l'École nationale supérieure des mines de Paris

Spécialité « Mécanique Numérique »

présentée et soutenue publiquement par

Nadine EL KOSSEIFI

le 27 juin 2012

Numerical Simulation of Boiling for Industrial Quenching Processes

~~~

**Simulation numérique de l'ébullition pour les procédés de trempe industrielle**

Directeur de thèse : **Thierry COUPEZ, Elisabeth MASSONI**

Co-encadrement de la thèse : **Elie HACHEM**

#### **Jury**

**M. Marwan DARWISH**, Professeur, American University of Beirut  
**M. Pascal FREY**, Professeur, Laboratoire JLL, Université Pierre et Marie Curie 4  
**M. Arnaud POITOU**, Professeur, GEM, Ecole Centrale de Nantes  
**M. Thierry COUPEZ**, Professeur, CEMEF, MINES ParisTech  
**Mme. Elisabeth MASSONI**, Maitre de Recherches, CEMEF, MINES ParisTech  
**M. Elie HACHEM**, Docteur, CEMEF, MINES ParisTech  
**Mme. Chantal DAVID**, Sciences Computer Consultants SCC, France  
**Mme Séverine BOYER**, Chargée de recherche, INSTITUT P', Ecole Nationale Supérieure de Mécanique et D'Aérotechnique

Président  
Rapporteur  
Rapporteur  
Examineur  
Examineur  
Examineur  
Examineur

**T  
H  
È  
S  
E**

**MINES ParisTech**

**Centre de Mise en Forme des Matériaux**

Rue Claude Daunesse, BP 207, 06904 Sophia-Antipolis Cedex, France

أهدي هذه الأطروحة إلى والدي.

## Acknowledgments

I would like to express my gratitude to my supervisor, Pr. Thierry Coupez, whose expertise, understanding, and patience, added considerably to my graduate experience. I particularly express my warmest thanks to the other supervisors, Dr. Elisabeth Massoni, and Dr. Elie Hachem for the assistance they provided at all levels of the research project. Finally, I would like to thank Dr. Luisa Silva for taking time out to serve as my external advisor.

I am extremely grateful to Dr. Séverine Boyer for the guidance in the experimental work and to the Group MEA for the designing and constructing of the experimental apparatus. I would like to thank the members of J.A. Dieudonné Laboratory of the Nice University, Christian Mathis, Harunori and Pascal Biwole for the help provided during the experimental work.

I would like to thank also all the staff at CEMEF, in particularly: Patrick Coels, Marie-Francoise, Genevieve, Florence and Murielle for their encouragements. I am grateful to the members of EII team in particularly Emmanuel, Valéry, Carole and Anne-Mari.

This work has been supported by SCC within the ThosT project context, which includes the following companies: Aubert & Duval, Snecma, ArcelorMittal Industeel, Manoir Industries, Creusot Forge, group Areva, Sciences Computers Consultants and Transvalor. Their financial support is gratefully acknowledged.

Pamela Mondalek is the one person who truly made a difference in my life, without her encouragement this thesis would certainly have not exist. Thanks for my friends, Rebecca, Fadi, Carole, Stephanie, Karim, Greg, Emile, Massiele, Jean François, Boris and Guillaume for being a constant source of moral support all along this work.

My sincerest appreciation goes to Mr and Mrs McGeachie for the examination of my manuscript. I would also like to thank my family and my best friend Micha for the support they provided me through my entire life. I must acknowledge Lionel, without his encouragement, I would not have finished this thesis.

The achievement of this thesis requires: Trust in God, Patience and Work.

I dedicate this thesis to my mother.



# Table of contents

|          |                                                                                                                |           |
|----------|----------------------------------------------------------------------------------------------------------------|-----------|
| <b>1</b> | <b>General Introduction</b>                                                                                    | <b>1</b>  |
| 1.1      | Steel heat treatment . . . . .                                                                                 | 2         |
| 1.2      | Introduction to quenching process . . . . .                                                                    | 4         |
| 1.3      | Regimes of boiling and heat transfer . . . . .                                                                 | 7         |
| 1.3.1    | Boiling curve . . . . .                                                                                        | 7         |
| 1.3.2    | Heat transfer during boiling . . . . .                                                                         | 7         |
| 1.3.3    | Boiling modes during quenching . . . . .                                                                       | 9         |
| 1.3.3.1  | Industrial case . . . . .                                                                                      | 9         |
| 1.3.3.2  | Micro quenching . . . . .                                                                                      | 11        |
| 1.4      | Role of Biot number in predicting the boiling duration . . . . .                                               | 12        |
| 1.4.1    | Mean Biot number . . . . .                                                                                     | 12        |
| 1.4.2    | Duration of boiling modes depends on the mean Biot number . . .                                                | 13        |
| 1.5      | Developing history of ThosT . . . . .                                                                          | 14        |
| 1.6      | Objectives and outline of the thesis . . . . .                                                                 | 15        |
| 1.7      | Résumé français . . . . .                                                                                      | 16        |
|          | <b>References</b>                                                                                              | <b>17</b> |
| <b>2</b> | <b>CFD for modelling quenching process</b>                                                                     | <b>19</b> |
| 2.1      | Stabilized finite element method of convection-diffusion equation . . . . .                                    | 20        |
| 2.1.1    | Resolution of the energy equation . . . . .                                                                    | 21        |
| 2.1.2    | Spatial discretization . . . . .                                                                               | 21        |
| 2.1.3    | Time integration . . . . .                                                                                     | 22        |
| 2.1.4    | Stabilized finite element method of unsteady diffusion problem . . .                                           | 23        |
| 2.1.4.1  | Stability condition . . . . .                                                                                  | 23        |
| 2.1.4.2  | Study of the time step, the mesh size and the thermal<br>diffusivity influence on the thermal shocks . . . . . | 23        |

|                                        |                                                                             |           |
|----------------------------------------|-----------------------------------------------------------------------------|-----------|
| 2.1.4.3                                | Cooling of a semi-infinite <b>3D</b> bar . . . . .                          | 24        |
| 2.1.4.4                                | Enriched method interpolation ( <b>EM-I</b> ) . . . . .                     | 26        |
| 2.2                                    | Stabilised finite element methods for incompressible Navier-Stokes flow . . | 32        |
| 2.2.1                                  | Weak form of the incompressible Navier-Stokes equations . . . . .           | 32        |
| 2.2.2                                  | Variational MultiScale Method . . . . .                                     | 33        |
| 2.3                                    | Immersed volume method for modelling quenching process . . . . .            | 36        |
| 2.3.1                                  | LevelSet Method . . . . .                                                   | 36        |
| 2.3.2                                  | Anisotropic mesh adaptation . . . . .                                       | 37        |
| 2.3.2.1                                | Basic definitions . . . . .                                                 | 38        |
| 2.3.2.2                                | The constructed metric . . . . .                                            | 40        |
| 2.4                                    | Numerical tests and validation . . . . .                                    | 41        |
| 2.4.1                                  | Study of the agitation influence . . . . .                                  | 41        |
| 2.4.2                                  | Industrial case . . . . .                                                   | 46        |
| 2.4.2.1                                | Results with an entrance velocity <b>3 m.s<sup>-1</sup></b> . . . . .       | 48        |
| 2.4.2.2                                | Results without agitation . . . . .                                         | 49        |
| 2.5                                    | Conclusions . . . . .                                                       | 52        |
| 2.6                                    | Résumé français . . . . .                                                   | 53        |
| <b>References</b>                      |                                                                             | <b>55</b> |
| <b>3 Modelling of nucleate boiling</b> |                                                                             | <b>59</b> |
| 3.1                                    | Nucleate boiling . . . . .                                                  | 61        |
| 3.2                                    | Interface tracking . . . . .                                                | 62        |
| 3.2.1                                  | Reinitialisation . . . . .                                                  | 62        |
| 3.2.2                                  | Convective Reinitialization . . . . .                                       | 63        |
| 3.2.3                                  | New distance function . . . . .                                             | 64        |
| 3.2.4                                  | Numerical test . . . . .                                                    | 67        |
| 3.3                                    | Growth . . . . .                                                            | 68        |
| 3.3.1                                  | Background of the isothermal bubble growth rate . . . . .                   | 68        |
| 3.3.2                                  | Numerical approach . . . . .                                                | 68        |
| 3.3.3                                  | Conservation of energy . . . . .                                            | 69        |
| 3.3.4                                  | Validation of the growth model . . . . .                                    | 70        |
| 3.3.5                                  | Modelling for the isothermal growth of a single bubble . . . . .            | 71        |
| 3.3.6                                  | Modelling for the isothermal bubble collapse . . . . .                      | 73        |
| 3.3.7                                  | Modelling for non-isothermal growth of a single bubble . . . . .            | 74        |

|          |                                                                                              |           |
|----------|----------------------------------------------------------------------------------------------|-----------|
| 3.4      | Anisotropic adaptative mesh . . . . .                                                        | 75        |
| 3.5      | Surface Tension . . . . .                                                                    | 76        |
| 3.5.1    | Surface Tension approximation . . . . .                                                      | 76        |
| 3.5.2    | Time step restriction . . . . .                                                              | 78        |
| 3.5.3    | Numerical Examples . . . . .                                                                 | 79        |
| 3.5.3.1  | Rising bubble shape in two-dimensional case . . . . .                                        | 79        |
| 3.5.3.2  | Rising bubble shape in three-dimensional case . . . . .                                      | 80        |
| 3.5.3.3  | Coalescence of two bubble towards a free surface . . . . .                                   | 83        |
| 3.5.3.4  | Bubble coalescence . . . . .                                                                 | 84        |
| 3.5.3.5  | Ascension . . . . .                                                                          | 85        |
| 3.5.3.6  | Numerical & Experimental investigation of bubble rising . . . . .                            | 88        |
| 3.6      | Conclusion . . . . .                                                                         | 90        |
| 3.7      | Résumé français . . . . .                                                                    | 91        |
|          | <b>References</b>                                                                            | <b>93</b> |
| <b>4</b> | <b>Temperature &amp; velocity field measurement during nucleate boiling by PIV &amp; LIF</b> | <b>97</b> |
| 4.1      | Experimental analysis of the bubble growth rate . . . . .                                    | 98        |
| 4.1.1    | Experimental apparatus . . . . .                                                             | 99        |
| 4.1.2    | Results and discussion . . . . .                                                             | 99        |
| 4.1.3    | Results and analysis for a higher superheat . . . . .                                        | 102       |
| 4.1.4    | Conclusion & motivation for further experimental investigations . . . . .                    | 105       |
| 4.2      | Particle Image Velocimetry . . . . .                                                         | 106       |
| 4.2.1    | Principle of PIV . . . . .                                                                   | 106       |
| 4.2.2    | Results . . . . .                                                                            | 109       |
| 4.3      | Laser Induced Fluorescence . . . . .                                                         | 112       |
| 4.3.1    | Principle of two color LIF thermometry . . . . .                                             | 112       |
| 4.3.2    | Fluorescence dyes selection and optical systems . . . . .                                    | 113       |
| 4.3.3    | Concentration choice . . . . .                                                               | 116       |
| 4.3.3.1  | First investigation . . . . .                                                                | 116       |
| 4.3.3.2  | Deeper investigation . . . . .                                                               | 116       |
| 4.3.4    | Camera calibration . . . . .                                                                 | 118       |
| 4.3.5    | Temperature calibration . . . . .                                                            | 119       |
| 4.3.6    | Results and discussion . . . . .                                                             | 119       |



---

|          |                                                                       |            |
|----------|-----------------------------------------------------------------------|------------|
| 4.4      | Conclusion & Perspectives . . . . .                                   | 122        |
| 4.5      | Résumé français . . . . .                                             | 123        |
|          | <b>References</b>                                                     | <b>125</b> |
| <b>5</b> | <b>Integrating boiling model to the quenching process</b>             | <b>129</b> |
| 5.1      | Micro-quenching . . . . .                                             | 130        |
| 5.1.1    | Experimental setup . . . . .                                          | 130        |
| 5.1.2    | Experimental results . . . . .                                        | 131        |
| 5.2      | Numerical simulation . . . . .                                        | 133        |
| 5.2.1    | Resolution algorithm . . . . .                                        | 134        |
| 5.2.2    | Two dimensional film boiling . . . . .                                | 135        |
| 5.2.3    | Three dimensional film boiling-Micro Scale . . . . .                  | 138        |
| 5.2.4    | Three dimensional film boiling-Meso Scale . . . . .                   | 140        |
| 5.2.5    | Numerical simulation of film boiling during industrial quenching case | 142        |
| 5.2.6    | Conclusion . . . . .                                                  | 143        |
| 5.3      | Résumé français . . . . .                                             | 144        |
|          | <b>References</b>                                                     | <b>145</b> |
| <b>6</b> | <b>Conclusion &amp; perspectives</b>                                  | <b>147</b> |

# List of Figures

|      |                                                                                                                                                                                                                                                                                    |    |
|------|------------------------------------------------------------------------------------------------------------------------------------------------------------------------------------------------------------------------------------------------------------------------------------|----|
| 1.1  | Steel thermal treatment . . . . .                                                                                                                                                                                                                                                  | 2  |
| 1.2  | Several steps of the heat treatment of shells, that has been done in Areva at Creusot Forge . . . . .                                                                                                                                                                              | 3  |
| 1.3  | Transformation in continuous cooling (CCT) diagrams of steel <i>C70</i> [1] . . . . .                                                                                                                                                                                              | 4  |
| 1.4  | Quenching by immersion: (a) In polymer (Snecma), (b) In water (Areva Creusot Forge) . . . . .                                                                                                                                                                                      | 5  |
| 1.5  | CAD installation of spray quenching (Industeel) . . . . .                                                                                                                                                                                                                          | 5  |
| 1.6  | Different baths (Snecma): (a) Polymer tank 18 m <sup>3</sup> , agitated by 6 pumps, (b) Water tank 35 m <sup>3</sup> , agitated by 2 pumps . . . . .                                                                                                                               | 6  |
| 1.7  | Boiling curve for a stagnant pool of liquid at its saturation temperature [2] . . . . .                                                                                                                                                                                            | 8  |
| 1.8  | Diagram presenting the different stages of Rayleigh-Taylor instability: (a) Instability at the liquid / vapor interface, ( b) Droplets going in the vapor blanket, (c) The liquid spreads over the plate and is heated to $T_{sat}$ , (d) The liquid film is removed [3] . . . . . | 8  |
| 1.9  | Different steps of heat treatment . . . . .                                                                                                                                                                                                                                        | 9  |
| 1.10 | Water agitated tank . . . . .                                                                                                                                                                                                                                                      | 10 |
| 1.11 | Boiling phenomenon at the shell interface . . . . .                                                                                                                                                                                                                                | 10 |
| 1.12 | Film vapor at the shell surface . . . . .                                                                                                                                                                                                                                          | 11 |
| 1.13 | Quenching of a steel in water . . . . .                                                                                                                                                                                                                                            | 11 |
| 1.14 | Relative duration of different boiling modes depending on the mean Biot number [4] . . . . .                                                                                                                                                                                       | 13 |
| 1.15 | Multi-Scale for Boiling . . . . .                                                                                                                                                                                                                                                  | 15 |
| 2.1  | Temperature (°C) evolution . . . . .                                                                                                                                                                                                                                               | 23 |
| 2.2  | Influence of thermal diffusivity and time step on the thermal shock . . . . .                                                                                                                                                                                                      | 24 |
| 2.3  | Problem configuration . . . . .                                                                                                                                                                                                                                                    | 25 |
| 2.4  | Comparison between numerical temperature and analytical one at nodes situated at $h$ and $2h$ from the heated side . . . . .                                                                                                                                                       | 25 |
| 2.5  | Influence of thermal diffusivity, mesh size and time step on the thermal shock . . . . .                                                                                                                                                                                           | 26 |
| 2.6  | Decomposition of a tetrahedra in coarse scale and micro-scale . . . . .                                                                                                                                                                                                            | 28 |
| 2.7  | Interpolation of the solution to the real time step . . . . .                                                                                                                                                                                                                      | 30 |

|      |                                                                                                                                                                                                                                    |    |
|------|------------------------------------------------------------------------------------------------------------------------------------------------------------------------------------------------------------------------------------|----|
| 2.8  | Evolution of the temperature ( $^{\circ}\text{C}$ ) at a node situated $2h$ far from the cooled side [1]                                                                                                                           | 31 |
| 2.9  | Anisotropic mesh                                                                                                                                                                                                                   | 39 |
| 2.10 | Geometric representation of a metric in <b>2D</b> and in <b>3D</b> [2]                                                                                                                                                             | 40 |
| 2.11 | (a) Representation of a <b>2D</b> interface with the anisotropic meshing technique, (b) Close-up along the interface                                                                                                               | 41 |
| 2.12 | (a) Computational domain, (b) Agitation system with an entrance velocity $3 \text{ m} \cdot \text{s}^{-1}$                                                                                                                         | 42 |
| 2.13 | Mesh adaptation in the vicinity of the interface                                                                                                                                                                                   | 42 |
| 2.14 | (a) Representation of a <b>3D</b> interface with the anisotropic meshing technique, (b) Close-up along the interface                                                                                                               | 43 |
| 2.15 | Position of thermal sensors                                                                                                                                                                                                        | 43 |
| 2.16 | Temperature evolution of a square body for different agitation velocities. From top to bottom: sensors a, b, c, d                                                                                                                  | 45 |
| 2.17 | (a) Quenching configuration, (b) Industrial water tank agitated by two pumps                                                                                                                                                       | 46 |
| 2.18 | Difference between the initial mesh and the final mesh of the cylinder (top), the final mesh and the interface of the agitation system (bottom)                                                                                    | 47 |
| 2.19 | (a) Computational domain after anisotropic mesh adaptation around the workpiece interface and an isotropic refinement near the agitation system, (b) Cut of mesh showing details of the refinement and anisotropic mesh adaptation | 47 |
| 2.20 | Velocity vector injected from bellow and getting out from the right side (left), Close-up along the injection system (right)                                                                                                       | 48 |
| 2.21 | Streamlines inside the bath at different time steps                                                                                                                                                                                | 48 |
| 2.22 | Position of thermal sensors                                                                                                                                                                                                        | 49 |
| 2.23 | Comparison of temperature profiles between experimental and numerical results. From top to bottom: sensors a, b, c, d                                                                                                              | 50 |
| 2.24 | (a) Problem configuration, (b) Temperature ( $^{\circ}\text{C}$ ) evolution at $t = 700 \text{ s}$                                                                                                                                 | 51 |
| 2.25 | Comparison of temperature profiles between experimental and numerical results                                                                                                                                                      | 52 |
| 3.1  | (a) A bubble forms in the crevice of a scratch along the bottom of a pan of water, (b-f) The bubble grows, pinches off, and then ascends through the water [1]                                                                     | 61 |
| 3.2  | The hyperbolic tangent                                                                                                                                                                                                             | 64 |
| 3.3  | Position of the circle at different time steps during one turn                                                                                                                                                                     | 67 |
| 3.4  | Growth of a spherical bubble in an infinite mass of liquid [2]                                                                                                                                                                     | 68 |
| 3.5  | Computational domain and resolution algorithm for modelling bubble growth                                                                                                                                                          | 70 |
| 3.6  | Radius evolution with time                                                                                                                                                                                                         | 71 |

---

|      |                                                                                                                                |     |
|------|--------------------------------------------------------------------------------------------------------------------------------|-----|
| 3.7  | (a-b) Isovalue zero of the LevelSet function at $t = 0$ s and $t = 1$ s, (b) Radius evolution with time in <b>2D</b> . . . . . | 72  |
| 3.8  | (a-b) Isovalue zero of the LevelSet function at $t = 0$ s and $t = 1$ s, (b) Radius evolution with time in <b>3D</b> . . . . . | 72  |
| 3.9  | Zero isovalue of the bubbles in <b>2D</b> at different time steps during the growth                                            | 73  |
| 3.10 | Zero isovalue of the bubbles in <b>3D</b> at different time steps during the growth                                            | 73  |
| 3.11 | Initial temperature ( $^{\circ}\text{C}$ ) distribution . . . . .                                                              | 74  |
| 3.12 | Zero isovalue of the bubbles at different time steps during the growth . . .                                                   | 74  |
| 3.13 | (a) Computed velocity field arrows at $t = 2$ s, (b) Zoom at the bubble interface . . . . .                                    | 75  |
| 3.14 | Evolution of the bubble interface . . . . .                                                                                    | 75  |
| 3.15 | Resolution algorithm for bubbles rising . . . . .                                                                              | 79  |
| 3.16 | (a) Schematic domain and boundary conditions, (b) Mesh refinement at the interface of the level. . . . .                       | 79  |
| 3.17 | Time evolution of air bubble interface . . . . .                                                                               | 80  |
| 3.18 | Bubble diagram of Grace reproduced from [3]: shape regimes for bubbles and drops . . . . .                                     | 81  |
| 3.19 | Initial bubble position . . . . .                                                                                              | 82  |
| 3.20 | Bubble rising simulation results corresponding to the regimes indicated in table 3.4 respectively . . . . .                    | 82  |
| 3.21 | The intersection of the interface with the center plane of the computational domain . . . . .                                  | 82  |
| 3.22 | (a) Properties distribution, (b) Schematic domain and boundary conditions, (c) Mesh refinement at the interface . . . . .      | 83  |
| 3.23 | Time evolution of fluid interface and the velocity field . . . . .                                                             | 84  |
| 3.24 | Isovalue zero of the LevelSet function for bubble coalescence . . . . .                                                        | 85  |
| 3.25 | Large air bubble ascension . . . . .                                                                                           | 87  |
| 3.26 | Small air bubble ascension . . . . .                                                                                           | 87  |
| 3.27 | Set-up for air bubble generation method . . . . .                                                                              | 88  |
| 3.28 | Experimental investigation of air bubble rising . . . . .                                                                      | 89  |
| 3.29 | Flow rising of a <b>3D</b> bubble with anisotropic mesh adaptation at the vapor-liquid interfaces . . . . .                    | 89  |
| 3.30 | Anisotropic mesh adaptation at different time steps . . . . .                                                                  | 90  |
| 4.1  | Schematic representation of the bubble growth on a heated wall [1] . . . .                                                     | 98  |
| 4.2  | Variation of bubble radius and temperature for hemispherical bubble growing on a heated wall [2] . . . . .                     | 99  |
| 4.3  | Experimental apparatus . . . . .                                                                                               | 100 |
| 4.4  | Bubble evolution . . . . .                                                                                                     | 101 |
| 4.5  | Bubble deformation [3] . . . . .                                                                                               | 101 |
| 4.6  | Evolution of $R_x$ and $R_y$ during the growth period . . . . .                                                                | 102 |

|      |                                                                                                                                                                                                                                                                                                                              |     |
|------|------------------------------------------------------------------------------------------------------------------------------------------------------------------------------------------------------------------------------------------------------------------------------------------------------------------------------|-----|
| 4.7  | Variation of bubble radiuses before the detachment . . . . .                                                                                                                                                                                                                                                                 | 102 |
| 4.8  | Cycle of events at the nucleation site . . . . .                                                                                                                                                                                                                                                                             | 103 |
| 4.9  | Variation of bubble radiuses during the growth . . . . .                                                                                                                                                                                                                                                                     | 104 |
| 4.10 | Comparison experimental and polynomial form for both radiuses . . . . .                                                                                                                                                                                                                                                      | 104 |
| 4.11 | (a) Radiuses evolution after the bubble detachment, (b) Area evolution<br>after the bubble detachment . . . . .                                                                                                                                                                                                              | 105 |
| 4.12 | (a) Experimental device, (b) Heater element . . . . .                                                                                                                                                                                                                                                                        | 106 |
| 4.13 | Apparatus of a Particle Image Velocimetry system . . . . .                                                                                                                                                                                                                                                                   | 107 |
| 4.14 | Intercorrelation algorithm of images (inspired from [4]) . . . . .                                                                                                                                                                                                                                                           | 107 |
| 4.15 | Frame and correlation windows . . . . .                                                                                                                                                                                                                                                                                      | 108 |
| 4.16 | Particles distribution around the bubble . . . . .                                                                                                                                                                                                                                                                           | 109 |
| 4.17 | Velocity field PIV measurements at the bubble edge . . . . .                                                                                                                                                                                                                                                                 | 110 |
| 4.18 | Experimental streamlines obtained by PIV measurements. The colors cor-<br>respond to the modulus of the velocity . . . . .                                                                                                                                                                                                   | 111 |
| 4.19 | Location of the vortices near the bubble interface at $t = 144$ ms . . . . .                                                                                                                                                                                                                                                 | 111 |
| 4.20 | Schematic of the two color LIF experimental setup . . . . .                                                                                                                                                                                                                                                                  | 113 |
| 4.21 | (a) Rhodamine B absorption (dotted line) and emission (full line) spectra,<br>(b) Rhodamine B emission as a function of the temperature [5] . . . . .                                                                                                                                                                        | 114 |
| 4.22 | (a) Sulforhodamine absorption (dotted line) and emission (full line) spectra,<br>(b) Sulforhodamine 101 emission as a function of the temperature [5] . . . . .                                                                                                                                                              | 114 |
| 4.23 | Rhodamine B and SR101 emission and absorption spectra when excited at<br>532 nm . . . . .                                                                                                                                                                                                                                    | 115 |
| 4.24 | View of the PLIF experimental setup . . . . .                                                                                                                                                                                                                                                                                | 115 |
| 4.25 | Visualization of RhB intensity for different RhB concentrations . . . . .                                                                                                                                                                                                                                                    | 116 |
| 4.26 | Two-color LIF images, RhB on the left and SR101 on the right . . . . .                                                                                                                                                                                                                                                       | 117 |
| 4.27 | (a) Output voltages of Cameras $\alpha$ and $\beta$ as a versus of RhB concentration,<br>the inset shows the same $V_\beta$ behavior with a magnified scale, (b) Output<br>voltages of Cameras $\alpha$ and $\beta$ as a versus of SR101 concentration . . . . .                                                             | 118 |
| 4.28 | Views of cameras with a calibration plate: (a) Camera $\alpha$ (b) Camera $\beta$ and<br>(c) Camera $\beta$ after the mapping $\mathcal{G}$ . The image size is $1000 \times 1600$ pix <sup>2</sup> .<br>Each square pattern on the calibration plate has sides of 2 mm. The spatial<br>resolution is 0.026 mm/pix . . . . . | 119 |
| 4.29 | (a) Normalized output voltages for a solution of $c_{\text{RhB}} = 0.4$ mg/l and<br>$c_{\text{SR101}} = 0.1$ mg/l, (b) the temperature calibration curve $T = -59.5 f + 265.0120$                                                                                                                                            |     |
| 4.30 | Nucleate boiling observed by Cameras $\alpha$ and $\beta$ , left and right, respectively,<br>and the determined temperature ( $^{\circ}\text{C}$ ) field by calculating $f$ -function . . . . .                                                                                                                              | 121 |
| 4.31 | The same result as above ( $t = 3$ s) with a different temperature scale ( $^{\circ}\text{C}$ )                                                                                                                                                                                                                              | 121 |
| 5.1  | (a) Nucleate boiling, (b) Film boiling . . . . .                                                                                                                                                                                                                                                                             | 130 |
| 5.2  | (a) Schema of the Micro quenching setup, (b) Photograph of the Micro<br>quenching setup . . . . .                                                                                                                                                                                                                            | 131 |

---

|      |                                                                                                                                                                                                                                                     |     |
|------|-----------------------------------------------------------------------------------------------------------------------------------------------------------------------------------------------------------------------------------------------------|-----|
| 5.3  | Boiling regimes for a ingot quenched in water at 20 °C . . . . .                                                                                                                                                                                    | 132 |
| 5.4  | Boiling regimes for a ingot at 700 °C quenched in water at 30 °C, 70 °C<br>and 80 °C . . . . .                                                                                                                                                      | 133 |
| 5.5  | Resolution algorithm for boiling model during quenching . . . . .                                                                                                                                                                                   | 134 |
| 5.6  | Two dimensional film boiling interface profile computed on a large scale grid                                                                                                                                                                       | 135 |
| 5.7  | Top: close-up on the film boiling interface profile. Bottom: close-up on the<br>temperature (°C) field . . . . .                                                                                                                                    | 136 |
| 5.8  | Velocity (m/s) vectors, the liquid vapor and the solid interface are plotted<br>as red and black line, respectively . . . . .                                                                                                                       | 137 |
| 5.9  | The film boiling interface profile. Isobar contour for the solid is plotted<br>with red color, the liquid vapor is plotted with blue at every grid point . .                                                                                        | 138 |
| 5.10 | Top: The temperature (°C) field. Bottom: Evolution of the velocity (m/s)<br>field on the left and the density (Kg/m <sup>3</sup> ) distribution across the liquid-<br>vapor interface on the right, through a vertical center plane for the solid . | 139 |
| 5.11 | Computational domain meso scale . . . . .                                                                                                                                                                                                           | 140 |
| 5.12 | Interface plot for a three-dimensional vapor film generation test . . . . .                                                                                                                                                                         | 141 |
| 5.13 | Evolution of the velocity (m/s) field through a vertical center plane for the<br>solid . . . . .                                                                                                                                                    | 142 |
| 5.14 | Computational domain after anisotropic mesh adaptation around the work-<br>piece interface and an isotropic refinement near the agitation system . . . .                                                                                            | 142 |
| 5.15 | Comparison of temperature (°C) profiles between experimental and numer-<br>ical results with/without boiling calculation. From left to right: sensors 3,<br>7 . . . . .                                                                             | 143 |



# Chapter 1

## General Introduction

### Contents

---

|            |                                                                       |           |
|------------|-----------------------------------------------------------------------|-----------|
| <b>1.1</b> | <b>Steel heat treatment . . . . .</b>                                 | <b>2</b>  |
| <b>1.2</b> | <b>Introduction to quenching process . . . . .</b>                    | <b>4</b>  |
| <b>1.3</b> | <b>Regimes of boiling and heat transfer . . . . .</b>                 | <b>7</b>  |
| 1.3.1      | Boiling curve . . . . .                                               | 7         |
| 1.3.2      | Heat transfer during boiling . . . . .                                | 7         |
| 1.3.3      | Boiling modes during quenching . . . . .                              | 9         |
| <b>1.4</b> | <b>Role of Biot number in predicting the boiling duration . . . .</b> | <b>12</b> |
| 1.4.1      | Mean Biot number . . . . .                                            | 12        |
| 1.4.2      | Duration of boiling modes depends on the mean Biot number .           | 13        |
| <b>1.5</b> | <b>Developing history of ThosT . . . . .</b>                          | <b>14</b> |
| <b>1.6</b> | <b>Objectives and outline of the thesis . . . . .</b>                 | <b>15</b> |
| <b>1.7</b> | <b>Résumé français . . . . .</b>                                      | <b>16</b> |

---



The quenching is a heat treatment operation that gives the material its final properties and microstructure as function of the cooling rate. In material science, the quenching is an efficient way to control mechanical and metallurgical characteristics of final metallic parts such as hardness, toughness and resistance. The heat transfer between the material and the tank must be very well controlled to avoid defects like distortion, cracking and to get good mechanical properties. To achieve higher treatment efficiency, the metallurgists are interested in predicting the heat transfer between the material and the tank. The heat transfer has not been fully characterized yet. With help of numerical simulations, the heat transfer can be predicted in different conditions. Such simulations are useful when new tanks have to be designed or to optimize the cooling in the existing ones.

During the quenching in a vaporizable fluid (oil, water, polymer), there is a coupling between the heat transfer rate and boiling regimes. The main objective of this work is to model the cooling during quenching as closely as possible of a real situation. This requires a creation and an integration of a boiling model to the quenching process. The work presented here takes place in the **ThosT** project, involving 7 industrial partners.

## 1.1 Steel heat treatment

Heat treatment is used for several industrial applications, particularly in metallurgical applications. In the case of steel, the heat treatment involves three successive operations (Figure 1.1-1.2):

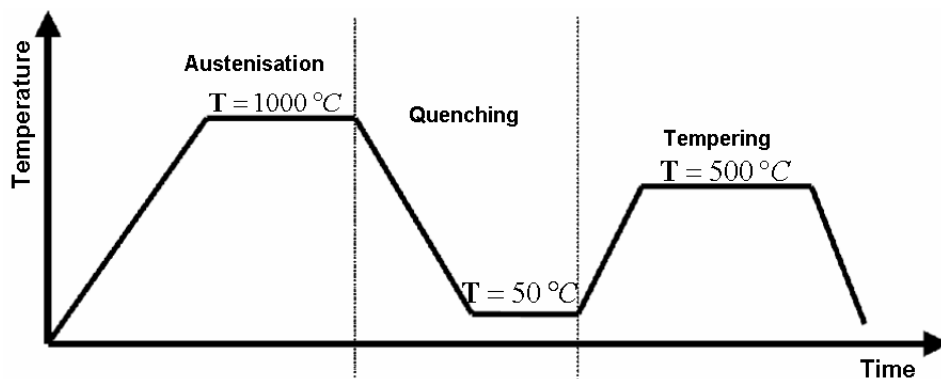


Figure 1.1: Steel thermal treatment

- i) **Heating:** most heat treatments begin by heating the steel long enough to be transformed into a homogeneous austenitic form (Figure 1.2(a)). Usually this form is reached when the solid had been heated to a temperature above the upper critical temperature;
- ii) **Quenching:** it is a cooling process usually used to improve the material properties (Figure 1.2(d));

- iii) **Tempering:** after quenching, some steel become very hard and too brittle to be used in several applications. For this reason tempering is necessary and is accomplished by a reheating of the steel to a temperature below the lower critical temperature. After tempering the steel is transformed from a brittle martensite or bainite into a combination of ferrite and cementite.



(a) Opening of the furnace door



(b) Shells taking out of the furnace



(c) Shell transportation to the bath



(d) Shell quenching in the bath

Figure 1.2: Several steps of the heat treatment of shells, that has been done in Areva at Creusot Forge

Figure 1.2 presents the heat treatment of large hollow metal ingots (shells), that has been done in Areva at Creusot Forge. Figures 1.2(a)-1.2(b) present the opening of the furnace door and the getting out of shells that were heated in a furnace at a temperature of 1000 °C during several hours. Shells are made of steel; they have a diameter and a thickness of 5.785 m and 0.4 m, respectively. They are used in the nuclear industry (60% of the production of shells Creusot Forge) or in the petrochemical industry (40% of the production of shells Creusot Forge). After the heating, one shell is transported to the bath while the other is turned back to the furnace. The purpose of quenching is to get as possible a homogeneous bainitic structure. The transportation from the furnace to the tank must be quick to keep the austenitic phase (Figure 1.2(c)).

## 1.2 Introduction to quenching process

After heating the steel goes to an austenitic region. A rapid quenching process produces a martensitic transformation, a slow one provides austenite and pearlite phases corresponding to a partly hard structure (Figure 1.3). Therefore the heat treatment gives the material its final properties and microstructure as function of the cooling rate. The heat

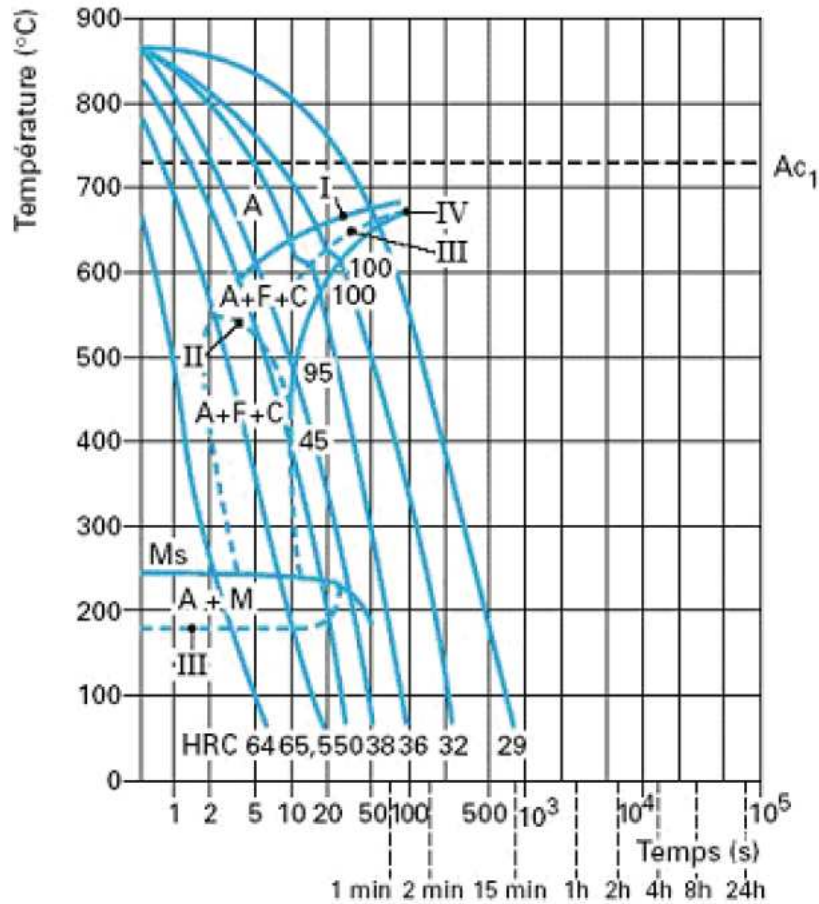


Figure 1.3: Transformation in continuous cooling (CCT) diagrams of steel C70 [1]

transfer between the material and the tank must be very well controlled to avoid defects like distortion, cracking, and to get good mechanical properties. A uniform cooling is essential and requires a bath control: temperature, agitation, flow, surface pressure [5]. . . . Well known quenching methods are: immersing into a bath (Figure 1.4), jet impingement [6] and spray quenching (Figure 1.5) [2].

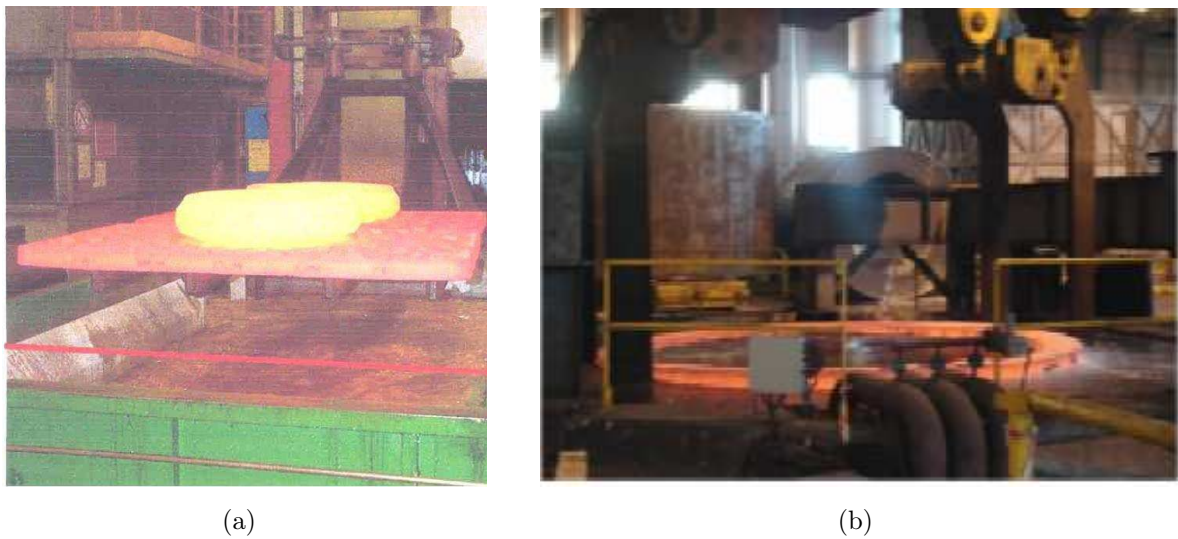


Figure 1.4: Quenching by immersion: (a) In polymer (Snecma), (b) In water (Areva Creusot Forge)

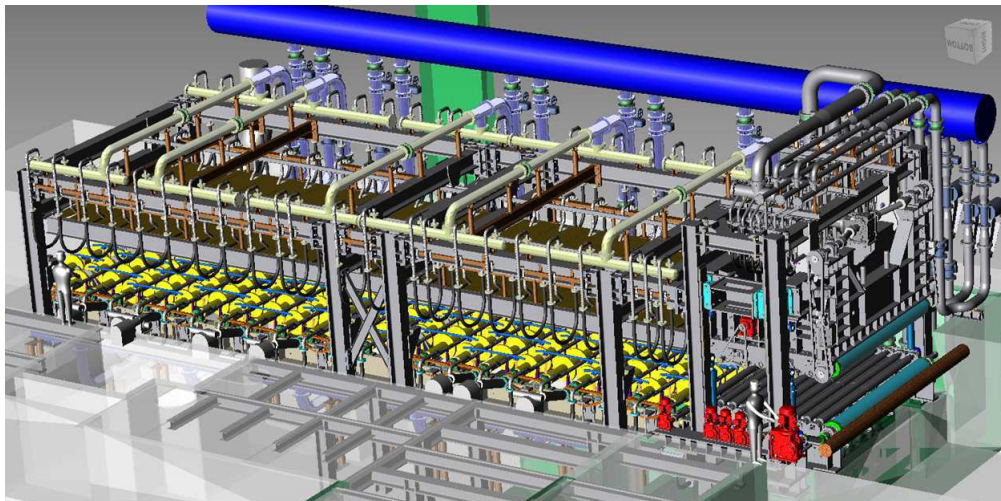


Figure 1.5: CAD installation of spray quenching (Industeel)

### Different quenching baths

In industrial application different kinds of bath are used, the main are:

- Water (with or without salt);
- Oil;
- Aqueous polymer;
- Molten salts;
- Gas.



Figure 1.6: Different baths (Snecma): (a) Polymer tank 18 m<sup>3</sup>, agitated by 6 pumps, (b) Water tank 35 m<sup>3</sup>, agitated by 2 pumps

The cooling rate is a function of the quenchant properties: concentration, viscosity, conductivity, molecular weight, latent heat. . . Quenching in pure water without agitation is rarely used because the metal is covered by a vapor film and the cooling rate decreases until the film breaks up. Several industries such as Snecma added some glycol polymers to speed up the breakdown of the vapor film and to obtain a rapid uniform cooling (Figure 1.4(a)). Ikkene [42] shows that when quenching in water mixed with 10% concentration of polyethylene glycol, the cooling is faster than in pure water. Polymer quenches are less corrosive than water. In fact, each of these quenchants has its own advantages and disadvantages as presented in Table 1.1.

Table 1.1: Advantages and disadvantages of quenchants

|         | Avantages                                                                                                                                                                                                                   | Disadvantages                                                                                                                                                                                                     |
|---------|-----------------------------------------------------------------------------------------------------------------------------------------------------------------------------------------------------------------------------|-------------------------------------------------------------------------------------------------------------------------------------------------------------------------------------------------------------------|
| Water   | <ol style="list-style-type: none"> <li>1. Least expensive quenching medium</li> <li>2. Most energetic environment</li> <li>3. Avoids appearance of strains</li> </ol>                                                       | <ol style="list-style-type: none"> <li>1. Risk of oxidation</li> <li>2. Highly corrosive environment</li> </ol>                                                                                                   |
| Polymer | <ol style="list-style-type: none"> <li>1. Higher quenching ability than water</li> <li>2. Uniform cooling</li> </ol>                                                                                                        | <ol style="list-style-type: none"> <li>1. Expensive quenching medium</li> </ol>                                                                                                                                   |
| Gas     | <ol style="list-style-type: none"> <li>1. Cleanliness and brightness of the steel [8]</li> <li>2. Reduction of the executional costs (unlike the case of quenching in oil)</li> <li>3. Lower rate of deformation</li> </ol> | <ol style="list-style-type: none"> <li>1. Expensive quenching medium (helium)</li> <li>2. Safety considerations due to the high flammability (hydrogen)</li> <li>3. Lower quenching ability than water</li> </ol> |

## 1.3 Regimes of boiling and heat transfer

Air cooling capability is much smaller than liquids (oil, water, polymer). The hardening of steel components by quenching in a stagnant bath or by a liquid spray induces a very high heat transfer rate due to boiling phenomena. This section is structured as follows: first, we introduce the different boiling regimes and the characteristic point (boiling crisis and Leidenfrost point). Next we describe more precisely the heat transfer during boiling regimes. Finally an experimental analysis of the boiling phenomenon during quenching process is presented.

### 1.3.1 Boiling curve

The boiling process has been observed by Nukiyama [9] in 1934. The heat transfer varies during three boiling phenomena phases (film boiling, nucleate boiling and convective heat transfer). Figure 1.7 presents the conventional log-log representation of heat flux versus wall superheat. The heat transfer coefficient and the wall superheat temperature are defined respectively by  $h_{boiling} = q/\Delta T$  and  $\Delta T = T - T_{sat}$ . Several ranges of the boiling curve are noted A-C, C-D and D-E, which describe four different regimes:

- i) **Natural convection:** until the point A, the liquid temperature is lower than the boiling temperature and the present regime is the natural convection;
- ii) **Nucleate boiling:** in the range A-B, the liquid near the superheated wall starts to evaporate by forming bubbles wherever there is nucleate sites. In the range B-C, the formed bubbles tend to collapse locally. The nucleate boiling regime is a very efficient heat transfer since the liquid is in direct contact with the heated surface. The high value of the heat flux (point C), is called the boiling crisis or the departure from nucleate boiling (DNB) [10]. It corresponds to a transition between two boiling regimes. In fact, at this point the population of bubbles becomes too intense and acts as an isolator between the solid and the liquid;
- iii) **Transition boiling:** after the point C, the boiling becomes unstable and the surface is covered by a vapor blanket. Surface conditions oscillate between nucleate boiling and film boiling;
- iv) **Film boiling:** the transition temperature between nucleate boiling and film boiling is called the "Leidenfrost point". In the range D-E, a stable vapor film is formed around the solid. This regime corresponds to a high superheated wall during which the heat transfer value is lower than in nucleate boiling.

### 1.3.2 Heat transfer during boiling

During the quenching process, there is a coupling between the heat transfer rate and the boiling regimes. When the bath temperature is below than the boiling point, no boiling occurs and the heat transfer rate is controlled by natural convection. As the surface temperature increases, liquid motion is strongly influenced by nucleation of bubbles at the

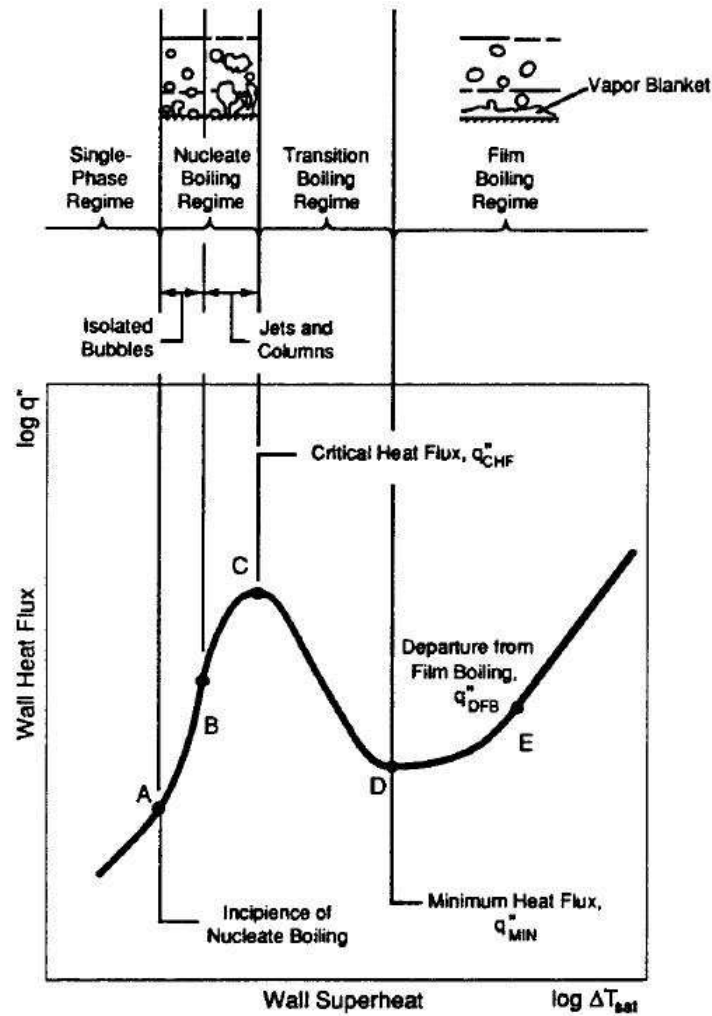


Figure 1.7: Boiling curve for a stagnant pool of liquid at its saturation temperature [2]

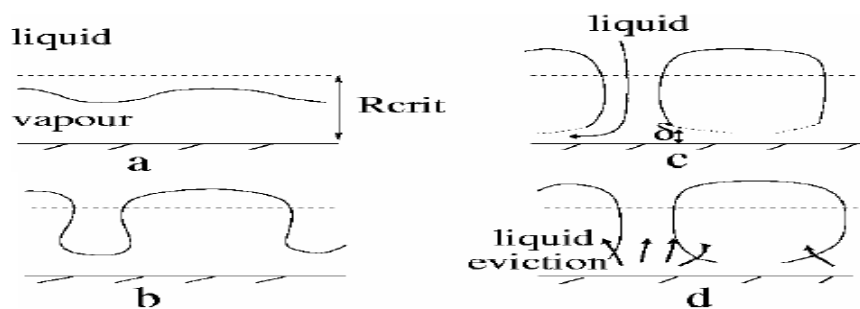


Figure 1.8: Diagram presenting the different stages of Rayleigh-Taylor instability: (a) Instability at the liquid / vapor interface, (b) Droplets going in the vapor blanket, (c) The liquid spreads over the plate and is heated to  $T_{sat}$ , (d) The liquid film is removed [3]

surface. In nucleate boiling, there are two kinds of heat transfer: conduction due to the contact between the solid and the liquid and turbulent convection due to the departure of the bubble from the surface. In the range D-E, the wall is covered by a film vapor and the heat flux is transmitted from the wall by radiation and conduction across the vapor film. From the point E, due to Rayleigh Taylor instability (RTI) a cyclic population of bubbles is detached from the film vapor (Figure 1.8). The detachment of film vapor induces an increase of the heat transfer.

The thermal conductivity of water vapor ( $0,025 \text{ W.m}^{-1}.\text{K}^{-1}$ ) is about 27 times lower than the value of water ( $0,68 \text{ W.m}^{-1}.\text{K}^{-1}$ ). Therefore the film vapor is a heat transfer insulator between the solid and the liquid. To get a better heat exchange, the duration of the film boiling regime must decrease. Therefore a localized agitation near the solid surface is required (Figure 1.6).

### 1.3.3 Boiling modes during quenching

#### 1.3.3.1 Industrial case

Figure 1.9 presents several steps of the heat treatment of a shell, that has been done in Areva at Creusot Forge. Figure 1.9(a) presents the getting out of the shell that was heated in a furnace at a temperature of  $1000 \text{ }^\circ\text{C}$  during several hours. A shell is a hollow cylinder (about 5 m in diameter, 4 m high and 400 mm thick). After the high heat treatment, a water quenching is performed. A set of flexible high temperature thermocouples has been fixed on the shell. The tank is an



(a) Shell taking out of the furnace



(b) Shell transportation to the bath

Figure 1.9: Different steps of heat treatment

octagonal bath about 7.5 m diameter by 6 m high (Figure 1.10). To reduce the duration of the



film boiling regime and to accelerate the cooling of the solid the tank is agitated. Figure 1.11(a) shows the boiling of water that occurs at the interface of the shell during its immersion. The boiling phenomenon becomes more important with the shell immersion Figure 1.11(b)). Before the total immersion, the volume of water covering its upper surface is not so important, then a vapor film is created on its surface as predicted in Figure 1.12.



Figure 1.10: Water agitated tank



(a)  $t = 10$  s



(b)  $t = 16$  s

Figure 1.11: Boiling phenomenon at the shell interface



Figure 1.12: Film vapor at the shell surface

### 1.3.3.2 Micro quenching

In order to obtain high cooling rates, most quenching processes are accomplished in water, oil and aqueous polymer. In this context, the study of heat transfer is complex due to boiling and the rewetting phenomena occurring on the surface of the metal. Figure 1.13 illustrates the quenching of a steel ingot in water; the initial fluid and solid temperature are respectively  $70\text{ }^{\circ}\text{C}$  and  $700\text{ }^{\circ}\text{C}$ . The solid dimensions are  $L = 8\text{ cm}$  and  $l = 2\text{ cm}$ . From left to the right, the pictures illustrate the boiling regime at the solid surface at different time steps. After dipping the solid into water, since

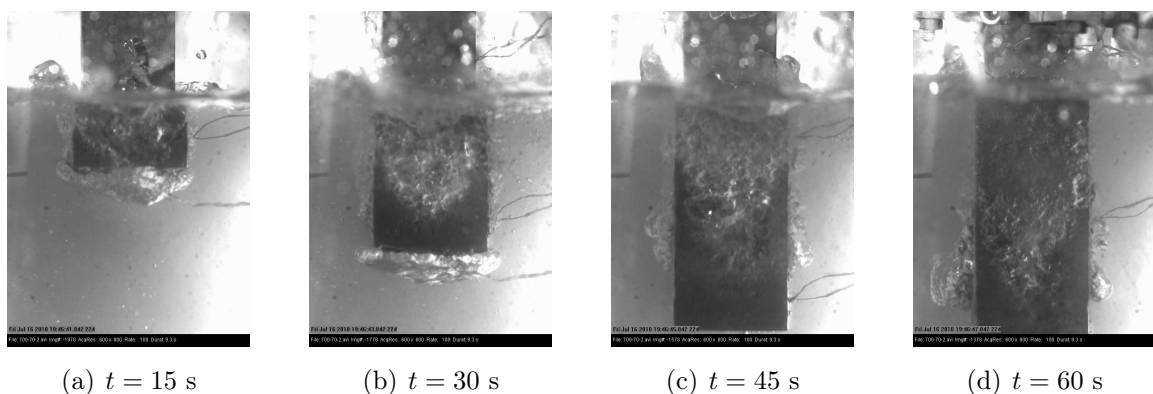


Figure 1.13: Quenching of a steel in water

the steel temperature is above the Leidenfrost temperature, the solid is covered by a vapor film (Figure 1.13(a)). During the immersion of the solid, on the time interval of  $0 - 20\text{ s}$  the boiling mode corresponds to film boiling. After a few seconds, the rewetting of the lower part of the solid begins and nucleate boiling occurs (Figure 1.13(b)). In the interval  $45 - 60\text{ s}$  the lower part

of the solid is cooled. When its temperature becomes lower than the leidenfrost point, intense population of bubbles is formed all over the lower part of the solid Figure 1.13(c)-1.13(d). For an optimized quenching process, the different boiling phases and rewetting phenomena occurring on the steel surface must be controlled. These complex phenomena depend on a lot of parameters such as surface roughness, bath temperature, solid temperature, solid orientation and others. This provides a non-uniform cooling during the quenching process from film boiling to pure convection. Boiling heat transfer analysis is important for many industrial applications. To predict the heat transfer due to boiling phenomena, a brief review of Bourouga [4] analysis is presented in the next section.

## 1.4 Role of Biot number in predicting the boiling duration

The cooling process for the steel during quenching is due to conduction in the part of the steel and to convection and boiling phenomena on its surface. This section is structured as follows. First, we introduce the mean Biot number. Then we describe more precisely a relation between the value of the mean Biot number and the duration of the different boiling regimes.

### 1.4.1 Mean Biot number

The Biot number ( $Bi$ ) is a dimensionless number which represents the ratio of the heat transfer resistance inside the solid to the superficial thermal resistance (1.1). During the heating or the quenching, the solid boundary exhibits a deep gradient and the variation of temperature inside the solid is evaluated by the Biot number.

$$Bi = \frac{hL}{k} \quad (1.1)$$

where  $h$  is the convective heat transfer coefficient,  $L$  is the characteristic length defined as the volume divided by the surface area of the solid ( $L = V/A$ ) and  $k$  is the thermal conductivity of the solid. Since the heat transfer coefficient is a function of space and time, Bourouga [4] defined a mean Biot number function of an average heat transfer coefficient as follows:

$$Bi_m = \frac{h_{av}L}{k} \quad \text{with} \quad h_{av} = \frac{1}{(T_{ini} - T_b)} \int_{T_{ini}}^{T_b} h(T_p) dT_p \quad (1.2)$$

where  $T_b$  is the external temperature and  $T_{ini}$  is the initial solid temperature.

The value of the Biot number informs about the propagation of temperature fields inside the solid. If  $Bi \gg 1$ , the superficial thermal resistance is very small in front of the internal thermal resistance. Then the heat transfer within the solid is governed by conduction and the boiling flow does not have any influence on the heat transfer. It can be assumed that the fluid imposes its temperature at the wall. If  $Bi \ll 1$  the conduction is negligible in front of the superficial thermal resistance, then the temperature field is uniform inside the solid.

### 1.4.2 Duration of boiling modes depends on the mean Biot number

During quenching, the heat transfer mechanism is the result of boiling phenomena and heat conduction. Figure 1.14 presents the duration of boiling modes versus of the mean Biot number.

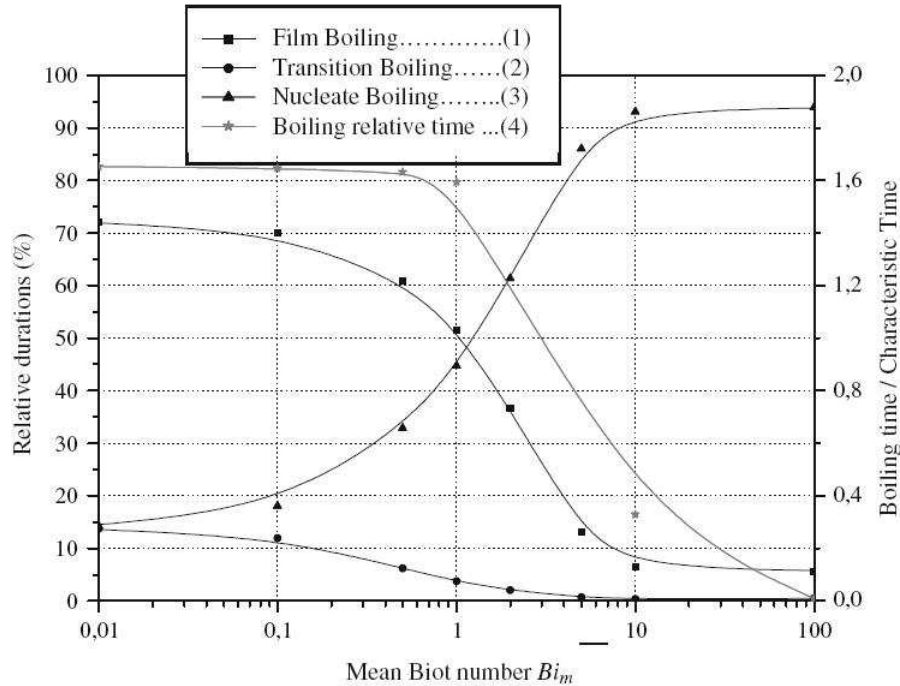


Figure 1.14: Relative duration of different boiling modes depending on the mean Biot number [4]

The curves (1) (2) and (3) correspond to the vertical axis on the left, and present the time value of different boiling phases accounted to the total durations of boiling phenomena. While the curve (4) corresponds to the vertical axis on the right and presents the ratio between the total duration of boiling and the characteristic time of the cooling part.

The characteristic time  $\tau_c$  is determined by:

$$\tau_c = \frac{e^2}{4\alpha r_1^2} \quad (1.3)$$

where  $\alpha$  is the thermal diffusivity,  $e$  is the thickness and  $r_1$  the fundamental eigenvalue which characterize the cooling time according to the thickness.

For  $Bi_m < 0.1$ , the ratio between the total duration of boiling and the characteristic time of cooling is equal to 1.65 then 80% of the entire heat transfer is ensured by the boiling heat transfer. More precisely, 73% of the cooling is assured by film boiling, 15% by transient boiling and 12% by nucleate boiling. In the range  $0.1 < Bi_m < 10.5$ , boiling heat transfer decreases progressively with a dominance of nucleate boiling mode. In the range  $10.5 < Bi_m < 100$ , the heat transfer is strongly ensured by convection and the boiling heat transfer is negligible.

## 1.5 Developing history of ThosT

CEMEF laboratory, within **ThosT** "Thermal Optimization SysTem" project context, has developed a computational methodology able to predict the furnace atmosphere as well as the transient heat transfer to the load in a continuous heat treatment process [28]. **ThosT** has the following characteristics:

- Resolution of incompressible Navier-Stokes equations with high Reynolds using a stabilized finite element method;
- Resolution of thermal problem with stabilized finite element method for convection-diffusion-reaction equations;
- Immersed volume method for modeling such multimaterial flows (fluid/solid);
- Resolution of momentum and energy equations by a monolithic approach, in order to avoid the acquaintance of heat transfer coefficient between the two domains.

These points were developed by Elie Hachem [28] in his Ph.D. work, on the simulation of heat transfer and turbulent flows inside industrial furnaces. In fact, the heat treatment involves three successive operations, by using this software an accurate simulation of the first operation (the heating) is achieved. The first version of **ThosT** were insufficient for the requirements of the industrial partners as it was unable to optimize the quenching process. Therefore the objective of this thesis is to develop the new version of **ThosT** integrating a quenching model where the boiling heat transfer can be considered, thus the industrial partner must be able to optimize the quenching process and to improve the mechanical properties of parts. This work was done within the **ThosT** project context, which includes the following industrial members:

- **Aubert & Duval** ([www.aubertduval.com](http://www.aubertduval.com)) : world leader in alloys, manganese and nickel activities
- **Snecma** ([www.snecma.fr](http://www.snecma.fr)) : aeronautic equipment
- **ArcelorMittal - Industeel** ([www.arcelormittal.com](http://www.arcelormittal.com)) : steelmaker company
- **Manoir Industries** ([www.manoir-industries.com](http://www.manoir-industries.com)): cast and forged metal components
- **Creusot Forge, group Areva** ([www.sfarsteel.com](http://www.sfarsteel.com)): heavy steel fabrication and mechanised welding of complex assemblies
- **SCC, Sciences Computers Consultants** ([www.sconsultants.com](http://www.sconsultants.com)) industrialization and commercialization of material forming software (Ximex, **ThosT**, Ludovic, Fakuma)
- **Transvalor** ([www.transvalor.fr](http://www.transvalor.fr)) : industrialization and commercialization of material forming software (FORGE2, FORGE3, TFORM3, THERCAST, REM3D)

## 1.6 Objectives and outline of the thesis

The main objective of this thesis is to develop a boiling model for quenching process. This model must be capable to handle with industrial equipment i.e. large **3D** problems (macro scale). To validate this model, numerical and experimental investigations were performed at the bubble size scale (meso-scale). In this thesis, modelling and analysis of boiling were achieved at different scales using the same mathematical approach, first at the bubble size scale (meso scale-Figure 1.15), second at the CFD scale (macro scale-Figure 1.15). Therefore the research

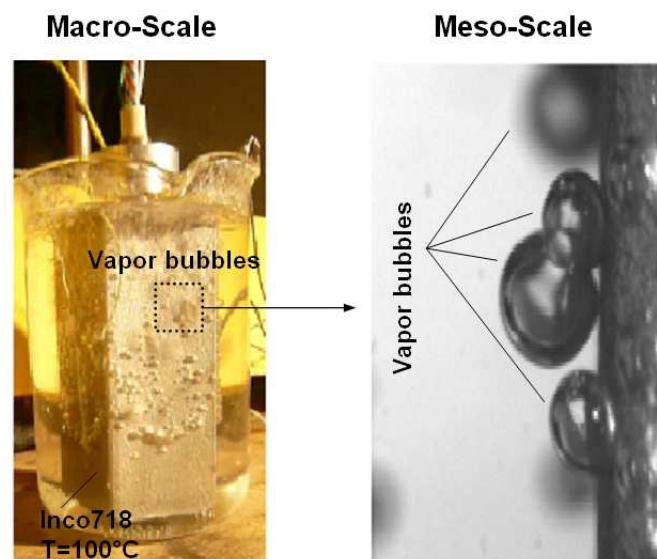


Figure 1.15: Multi-Scale for Boiling

objectives within this project were set in two lines:

- Meso-Scale
  - Development of a physical-mathematical model for bubble evolution (meso scale). This will mainly includes an interface tracking model, a growth model and a surface tension model.
  - Experimental investigation during bubble evolution is performed to validate the numerical approach. A high speed camera is used to capture the bubble shape evolution and two non-intrusive methods "Particle Image Velocimetry & Laser Induced Fluorescence" are used to measure the temperature and the velocity field.
- Macro-Scale
  - Establishment of a general model of boiling at macro scale by using the same mathematical model as in meso scale.
  - Simulation of an industrial case.

This thesis is divided in six chapters. Chapter 1 is a bibliographic review of the quenching process and the boiling phenomenon. Chapter 2 presents a detail description of the simulation of quenching without modelling the heat transfer due to boiling. Firstly, a study and an analysis of the thermal shocks was present, then the influence of mesh size and time step on the stability has been investigated. Finally the mathematical modelling of quenching without boiling was applied to an industrial application. Chapter 3 is devoted to the numerical simulation of nucleate boiling which requires an interface tracking model, a growth model and a surface tension model. The computation of different benchmarks of bubbles growth, coalescence and ascension has been carried out. Chapter 4 is predicted to an experimental investigation, which can offer an accurate measurement of the temperature and the velocity fields. These measurements were achieved by using the Particle Image Velocimetry & the Laser Induced Fluorescence. To avoid the nonuniform distribution of incident light, the two dyes LIF thermometry was used to provide an accurate measurement of the temperature. Experimental results are presented and discussed. A general model of boiling during quenching process is presented in chapter 5. The simulation of film boiling regime is predicted. The computational results of a benchmark test are present, as well as an application to an industrial case. In chapter 6, conclusion and future outlook are discussed.

## 1.7 Résumé français

Lors du procédé de trempe, le liquide vaporisable mis en contact avec la pièce métallique portée à très haute température s'échauffe localement de façon très brutale pouvant conduire à l'ébullition. Différents régimes apparaissent au cours de la trempe en fonction de l'évolution des phases liquide et vapeur: le régime de caléfaction, le régime d'ébullition nucléée et le régime de convection. La modélisation numérique du phénomène d'ébullition lors de la trempe est complexe et nécessite à la fois des études expérimentales et des simulations numériques directes. Les phénomènes étudiés lors de cette thèse sont liés aussi bien au changement de phase aux petites échelles (germination et croissance d'une bulle de vapeur) ainsi qu'à l'ébullition aux grandes échelles intervenant lors de la trempe (dizaine de mètres). L'ébullition turbulente, aussi bien d'un point de vue expérimental (visualisation, mesure de champ ...) que d'un point de vue numérique (couplage Navier Stokes, thermique, vaporisation, turbulence induite), représente un challenge tant scientifique qu'industriel. Dans cette thèse on développera un modèle multiphasique qui sera intégré dans le logiciel "**ThosT**" afin de prendre en compte la phase de transition liquide vapeur, l'ébullition, qui s'avère jouer un rôle fondamental dans le refroidissement des pièces trempées.

# References

- [1] H. Macklouf. *Modélisation numérique du soudage à l'arc*. PhD thesis, Mines Paris, 2008.
- [2] J. C. Rozzi, W. P. Klinzing, and I. Mudawar. Effects of spray configuration on the uniformity of cooling rate and hardness in the quenching of aluminum parts with nonuniform shapes. *ASM International*, 1:49–60, 1992.
- [3] N. Seiler-Marie. *Modélisation et simulation des phénomènes d'ébullition et du transfert de chaleur dans la zone d'impact d'un jet sur une plaque chaude*. PhD thesis, Institut National Polytechnique de Toulouse, 2003.
- [4] B. Bourouga and J. Gilles. Roles of heat transfer modes on transient cooling by quenching process. *International Journal Mater Form*, 3(2):77–88, 2009.
- [5] L. F. Canale and G. E. Totten. Quenching technology: a selected overview of the current state-of-the-art. *Mater*, 4:461–467, 2005.
- [6] P. L. Woodfield, A. K. Mozumber, and M. Monde. On the size of the boiling region in jet impingement quenching. *International Journal of Heat and Mass Transfer*, 52:460–465, 2009.
- [7] R. Ikkene, Z. koudil, and M. Mouzali. Pouvoir de refroidissement des solutions de trempe à base de polymères hydrosolubles. *Comptes Rendus Chimie*, 11:297–306, 2007.
- [8] L. lefèvre and V. Perrin. Trempe gazeuse en conditions optimisées. *Traitement Thermique*, 2000.
- [9] S. Nukiyama. The maximum and minimum values of the heat  $q$  transmitted from metal to boiling water under atmospheric pressure (english translation of the original paper published in journal japan soc. mech. engrs vol. 37 ,367-374 (1934)). *International Journal of Heat and Mass Transfer*, 9:1419–1433, 1966.
- [10] L. S. Tong and Y. S. Tang. *Boiling Heat transfer and two-phase flow*. Chemical and Mechanical Engineering. 1997.
- [11] E. Hachem. *Stabilized Finite Element Method for Heat Transfer and Turbulent Flows inside Industrial Furnaces*. PhD thesis, Ecole Nationale Supérieure des Mines de Paris, 2009.





# Chapter 2

## CFD for modelling quenching process

### Contents

---

|            |                                                                                          |           |
|------------|------------------------------------------------------------------------------------------|-----------|
| <b>2.1</b> | <b>Stabilized finite element method of convection-diffusion equation . . . . .</b>       | <b>20</b> |
| 2.1.1      | Resolution of the energy equation . . . . .                                              | 21        |
| 2.1.2      | Spatial discretization . . . . .                                                         | 21        |
| 2.1.3      | Time integration . . . . .                                                               | 22        |
| 2.1.4      | Stabilized finite element method of unsteady diffusion problem                           | 23        |
| <b>2.2</b> | <b>Stabilised finite element methods for incompressible Navier-Stokes flow . . . . .</b> | <b>32</b> |
| 2.2.1      | Weak form of the incompressible Navier-Stokes equations . . .                            | 32        |
| 2.2.2      | Variational MultiScale Method . . . . .                                                  | 33        |
| <b>2.3</b> | <b>Immersed volume method for modelling quenching process .</b>                          | <b>36</b> |
| 2.3.1      | LevelSet Method . . . . .                                                                | 36        |
| 2.3.2      | Anisotropic mesh adaptation . . . . .                                                    | 37        |
| <b>2.4</b> | <b>Numerical tests and validation . . . . .</b>                                          | <b>41</b> |
| 2.4.1      | Study of the agitation influence . . . . .                                               | 41        |
| 2.4.2      | Industrial case . . . . .                                                                | 46        |
| <b>2.5</b> | <b>Conclusions . . . . .</b>                                                             | <b>52</b> |
| <b>2.6</b> | <b>Résumé français . . . . .</b>                                                         | <b>53</b> |

---

The cooling process during quenching of the metal is due to conduction inside the solid part and to convection and boiling phenomena on its surface. This chapter is dedicated to the modelling of the quenching process without considering the heat transfer due to boiling. In the first section, the unsteady convection diffusion equation is discretized by the Galerkin finite element method. Since in quenching process the solid boundary exhibits a deep gradient, this polynomial piecewise method in unsteady diffusion problem is polluted by thermal shocks and oscillations. This Galerkin method is not sufficient to get an accurate solution for the thermal problem. To understand the reason of these oscillations, the stability condition and the effect of several parameters on the thermal shocks are presented. Different unstructured grids were considered to study the mesh size influence. By varying the time step and the thermal diffusivity, the influence of these parameters on thermal shocks was also predicted. This analysis has been achieved in **2D** and **3D** case. To overcome this drawback, we present the extension of the enriched method by interpolating the solution to the real time, referred as an enriched method with time interpolation **EM-I**. This method shows good stability and accuracy for the **3D** cooling case. In the next section, the resolution of the governing Navier-Stokes equations with a variational multiscale method is presented. This stabilizing scheme is recommended to deal with convection dominated problems. Both the velocity and the pressure spaces are enriched by a space of bubbles that cures the spurious oscillations in the convection-dominated regime as well as the pressure instability. In the third section, we introduce the immersed volume method that was adopted to simulate the quenching process. This method is based on several parameters: the LevelSet Method to immerse and prescribe the heated solid interface, the anisotropic mesh refinement to adapt the interface between the solid and the fluid and the mixing laws to define a single physical property (as thermal conductivity, mass density, specific heat capacity and viscosity....) all over the domain of computation. In the last section, a modelling of an industrial case with a study of the bath agitation influence on the solid cooling has been achieved. Then, the quenching of the heated solid in a calm bath has been performed, followed by a comparison between numerical and experimental results showing the necessity to model the heat transfer due to boiling.

## 2.1 Stabilized finite element method of convection-diffusion equation

This section is structured as follows: First, we introduce the resolution of the energy equation governed by a conduction-convection equation. In fact, during quenching some boundary side exhibits a steep gradient which can induce nonphysical thermal evolution when solving it with a polynomial piecewise method. Second, we present a study of several parameters on the thermal shocks; this study has been done in a **2D** case and in a **3D** benchmark offering an exact solution. After showing the affection of these parameters on the Galerkin solution, it is clear that to have an accurate solution without oscillations this polynomial method is not sufficient. For this reason, the stabilized finite element methods are introduced in the end of this section. Particularly details of the enriched method interpolation **EM-I** and the validation of this method in the **3D** benchmark are presented.

### 2.1.1 Resolution of the energy equation

In this part, the equation governing the heat transfer in the quenching process is presented. The thermal analysis is performed using the energy conservation equation with the following boundary and initial conditions:

$$\begin{cases} \rho c_p \left( \frac{dT}{dt} + \mathbf{v} \cdot \nabla T \right) - \nabla \cdot (k \nabla T) = f & \text{in } \Omega \\ T = T_0 & \text{at } t = 0 \\ T = T_{imp} & \text{on } \partial\Omega_T \\ -k \nabla T \cdot \mathbf{n} = \phi_{imp} & \text{on } \partial\Omega_q \\ -k \nabla T \cdot \mathbf{n} = h_c (T - T_{out}) & \text{on } \partial\Omega_c \end{cases} \quad (2.1)$$

Where  $T$  and  $T_0$  are respectively the temperature and the initial temperature of the domain  $\Omega$  having the following properties:  $k$  is the thermal conductivity,  $\rho$  is the mass density,  $c_p$  is the specific heat capacity,  $\mathbf{v}$  is a computed fluid velocity and  $f$  is the energy source term.

The boundary of the domain  $\Omega$  is divided as follows:

$\partial\Omega_T$  is the boundary on which the temperature  $T_{imp}$  is imposed.

$\partial\Omega_q$  is the boundary on which an inflow heat flux is imposed  $\phi_{imp}$ .

$\partial\Omega_c$  is the boundary on which the heat exchange is defined by a convection heat transfer  $h_c$  with the external temperature  $T_{out}$ .

Considering the following functional spaces:

$$\begin{cases} L^2(\Omega) = \{w, \int_{\Omega} w^2 < \infty\} \\ H_0^1(\Omega) = \{w \in L^2(\Omega), \nabla w \in [L^2(\Omega)]^d \mid w = 0 \forall x \in \partial\Omega\} \end{cases} \quad (2.2)$$

The  $L^2(\Omega)$  inner product is defined by  $(u, v)_{\Omega} = \int_{\Omega} u v \, d\Omega$ , then the weak formulation of the thermal problem is expressed as follows:

$$\begin{cases} \left( \rho c_p \frac{\partial T}{\partial t}, \varphi \right)_{\Omega} + a(T, \varphi) = (f, \varphi) & \forall \varphi \in H_0^1(\Omega) \\ a(T, \varphi) := \rho c_p (\mathbf{v} \cdot \nabla T, \varphi) + (k \nabla T, \nabla \varphi) \end{cases} \quad (2.3)$$

### 2.1.2 Spatial discretization

The computational domain is decomposed into a set of  $N_{el}$  elements  $K$ . Using this partition, the functional space  $H_0^1(\Omega)$  can be approached by a finite discrete space

$$V_h = \{ \varphi_h \in C^0(\Omega), \varphi_h|_K \in P^n(K), \forall K \in \mathcal{T}_h \} \quad (2.4)$$

The above weak Galerkin equation (2.3) is written in a discrete form as follows:

$$\left( \rho c_p \frac{\partial T_h}{\partial t}, \varphi_h \right)_{\Omega} + a(T_h, \varphi_h) = (f, \varphi_h) \quad \forall \varphi_h \in V_h \subset H_0^1(\Omega) \quad (2.5)$$

If  $n = 1$ , the  $P^1$  linear interpolation functions  $N$  at node  $i$  is denoted by  $N_i$ . The standard Galerkin method is applied to equation (2.5), leading to:

$$\mathbf{C} \frac{\partial T}{\partial t} + \mathbf{K}T = \mathbf{F} \quad (2.6)$$

- $T$  is the solution vector of nodal temperatures  $T_i$ .
- $\mathbf{C}$  is the mass matrix, symmetric positive definite, defined as follows:

$$\mathbf{C}_{ij} = \int_{\Omega} \rho c_p N_i N_j d\Omega$$

- $\mathbf{K}$  is the stiffness matrix result of the sum of the conductive and diffusion terms:

$$\mathbf{K}_{ij} = \int_{\Omega} \rho c_p \mathbf{v} \cdot \nabla N_i N_j d\Omega + \int_{\Omega} k \nabla N_i \cdot \nabla N_j d\Omega \quad (2.7)$$

- $\mathbf{F}$  is the internal source:

$$\mathbf{F}_{ij} = \int_{\Omega} f N_j d\Omega$$

where  $N_j$  is the linear interpolation function at node  $j$ . Finite element method applied to (2.1) brings us to solve a system of  $N_{el}$  equations. The solution of the differential equations requires a time discretization, which is necessary to approximate the time derivative of the temperature.

### 2.1.3 Time integration

By using the  $\theta$  scheme the time derivative can be approximated at  $t = n\Delta t$ , the parameter  $\theta$  of the method taken to be in the interval  $[0, 1]$ :

$$\mathbf{C} \frac{T^n - T^{n-1}}{\Delta t} + \mathbf{K} (\theta T^n + (1 - \theta) T^{n-1}) = \theta \mathbf{F}^{n+1} + (1 - \theta) \mathbf{F}^n \quad (2.8)$$

By considering ( $\theta = 1$ ) the  $\theta$  scheme corresponds to the backward Euler scheme, ( $\theta = 0.5$ ) to the Crank-Nicolson scheme and ( $\theta = 0$ ) to the forward Euler scheme. The forward and backward Euler schemes have first-order accuracy. The forward scheme solution can be polluted by oscillations if the time step is chosen too large for the critical problem. However, the Backward Euler and the Crank-Nicholson schemes are unconditionally stable. The Crank-Nicholson is a second order accuracy scheme; thus this scheme offers two advantages. For simplicity, the backward Euler method is considered, then the temperature at time  $n$  depends explicitly on the temperature at time  $n - 1$ . The finite difference discretization of equation (2.1) is given by:

$$\rho c_p \left( \frac{T^n - T^{n-1}}{\Delta t} \right) + \rho c_p \mathbf{v} \cdot \nabla T^n - \nabla \cdot (k \nabla T^n) = f^n \quad \text{in } \Omega \times ]0, t[ \quad (2.9)$$

## 2.1.4 Stabilized finite element method of unsteady diffusion problem

### 2.1.4.1 Stability condition

The classical Galerkin discretization normally exhibits high thermal shocks and spurious oscillations. For example during the cooling process, in the vicinity of the interface, a heating can be measured in a particular position while a cooling was imposed on the boundary [3]. This non physical result indicates the necessity to introduce the stabilized finite method. The numerical stability condition connecting the time step to the space step is [4]:

$$\Delta t \geq \frac{h^2}{4a} = \Delta t_{critical} \quad (2.10)$$

where  $h$  is the mesh size defined on each element,  $\Delta t$  denotes the chosen time step, and  $a$  is the diffusion coefficient. The critical time step is the smallest time step for which the thermal solution does not present any oscillations. It can be noted that the stability condition is not satisfied for low thermal diffusivity materials and/or when the time step is small. One of the objective of this thesis is to simulate boiling phenomena during quenching process. In fact, the numerical simulation of this process in a vaporizable liquid, recommends a small time step since the duration of the boiling phenomena is too short (it rarely exceeds the second). Then, it will be difficult to satisfy the stability condition (2.10) and we prefer to use the stabilized finite element method to get a proper solution for the thermal problem.

### 2.1.4.2 Study of the time step, the mesh size and the thermal diffusivity influence on the thermal shocks

We consider the unit square initially at a uniform temperature of 50 °C. A Dirichlet boundary condition is applied on the left side, the temperature is set to 200 °C (Figure 2.1). Actually, the Galerkin method is affected by thermal shocks and spurious oscillations near the heated wall. Thus the solution of thermal problem presents a wrong behavior, to get an accurate result the stability condition must be verified. In order to study the influence of each parameter present in the stability condition on the thermal shocks several numerical simulations were made. Here we consider  $h = 2.5$  mm,  $a = 2.5$  w · m<sup>-1</sup> · °C<sup>-1</sup> and  $\Delta t = 0.1$  s. Then each of the time step and the thermal diffusivity was modified separately to evaluate its influence on the temperature oscillation.

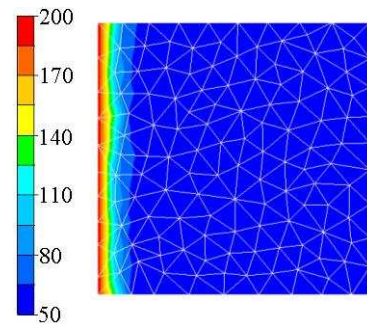
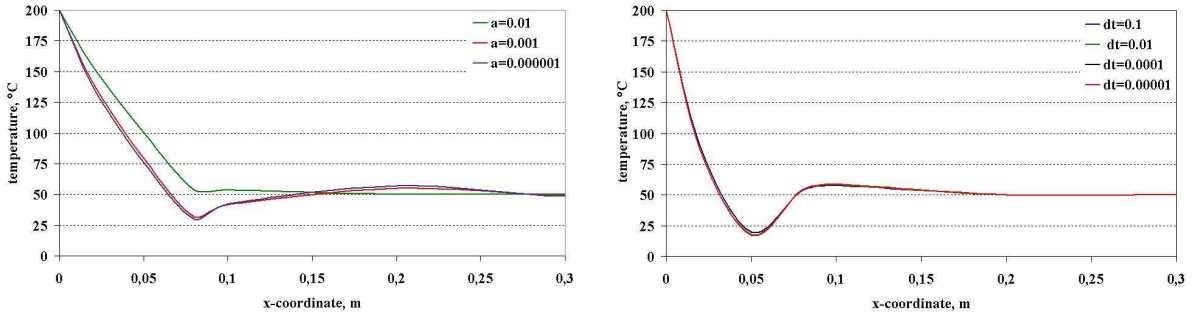


Figure 2.1: Temperature (°C) evolution

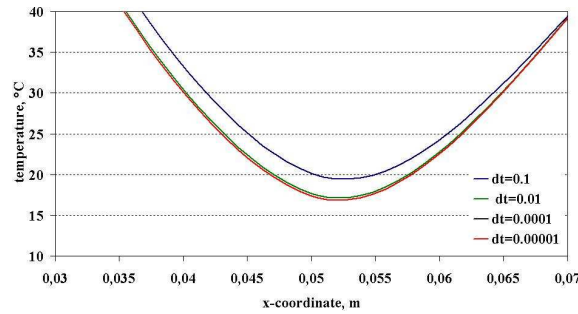
The temperature profiles for different time steps and different thermal diffusivities are illustrated in (Figure 2.2). As expected, for low  $\Delta t$  (Figure 2.2(c)) and small thermal diffusivity  $a$  (Figure 2.2(a)), the solution is polluted by oscillations. It can be noted that the thermal shocks (oscillations) increase whenever the time step decreases. During quenching process the solid boundary exhibits a steep gradient due to the rapid cooling. Then the use of the Galerkin

method will provide oscillation as it was observed in this paragraph. Since in quenching a small time step is needed to model the boiling phenomenon, then the thermal solution is polluted by oscillation (Figure 2.2(c)). Despite the fact that the mesh refinement can decrease this oscillation, this refinement can not be a solution because it increases the computational cost neither the thermal diffusivity because it is fixed by the material properties. This is why to get an accurate evolution of the temperature during quenching, the stabilized method is the only solution.



(a) Predicted temperature profiles for different thermal diffusivities

(b) Predicted temperature profiles for different time steps



(c) Close-up on the thermal shock of Figure 2.2(b)

Figure 2.2: Influence of thermal diffusivity and time step on the thermal shock

### 2.1.4.3 Cooling of a semi-infinite 3D bar

We consider the classical cooling problem of a semi-infinite steel bar. This test has been treated before in several PHD works [5, 6, 3]; the advantage of this test is the existence of analytical solutions. Thus a comparison can be made between the analytical solution (2.11) and the numerical one. We take a three-dimensional bar  $10 \times 10 \times 100 \text{ mm}^3$  at an initially temperature of  $T_0 = 800 \text{ °C}$ . Here, we assume that there is no heat exchange with the external environment and that on the left face of the bar a Dirichlet boundary condition ( $T_s = 25 \text{ °C}$ ) is applied. The analytical solution is given by:

$$T(x, t) = T_s + (T_0 - T_s) \operatorname{erf} \left( \frac{x}{2\sqrt{at}} \right) \quad (2.11)$$

Here,  $x$  is the depth in uniaxial direction.

During the numerical simulation of this benchmark, the bar physical properties are considered constant with the following value: the conductivity  $k = 15 \text{ W} \cdot \text{m}^{-1}\text{K}^{-1}$ , the density  $\rho = 7800 \text{ Kg} \cdot \text{m}^{-3}$  and the specific heat  $c_p = 360 \text{ J} \cdot \text{Kg}^{-1}\text{K}^{-1}$ . An unstructured triangulation with a mesh size  $h = 10 \text{ mm}$  and a time step  $\Delta t = 0.25 \text{ s}$  are used.

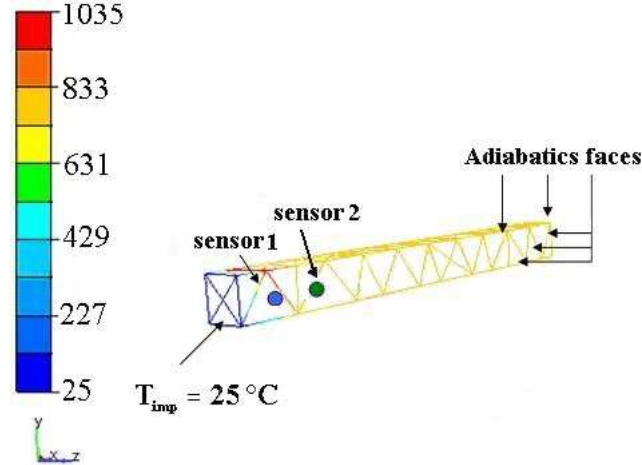


Figure 2.3: Problem configuration

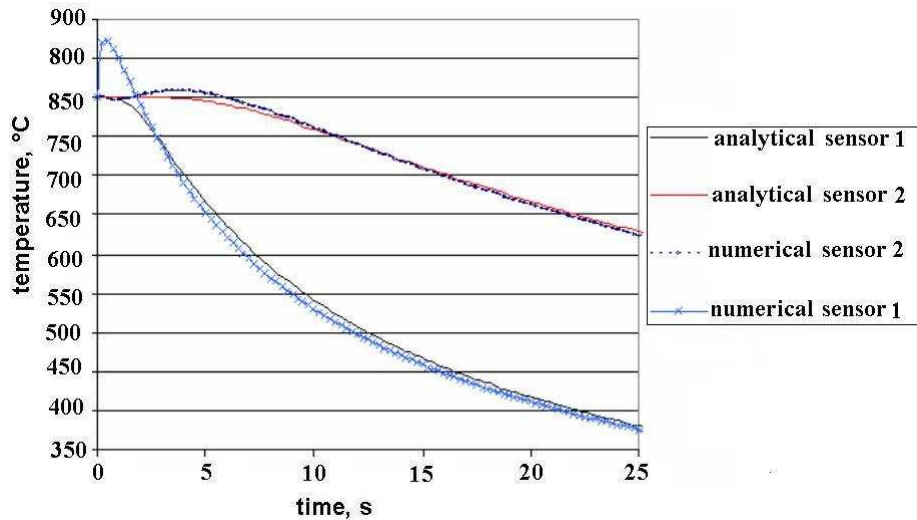
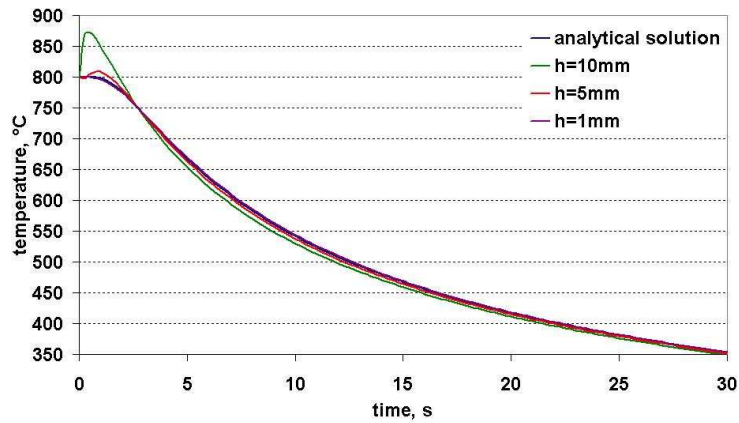


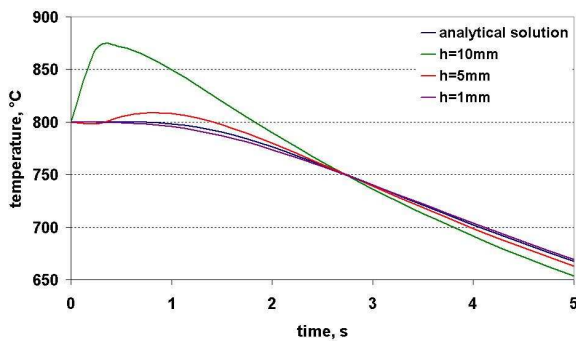
Figure 2.4: Comparison between numerical temperature and analytical one at nodes situated at  $h$  and  $2h$  from the heated side

Figure 2.4 presents the evolution in time of the temperature for two nodes placed respectively at  $h$  and  $2h$  (Figure 2.3). We compare temperature evolution given by the Galerkin with the analytical solution. It can be noted how the Galerkin method is affected by thermal shocks and how spurious oscillations appear near the cooled boundary. Since the shock is higher at the first sensor, we evaluate in this **3D** test, the influence of the time step and the mesh size at this node. When the time step decreases and/or the mesh size increases, the thermal shock becomes more

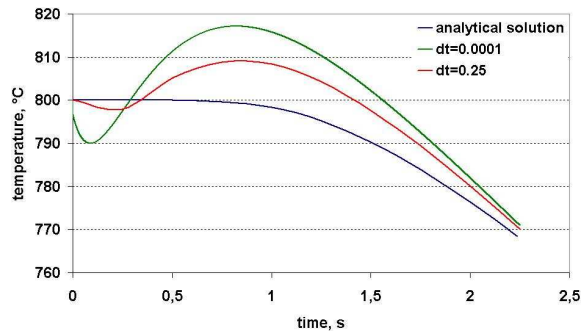




(a) Predicted temperature profiles for different mesh sizes



(b) Close-up on the thermal shock



(c) Predicted temperature profiles for different time steps

Figure 2.5: Influence of thermal diffusivity, mesh size and time step on the thermal shock

noticed (Figures 2.5(c)- 2.5(b)). This situation may be viewed as modelling the cooling of a solid at 800 °C facing an injected cold water at 25 °C in an agitated bath, such quenching process has been presented in section 2.4.1. In quenching process the cooling is not due to a Dirichlet condition but to water injection; in both cases the solution is polluted by oscillations due to the high gradient of temperature. Therefore, in this thesis it is important to present a review of the stabilized method used to compute properly the temperature in the numerical simulation of quenching.

#### 2.1.4.4 Enriched method interpolation (EM-I)

Actually, in many heat treatment processes such as heating or/and quenching, some boundary side exhibits a steep gradient which can induce nonphysical thermal evolution. As it can be seen in the previous paragraphs; when the stability condition is not verified, the Galerkin method is often affected by nonphysical oscillations. In order to get an accurate solution for the unsteady diffusion problem, we present a brief review of the stabilized methods devoted to the transient conduction heat transfer. A diffusion-split method has been developed by Fachinotti [7], the concept of this method is to add an artificial conductivity when the stability condition is not verified. The authors [8, 9] present new approaches to get Galerkin Least Square (GLS) and the

Galerkin Gradient Least Square (GGLS), which consist on modifying the differential equation in a residual method and then getting the weak formulation by the integration by part. These methods satisfy consistency, however the (GLS) method can be equivalent to the polynomial interpolation (Galerkin method) with a much larger time step. Harari [10] offers a coupling between the stabilized finite element method and finite time integration efficient for advection diffusion reaction problem. The stabilized method used in this work, has been developed in the first year of my Ph.D. (for more details see Hachem [1] and al.). Similarly to [10], this method proposed an extension of the enriched method by interpolating the solution to the real time step and it is known as enriched method with interpolation **EM-I**. In this part we present **EM-I**, starting with the enriched space approach, passing to the time step interpolation and we conclude by presenting the numerical result and a validation of this method in the **3D** bar cooling case.

### The enriched space approach

The main idea of the enriched space approach is to decompose the usual space in macro-scales which is the space of the piecewise polynomials and micro-scales which is represented by the so-called bubbles (Figure 2.6). In fact let's start by describing the diffusion problem, then once the space discretization and time integration are defined, the multiscale method is presented. Here, we suppose that the diffusion is the only mode of heat transfer, then the energy equation (2.1) becomes:

$$\begin{cases} \text{Find a scalar valued function } T(x,t): \\ \rho c_p \frac{dT}{dt} - \nabla \cdot (k \nabla T) = f & \text{in } \Omega \times (0, t_f) \\ T = T_0 & \text{at } t = 0 \\ T = 0 & \text{on } \partial\Omega \times (0, t_f) \end{cases} \quad (2.12)$$

Where  $f$  is the energy source term assuming to be square integrable in  $\Omega$ . Using the implicit time integration presented in section 2.1.3 and the classical Galerkin approximation, the weak formulation of the unsteady diffusion problem (2.12) is:

$$\begin{cases} \text{Find } T_h \in V_h \subset H_0^1(\Omega) \text{ such that:} \\ \rho c_p \left( \frac{T_h^n}{\Delta t}, w_h \right) + (k \nabla T_h^n, \nabla w_h) = (f, w_h) + \rho c_p \left( \frac{T_h^{n-1}}{\Delta t}, w_h \right) & \forall w_h \in V_h \end{cases} \quad (2.13)$$

Let us rewrite the governing discrete equation (2.13) by a simple form:

$$\begin{cases} \text{Find } T_h \in V_h \subset H_0^1(\Omega) \text{ such that:} \\ \rho c_p \left( \frac{T_h^n}{\Delta t}, w_h \right) + (k \nabla T_h^n, \nabla w_h) = (g, w_h) & \forall w_h \in V_h \end{cases} \quad (2.14)$$

where  $g = f + \rho c_p T_h^{n-1} / \Delta t$ .

The finite dimensional spaces  $V_h$  is enriched and enlarged into:

$$V = V_h \oplus V' \quad (2.15)$$

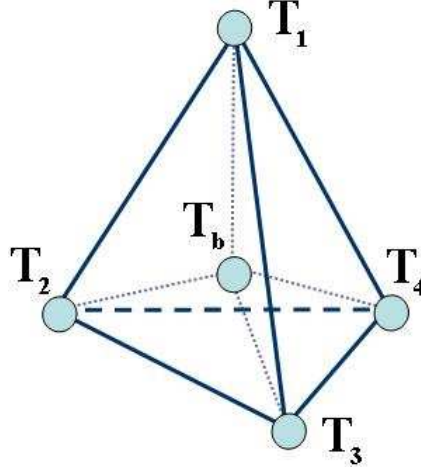


Figure 2.6: Decomposition of a tetrahedra in coarse scale and micro-scale

where  $V_h$  is the space spanned by continuous piecewise polynomials and  $V'$  denotes the space of bubble function. The bubble basis function satisfies:

$$\begin{cases} \varphi(x) > 0 & x \in K \\ \varphi(x) = 0 & x \in \partial K \\ \varphi(x) = 1 & \text{at the barycenter of } K \end{cases} \quad (2.16)$$

Then a new functional space  $V$  is created and the scalar field  $T \in V$  is the sum of a coarse scale (space of polynomial) and a fine scale (space of bubble).

$$T = T_h + T' = T_h + \sum_{K \in \tau_h} T_{b_K} \varphi \quad (2.17)$$

where  $T_h$  is the linear part and  $T_{b_K}$  is the unknown bubble coefficient.

First, we begin by solving equation (2.14) on the local-scale, called "bubble equation":

$$\rho c_p \left( \frac{T^n}{\Delta t}, \varphi \right)_K + (k \nabla T^n, \nabla \varphi)_K = (g, \varphi)_K \quad (2.18)$$

By using the decomposition of the solution  $T^n$  and substituting it into (2.18), we get:

$$\rho c_p \left( \frac{T_h^n}{\Delta t}, \varphi \right)_K + T_{b_K} \left( \frac{\rho c_p}{\Delta t} \varphi, \varphi \right)_K + (k \nabla T_h^n, \nabla \varphi)_K + T_{b_K} (k \nabla \varphi, \nabla \varphi)_K = (g, \varphi)_K \quad (2.19)$$

By integrating by parts within each element the third term of equation (2.19) becomes  $-(k T_h^n, \Delta \varphi)_K$ . Since a linear shape functions are used, then the second derivatives vanishes, and we get:

$$(k \nabla T_h^n, \nabla \varphi)_K = -(k T_h^n, \Delta \varphi)_K = 0 \quad (2.20)$$

Let us consider the  $L^2(\Omega)$  norm  $\|\varphi\|_{0,K} = \int_K \varphi d\Omega$ , equation (2.19) becomes:

$$\rho c_p \left( \frac{T_h^n}{\Delta t}, \varphi \right)_K + T_{b_K} \frac{\rho c_p}{\Delta t} \|\varphi\|_{0,K}^2 + T_{b_K} k \|\nabla \varphi\|_{0,K}^2 = (g, \varphi)_K \quad (2.21)$$

We compute the bubble coefficient in each element  $K \in \mathcal{T}_h$  as follows:

$$T_{b_K} = \frac{1}{\frac{\rho c_p}{\Delta t} \|\varphi\|_{0,K}^2 + k \|\nabla \varphi\|_{0,K}^2} \left( g - \frac{\rho c_p}{\Delta t} T_h^n, \varphi \right)_K \quad (2.22)$$

Once the bubble is computed, it will be substituted by its value in equation (2.13) on the macro scale. The bubbles considered here are quasi-static, i.e., that the effect of their time variation may be neglected. The static condensation procedure will eliminate the bubbles function at the element level

$$\rho c_p \left( \frac{T_h^n}{\Delta t}, w_h \right) + \sum_{K \in \mathcal{T}_h} T_{b_K} \left( \frac{\rho c_p}{\Delta t} \varphi, w_h \right)_K + (k \nabla T_h^n, \nabla w_h) = (g, w_h) \quad (2.23)$$

Substituting (2.22), The small-scale term can be expressed on each element  $K$  as:

$$\begin{aligned} T_{b_K} \left( \frac{\rho c_p}{\Delta t} \varphi, w_h \right)_K &= \frac{1}{\frac{\rho c_p}{\Delta t} \|\varphi\|_{0,K}^2 + k \|\nabla \varphi\|_{0,K}^2} \left( g - \frac{\rho c_p}{\Delta t} T_h^n, \varphi \right)_K \left( \frac{\rho c_p}{\Delta t} \varphi, w_h \right)_K \\ &= \frac{1}{\frac{\rho c_p}{\Delta t} \|\varphi\|_{0,K}^2 + k \|\nabla \varphi\|_{0,K}^2} \left( g - \frac{\rho c_p}{\Delta t} T_h^n, \frac{\rho c_p}{\Delta t} w_h \right)_K \end{aligned} \quad (2.24)$$

Following the lines in [11, 12], one can simplify the expression of (2.24) into

$$T_{b_K} \left( \frac{\rho c_p}{\Delta t} \varphi, w_h \right)_K = \frac{Ch_K^2}{\frac{\rho c_p}{\Delta t} h_K^2 + k\bar{C}} \left( g - \frac{\rho c_p}{\Delta t} T_h^n, \frac{\rho c_p}{\Delta t} w_h \right)_K \quad (2.25)$$

where  $C$  and  $\bar{C}$  are positive constants. The stabilizing parameter  $\varsigma_K$  is computed for each element separately:

$$\varsigma_K = \frac{Ch_K^2}{\frac{\rho c_p}{\Delta t} h_K^2 + k\bar{C}} \quad (2.26)$$

In this work, we take  $C = 1$  and  $\bar{C} = 6$ , see [13] for more details. By substituting the small-scale term by its value in (2.23), the resulting equation is equivalent to the standard Galerkin method plus a stabilization term weighted by  $\varsigma_K$ .

$$\rho c_p \left( \frac{T_h^n}{\Delta t}, w_h \right) + (k \nabla T_h^n, \nabla w_h) - \sum_{K \in \mathcal{T}_h} \varsigma_K \left( \frac{\rho c_p}{\Delta t} T_h^n, \frac{\rho c_p}{\Delta t} w_h \right)_K = (g, w_h) - \sum_{K \in \mathcal{T}_h} \varsigma_K \left( g, \frac{\rho c_p}{\Delta t} w_h \right)_K \quad (2.27)$$

The bubble contribution took effect in one hand on transient term and in other hand on the modified source term  $g$  which represents the previous time step solution and the source term. The stabilization term contains a zero order term in the test function  $w_h$  and is equivalent to a change in the test function as follows:

$$v_h = w_h \left( 1 - \varsigma_K \frac{\rho c_p}{\Delta t} \right) \quad (2.28)$$

In the absence of the source term  $f$ , this can be seen as a modified problem by the Galerkin method with a much larger time step. The authors in [8] pointed out that the solution is free of oscillations but will no longer be the solution to the original problem.

### Time interpolation

The previous method improves stability by adding a stabilizing term obtained after condensation of the bubble function in the original problem. But as mentioned before, this can work only in particular cases when the source term is zero. To fix ideas, we rewrite the new stabilized formulation of (2.27) after replacing  $g$  by its value:

$$\rho c_p \left( \frac{T_h^n}{\Delta t}, w \left( 1 - \varsigma_K \frac{\rho c_p}{\Delta t} \right) \right) + (k \nabla T_h^n, \nabla w) = \left( f + \rho c_p \frac{T_h^{n-1}}{\Delta t}, w \left( 1 - \varsigma_K \frac{\rho c_p}{\Delta t} \right) \right) \quad (2.29)$$

It is clear when this method is applied to an unsteady diffusion problem without a source term, it can be interpreted as a Galerkin method with a modified larger time step:

$$\rho c_p \left( \frac{T^*}{\Delta t^*}, w \right) + (k \nabla T^*, \nabla w) = \left( \rho c_p \frac{T_h^{n-1}}{\Delta t^*}, w \right) \quad (2.30)$$

where  $T^*$  is the modified solution and  $\Delta t^*$  is the new time step given on each  $K$  by:

$$\frac{\Delta t}{\Delta t^*} = \left( 1 - \varsigma_K \frac{\rho c_p}{\Delta t} \right) = \frac{1}{\xi} \quad , \quad \xi > 0 \quad (2.31)$$

An easy way to correct the time step distortion introduced by the previous stabilization is to use an interpolation of the solution to the real time step (Figure 2.7):

$$\begin{aligned} T_h^n &= T_h^{n-1} + (T^* - T_h^{n-1}) \frac{\Delta t}{\Delta t^*} \implies \\ T^* &= \xi T_h^n + (1 - \xi) T_h^{n-1} \end{aligned} \quad (2.32)$$

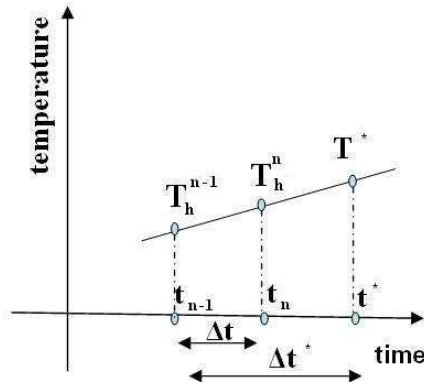


Figure 2.7: Interpolation of the solution to the real time step

By substituting (2.32) into (2.30) we obtain:

$$\left( \frac{\rho c_p}{\Delta t^*} (\xi T_h^n + (1 - \xi) T_h^{n-1}), w \right) + (k \nabla (\xi T_h^n + (1 - \xi) T_h^{n-1}), \nabla w) = \left( \rho c_p \frac{T_h^{n-1}}{\Delta t^*}, w \right) \quad (2.33)$$

since  $\Delta t = \frac{\Delta t^*}{\xi}$

$$\implies \left( \rho c_p \frac{T_h^n}{\Delta t}, w \right) + (\xi k \nabla T_h^n, \nabla w) = \left( \rho c_p \frac{T_h^{n-1}}{\Delta t}, w \right) + ((\xi - 1) k \nabla T_h^{n-1}, \nabla w) \quad (2.34)$$

Finally, we get:

$$\left( \rho c_p \frac{T_h^n - T_h^{n-1}}{\Delta t}, w \right) + (\xi k \nabla T_h^n, \nabla w) = ((\xi - 1) k \nabla T_h^{n-1}, \nabla w) \quad (2.35)$$

Comparing (2.35) with the original version (2.14), we see that the process of enlarging our space with bubbles and then modifying the time step yields a stabilized finite element formulation for the unsteady heat diffusion problem. This contribution acts as a new artificial, time-dependent thermal conductivity  $\xi k$  integrated over the element's interior and tuned by a local stabilization term  $\varsigma_K$  that ensures an oscillating-free solution. Details on the approach and numerical examples are published in [1].

#### **Numerical validation of the EM-I method:**

Several numerical simulations have been done to show the efficiency of the new method [1]. In this paragraph, we present only the validation of this method on the **3D** case presented above. We compare the results given by the Galerkin and the new method with the exact solution at a node situated at  $2h$  far from the cooled side. The Galerkin method is affected by thermal shocks and spurious oscillations near the cooled boundary. These instabilities appear at the initial time steps and decrease as the solution converges to the steady state. The new solution has no oscillations. Both predictions converge to the analytical solution at the end of the simulation (Figure 2.8).

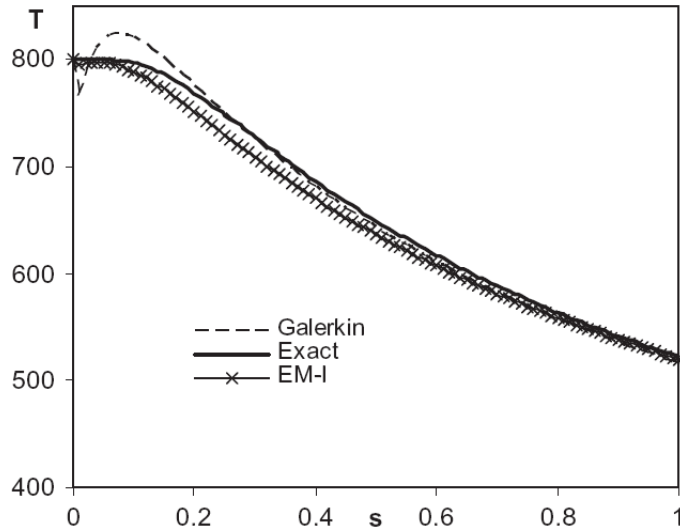


Figure 2.8: Evolution of the temperature ( $^{\circ}\text{C}$ ) at a node situated  $2h$  far from the cooled side [1]

## 2.2 Stabilised finite element methods for incompressible Navier-Stokes flow

The aim of this section is to give the mathematical model, based on eulerian formulation discretized by the finite element method, for the incompressible Navier-Stokes equations. We start by introducing the weak formulation in velocity-pressure variables, then by presenting the Variational MultiScale stabilization method. The incompressible flow of a Newtonian fluid in a domain  $\Omega$  is described by the incompressible Navier-Stokes equations and by the continuity equation:

$$\begin{cases} \rho \partial_t \mathbf{u} + \rho \mathbf{u} \cdot \nabla \mathbf{u} - \nabla \cdot (2\mu \boldsymbol{\varepsilon}(\mathbf{u})) + \nabla p = \mathbf{f} \\ \nabla \cdot \mathbf{u} = 0 \end{cases} \quad (2.36)$$

### 2.2.1 Weak form of the incompressible Navier-Stokes equations

We begin with the classic form of the Navier-Stokes equations. The function spaces for the velocity, the pressure and the weighting functions are respectively defined by:

$$V = \left\{ \mathbf{u}(\mathbf{x}, t) \mid \mathbf{u}(\mathbf{x}, t) \in H^1(\Omega)^d, \mathbf{u} = \mathbf{h} \text{ on } \Gamma_h \right\} \quad (2.37)$$

$$Q = \left\{ p(\mathbf{x}, t) \mid p(\mathbf{x}, t) \in L^2(\Omega), \int_{\Omega} p \, d\Omega = 0 \right\} \quad (2.38)$$

The momentum equation is multiplied by a velocity basis function  $\mathbf{w}$  and the continuity equation by a pressure basis function  $q$ . After integrating these equations all over the domain  $\Omega$ , the weak form of the Navier-Stokes equations becomes:  $(\mathbf{u}, p) \in V \times Q$  such that:

$$\begin{cases} \rho (\partial_t \mathbf{u}, \mathbf{w})_{\Omega} + \rho (\mathbf{u} \cdot \nabla \mathbf{u}, \mathbf{w})_{\Omega} + \\ \quad (2\mu \boldsymbol{\varepsilon}(\mathbf{u}) : \boldsymbol{\varepsilon}(\mathbf{w}))_{\Omega} - (p, \nabla \cdot \mathbf{w})_{\Omega} = (\mathbf{f}, \mathbf{w})_{\Omega} + (\mathbf{h}, \mathbf{w})_{\Gamma_h} \quad \forall \mathbf{w} \in V_0 \\ (\nabla \cdot \mathbf{u}, q)_{\Omega} = 0 \quad \forall q \in Q_0 \end{cases} \quad (2.39)$$

where  $(\varphi, \psi)_{\Omega} = \int_{\Omega} \varphi \psi \, d\Omega$  is simply the  $L^2(\Omega)$  inner product.

The standard Galerkin approximation consists in multiplying the strong equation by a set of test functions, and then integrating. The domain  $\Omega$  is decomposed into  $N_{el}$  elements  $K$ . These  $K$  elements cover the domain and are either disjointed or share a complete edge (or face in **3D**). Applying this partition  $\mathcal{T}_h$ , the above-defined functional spaces (2.37) and (2.38) are approached by finite dimensional spaces spanned by continuous piecewise polynomials such that:

$$V_h = \left\{ \mathbf{u}_h \mid \mathbf{u}_h \in C^0(\Omega)^n, \mathbf{u}_{h|K} \in P^1(K)^d, \forall K \in \mathcal{T}_h \right\} \quad (2.40)$$

$$Q_h = \left\{ p_h \mid p_h \in C^0(\Omega), p_{h|K} \in P^1(K), \forall K \in \mathcal{T}_h \right\} \quad (2.41)$$

The Galerkin discrete problem leads to solve the following mixed problem:

$$\begin{aligned} & \text{Find a pair } (\mathbf{u}_h, p_h) \in V_h \times Q_h, \text{ such that: } \forall (\mathbf{w}_h, q_h) \in V_{h,0} \times Q_h \\ & \left\{ \begin{array}{l} \rho (\partial_t \mathbf{u}_h, \mathbf{w}_h)_\Omega + \rho (\mathbf{u}_h \cdot \nabla \mathbf{u}_h, \mathbf{w}_h)_\Omega \\ \quad + (2\mu \boldsymbol{\varepsilon}(\mathbf{u}_h) : \boldsymbol{\varepsilon}(\mathbf{w}_h))_\Omega - (p_h, \nabla \cdot \mathbf{w}_h)_\Omega = (\mathbf{f}, \mathbf{w}_h)_\Omega + (\mathbf{h}, \mathbf{w}_h)_{\Gamma_h} \\ (\nabla \cdot \mathbf{u}_h, q_h)_\Omega = 0 \end{array} \right. \end{aligned} \quad (2.42)$$

The finite element discretization spaces for the velocity and the pressure need to satisfy a condition, known as "Ladyzhenskaya-Babuska-Brezzi (LBB) condition". The use of inappropriate combinations of interpolation functions to represent the velocity and pressure fields [14, 15, 16, 17, 18, 19, 20] yields to instable schemes. In this thesis, we are interested in the numerical simulation of the quenching in an agitated bath. In fact, during the numerical simulation, the solution oscillations can appear due to convection dominated flows and to the pressure instability. The Galerkin approximation is not sufficient to prevent the solution oscillations. Regarding these instabilities, the velocity and the pressure fields need to be stabilized by addition of stabilization terms, e.g. residual terms weighted by tuned parameters.

## 2.2.2 Variational MultiScale Method

The multiscale decomposition applied to the weak form of the Navier-Stokes equations (2.42) presented in this section, has been developed by Hachem [1]. The velocity and pressure fields are decomposed into resolvable coarse-scale and unresolved fine-scale (subgrid scale which can not be captured by the finite element mesh) [15, 18, 21, 20]. Let  $V = V_h \oplus V'$  and  $Q = Q_h \oplus Q'$ , where,  $V_h$  and  $Q_h$  represent the coarse scale spaces and  $V'$  and  $Q'$  represent the subgrid spaces. The spaces were enriched by a space of bubbles that leads to better accuracy (in terms of numerical dissipation and stability) and to eliminate the spurious pressure oscillations. This corresponds to a decomposition of the unknowns  $u$  and  $p$  as

$$\mathbf{u} = \mathbf{u}_h + \mathbf{u}' \quad (2.43)$$

$$p = p_h + p' \quad (2.44)$$

The same decomposition is applied for the weighting functions  $\mathbf{w} = \mathbf{w}_h + \mathbf{w}'$  and  $q = q_h + q'$ . Here, we consider a Dirichlet boundary condition and we split equations (2.42) into two sub-problems, the coarse-scale problem (2.45) and the subgrid-scale problem (2.46). By integrating by parts within each element and by considering the subgrid scale  $H^1$  orthogonal to the finite element space, the viscous terms  $(2\mu \boldsymbol{\varepsilon}(\mathbf{u}') : \boldsymbol{\varepsilon}(\mathbf{w}_h))_\Omega$  and  $(2\mu \boldsymbol{\varepsilon}(\mathbf{u}) : \boldsymbol{\varepsilon}(\mathbf{w}'))_K$  vanish and we obtain:

$$\left\{ \begin{array}{l} \rho (\partial_t (\mathbf{u}_h + \mathbf{u}'), \mathbf{w}_h)_\Omega + \rho ((\mathbf{u}_h + \mathbf{u}') \cdot \nabla (\mathbf{u}_h + \mathbf{u}'), \mathbf{w}_h)_\Omega \\ \quad + (2\mu \boldsymbol{\varepsilon}(\mathbf{u}_h) : \boldsymbol{\varepsilon}(\mathbf{w}_h))_\Omega - ((p_h + p'), \nabla \cdot \mathbf{w}_h)_\Omega \\ \quad = (\mathbf{f}, \mathbf{w}_h)_\Omega \quad \forall \mathbf{w}_h \in V_{h,0} \\ (\nabla \cdot (\mathbf{u}_h + \mathbf{u}'), q_h)_\Omega = 0 \quad \forall q_h \in Q_{h,0} \end{array} \right. \quad (2.45)$$



$$\left\{ \begin{array}{l} \rho (\partial_t (\mathbf{u}_h + \mathbf{u}'), \mathbf{w}')_K + \rho ((\mathbf{u}_h + \mathbf{u}') \cdot \nabla (\mathbf{u}_h + \mathbf{u}'), \mathbf{w}')_K \\ \quad + (2\mu \epsilon(\mathbf{u}') : \epsilon(\mathbf{w}'))_K - ((p_h + p'), \nabla \cdot \mathbf{w}')_\Omega \\ = (\mathbf{f}, \mathbf{w}')_\Omega \quad \forall \mathbf{w}' \in V'_0 \\ (\nabla \cdot (\mathbf{u}_h + \mathbf{u}'), q')_\Omega = 0 \quad \forall q' \in Q'_0 \end{array} \right. \quad (2.46)$$

The stabilized formulation is achieved by two steps. First, we solve the subgrid-scale problem (2.46) to compute  $(u', p')$  using residual terms. Then, the subgrid scales solution is substituted into the coarse scale problem (2.45), this will provide additional terms known as the stabilization terms. The subgrid scale problem equations are highly coupled and are extremely difficult to solve because of the subscale time dependency term  $\partial_t \mathbf{u}'$  and the non-linear convection term  $(\mathbf{u}_h + \mathbf{u}') \cdot \nabla (\mathbf{u}_h + \mathbf{u}')$ . For these reasons several assumptions need to be considered to solve the subgrid scale problem:

- i) the subgrid scale function  $\mathbf{u}'$  is considered time independent, then the subgrid scales are quasi-static, e.g.  $\partial_t \mathbf{u}' = 0$ ;
- ii) since linear interpolation functions are used, the second derivative term of the momentum residual  $-(\nabla \cdot (2\mu \epsilon(\mathbf{u}_h)), \mathbf{w}')_\Omega$  vanishes;
- iii) the non-linear convection term is approximated by considering the large scale velocity as the only convection velocity  $(\mathbf{u}_h + \mathbf{u}') \cdot \nabla (\mathbf{u}_h + \mathbf{u}') \approx \mathbf{u}_h \cdot \nabla (\mathbf{u}_h + \mathbf{u}')$ ;
- iv) the subgrid scale velocity is assumed to vanish on the element  $K$  boundary and on the domain boundary.

By considering these assumptions, the subgrid-scale problem (2.46) becomes:

$$\left\{ \begin{array}{l} \rho (\mathbf{u}_h \cdot \nabla \mathbf{u}', \mathbf{w}')_\Omega + (2\mu \epsilon(\mathbf{u}') : \epsilon(\mathbf{w}'))_\Omega + (\nabla p', \mathbf{w}')_\Omega \\ = (\mathcal{R}_M, \mathbf{w}')_\Omega \quad \forall \mathbf{w}' \in V'_0 \\ (\nabla \cdot \mathbf{u}', q')_\Omega = (\mathcal{R}_C, q')_\Omega \quad \forall q' \in Q'_0 \end{array} \right. \quad (2.47)$$

where  $\mathcal{R}_M$  and  $\mathcal{R}_C$  are the momentum and the continuity residual terms for the large resolved scales defined by:

$$\mathcal{R}_M = \mathbf{f} - \rho \partial_t \mathbf{u}_h - \rho \mathbf{u}_h \cdot \nabla \mathbf{u}_h - \nabla p_h \quad (2.48)$$

$$\mathcal{R}_C = \nabla \cdot \mathbf{u}_h \quad (2.49)$$

This formulation (2.47) leads to accurate solution and stability especially in high convection dominated flows [21] because it counts the small scale pressure effect. To solve the small scale problem Franca and Oliveira [22] separate the small scales unknowns and replace the continuity equation by the small scale pressure Poisson equation (PPE) terms. Then they express the small

scale pressure as a function of the residual terms. For the numerical implementation, Hachem [1] adopts the stabilization coefficient proposed by Codina in [23]:

$$p' \approx \tau_C \mathcal{R}_C \quad \text{with} \quad \tau_C = \left( \left( \frac{\mu}{\rho} \right)^2 + \left( \frac{c_2 \|\mathbf{u}\|_K}{c_1 h} \right)^2 \right)^{1/2} \quad (2.50)$$

where  $c_1$  and  $c_2$  are constants independent from the mesh size  $h$ . It remains to compute the small scale velocity. As pointed out in Codina [23] the small scale velocity is function of the large scale momentum equation residual and not of the continuity equation residual. Following Masud and Khurram [24] and assuming that the large scale momentum residual  $\mathcal{R}_M$  is constant, Hachem [1] presents the fine scale velocity as follows:

$$\mathbf{u}' = \tau_K \mathcal{R}_M \quad (2.51)$$

The stabilization parameter  $\tau_K$  is naturally obtained by the resolution of the fine scale problem. By considering the assumptions that were used before for the subgrid scale, equation (2.45) becomes:

$$\left\{ \begin{array}{l} \rho (\partial_t \mathbf{u}_h, \mathbf{w}_h)_\Omega + (\rho \mathbf{u}_h \cdot \nabla \mathbf{u}_h, \mathbf{w}_h)_\Omega + (\rho \mathbf{u}_h \cdot \nabla \mathbf{u}', \mathbf{w}_h)_\Omega + (2\mu \epsilon(\mathbf{u}_h) : \epsilon(\mathbf{w}_h))_\Omega \\ - (p_h, \nabla \cdot \mathbf{w}_h)_\Omega - (p', \nabla \cdot \mathbf{w}_h)_\Omega = (\mathbf{f}, \mathbf{w}_h)_\Omega \quad \forall \mathbf{w}_h \in V_{h,0} \\ (\nabla \cdot \mathbf{u}_h, q_h)_\Omega + (\nabla \cdot \mathbf{u}', q_h)_\Omega = 0 \quad \forall q_h \in Q_{h,0} \end{array} \right. \quad (2.52)$$

Furthermore using an integration by parts the following terms become:

$$(\rho \mathbf{u}_h \cdot \nabla \mathbf{u}', \mathbf{w}_h)_\Omega = -(\mathbf{u}', \rho \mathbf{u}_h \cdot \nabla \mathbf{w}_h)_\Omega \quad (2.53)$$

$$(\nabla \cdot \mathbf{u}', q_h)_\Omega = -(\mathbf{u}', \nabla q_h)_\Omega \quad (2.54)$$

Using the above relations and by substituting the expressions of both the fine-scale pressure (2.50) and the fine-scale velocity (2.51) in equation (2.52), we get:

$$\left\{ \begin{array}{l} \rho (\partial_t \mathbf{u}_h, \mathbf{w}_h)_\Omega + (\rho \mathbf{u}_h \cdot \nabla \mathbf{u}_h, \mathbf{w}_h)_\Omega \\ - \sum_{K \in \Omega_h} (\tau_K \mathcal{R}_M, \rho \mathbf{u}_h \cdot \nabla \mathbf{w}_h)_K + (2\mu \epsilon(\mathbf{u}_h) : \epsilon(\mathbf{w}_h))_\Omega \\ - (p_h, \nabla \cdot \mathbf{w}_h)_\Omega - \sum_{K \in \Omega_h} (\tau_C \mathcal{R}_C, \nabla \cdot \mathbf{w}_h)_K \\ = (\mathbf{f}, \mathbf{w}_h)_\Omega \quad \forall \mathbf{w}_h \in V_{h,0} \\ (\nabla \cdot \mathbf{u}_h, q_h)_\Omega - \sum_{K \in \Omega_h} (\tau_K \mathcal{R}_M, \nabla q_h)_K = 0 \quad \forall q_h \in Q_{h,0} \end{array} \right. \quad (2.55)$$

The advantage of this method is that the stabilization terms appear naturally. Equation (2.55) is made of the Galerkin terms and stabilization terms that are evaluated on the elements  $K$  of the domain. The Variational Multiscale Method offers several benefits:

- i) it cures the solution instability in the convection-dominated regime;
- ii) it satisfies the inf-sup condition for the velocity and pressure interpolations and it overcomes the pressure instability;
- iii) the stabilization terms are added in a consistent way to the Galerkin formulation.

Many different approximations have been proposed and several estimations of stabilizing parameters can be found in the literature, the most common [25, 26, 27, 20] is:

$$\tau_K = \left( \left( \frac{2}{\Delta t} \right)^2 + \left( \frac{4\mu}{\rho h^2} \right)^2 + \left( \frac{2|u_k|}{h} \right)^2 \right)^{-1/2} \quad (2.56)$$

## 2.3 Immersed volume method for modelling quenching process

This section describes the immersed volume method (IVM). First we present the LevelSet Method to immerse and prescribe the heated solid. Then to adapt the interface between the solid and the fluid, an anisotropic mesh refinement is used. Finally, Mixing laws are applied to define a single physical property (as thermal conductivity, mass density, specific heat capacity and viscosity....) all over the domain of computation.

### 2.3.1 LevelSet Method

LevelSet approach, volume of fluid and phase field are several methods to define implicitly the interface between two phase-flows. By using the LevelSet methods, the interface  $\Gamma$  is defined by the zero iso-value of a signed distance function:

$$\alpha(\mathbf{x}) = \begin{cases} \text{dist}(\mathbf{x}, \Gamma) & \text{inside } \Gamma \\ -\text{dist}(\mathbf{x}, \Gamma) & \text{outside } \Gamma \end{cases} \quad (2.57)$$

In multidomain problems the physical and thermodynamic properties may be discontinuous across the interface. By using a distance function, single continuous physical properties (such as density or viscosity ...) are defined for the whole computational domain. Thanks to this single properties a single set of equations can describe the coupled problem in the whole domain  $\Omega$ . Let  $\Omega_f$  and  $\Omega_s$  be respectively the fluid and the solid domain, the density, the viscosity and the

heat capacity are computed using a linear interpolation mixing law as follows:

$$\left\{ \begin{array}{l} \rho = H(\alpha)\rho_f + (1 - H(\alpha))\rho_s \\ \mu = H(\alpha)\mu_f + (1 - H(\alpha))\mu_s \\ C_p = H(\alpha)C_{pf} + (1 - H(\alpha))C_{ps} \\ \rho C_p = H(\alpha)\rho_f C_{pf} + (1 - H(\alpha))\rho_s C_{ps} \\ \rho C_p T_0 = H(\alpha)\rho_f C_{pf} T_f + (1 - H(\alpha))\rho_s C_{ps} T_s \\ \kappa = \left( \frac{H(\alpha)}{\kappa_f} + \frac{1 - H(\alpha)}{\kappa_s} \right)^{-1} \end{array} \right. \quad (2.58)$$

where  $H$  is a smoothed Heaviside function given by:

$$H(\alpha) = \begin{cases} 1 & \text{if } \alpha > \varepsilon \\ \frac{1}{2} \left( 1 + \frac{\alpha}{\varepsilon} + \frac{1}{\pi} \sin \left( \frac{\pi\alpha}{\varepsilon} \right) \right) & \text{if } |\alpha| \leq \varepsilon \\ 0 & \text{if } \alpha < -\varepsilon \end{cases} \quad (2.59)$$

Here  $\varepsilon$  is the interface thickness,  $\varepsilon = O(h)$  function of the mesh size  $h$ . The system (2.58) represents all global physical and thermodynamical properties and the initial temperature. The computation of the conductivity by a linear mixing law lead to inaccurate solution [28], for this reason we use an harmonic mean formulation to calculate the global conductivity. Throughout the domain  $\Omega$ , the density and the specific heat capacity vary inversely proportional, for this reason in the thermal problem (2.1) the product of these parameters is used as an entry parameters. Like other parameters, the product is defined by a linear mixing law. Since initially the solid and the fluid do not have the same temperature, the initial temperature is computed in the same way (2.58).

### 2.3.2 Anisotropic mesh adaptation

In many numerical simulations, it is noted that coupling the adaptive finite element analysis with error estimation offers several advantages. A coarse isotropic mesh can be used for the construction of the simplified solid geometries, but mesh refinement is critical at the liquid-solid interface, for two reasons: firstly the very different physical and thermodynamical properties of the solid and liquid phases, secondly to pre-adapt complex three-dimensional geometries more precisely the sharp corners [29]. In this subsection we present a **3D** tetrahedral, unstructured and anisotropic mesh adaptation, based on a local optimizations. In general, the generation of an anisotropic mesher is more difficult and more complicated than isotropic mesher since the refinement is realized in a specific direction [30]. The metric fields used in anisotropic adaption are computed by a posteriori error estimator [31, 32]. The use of the anisotropic mesh adaptation in application involving complex three-dimensional geometries offers several advantages:

- capturing the interface between subdomains (fluid and structure for example);
- comparing to an isotropic mesh a great number of nodes is saved, which provides a lower computational time and less memory capacity;
- construction of a metric that fix the mesh size in the the LevelSet gradient direction.

Gruau [33] presents an anisotropic adaptive mesh created by using a mesh generator "MTC" developed at CEMEF by Coupez [30]. This mesher is based on local mesh topology optimizations and the minimal volume principle [34, 35]. The mesh topology is ameliorate by improving the quality of the worst element of the triangulation [36]. A brief review of definitions used in mesh topologies and the metric offering a refinement in a precise direction near the interface are presented in the next paragraph.

### 2.3.2.1 Basic definitions

**Mesh adaptation:** In particular, since consecutive remeshing processes are needed in metal forming simulations [30, 37, 38], mesh generation becomes mandatory. Several adaptation methods exist, the most common are the following:

- h-adaptation: which changes the mesh size (refinement in a specified region);
- p-adaptation: which increases the polynomial order of the shape function;
- r-adaptation: which repositions the nodes specially near the interface;
- hp-adaptation: it is a combination of h-adaptation and p-adaptation.

In this work, an h-adaptation is considered as a mesh refinement tool. In fact the solution is computed in the initial coarse mesh and a mesh refinement is realized in a certain region where the solution errors are important. The objective of this paragraph is to develop a metric tensor used for h-adaptation and to generate a unstructured anisotropic meshes [39].

**A metric:** It is a symmetric  $d \times d$  matrix, positive defined tensor, which can be diagonalized in:

$$\mathbb{M} = \mathbb{R} \begin{pmatrix} \frac{1}{h_1^2} & & 0 \\ & \ddots & \\ 0 & & \frac{1}{h_d^2} \end{pmatrix} \mathbb{R}^\top \quad (2.60)$$

Where  $d$  is the space dimension and  $\mathbb{R}$  is a rotation matrix whose columns are the eigenvectors of  $\mathbb{M}$ , defining the remeshing directions.  $(h_i^{-2})_{1 \leq i \leq d}$  is the corresponding eigenvalues which are function of the mesh sizes  $(h_i)_{1 \leq i \leq d}$ .

Example:

By considering the metric  $\mathbb{M} = \begin{pmatrix} 5 & 0 \\ 0 & 50 \end{pmatrix}$  in cartesian axes, the mesh sizes correspond to  $h_1 = 0.447$  in the  $x$  direction and  $h_2 = 0.141$  in the  $y$  direction. Remeshing the two dimensional domain  $\Omega = [0;1]^2$  by using the metric  $M$ , we get the anisotropic mesh predicts in Figure 2.9.

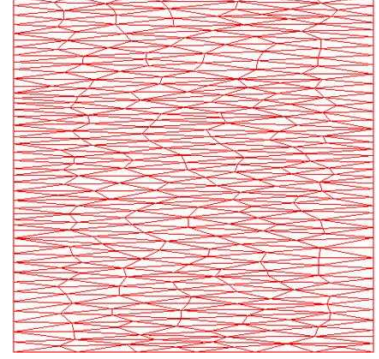


Figure 2.9: Anisotropic mesh

**Scalar product and distance computation:**

This metric represents a local base in a Euclidean space, then a scalar product and a distance computation can be defined:

$$\|\mathbf{x}\|_{\mathbb{M}} = \sqrt{\mathbf{x}^t \cdot \mathbb{M} \cdot \mathbf{x}} \quad \langle \mathbf{x} \cdot \mathbf{y} \rangle_{\mathbb{M}} = \mathbf{x}^t \cdot \mathbb{M} \cdot \mathbf{y}$$

**A simplex:** A  $K$ -simplex of  $\mathbb{R}^d$  is the convexhull of  $K + 1$  nodes in  $\mathbb{R}^d$ . For example a 2 simplex is a triangle and a 3 simplex is a tetrahedron.

**A unit metric:** The objective is to construct a unit mesh (in which all edges have a length close to 1) [40].

**Geometric representation of a metric:**

A metric tensor can be represented geometrically by its unit sphere. Let  $P$  be a point of the mesh  $\tau_h$  of  $\Omega$ , the unit ball conform to metric  $\mathbb{M}$  of center  $P$  is defined geometrically as the set of points that confirm the following relation:

$$\|\mathbf{PY}\|_{\mathbb{M}} = 1 \tag{2.61}$$

The set of points corresponding to metric  $\mathbb{M}$  at point  $P$  describes an ellipse in **2D** and an ellipsoidal in **3D** (Figure 2.10). It can be noted that the principal axes of the ellipsoidal are given by the eigenvectors of  $\mathbb{M}$  and the radius of each axis by the square root of the inverse eigenvalues.

**Anisotropic Mesh Adaptation based on a posteriori error estimate:**

The mesh adaptation methods are based on the approximation error estimate. The approximation error is the difference between the exact and the numerical solution). Cea's lemma shows that the approximation error is upper bounded by the interpolation error. Thus the generation of the mesh is based on the controlling of the interpolation error; Frey [2] used the Taylor series expansion with integral rest and demonstrates that the interpolation error is a function of the hessian of the variable. Then informations about the anisotropic directions and the stretching factor are given by the Hessian as follows:

$$\|u - \Pi_h u\|_{\infty, K} \leq c_d \max_{x \in K} \max_{e \in E_K} \langle \vec{e}, |H_u(x)|, \vec{e} \rangle \tag{2.62}$$

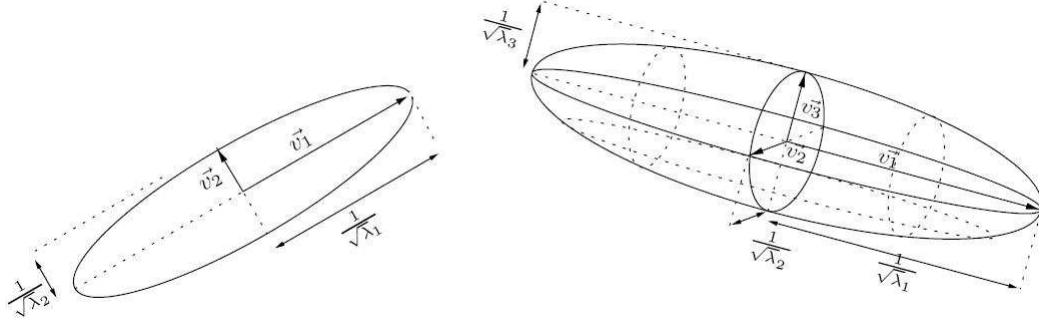


Figure 2.10: Geometric representation of a metric in **2D** and in **3D** [2]

with  $|H_u| = R|\Lambda|R^{-1}$ ,  $|\Lambda| = \text{diag}(|\lambda_i|)$  and  $c_d$  is a constant depending on the space dimension. It is not easy to evaluate this bound because it depends on the mesh extremums that are unknown a priori. The author in [2] defines a metric tensor  $\overline{M}(K)$  as:

$$\max_{x \in K} \langle \vec{e}, |H_u(x)|, \vec{e} \rangle \leq \langle \vec{e}, \overline{M}(K), \vec{e} \rangle, \quad \forall e \in E_K \quad (2.63)$$

where  $E_K$  is the sets of edges of the element  $K$ .

By fixing the tolerated error, the edges of the mesh must be constructed so that the interpolation error is close to the tolerated error  $\varepsilon$  on each element of the mesh:

$$\varepsilon = c \langle \vec{e}, \overline{M}(K), \vec{e} \rangle \implies \langle \vec{e}, M(K), \vec{e} \rangle = 1 \quad \forall e \in E_K \quad \text{with} \quad M(K) = \frac{c_d}{\varepsilon} \overline{M}(K) \quad (2.64)$$

So the mesh adaptation is based on creating a unit mesh with the specified metric  $M(K)$ . To avoid unrealistic results, the minimal ( $h_{min}$ ) and the maximal ( $h_{max}$ ) length of the edges were introduced and the metric tensor is defined as follows:

$$M = R\tilde{\Lambda}R^{-1}, \quad \text{with} \quad \tilde{\Lambda} = \text{diag}(\tilde{\lambda}_i) \quad , \quad \tilde{\lambda}_i = \min \left( \max \left( \frac{c_d |\lambda_i|}{\varepsilon}, \frac{1}{h_{max}^2} \right), \frac{1}{h_{min}^2} \right) \quad (2.65)$$

here  $R$  represents the eigenvectors matrix and  $(\lambda_i)_{1 \leq i \leq 3}$  are the eigenvalues of the Hessian matrix  $H_u$ .

### 2.3.2.2 The constructed metric

In this work the direction of mesh refinement is given by the unit normal to the interface which corresponds to the gradient of the LevelSet function:

$$\mathbf{n} = \frac{\nabla \alpha}{\|\nabla \alpha\|} \quad (2.66)$$

A coarse mesh size is imposed far from the interface and a mesh refinement takes place near the liquid-solid interface. The refinement operates only in the direction perpendicular to the interface, which leads to anisotropic meshes on a layer of thickness  $e$  (Figure 2.11(a)). Let  $h_2$  be the mesh size in the direction of the interface (Figure 2.11(b)) and  $h_1$  the desired mesh size in

the directions perpendicular to the interface. The corresponding metric  $\mathbb{M}$  is then expressed as follows:

$$\mathbb{M} = C(\mathbf{n} \otimes \mathbf{n}) + \frac{1}{h_1^2} \mathbb{I} \quad \text{with} \quad C = \begin{cases} 0 & \text{if } |\alpha(x)| \geq e/2 \\ \frac{1}{h_2^2} - \frac{1}{h_1^2} & \text{if } |\alpha(x)| < e/2 \end{cases} \quad (2.67)$$

where  $\mathbb{I}$  is the identity tensor.

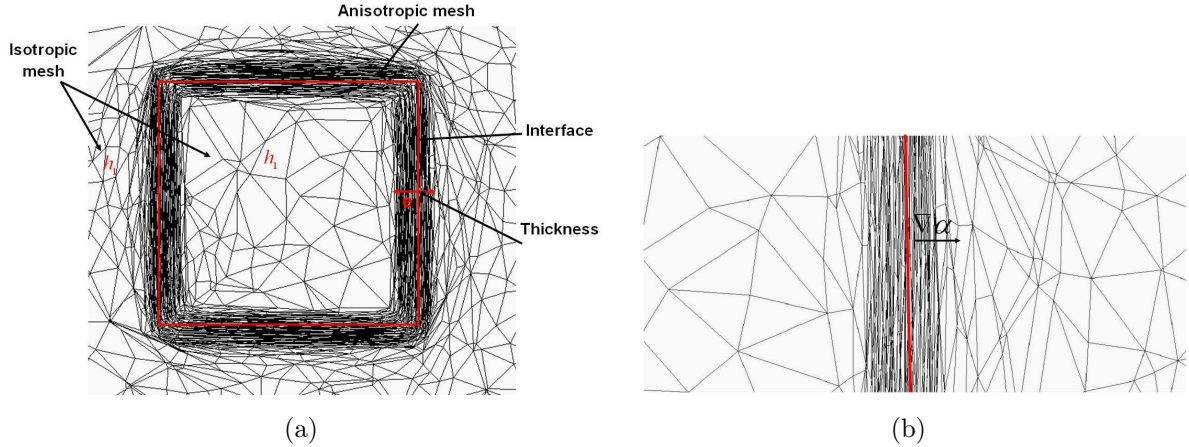


Figure 2.11: (a) Representation of a **2D** interface with the anisotropic meshing technique, (b) Close-up along the interface

## 2.4 Numerical tests and validation

The numerical methods introduced in the previous sections (stabilized finite element method for solving conjugate heat transfer, VMS stabilized finite elements for resolution of the incompressible Navier Stokes equations, LevelSet and anisotropic adaptation) are used in this section to simulate the heat transfer during the quenching process.

### 2.4.1 Study of the agitation influence

We consider a water tank at 20 °C and a cube of a nickel-based alloy (inconel718) heated at 985 °C. The cube with an edge 0.22 m is immersed in water and positioned at (1.402; 1.4; 0.79). In this example, a quench system with three different agitation velocities was simulated to study the influence of the agitation on the solid cooling. The agitation in the bottom of the rectangular tank is produced by imposing a vertical velocity field on a submerged slab. For case one, the quenching has been achieved without agitation. In order to study this processing, the injected water has a constant temperature of 20 °C and an entrance velocity (in direction of axis Z) of  $1 \text{ m} \cdot \text{s}^{-1}$  and  $3 \text{ m} \cdot \text{s}^{-1}$ . In this simulation, the knowledge of the heat transfer coefficient between the two materials was not needed and it was naturally treated by coupling between thermal and mechanical problem. Bineli [41] shows that the cooling is not uniform by using such an agitation



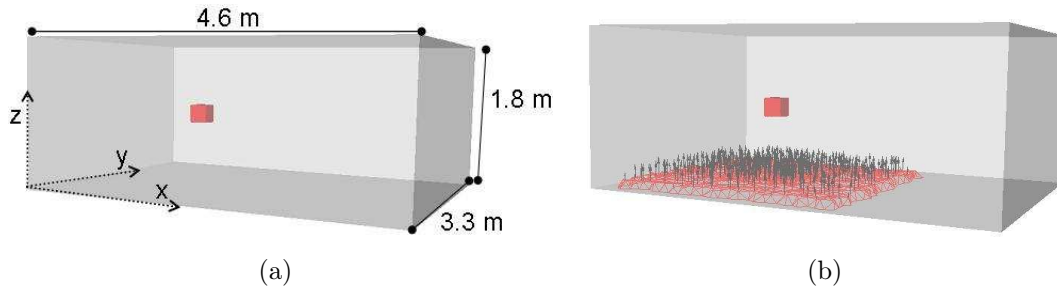


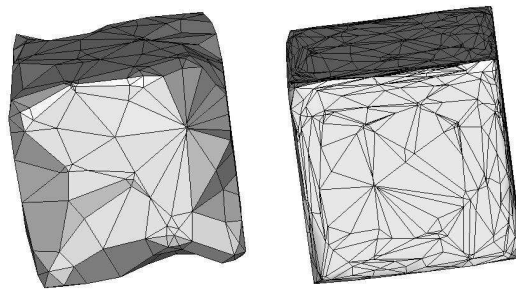
Figure 2.12: (a) Computational domain, (b) Agitation system with an entrance velocity  $3 \text{ m} \cdot \text{s}^{-1}$

| Domain | Temperature<br>( $^{\circ}\text{C}$ ) | Density<br>( $\text{kg}/\text{m}^3$ ) | Specific heat<br>capacity ( $\text{J}/\text{Kg}^{\circ}\text{C}$ ) | Thermal<br>conductivity ( $\text{W}/\text{mK}$ ) | Viscosity<br>( $\text{Pa} \cdot \text{s}$ ) |
|--------|---------------------------------------|---------------------------------------|--------------------------------------------------------------------|--------------------------------------------------|---------------------------------------------|
| Water  | 20                                    | 1000                                  | 4182                                                               | 0.597                                            | 0.001                                       |
| Alloy  | 985                                   | 8200                                  | 617.42                                                             | 274                                              |                                             |

Table 2.1: Materials properties and initial temperature

system. Thermal and momentum equations will be coupled and used to study the numerical influence of the agitation on the acceleration of the cooling.

Figure 2.12(a) represents the geometric model used in this simulation. The creation of this geometry was obtained by applying the IVM method. The LevelSet function defines the workpiece and the agitator. The mesh is created by using the anisotropic mesh adaptation, then the shape of the workpiece is well captured and well represented despite of edges and corners singularities (Figure 2.13). Thanks to this mesh adaptation, nodes are added only at the vicinity of the interface which provides stretched elements along the solid interface (Figure 2.14(b)). The mesh used for this numerical simulation consists of 126832 nodes and 698181 tetrahedral elements (Figure 2.14(a)).



(a) Initial square mesh (b) Final square mesh

Figure 2.13: Mesh adaptation in the vicinity of the interface

In this simulation, we consider that the properties of water and solid vary with the temperature and values are provided by our industrial partner Snecma. Table 2.1 presents mechanical and physical properties of the solid and the fluid. The top surface of the tank that is in contact

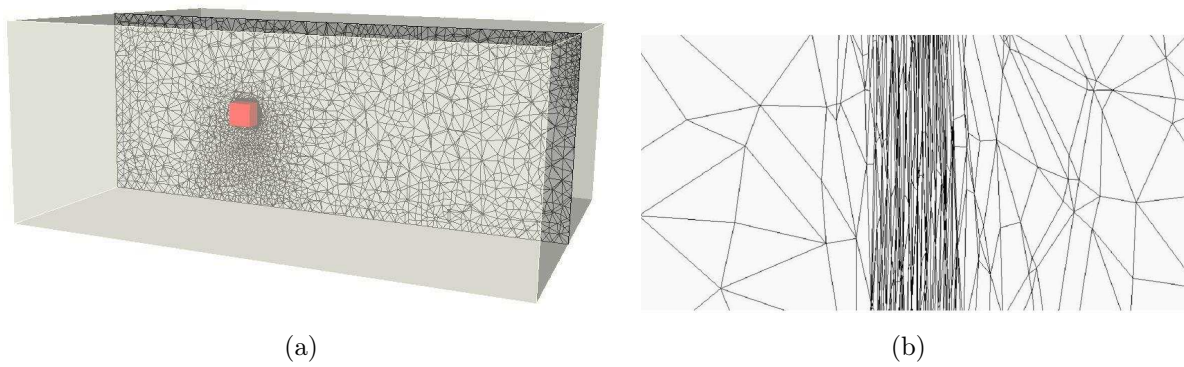


Figure 2.14: (a) Representation of a **3D** interface with the anisotropic meshing technique, (b) Close-up along the interface

with the atmosphere was defined as a free slip surface and for the other wall tank a no slip condition is applied.

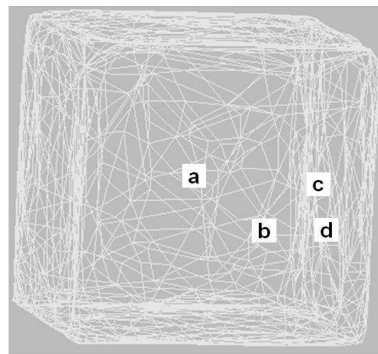


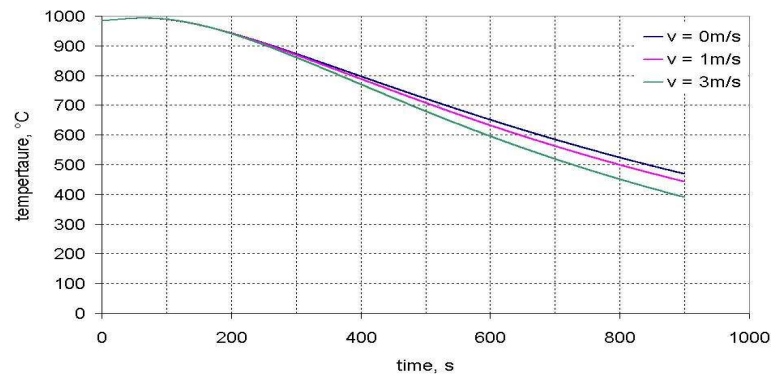
Figure 2.15: Position of thermal sensors

| Thermal sensors | Position              |
|-----------------|-----------------------|
| a               | (1.512; 1.51; 0.9)    |
| b               | (1.56; 1.51; 0.8625)  |
| c               | (1.6; 1.51; 0.9)      |
| d               | (1.612; 1.51; 0.8625) |

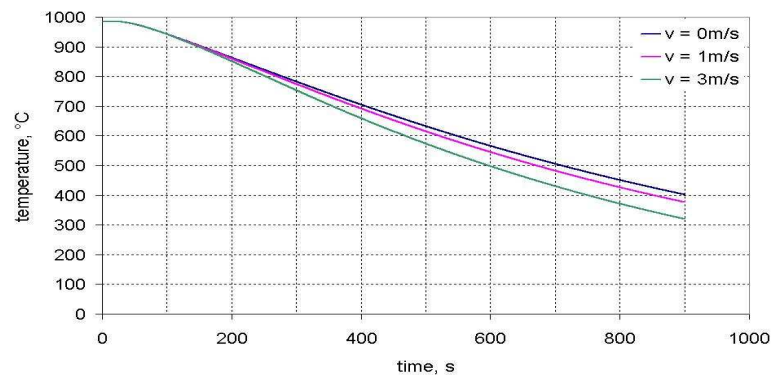
Table 2.2: Coordinates of thermocouple positions

**Results:**

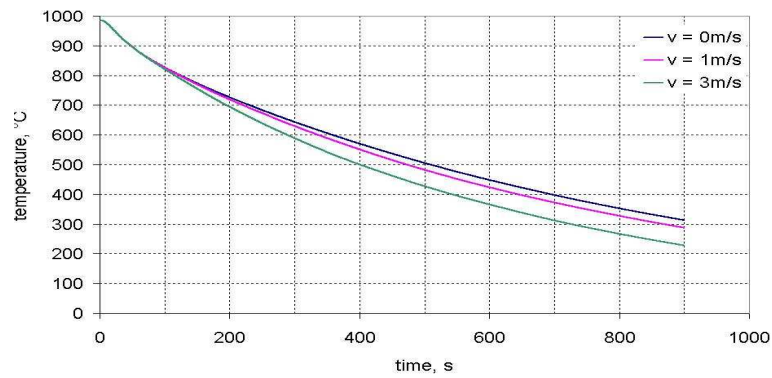
The locations and the coordinates of thermocouples, used to measure the temperature, are presented in Figure 2.15 and Table 2.2. As it can be seen, the thermocouple (a) is located in the center of the solid, (c,d) are fixed on its surface and (b) is located in between. Figure 2.16 presents the distribution of the temperature at different locations of the solid body and for different agitation velocities. It can be observed that the cooling rate is higher than inside the part. An increase in the agitation speed leads to a faster cooling for each sensor. In fact, the agitation favors the heat transfer between the piece and the bath and promotes the formation of martensite in both areas, heart and surface, of the workpiece [42]. In quench process, the knowledge of the heat transfer coefficient is complicated because it depends on several parameters as the bath temperature, the fluid nature, the metal temperature, the agitation velocity . . . . Summing up, the advantage offered by the proposed method, is that this process can be simulated for different geometries without any knowledge of the heat transfer coefficient; it only requires the knowledge of the composite material properties.



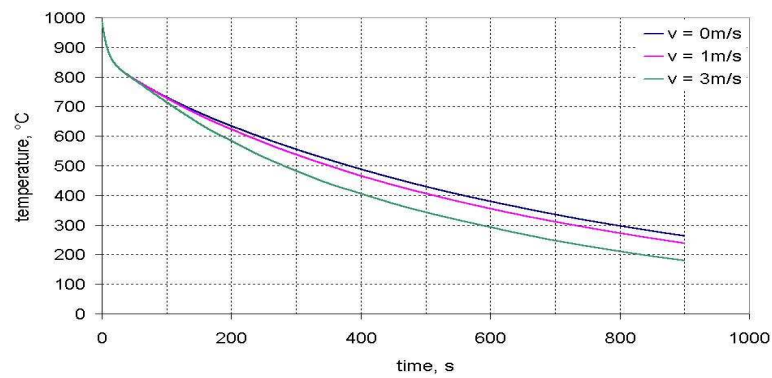
(a)



(b)



(c)



(d)

Figure 2.16: Temperature evolution of a square body for different agitation velocities. From top to bottom: sensors a, b, c, d

## 2.4.2 Industrial case

Figure 2.17(b) presents a water 20 °C tank provided by our industrial partner Snecma, in which a heated cylinder 985 °C with 30 mm in diameter and 30 mm long is quenched. This bath is used for continuous heat treatment of a cylinder nickel-based alloy (inconel718) positioned usually on a support grid. The support is made by three cylinders all placed in the center of the bath as shown in Figure 2.17(a). The bath was modelled as a rectangular domain,  $4.6 \times 3.3 \times 2.3 \text{ m}^3$  and the cylinder is placed at (1.512; 1.51; 0.9).

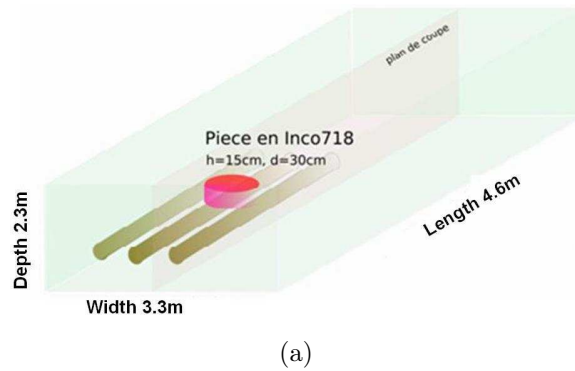


Figure 2.17: (a) Quenching configuration, (b) Industrial water tank agitated by two pumps

By applying the IVM method, thanks to the LevelSet function and the anisotropic mesh adaptation the shape of the workpiece is well captured and well presented in terms of curvature (Figure 2.18). A uniform cooling usually requires a uniform agitation system. In this quenching configuration, the bath has been agitated by bottom water injection through a centered set of holes (Figure 2.19(a)). The water, pumped into the bath, has a constant temperature of 20 °C. The agitation system has a complicated geometry that cannot be given by any implicit function. In this work a distance function is used and the region of the agitator was refined to capture the interface of the immersed agitator system (Figure 2.19(b)). We did not use the anisotropic adaptation mesh adaptation because the slab thickness (0.03 m) is smaller than the coarse mesh size (0.1 m). By using the isotropic remeshing, the agitation system is well represented

(Figure 2.18(d)). The time step is equal to 0.05 s. Here we consider a free slip condition on the top surface and a no slip condition on the other wall tank. To model the water evacuation, we consider a thin slab (height of 0.235 m) on which a free boundary condition was applied in the  $x$  direction.

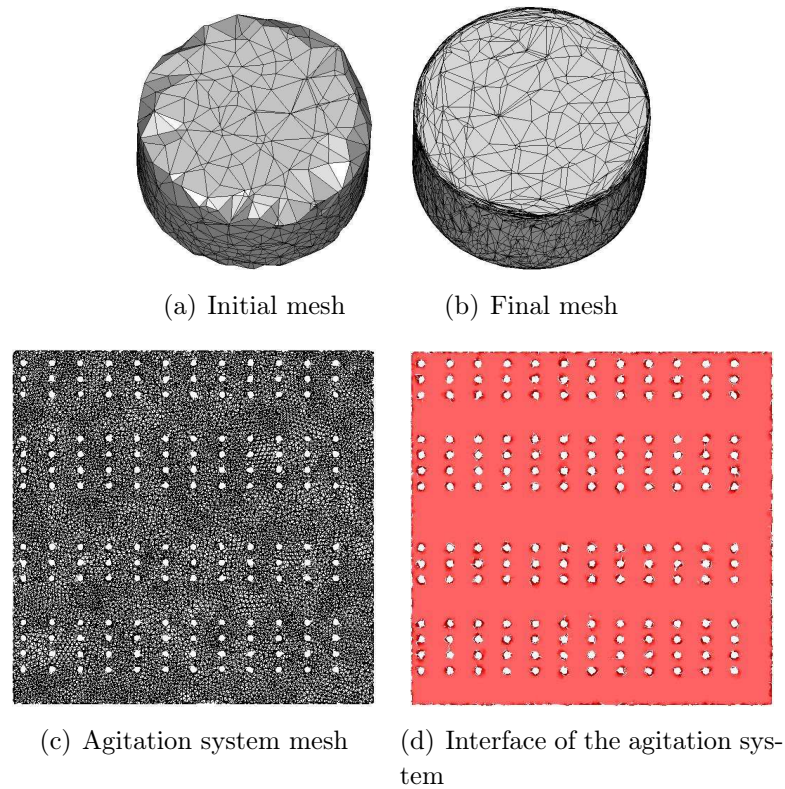


Figure 2.18: Difference between the initial mesh and the final mesh of the cylinder (top), the final mesh and the interface of the agitation system (bottom)

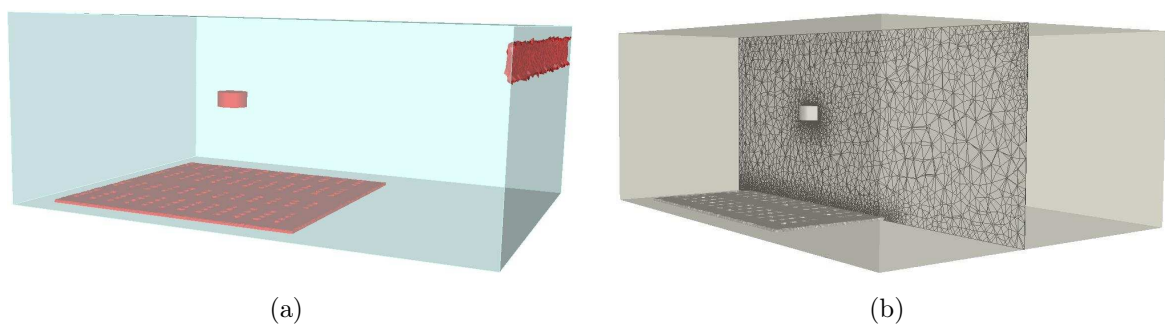


Figure 2.19: (a) Computational domain after anisotropic mesh adaptation around the workpiece interface and an isotropic refinement near the agitation system, (b) Cut of mesh showing details of the refinement and anisotropic mesh adaptation

### 2.4.2.1 Results with an entrance velocity $3 \text{ m.s}^{-1}$

Figure 2.20(a) presents the bottom water injection through a centered set of hole. By zooming on the agitation system, a number of small vortexes on the slab can be observed in Figure 2.20(b), they are due to the bath turbulence. Figure 2.21 presents the streamlines at different time steps. The water injection with a velocity equal to  $3 \text{ m.s}^{-1}$  induces a turbulent motion within the bath. This forced convection is necessary to get a uniform cooling of solid regions. The water movement around the cylinder is quite complex; this result shows that the IVM approach is adequate for the turbulence of the water surrounding the workpieces. This **3D** computation has required 4 days on 16 cores. Thus, a great effort is still necessary to reduce the computational time. This numerical result shows that this version of **ThosT**, used in the first year of the PHD, is suitable for numerical simulation of industrial quenching process with different conditions and parameters. Such computations lead our industrial partner to improve the cooling by studying the flow behavior around the workpieces.

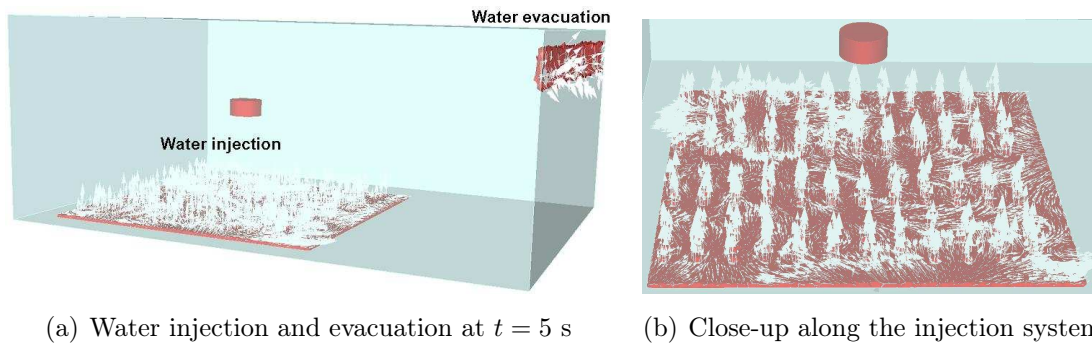


Figure 2.20: Velocity vector injected from bellow and getting out from the right side (left), Close-up along the injection system (right)

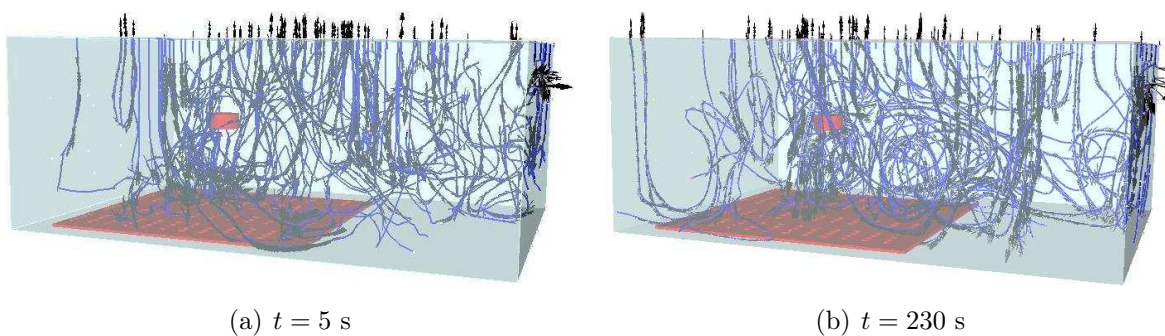


Figure 2.21: Streamlines inside the bath at different time steps

### 2.4.2.2 Results without agitation

The cylinder was instrumented with 4 thermal sensors at different locations (Figure 2.22). The coordinates of these thermocouples are presented in Table 2.3. Data were acquired via a computer controlled data acquisition system, tabulated and then reported by our industrial partner. Figure 2.23 presents a comparison of experimentally measured temperature results with the numerical simulation results at these different locations.

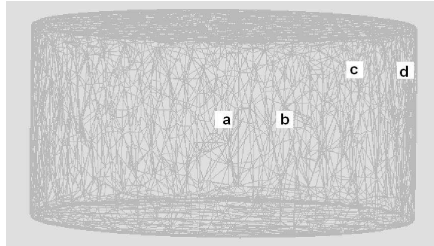
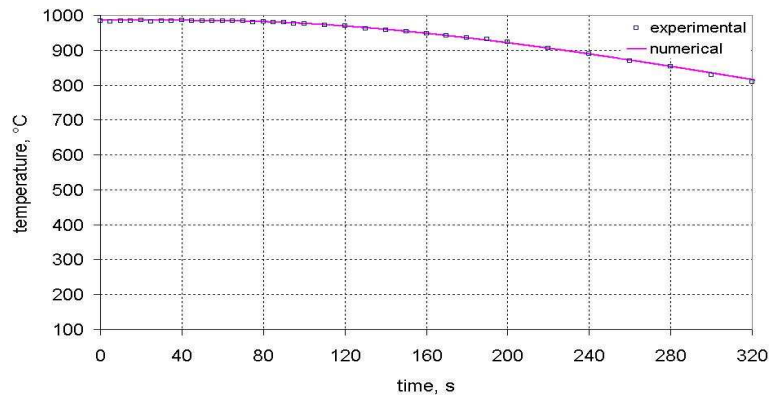


Figure 2.22: Position of thermal sensors

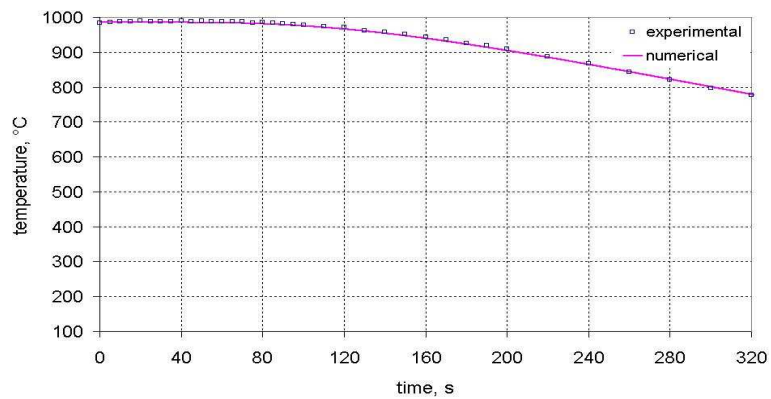
| Thermal sensors | Position              |
|-----------------|-----------------------|
| a               | (1.5; 1.65; 0.875)    |
| b               | (1.55; 1.65; 0.875)   |
| c               | (1.6; 1.65; 0.8375)   |
| d               | (1.645; 1.65; 0.8375) |

Table 2.3: Coordinates of thermocouple positions

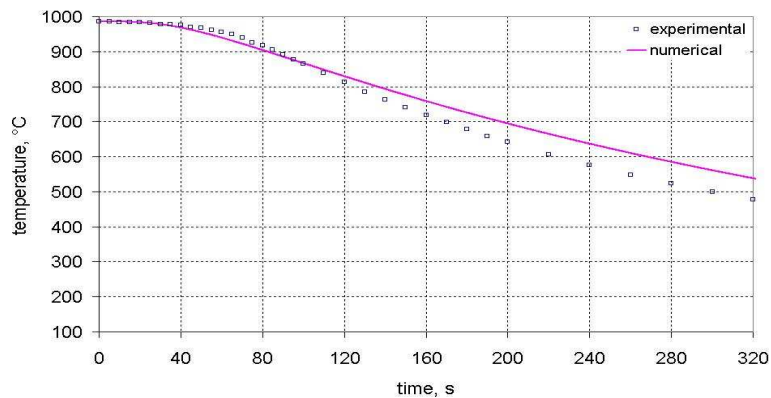




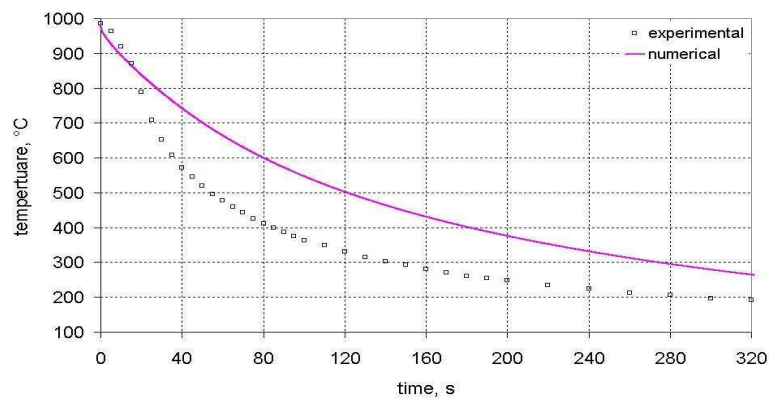
(a)



(b)



(c)



(d)

Figure 2.23: Comparison of temperature profiles between experimental and numerical results. From top to bottom: sensors a, b, c, d

### Results analysis

As it can be seen, the agreement is generally good for thermal sensors fixed inside the solid part (sensor a, b). In fact, during quenching in a vaporizable fluid, heat conduction occurs within the solid part. Whereas on the surface of the solid the heat transfer occurs by convection and boiling. The discrepancy shown at the surface of the heated solid (sensor c, d) indicates the necessity to take into account the boiling heat transfer. To know the duration of boiling phenomenon, we calculate the mean Biot number defined in section 1.4:

$$Bi_m = \frac{h_{av}L}{k} = \frac{h_{av} \times r}{3k} \quad (2.68)$$

Here,  $r$  is the radius of the cylinder,  $h_{av}$  is the average value of the convection heat transfer coefficient:

$$-k\nabla T \cdot n = h_{av}(T - T_{out}) \quad \text{on } \partial\Omega \quad (2.69)$$

The convection heat transfer between the solid (inconel718) and water at 20 °C is equal to  $880 \text{ W} \cdot \text{m}^{-2} \cdot \text{°C}^{-1}$  [43]. This parameter depends on several other parameters such as the metal nature, the solid orientation, the fluid nature and temperature. To verify that the value provided by Vanmeensel [43] fits our experimental condition, in the next paragraph we consider  $h = 880 \text{ W} \cdot \text{m}^{-2} \cdot \text{°C}^{-1}$  and we simulate the cylinder cooling by a convective heat transfer condition. Once the temperature evolution is predicted, we compare this result with the experimental one.

### Computation of heat transfer coefficient

On the boundary of a heated cylinder (985 °C) a convective heat transfer condition is imposed (Figure 2.24(a)), with a heat transfer coefficient  $h_{av} = 880 \text{ W} \cdot \text{m}^{-2} \cdot \text{°C}^{-1}$  and an external temperature  $T_{out} = 20 \text{ °C}$ . The cylinder was instrumented with 3 thermal sensor at the center and on its surface (Figure 2.24(a)). Figure 2.25 presents a comparison of experimentally measured temperature with numerical results at these different locations. It can be noted that results are in good agreement, then the value of the convective heat transfer coefficient is convenient.

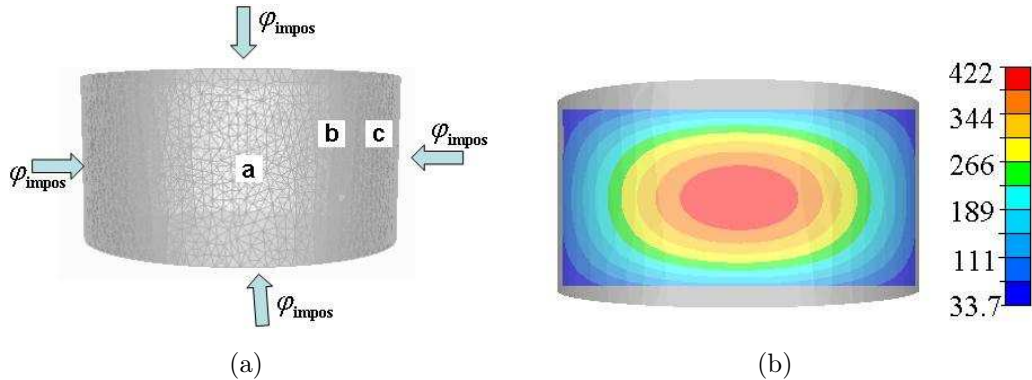


Figure 2.24: (a) Problem configuration, (b) Temperature (°C) evolution at  $t = 700 \text{ s}$

By substituting  $h_{av}$  by its value in (2.68), the mean Biot number is equal to 1.6. According to (Figure 1.14), it can be noted that the ratio between the duration of boiling phase and the

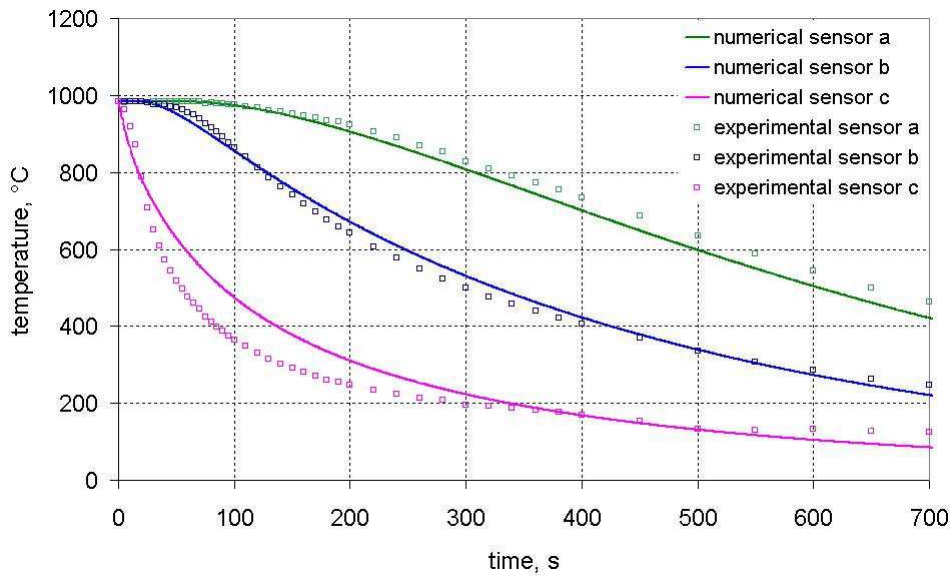


Figure 2.25: Comparison of temperature profiles between experimental and numerical results

characteristic time is approximately equal to 1.1 , then the boiling heat transfer ensures 50% of the cooling. This analysis shows the need of a model able to simulate boiling during quenching. This issue will be the subject of the next chapter.

## 2.5 Conclusions

The thermal problem is described by the convection-diffusion equation. The need for stabilization in the case of unsteady diffusion problem has been revisited with a study of the influence of several parameters on the thermal shock. An original stabilization method, known as the enriched method with time interpolation was introduced. Then it was validate in a **3D** cooling case. The governing Navier-Stokes equations with a variational multiscale method is presented, this stabilizing scheme is recommended to deal with convection dominated problems. The immersed volume method was proposed to model the quenching process. Different numerical simulations of industrial quenching process have been achieved and analyzed. It can be noted that the cooling becomes more uniform while increasing the agitation velocity. In this chapter, we point out that the proposed method is capable of modelling a unsteady three dimensional heat transfer and turbulent flows in an industrial quenching configurations. A comparison between numerical and experimental results shows the industrial need of a software tool which integrates the boiling to the quenching model.

## 2.6 Résumé français

La première partie de ce chapitre est consacrée à la description de l'équation de convection diffusion, avec dans un premier temps sa formulation (forte et faible), et dans un second temps sa résolution avec la méthode élément fini stabilisée. La seconde partie de ce chapitre est consacrée à la résolution numérique de l'équilibre mécanique. Nous présentons une méthode de résolution par éléments finis stabilisés. La troisième partie décrit l'approche numérique du couplage fluide solide utilisée. Cette approche est connue par la méthode d'Immersion de Volume (IVM), elle permet de représenter de façon très flexible les pièces trempées. Cette méthode permet de simplifier considérablement la définition géométrique et la gestion du maillage des différents objets en présence : charges et positionnement des ressources dans l'enceinte et prise en compte de plusieurs géométries (murs, pièces, supports). En effet il est juste nécessaire de calculer des fonctions distances (LevelSet) pour insérer n'importe quel objet de forme géométrique quelconque. Le maillage est ensuite adapté automatiquement de façon anisotrope aux interfaces, permettant ainsi d'améliorer la précision des calculs monolithiques fluides et structures, quel que soit leur niveau de détail et donc de complexité. La dernière partie de ce chapitre sera consacrée à la simulation numérique de plusieurs cas de trempe. Après comparaison des résultats numériques et expérimentaux, on remarque que, pour les capteurs au coeur de la pièce nos résultats numériques sont en bon accord avec ceux fournis par nos partenaires industriels; mais pour les capteurs en surface de la pièce, il y a une différence due au fait que le transfert de chaleur induit par ébullition n'a pas été modélisé. Ce chapitre montre alors la nécessité de créer un modèle diphasique pour avoir un outil de simulation de trempe optimisé.



# References

- [1] E. Hachem, H. Digonnet, N. Kosseifi, E. Massoni, and T. Coupez. Enriched finite element spaces for transient conduction heat transfer. *Applied Mathematics and Computation*, 217:3929–3943, 2010.
- [2] F. Alauzet and P. J. Frey. Estimateur d’erreur géométrique et métriques anisotropes pour l’adaptation de maillage. partie 1 : aspects théoriques. *rapport de recherche*, RR-4759, 2003.
- [3] C. Aliaga. *Simulation numérique par éléments finis en 3D du comportement thermomécanique au cours du traitement d’aciers : application à la trempe de pièces forgées ou colées*. PhD thesis, Ecole Nationale Supérieure des Mines de Paris, 2000.
- [4] S. Badia and R. Codina. On a multiscale approach to the transient stokes problem. transient subscales and anisotropic space-time discretization. *Applied Mathematics and Computation*, 207:415–433, 2003.
- [5] C. Pelissou. *Discrétisation spatio-temporelle du problème thermique à deux champs. Application au procédé de forgeage à chaud*. PhD thesis, Ecole Nationale Supérieure des Mines de Paris, 2005.
- [6] S. Batkam Hemo. *Thermique multidomaines en simulation numérique du remplissage 3D*. PhD thesis, Ecole Nationale Supérieure des Mines de Paris, 2002.
- [7] V. Fachinotti and M. Bellet. Linear tetrahedral finite elements for thermal shock problems. *International Journal of Numerical Methods for Heat & Fluid Flow*, 16:590–601, 2006.
- [8] F. Ilinca and J.-F. Héту. Galerkin gradient least-squares formulations for transient conduction heat transfer. *Computer Methods in Applied Mechanics and Engineering*, 191(27-28):3073–3097, 2002.
- [9] L. P. Franca and E. G. D. D. Carmo. The galerkin gradient least-squares method. *Computer Methods in Applied Mechanics and Engineering*, 74(1):41 – 54, 1989.
- [10] I. Harari. Stability of semi discrete formulations for parabolic problems at small time steps. *Computer methods in applied mechanics and engineering*, 193:491–1516, 2003.
- [11] L. P. Franca and C. Farhat. Bubble functions prompt unusual stabilized finite element methods. *Computer Methods in Applied Mechanics and Engineering*, 123:229–308, 1995.

- [12] I. Harari and T. J. R. Hughes. What are  $c$  and  $h$ ?: inequalities for the analysis and design of finite element methods. *Computer Methods in Applied Mechanics and Engineering*, 97:157–192, 1995.
- [13] C. Baiocchi, F. Brezzi, and L. P. Franca. Virtual bubbles and the Galerkin-least-squares method. *Computer Methods in Applied Mechanics and Engineering*, 105:125–141, 1993.
- [14] A. Brooks and T. Hughes. Streamline upwind /petrov-galerkin formulations for convection dominated flows with particular emphasis on the incompressible navier-stokes equations. *Computer Methods In Applied Mechanics And Engineering*, 32:199–259, 1982.
- [15] T. J. R. Hughes, G. R. Feijoo, L. Mazzei, and J. B. Quincy. The Variational Multiscale Method - A Paradigm For Computational Mechanics. *Computer Methods In Applied Mechanics And Engineering*, 166(1-2):3–24, Nov 13 1998.
- [16] T. J. R. Hughes, L. P. Franca, and M. Balestra. A New Finite-Element Formulation For Computational Fluid-Dynamics .5. Circumventing The Babuska-Brezzi Condition - A Stable Petrov-Galerkin Formulation Of The Stokes Problem Accommodating Equal-Order Interpolations. *Computer Methods In Applied Mechanics And Engineering*, 59(1):85–99, Nov 1986.
- [17] L. P. Franca, A. Nesliturk, and M. Stynes. On the stability of residual-free bubbles for convection-diffusion problems and their approximation by a two-level finite element method. *Computer Methods in Applied Mechanics and Engineering*, 166:35–49, 1998.
- [18] G. Scovazzi. A Discourse On Galilean Invariance, Supg Stabilization, And The Variational Multiscale Framework. *Computer Methods In Applied Mechanics And Engineering*, 196(4-6):1108–1132, 2007.
- [19] A. Nesliturk. *Approximating The Incompressible NAVier-STokes Equations Using A Two Level Finite Element Method*. PhD thesis, University Of Colorado, 1999.
- [20] E. F. Lins, R. N. Elias, G. M. Guerra, F. A. Rochinha, and A. L. G. A. Coutinho. Edge-Based Finite Element Implementation Of The Residual-Based Variational Multiscale Method. *International Journal For Numerical Methods In Fluids*, 61(1):1–22, Sep 10 2009.
- [21] E. Hachem, B. Rivaux, T. Kloczko, H. Dignonnet, and T. Coupez. Stabilized finite element method for incompressible flows with high reynolds number. *Journal of Computational Physics*, 229(23):8643–8665, 2010.
- [22] L. P. Franca and S. P. Oliveira. Pressure Bubbles Stabilization Features In The Stokes Problem. *Computer Methods In Applied Mechanics And Engineering*, 192(16-18):1929–1937, 2003.
- [23] R. Codina. Stabilization Of Incompressibility And Convection Through Orthogonal Sub-Scales In Finite Element Methods. *Computer Methods In Applied Mechanics And Engineering*, 190(13-14):1579–1599, 2000.

- 
- [24] A. Masud and R. A. Khurram. A Multiscale/Stabilized Finite Element Method For The Advection-Diffusion Equation. *Computer Methods In Applied Mechanics And Engineering*, 193(21-22):1997–2018, 2004.
- [25] T. E. Tezduyar and Y. Osawa. Finite Element Stabilization Parameters Computed From Element Matrices And Vectors. *Computer Methods In Applied Mechanics And Engineering*, 190(3-4, Sp. Iss. Si):411–430, 2000.
- [26] R. Codina. Stabilized Finite Element Approximation Of Transient Incompressible Flows Using Orthogonal Subcales. *Computer Methods In Applied Mechanics And Engineering*, 191(39-40):4295–4321, 2002.
- [27] R. Codina and J. Blasco. Analysis of a stabilized finite element approximation of the transient convection-diffusion-reaction equation using orthogonal subcales. *Comput. Visual. Sci.*, 4(3):167–174, 2002.
- [28] E. Hachem. *Stabilized Finite Element Method for Heat Transfer and Turbulent Flows inside Industrial Furnaces*. PhD thesis, Ecole Nationale Supérieure des Mines de Paris, 2009.
- [29] Z. Sun, R. E. Logé, and M. Bernacki. 3d finite element model of semi-solid permeability in an equiaxed granular structure. *Computational Materials Science*, 49:158–170, 2010.
- [30] T. Coupez. *Grandes Transformations Et Remaillage Automatique*. PhD thesis, Ecole Nationale Supérieure des Mines de Paris, 1991.
- [31] F. Alauzet, P. Frey, and B. Mohammadi. Adaptation de maillage non structurés pour les problèmes instationnaires en trois dimensions. In *35ème Congrès National d'Analyse Numérique, La Grande Motte, France*, 2003.
- [32] C. Dobrzynski, O. Pironneau, and P. Frey. Numerical coupling for air flow computations in complex architectures. In *European Congress on Computational Methods in Applied Sciences and Engineering, La Grande Motte, Jyväskylä*, 2004.
- [33] C. Gruau and T. Coupez. 3D tetrahedral, unstructured and anisotropic mesh generation with adaptation to natural and multidomain metric. *Computer Methods In Applied Mechanics And Engineering*, 194:4951–4976, 2005.
- [34] T. Coupez. Génération de maillage et adaptation de maillage par optimisation locale. *Revue Européenne Des Eléments Finis*, 9:403–423, 2000.
- [35] T. Coupez, H. Dignonnet, and R. Ducloux. Parallel meshing and remeshing. *Appl. Math. Model.*, 25:153–175, 2000.
- [36] Y. Mesri, W. Zerguine, H. Dignonnet, L. Silva, and T. Coupez. Dynamic parallel adaption for three dimensional unstructured meshes: Application to interface tracking. *17Th International meshing roundtable*, 3:195–212, 2008.



- [37] J. Bruchon, H. Dignonnet, and T. Coupez. Using a signed distance function for the simulation of metal forming processes: formulation of the contact condition and mesh adaptation. from a lagrangian approach to an eulerian approach. *International Journal for Numerical Methods in Engineering*, 78:980–1008, 2009.
- [38] R. Boussetta, T. Coupez, and L. Fourment. Adaptive remeshing based on a posteriori error estimation for forging simulation. *Computer Methods in Applied Mechanics and Engineering, special issue on "Advances in Computational Metal Forming", Fourment Lionel et Chenot Jean-Loup (Eds)*, 195:6579–6858, 2006.
- [39] F. Alauzet and P. J. Frey. Estimateur d'erreur géométrique et métriques anisotropes pour l'adaptation de maillage. partie 2 : exemples d'applications. *rapport de recherche*, RR-4789, 2003.
- [40] F. Alauzet, P. L. George, B. Mohammadi, P. Frey, and H. Borouchaki. Transient fixed point-based unstructured mesh adaptation. *International Journal for Numerical Methods in Fluids*, 43:729–745, 2003.
- [41] A. R. R. Bineli, M. I. R. Barbosa, A. L. Jardini, and R. M. Filho. Simulation to analyse two models of agitation system in quench process. In *20<sup>th</sup> European symposium on computer aided Process Engineering-ESCAPE20*, 2010.
- [42] R. Ikkene, Z. koudil, and M. Mouzali. Pouvoir de refroidissement des solutions de trempe à base de polymères hydrosolubles. *Comptes Rendus Chimie*, 11:297–306, 2007.
- [43] K. Vanmeensel, A. Laptev, J. Hennicke, J. Vleugels, and O. Van der Biest. Modelling of the temperature distribution during field assisted sintering. *Acta Mat.*, 53:4379–4388, 2005.

# Chapter 3

## Modelling of nucleate boiling

### Contents

---

|            |                                                        |           |
|------------|--------------------------------------------------------|-----------|
| <b>3.1</b> | <b>Nucleate boiling</b>                                | <b>61</b> |
| <b>3.2</b> | <b>Interface tracking</b>                              | <b>62</b> |
| 3.2.1      | Reinitialisation                                       | 62        |
| 3.2.2      | Convective Reinitialization                            | 63        |
| 3.2.3      | New distance function                                  | 64        |
| 3.2.4      | Numerical test                                         | 67        |
| <b>3.3</b> | <b>Growth</b>                                          | <b>68</b> |
| 3.3.1      | Background of the isothermal bubble growth rate        | 68        |
| 3.3.2      | Numerical approach                                     | 68        |
| 3.3.3      | Conservation of energy                                 | 69        |
| 3.3.4      | Validation of the growth model                         | 70        |
| 3.3.5      | Modelling for the isothermal growth of a single bubble | 71        |
| 3.3.6      | Modelling for the isothermal bubble collapse           | 73        |
| 3.3.7      | Modelling for non-isothermal growth of a single bubble | 74        |
| <b>3.4</b> | <b>Anisotropic adaptative mesh</b>                     | <b>75</b> |
| <b>3.5</b> | <b>Surface Tension</b>                                 | <b>76</b> |
| 3.5.1      | Surface Tension approximation                          | 76        |
| 3.5.2      | Time step restriction                                  | 78        |
| 3.5.3      | Numerical Examples                                     | 79        |
| <b>3.6</b> | <b>Conclusion</b>                                      | <b>90</b> |
| <b>3.7</b> | <b>Résumé français</b>                                 | <b>91</b> |

---

During the quenching in a vaporizable fluid such as water, oil or aqueous polymers, the heat transfer must be uniform to avoid defects like cracking, distortion, residual stress and spotty hardness. When the metal is quenched in a vaporizable liquid, the heat transfer is carried out by conduction, convection and boiling. In this chapter, we are interested on modelling the boiling mode, which is complicated and presents a big challenge. Many empirical studies, based on experimental data, have been achieved to offer a deep knowledge of boiling heat transfer. They were performed for nucleate boiling and for the study of film boiling in a tube [4]. These models offer details analysis of boiling process, however they are based on assumptions and are valid for a specific fluid [5]. Numerical models are based on modifying the computational fluid dynamics **CFD** solver to take into account boiling effects. In this paragraph, we present a brief review of these numerical approaches and the one adopted in this work.

1. Phases are solved separately using two sets of governing equations and the solutions matched through jump conditions across the interface. This method offers good qualitative results but it requires a high computational cost [3];
2. A set of single governing equations is used for both phases; using the void fraction to describe the concentration of the vapor phase and treating the phase boundary as a source term in heat and momentum equation [7, 3];
3. Robinson [8] considers an incompressible single phase simulation with an empirical correlation to account for heat transfer due to boiling. This approach presents a major disadvantage which is lack of accuracy due to the energy addition [3];
4. Srinivasan [5, 4] takes into account boiling during quenching process by using a boiling mass transfer between phases. Different modes of boiling (film boiling and transition boiling) have been covered but not the nucleate boiling and the natural convection modes.

In this work, the adopted approach is similar to the second method in the respect that one governed equation is solved for both fluids. However, the formation and the evolution of a bubble or a film vapor is modelled via a germination and a growth approach. Thanks to this model different boiling regimes (film boiling, nucleate boiling and pure convection) can be simulated. Boiling of fluids is one of the most efficient ways of removing heat during the quenching process at the same time it is the least understood phase change process [11]. Due to the complexity of this phenomena, we subdivide the numerical study in two parts: nucleate boiling and film boiling. In this chapter, we develop a numerical model for nucleate boiling more precisely a simulation tool that is able to model bubble behavior: growth, detachment and coalescence. Chapter 5 is devoted to develop a general model for boiling able to simulate both regimes (nucleate boiling and film boiling).

## 3.1 Nucleate boiling

Details of the cycle of events at a nucleation site is given in (Figure 3.1) and it consists of:

1. Nucleation: is usually originated from pre-existing microvoids on the solid surface [12];
2. Growth: begins at step c of Figure 3.1, the heat is provided by convection around the bubble and by conduction through the microlayer (areas adjacent to the superheated bubble);
3. Detachment: the bubble detaches from the solid surface when the upward buoyancy forces overreach the surface tension forces acting at the bubble-wall contact line;
4. Ascension: is due to the buoyancy force. The surface tension plays a preliminary role in predicting the final bubble shape and its terminal velocity.

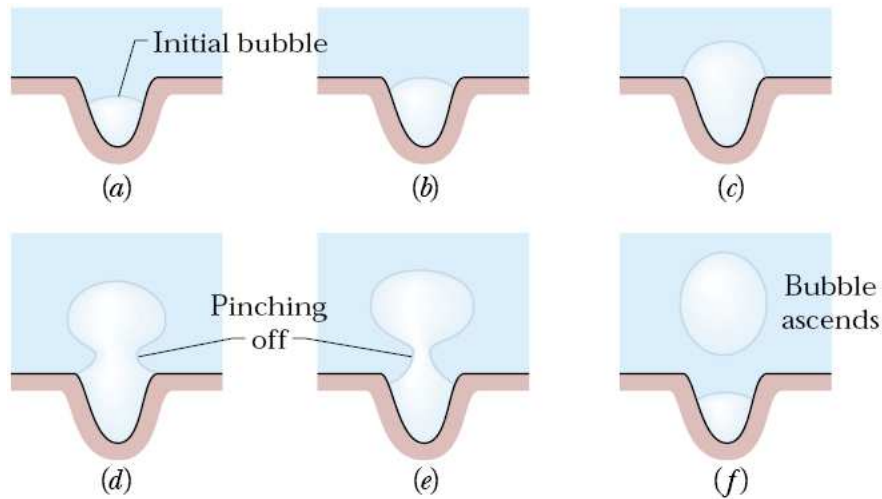


Figure 3.1: (a) A bubble forms in the crevice of a scratch along the bottom of a pan of water, (b-f) The bubble grows, pinches off, and then ascends through the water [1]

One of the aims of this work is to simulate the behavior of a bubble over time. The growth and the ascension of the bubble require an accurate representation of the evolution of the interface. Therefore in the following part we will review the LevelSet function and propose a new solver to describe the motion of the interface. In this work, there is no need to treat the bubble formation, since in the quenching application the film vapor generation is automatically done by assuming that the film vapor interface is the solid surface. The next part of this chapter is then dedicated to study the bubble growth. The numerical simulation of nucleate boiling represents a big challenge because it must be capable to handle with large density and viscosity ratio between the gas phase and the liquid phase (1/1000). In this approach the Navier-Stokes equations are solved directly by using a Variational MultiScale method which can account for a strong ratio of the density and the viscosity. This numerical approach must also provide an accurate representation of the surface tension. The main challenge in computing the surface tension is to calculate the curvature of the fluid interface since a linear finite element method is

used. In this work, the normal and the curvature are calculated based on the recovered gradient defined at the nodal points. By using this whole numerical approach, the results concerning the bubble rising problem are in good agreement with those found in the literature.

## 3.2 Interface tracking

The behavior of a single gas bubble rising in a viscous liquid due to buoyancy force has been extensively studied by different authors using different numerical methods. Numerical simulation of such a problem is a great challenge due to: the accuracy of the interface, the discontinuities between the fluids properties, the topological change in the bubble shape and the effect of surface tension. In the literature, two techniques are available to capture the interface: front tracking (lagrangian, i.e. explicit mesh) and front capturing (eulerian, i.e. fixed mesh) methods. The front tracking method is very efficient for small deformation (rigid moving boundaries). However, when the topology of the interface changes as in coalescence or in a bubble shape evolution, this method presents difficulty to evaluate the interface grid [3]. There are different approaches of front capturing method, volume of fluid (VOF), LevelSet method, coupled LevelSet/ volume of fluid (CLSVOF) and phase field. Each of these robust approaches have their own advantages and disadvantages [13], the most important advantage of LevelSet methods is that the interfaces can easily merge. Bubbles coalescence and bubble deformation [14] can be well presented. In this section, we will review the basic concept behind the transport of the interface described by the LevelSet methods. In chapter 2, the interface between two phases has been predicted with an implicit LevelSet function, for which the value at each node of the mesh is the signed distance to the interface. The velocity is used to update the LevelSet in a Eulerian approach which is based on the use of a fixed mesh. Then an advection equation (3.1) is used to transport the LevelSet with the velocity field  $\mathbf{v}$ .

$$\begin{cases} \frac{\partial \alpha}{\partial t} + \mathbf{v} \cdot \nabla \alpha = 0 \\ \alpha(t = 0, x) = \alpha_0(x) \end{cases} \quad (3.1)$$

### 3.2.1 Reinitialisation

The LevelSet method has been proved to be successful for dealing with moving interfaces, but the transport equation does not maintain the distance function property (i.e.  $\|\nabla \alpha\| \neq 1$ ). For this reason the reinitialisation scheme is necessary to keep  $\alpha$  a distance function. This reinitialisation is done by solving a Hamilton-Jacobi equation as follows:

$$\begin{cases} \frac{\partial \alpha}{\partial \tau} + s(\alpha)(\|\nabla \alpha\| - 1) = 0 \\ \alpha(\tau = 0, x) = \alpha_0(x) \end{cases} \quad (3.2)$$

Where  $\tau$  is a virtual time and  $s(\alpha)$  is the sign function defined as follows:

$$\begin{cases} s(\alpha) = 1 & \alpha > 0 \\ s(\alpha) = 0 & \alpha = 0 \\ s(\alpha) = -1 & \alpha < 0 \end{cases} \quad (3.3)$$

By solving equation (3.2) the LevelSet function is modified wherever its gradient is not unit. The presence of the sign function keeps the LevelSet function unchanged at the interface and away from the interface the LevelSet converges to  $\|\nabla\alpha\| = 1$ . For numerical purposes it is useful to smooth the sign function [15] as

$$s(\alpha) = \frac{\alpha}{\sqrt{\alpha^2 + \|\nabla\alpha\|^2 h^2}} \quad (3.4)$$

The reinitialisation equation (3.4) is a non linear equation, Peng [16] linearized it by introducing the gradient at the preceding increment:

$$\|\nabla\alpha\| = \frac{\|\nabla\alpha\|^2}{\|\nabla\alpha\|} \approx \frac{\nabla\alpha \cdot \nabla\alpha^-}{\|\nabla\alpha^-\|} \quad (3.5)$$

Then the reinitialisation equation becomes:

$$\frac{\partial\alpha}{\partial\tau} + s(\alpha^-) \frac{\nabla\alpha^-}{\|\nabla\alpha^-\|} \nabla\alpha = s(\alpha^-) \quad (3.6)$$

It can be noticed that equation (3.6) is a convection equation with a velocity  $\mathbf{w} = s(\alpha^-) \frac{\nabla\alpha^-}{\|\nabla\alpha^-\|}$

$$\frac{\partial\alpha}{\partial\tau} + \mathbf{w} \nabla\alpha = s(\alpha^-) \quad (3.7)$$

Maintaining  $\alpha$  as a distance function is a necessity for simulating any Multiphase problem [17]. Specially in different nucleate boiling events (bubble rising in a stagnant fluid, bubbles collapsing or breaking) because a steep gradient can occur in the LevelSet interface and the computation of the surface tension will be difficult. In the literature, authors [17, 18] usually recommend to reinitialize  $\alpha$  after every time step to have an accurate solution. Regarding the choice of virtual time step, Coupez advocates it to be equal or less than the mesh size.

### 3.2.2 Convective Reinitialization

The reinitialization scheme causes additional costs due to the resolution of an additional system with a discretization time step 5-8 times smaller than the time step  $\Delta t$  [19]. Since the convection and the reinitialization equation are both hyperbolic PDE equations, Coupez [20, 21] showed that it is possible to couple their resolution in a single step.

$$\frac{\partial\alpha}{\partial t} = \frac{\partial\alpha}{\partial\tau} \times \frac{\partial\tau}{\partial t} = \frac{\partial\alpha}{\partial\tau} \times \frac{h}{\Delta t} \quad (3.8)$$

The virtual time is eliminated from equation (3.8) by substituting it with the mesh size  $h$ .

By substituting  $\frac{\partial\alpha}{\partial\tau}$  by its value in (3.8), we get:

$$\frac{\partial\alpha}{\partial t} = (s(\alpha^-) - \mathbf{w} \cdot \nabla\alpha) \frac{h}{\Delta t} \quad (3.9)$$

In an Eulerian approach, the time derivation  $\frac{\partial\alpha}{\partial t}$  of (3.9) is changed into the total derivative  $\frac{d\alpha}{dt} = \frac{\partial\alpha}{\partial t} + \mathbf{v} \cdot \nabla\alpha$ . Thus, in an Eulerian approach, the convective reinitialization equation becomes:

$$\frac{\partial\alpha}{\partial t} + \left( \mathbf{v} + \frac{h}{\Delta t} \mathbf{w} \right) \cdot \nabla\alpha = \frac{h}{\Delta t} s(\alpha^-) \quad (3.10)$$

Equation (3.10) can be rewritten as an advection equation by:

$$\frac{\partial \alpha}{\partial t} + U \nabla \alpha = F \quad (3.11)$$

Where the velocity  $U$  is equal to the sum of the velocity given by reinitialisation and the transport velocity  $\mathbf{v}$ . The source term  $F$  is equal to  $\frac{h}{\Delta t} s(\alpha^-)$ . Multiplying this equation by a test function  $\tilde{\alpha}$  and integrating over the entire computational domain, we obtain the weak formulation given below:

$$\int_{\Omega} \frac{\partial \alpha}{\partial t} \tilde{\alpha} dV + \int_{\Omega} U \nabla \alpha \tilde{\alpha} dV = \int_{\Omega} F \tilde{\alpha} dV \quad (3.12)$$

Using the same type of notation as the previous chapter, the discrete weak formulation becomes:

$$\int_{\Omega_h} \frac{\partial \alpha_h}{\partial t} \tilde{\alpha}_h dV + \int_{\Omega_h} U \nabla \alpha \tilde{\alpha}_h dV = \int_{\Omega_h} F \tilde{\alpha}_h dV \quad (3.13)$$

$$\frac{\partial \alpha_h}{\partial t} = \frac{\alpha_h - \alpha_h^-}{\Delta t} \quad (3.14)$$

### 3.2.3 New distance function

Since the interface is predicted by the zero isovalue of the LevelSet function, then it is not necessary to resolve the advection problem on the complete domain. In a previous work [20, 21] a sinusoidal filter has been used to truncate the LevelSet. Recently Coupez [22] developed a new solver based on using the Convective Reinitialization equation, while the truncation of the LevelSet is done by a hyperbolic tangent  $u$ . The interface is then defined as the iso value of the function  $u$ :

$$u(x) = \begin{cases} e + E \tanh\left(\frac{\alpha(x) - e}{E}\right) & \text{for } \alpha > e \\ \alpha(x) & \text{for } |\alpha| < e \\ -e + E \tanh\left(\frac{\alpha(x) + e}{E}\right) & \text{for } \alpha < -e \end{cases} \quad (3.15)$$

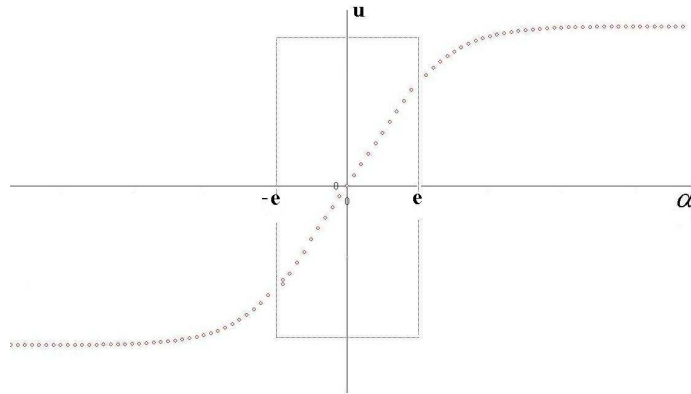


Figure 3.2: The hyperbolic tangent

The numerical parameter  $e$  is called the LevelSet thickness and depends on the mesh size. The other numerical parameter  $E$  is called the truncation thickness. This approach offers several advantages firstly, it makes the system stiffer and more conservative, secondly it fits well with the simulation including surface tension effect.

Note that if  $e = 0$ , the function  $g(u)$  is defined in all the domain as  $u(x) = E \tanh\left(\frac{\alpha(x)}{E}\right)$ . However by considering  $e \neq 0$ ,  $u$  is computed by system (3.15) and this offers two benefits:

- i) Since  $u$  is equal to the LevelSet function (linear function) on the vicinity of the interface, then the band on which the gradient is unitary is extended to the narrow band  $[-e, +e]$ .
- ii) Since  $u$  is extended by a tangent hyperbolic function, the derivative  $g(u)$  of  $u$  depends on the function itself. Then  $u$  can be computed as a solution of a PDE equation.

$$g(u) = \begin{cases} 1 - \left(\frac{u(x) - e}{E}\right)^2 & \text{for } \alpha > e \\ 1 & \text{for } |\alpha| < e \\ 1 - \left(\frac{u(x) + e}{E}\right)^2 & \text{for } \alpha < -e \end{cases} \quad (3.16)$$

The gradient of  $u$  is

$$\nabla u = \frac{\partial u}{\partial x} = \frac{\partial u}{\partial \alpha} \frac{\partial \alpha}{\partial x} = g(u) \nabla \alpha \quad (3.17)$$

By considering  $\|\nabla \alpha\| = 1$ , then  $\|\nabla u\| = g(u)$ .

By resolving a classical advection equation (3.18),  $\|\nabla u\| = g(u)$  is not anymore ensured.

$$\begin{cases} \frac{\partial u}{\partial t} + \mathbf{v} \cdot \nabla u = 0 \\ u(t = 0, x) = u_0(x) \end{cases} \quad (3.18)$$

Then it is necessary to reinitialize the function  $u$  by solving a Hamilton-Jacobi equation as follows:

$$\frac{\partial u}{\partial \tau} = s(u) (g(u) - \|\nabla u\|) \quad (3.19)$$

By combining the above equation with the convection equation, we get a convective reinitialization equation similar to the one determined in section 3.3.2:

$$\frac{\partial u}{\partial t} + \left[ \mathbf{v} + \lambda s(u^-) \frac{\nabla u^-}{\|\nabla u^-\|} \right] \nabla u = \lambda s(u^-) g(u^-) \quad (3.20)$$

Where  $\lambda$  is equal to  $h/\Delta t$ . By introducing the convected velocity  $U = s(u^-) \frac{\nabla u^-}{\|\nabla u^-\|}$ , equation (3.20) is written as follows :

$$\frac{\partial u}{\partial t} + (\mathbf{v} + \lambda U) \nabla u = \lambda s(u^-) g(u) \quad (3.21)$$

Equation (3.21) presents a combination between the advection equation and the reinitialization step necessary to keep the property of the function hyperbolic tangent  $\|\nabla u\| = g(u)$ . The motion



of the interface is then implemented thanks to a convection-reinitialization equation and it can be present as an advection equation:

$$\frac{\partial u}{\partial t} + w \nabla u = \lambda s g(u) \quad (3.22)$$

where  $w = \mathbf{v} + \lambda U$  denotes the advection velocity.

Remarks:

1. The dominance of the nonlinear convective term can generate spurious oscillations that will pollute the whole numerical solution. In order to overcome this numerical difficulty, the finite element formulation for the LevelSet method is based on the use of the classical SUPG (Streamline upwind Petrov-Galerkin) method. More details are given in [23, 21]. In brief, the finite element formulation of equation (3.22) can be written as follows: find  $u_h \in V_h$ , such that,  $\forall w_h \in W_h$

$$\begin{aligned} & \int w_h \left( \frac{\partial u_h}{\partial t} + (\mathbf{v}_h + \lambda U_h) \cdot \nabla u_h \right) d\Omega - \int w_h \lambda .s.g(u) d\Omega \\ & + \sum_{e=1}^{n_{el}} \int_{\Omega^e} \tau_{SUPG} \mathbf{v}_h \cdot \nabla w_h \left( \frac{\partial u_h}{\partial t} + (\mathbf{v}_h + \lambda U_h) \cdot \nabla u_h - \lambda .s.g(u) \right) d\Omega^e = 0 \end{aligned} \quad (3.23)$$

where  $V_h$  and  $W_h$  are standard test and weight finite element spaces. The classical Galerkin terms are represented by the first two integrals whereas the element-wise summation, tuned by the stabilization parameter  $\tau_{SUPG}$ , represents the SUPG term needed to control the convection in the streamline direction. More details about the use of stabilized finite element methods for the convection equation and the evaluation of this parameter can be found in [23].

2. At the interface, the sharp discontinuity of fluid properties is smoothed over a transition thickness using the following expressions:

$$\rho = H(u)\rho_1 + (1 - H(u))\rho_2 \quad (3.24)$$

$$\mu = H(u)\mu_1 + (1 - H(u))\mu_2 \quad (3.25)$$

where  $H(u)$  is a smoothed Heaviside function given by:

$$H(u) = \begin{cases} \frac{1 + \max\left(\frac{u}{\varepsilon}, 1\right)}{2} & \text{if } u > \varepsilon \\ \frac{1}{2} \left(1 + \frac{u}{\varepsilon}\right) & \text{if } |u| \leq \varepsilon \\ \frac{1 + \min\left(\frac{u}{\varepsilon}, -1\right)}{2} & \text{if } u < -\varepsilon \end{cases} \quad (3.26)$$

### 3.2.4 Numerical test

In this two-dimensional example, a circle initially centered at (0.25,0.5) with a radius of 0.15 meters, is rotating. The velocity field is imposed as:

$$\begin{cases} V_X = -2\Pi(Y - Y_{SquareCenter}) \\ V_Y = 2\Pi(X - X_{SquareCenter}) \end{cases} \quad (3.27)$$

where the conservation is the change between initial and final surface of the circle.

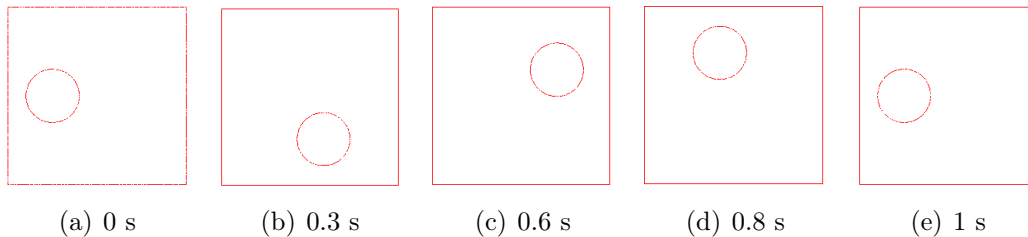


Figure 3.3: Position of the circle at different time steps during one turn

With such a velocity field, the circle turns around the center of the field in the counterclockwise direction while keeping its original shape. It takes 1 s to return to its starting position (Figure 3.3). A series of tests were performed using the convected LevelSet method truncated by a sinusoidal function or by an hyperbolic tangent, in order to compare both methods. Table 3.1 sets out the data of a selected number of simulations. When using the convected LevelSet method truncated by an hyperbolic tangent to transport the interface, the disk surface is better conserved.

| case | Mesh Grid | Time Step | Conservation LevelerS | Conservation LevelerTu |
|------|-----------|-----------|-----------------------|------------------------|
| a    | 50×50     | 0.02      | 22.64                 | 1.27                   |
| b    | 50×50     | 0.01      | 11.21                 | 0.24                   |
| c    | 50×50     | 0.005     | 1.36                  | 0.2                    |
| d    | 100×100   | 0.005     | 13.44                 | 1.79                   |
| e    | 100×100   | 0.0025    | 1.2                   | 0.095                  |
| f    | 100×100   | 0.00125   | 0.73                  | 0.0356                 |
| g    | 200×200   | 0.005     | 32.7                  | 15.58                  |
| h    | 200×200   | 0.0025    | 13.7                  | 0.048                  |
| i    | 200×200   | 0.00125   | 0.62                  | 0.022                  |
| j    | 200×200   | 0.000625  | 0.42                  | 0.02                   |

Table 3.1: Parameters of different circle rotation simulations performed. Comparison between the convected LevelSet method truncated by a sinusoidal function and by an hyperbolic tangent

### 3.3 Growth

The growth of a spherical vapor bubble in an infinite pool of liquid (Figure 3.4) has been treated by several authors [9, 2]. In this configuration, the timescale of the growth period is divided into inertia-controlled and thermal-controlled. The inertia growth period is controlled by the pressure difference and is a short interval of the growth period. The thermal growth is controlled by conduction through the liquid and is the largest part of the growth period. Since the thermal growth is the largest part of the growth period, we treat the variation of the radius during it.

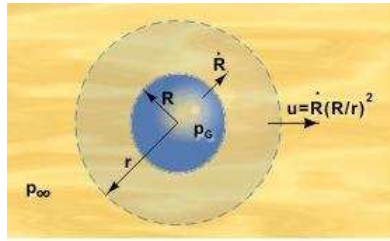


Figure 3.4: Growth of a spherical bubble in an infinite mass of liquid [2]

#### 3.3.1 Background of the isothermal bubble growth rate

In this subsection, a review of the isothermal bubble growth rate is presented. In the next paragraph the numerical approach is presented followed by its validation and several numerical examples. During the bubble growth controlled by the inertia forces, the characteristic length  $R(t)$  varies as a function of the time  $t$ , the Jacob number  $Ja_l$  and the liquid thermal diffusivity  $a_l$  [26, 27, 28].

$$R(t) = C_0^* Ja_l \sqrt{a_l t} \quad \text{with} \quad Ja_l = \frac{\rho_l c_l (T_{l-\infty} - T_e)}{\rho_v L} \quad (3.28)$$

Here,  $T_{l-\infty}$  denotes the far field liquid temperature and  $T_e$  the ebullition point.

The authors in [1] analyzed the bubble growth of a single vapor bubble created under a downward facing heating element in a degassed liquid Fluorinert (FC-72) and determined  $C_0^*$  as a function of the thermal parameters.

To sum up in a uniformly superheated liquid, during the thermal growth period, the radius varies proportional to the square root of time.

#### 3.3.2 Numerical approach

During the last decade, numerical simulations of phase change, whether it's in boiling or in solidification, have been present as a challenging problem. These two problems have many similarities, they requires to solve the energy equation, the momentum equation and the mass conservation [29]. In this section, the evolution of a bubble is simulated via a growth approach. Zabarar [30] computed the dendritic growth velocity by using the Gibbs Thomson relation:

$$T = T_m - \varepsilon_c K - \varepsilon_v V \quad (3.29)$$

where  $K$  is the curvature of the interface,  $V$  is the normal component of the interface velocity,  $\varepsilon_c$  is the surface tension coefficient,  $\varepsilon_v$  is the kinetic mobility coefficient and  $T_m$  is the melting temperature. By considering  $\varepsilon_c = 0$ , the normal interface velocity becomes:

$$\mathbf{V} = \frac{(T - T_m)}{\varepsilon_v} \quad (3.30)$$

In this work, the adopted growth velocity has been deduced from Gibbs Thomson relation and has the following form:

$$\mathbf{v}_\Gamma = C_0 (T - T_e) \cdot \mathbf{n} \quad (3.31)$$

Where  $C_0$  is the growth constant function of the used fluid and  $T_e$  is the ebullition temperature. The normal pointed from the gas phase to the liquid phase  $\mathbf{n}$  corresponds to the gradient of the LevelSet function. In this growth approach, the pressure dependency of evaporation (due to cavitation) was not taken into account.

### 3.3.3 Conservation of energy

The latent heat of evaporation for water is  $2.25 \cdot 10^6 \text{ J.Kg}^{-1}$  and the specific heat is  $4.2 \cdot 10^3 \text{ J.Kg}^{-1}$ . Thus, the energy needed to vaporize a pound of hot water is 500 greater than the one used to raise its temperature by  $1 \text{ }^\circ\text{C}$  [31]. Therefore the latent heat has a preliminary role in the evaporation phenomenon. For flows with phase change, it is necessary to solve the energy equation and to account the latent heat as a source term. The heat transfer, governed by the energy equation, accounts for the Stephan condition by treating its contribution as an external force term as follows, (3.32):

$$\begin{cases} \frac{d\mathbf{h}_e}{dt} - \nabla \cdot (k\nabla T) = 0 \\ \mathbf{h}_e = \rho c_p (T - T_e) + \rho_v LH(u) \end{cases} \quad (3.32)$$

Here,  $L$  is the latent heat of vaporization per unit mass and  $H(u)$  is the smooth Heaviside function defined above. By substituting  $\mathbf{h}_e$  in the first equation of system (3.32) we obtain (3.33):

$$\begin{cases} \rho c_p \frac{dT}{dt} - \nabla \cdot (k\nabla T) = \left[ \rho_v L + (T - T_e) \left( \rho_v c_p^v - \rho_l c_p^l \right) \right] \delta_\Gamma^e(u) \frac{du}{dt} & \text{in } \Omega \\ T(\mathbf{x}, 0) = T_0 & \text{in } \Omega \\ \nabla T(\mathbf{x}, t) \cdot \mathbf{n} = 0 & \text{in } \partial\Omega \end{cases} \quad (3.33)$$

Since the latent heat acts at the phase transition, the force term is multiplied by the  $\delta_\Gamma^e(u)$  and it will act only at the interface. There are many possible choices for  $\delta_\Gamma^e(u)$ , here we choose the following form:

$$\delta_\Gamma^e(u) = \begin{cases} 0 & \text{if } |u| > e \\ \frac{1}{2e} \left[ 1 - \left( \frac{u}{e} \right)^2 \right] & \text{if } |u| < e \end{cases} \quad (3.34)$$

Where  $u$  is the distance function obtained by truncating the LevelSet by the hyperbolic tangent, it was introduced in section 3.3.3. Since  $\delta_\Gamma^e(u)$  denotes the one dimensional Dirac function, the following conditions (3.35-3.36) must be verified.

$$\int_{\mathbb{R}} f(x) \delta_{\Gamma}^e(x) dx = f(0) \quad (3.35)$$

for  $f : \mathbb{R} \rightarrow \mathbb{R}$

$$\int_{\mathbb{R}^3} \delta_{\Gamma}^e(u(x)) dx = \int_{\Gamma} 1 ds \quad (3.36)$$

Then the energy equation becomes a heat transfer equation (3.33), where the latent heat at the phase transition acts as a source term.

### 3.3.4 Validation of the growth model

Zabaras [30] computed the dynamic evolution of a sphere in an undercooled melt by using the Gibbs Thomson equation without the surface tension or kinetic undercooling. By using the above technique, we simulate the same solidification example in two and three dimensional test. The aim of this test is to show that the radius varies linearly with the square root of time in three dimensions. Then, by adopting the above technique numerical results agree with the literature. The computational domain in non-dimensional coordinates is  $\{(x, y, z) : -5 \leq x, y, z \leq 5\}$ . The initial drop is located at the center of the domain with an initial non-dimensional radius 1. The temperature is initially 0 in the body and  $-0.5$  in the rest of the domain. Conductivity and specific heat in both phases are equal to one. The growth velocity is calculated by equation (3.30) with the following parameter  $L = 1$  and a melting temperature  $T_m = 0$ . A Dirichlet boundary condition is imposed  $T = -0.5$  on  $\Gamma$  (Figure 3.5(b)). In this simulation a structured mesh with three millions elements is considered. This mesh is obtained by taking 50 cubes in each direction and dividing each cube in 24 tetrahedrons, giving  $h = 0.155$  (Figure 3.5(a)). This kind of mesh allows a better conservation of spherical shape. The time step is set to be  $\Delta t = 0.001$  s and the thickness is  $E = 2h$ .

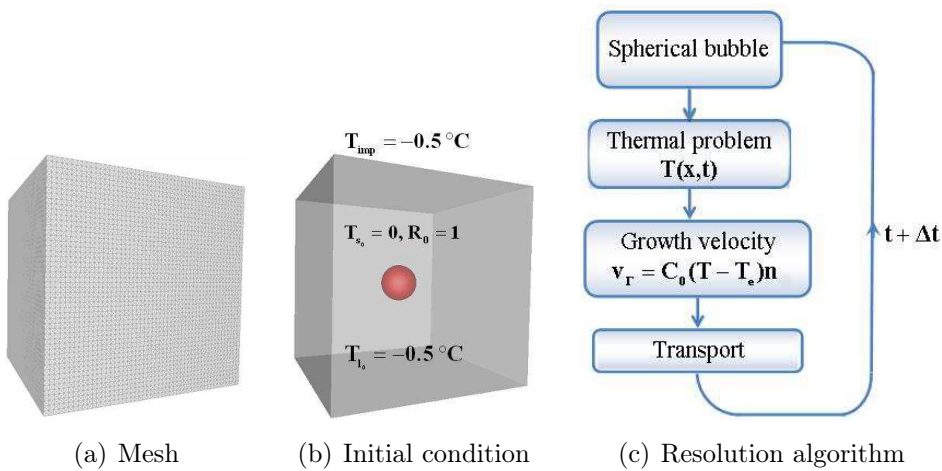


Figure 3.5: Computational domain and resolution algorithm for modelling bubble growth

The computational procedure is given by the resolution algorithm (Figure 3.5(c)):

1. Given the initial bubble shape and the boundary condition;
2. Energy equation is solved to obtain the temperature;
3. The growth velocity  $v_{\Gamma}$  is obtained by (3.31);
4. Advancing  $\alpha$  by the transport equation;
5. Repeat steps (1) to (4) until the final time is reached.

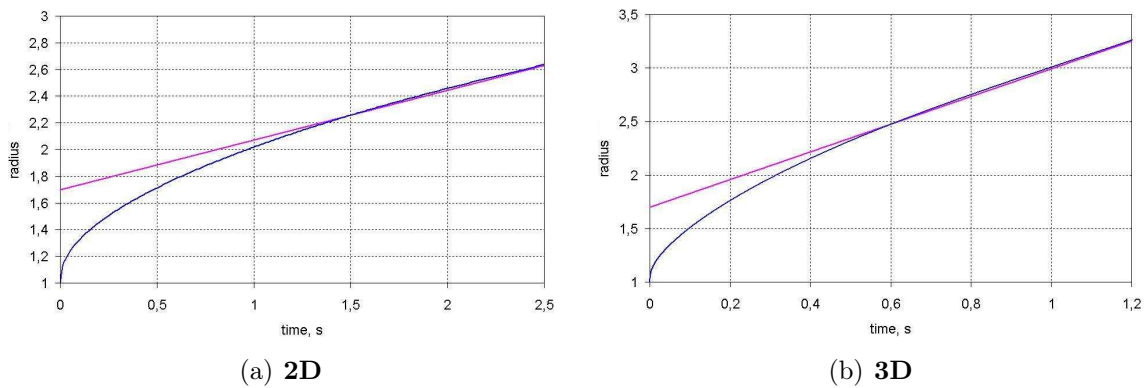


Figure 3.6: Radius evolution with time

In this test, the constant growth velocity  $C_0$  is considered equal to 100. Figures 3.6 plots the radius evolution in time for both **2D** and **3D** calculations. We can see that the growing radius satisfies  $R(t) \approx t$  in **2D** and  $R(t) \approx \sqrt{t}$  in **3D**.

### 3.3.5 Modelling for the isothermal growth of a single bubble

In this paragraph, a modelling of bubbles growth and collapse in isothermal condition has been achieved.

- **2D case:**

The computation domain  $\Omega = [0, 1] \times [0, 1] \text{ m}^2$  is now considered and discretized by using a homogenous mesh size equal to 0.01 m. To study the growth of a circle, a constant velocity  $\mathbf{v}_{\Gamma} = 0.02\nabla\alpha$  is imposed on the bubble interface. Figures 3.7(a)-3.7(b) illustrate the bubble interface for the initial and the final snapshot. During the growth, the radius is plotted as a function of time (Figure 3.7(c)). The estimation error is calculated with the following formula:

$$e = \frac{|v_{exact} - v_{num}|}{v_{exact}} * 100 = 2.5\% \quad (3.37)$$

The vapor bubble grows from its initial size to a radius of 6.95 cm in a time of the order 1 s. The corresponding numerical velocity of  $1.95 \text{ cm} \cdot \text{s}^{-1}$  matches well with the exact velocity.

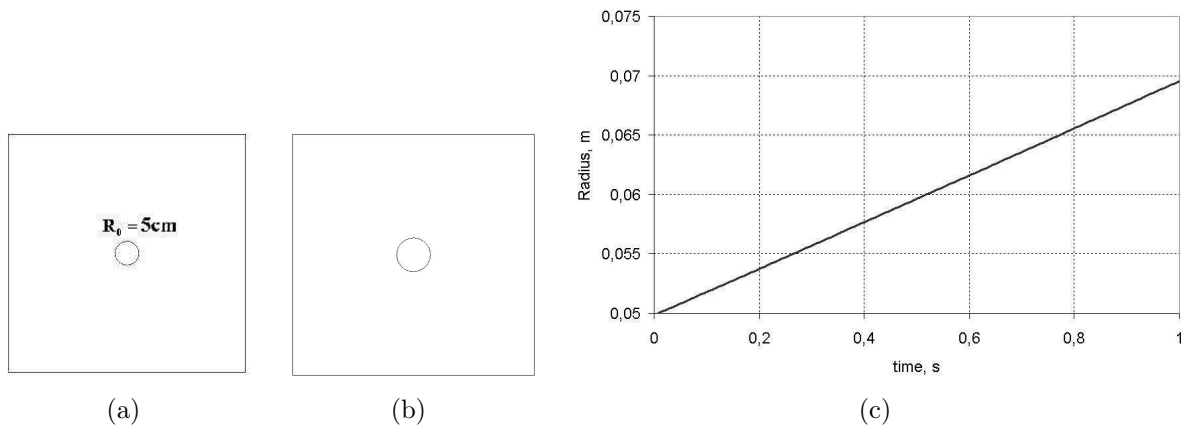


Figure 3.7: (a-b) Isovalue zero of the LevelSet function at  $t = 0$  s and  $t = 1$  s, (b) Radius evolution with time in **2D**

- **3D case:**

We consider a 0.5 m side-length **3D** square domain discretized over  $50 \times 50$  cell mesh. The bubble is located in the center of the domain with an initial radius  $r = 0.05$  m. The simulation of the bubble growth is performed using a time step  $\Delta t = 0.005$  s and a constant velocity  $\mathbf{v}_\Gamma = 0.02\nabla\alpha$ . In Figures 3.8(a)-3.8(b), the bubble interface is illustrated for the initial and the final snapshot. Figure 3.8(c) presents the evolution of the radius as a function of time. Note that the error estimation  $e = 5\%$  is higher than the one noted in **2D**, this error can be reduced by using a mesh refinement.

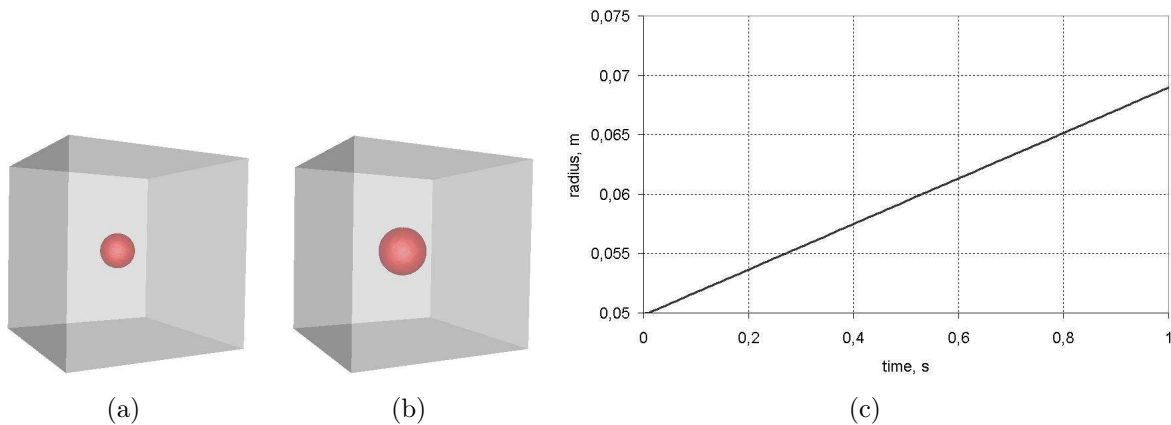


Figure 3.8: (a-b) Isovalue zero of the LevelSet function at  $t = 0$  s and  $t = 1$  s, (b) Radius evolution with time in **3D**

### 3.3.6 Modelling for the isothermal bubble collapse

- **Set of bubbles growth in 2D:**

We consider a two-dimensional domain  $\Omega = [0, 1] \times [0, 1] \text{ m}^2$  discretized by using an unstructured mesh with  $100 \times 100$  simplex elements  $K$  (triangles in **2D**); the growth velocity is constant and equal to  $\mathbf{v}_\Gamma = -0.00002 \mathbf{n}$ . In Figure 3.9, numerical results show a stable growth using an imposed velocity. As expected, bubbles begin to interfere with each other and a collapsed phenomenon appears.

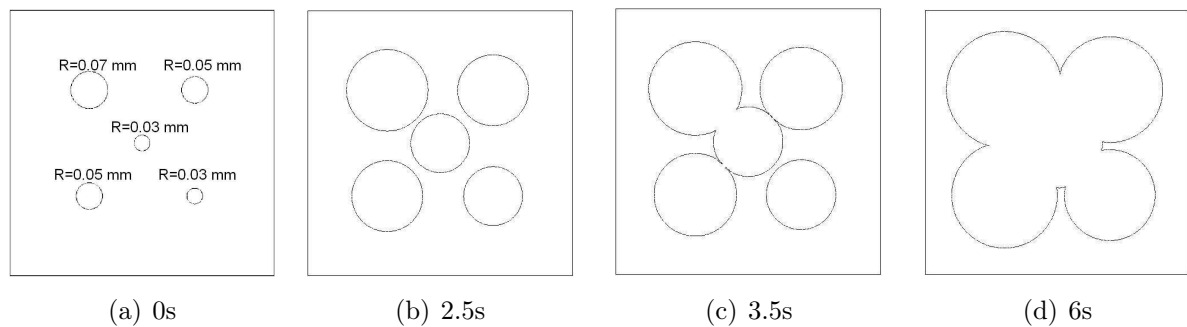


Figure 3.9: Zero isovalue of the bubbles in **2D** at different time steps during the growth

- **Two bubbles in 3D:**

We present the modelling of two bubbles growth. The same domain as above and two bubbles with initial radius  $r = 0.5 \text{ m}$  centered at  $(0.3; 0.3; 0.2)$  and  $(0.15; 0.15; 0.2)$  are considered. As time progresses, bubbles grow and begin to interfere with each other (Figure 3.10) at times  $t = 0 \text{ s}$ ,  $t = 0.5 \text{ s}$ ,  $t = 1 \text{ s}$  and  $t = 2 \text{ s}$ .

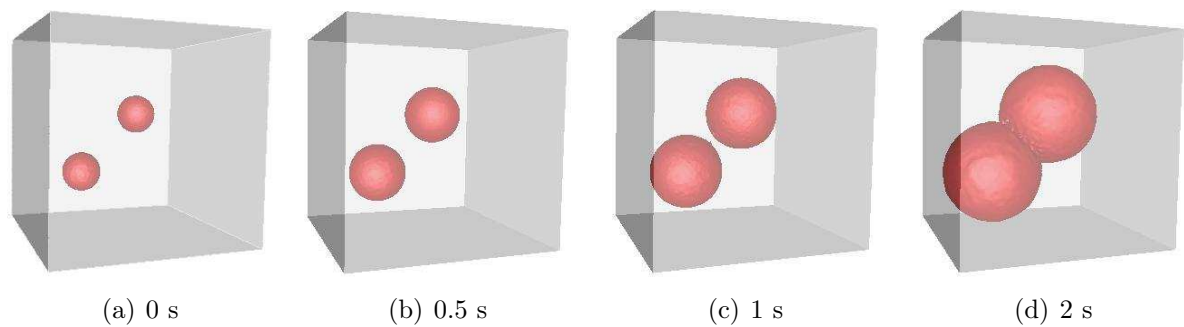


Figure 3.10: Zero isovalue of the bubbles in **3D** at different time steps during the growth



### 3.3.7 Modelling for non-isothermal growth of a single bubble

Let us consider the computational domain  $\Omega$  as a unit square if  $d = 2$  and a cube of edge 0.5 m if  $d = 0.3$ . In both cases the domain is discretized with a homogenous mesh size  $h = 0.01$  m and filled with a bubble vapor submerged in a superheated liquid of the same substance (see Figure 3.11). During the bubble growth process, the phase change takes place on the bubble interface. The bubble absorbs heat from the liquid and increases under this thermal effect. This growth is related to the superheat  $\Delta T = T_l - T_e = 3$  °C. Table 3.2 presents physical properties of the water and the vapor. The resolution algorithm is present in Figure 3.5(c) with a constant growth velocity  $C_0 = 0.008$  and a time step  $\Delta t = 0.005$  s. We simulate the growth of a bubble with radius 1 m and an initial temperature 100 °C located in the middle of the domain; the surrounding liquid is at initial temperature 103 °C. A Dirichlet condition  $T_{imp} = 103$  °C is applied at the boundary of the domain. The latent heat  $2.25 \cdot 10^6$  J.Kg<sup>-1</sup> was taken into account as a source term added to the energy equation (3.33). Figures 3.12-3.14 show the evolution of the bubble characteristic function. The arrows of the computed velocity field (Figure 3.13) indicate the direction of bubble expansion; it can be noted that the bubble conserves its spherical form.

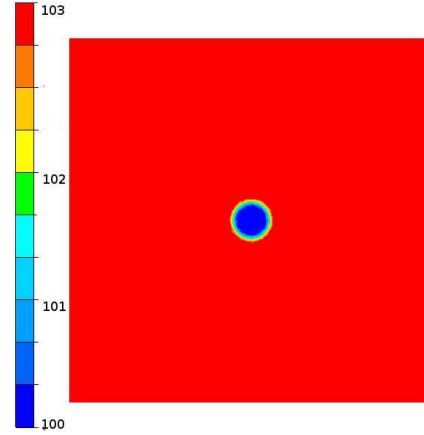


Figure 3.11: Initial temperature (°C) distribution

| Domain | Temperature (°C) | Density (kg/m <sup>3</sup> ) | Specific heat capacity (J/Kg°C) | Thermal conductivity (W/mK) |
|--------|------------------|------------------------------|---------------------------------|-----------------------------|
| Water  | 103              | 1000                         | 4182                            | 0.597                       |
| Vapor  | 100              | 0.6                          | 2054                            | 0.0371                      |

Table 3.2: Water and vapor properties and initial temperature

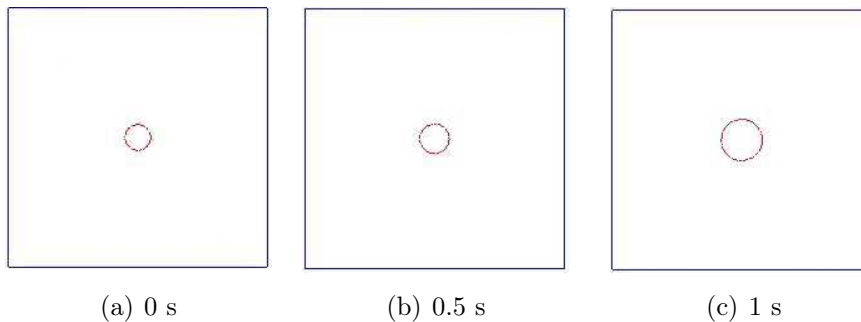


Figure 3.12: Zero isovalue of the bubbles at different time steps during the growth

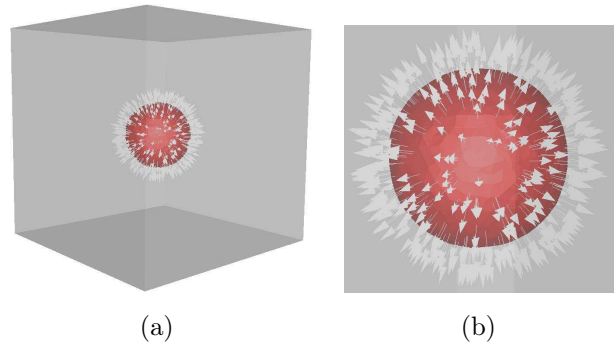


Figure 3.13: (a) Computed velocity field arrows at  $t = 2$  s, (b) Zoom at the bubble interface

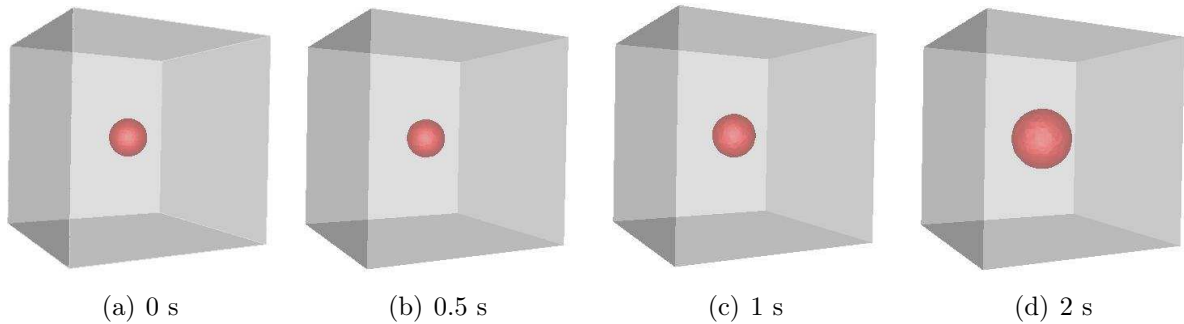


Figure 3.14: Evolution of the bubble interface

The growth approach exposed in this section offers a simple way to model the bubble expansion while accounting for both latent heat and different fluids properties. The advantage of this approach is that the bubble can have any shape. So in Chapter 5, the same approach can be used to simulate the growth of a film vapor.

## 3.4 Anisotropic adaptative mesh

During multiphase flows problem the topology of the interface (liquid-vapor) changes in many simulations: such as bubbles coalescence, bubble rising towards a free surface. To capture this interface accurately, we propose to coupled the LevelSet formulation with an anisotropic adaptative remeshing. In the literature, different anisotropic mesh adaptation methods using a priori and a posteriori error estimator have been proposed. In general, the metric tensor is estimated based on the Hessian of the solution. In this section, we briefly present the error estimator that allows the creation of extremely stretched elements along the dynamic vapor-liquid interface. It is based on the length distribution tensor approach and the associated edge based error analysis (see Coupez [32] for details). Instead of using Hessian based metric for error estimation [14], the latter is computed based on the variation of the gradient in space. The metric will be constructed at the nodes of the mesh, and its calculation requires only the computation

of the edge error estimation, defined for a function as:

$$e_{ij} = |\mathbb{G}^{ij} \cdot \mathbf{X}^{ij}| \quad (3.38)$$

where  $\mathbf{X}^{ij}$  is the edge vector made of nodes  $i$  and  $j$  that share at least one element and  $\mathbb{G}^{ij}$  is the difference between the gradient of the function  $u$  at the nodes  $i$  and  $j$  given by:

$$(\mathbb{G}u_h)^{ij} = (\mathbb{G}u_h)^j - (\mathbb{G}u_h)^i \quad (3.39)$$

Furthermore, the error estimates will be computed along each element then determined all over the domain  $\Omega$ . A continuous gradient operator based on the length distribution tensor and the projection of the gradient along the edges is defined as:

$$\mathbb{G}^i(u_h) = \arg \min_{\mathbf{G}} \left( \sum_{j \in \Gamma(i)} |(\mathbf{G} - \nabla u_h) \cdot \mathbf{X}^{ij}|^2 \right) = \arg \min_{\mathbf{G}} \left( \sum_{j \in \Gamma(i)} |(\mathbf{G} \cdot \mathbf{X}^{ij} - U^{ij})|^2 \right) \quad (3.40)$$

Consequently the gradient  $\mathbb{G}^i$  is given by

$$\mathbb{G}^i = (X^i)^{-1} U^i \quad \text{where} \quad U^i = \sum_{j \in \Gamma(i)} U^{ij} \mathbf{X}^{ij} \quad (3.41)$$

Here  $X^i$  denotes the positive tensor at the node  $i$  and  $U^{ij}$  is the difference of the function values at the nodes  $j$  and  $i$ . The optimal stretching factor field  $s_{ij}$  is then obtained by solving an optimization problem under the constraint of a fixed number of edges  $A$  in the mesh. Accordingly, the new continuous metric is built and for each edge  $\mathbf{X}^{ij}$  a new length  $s_{ij}$  is computed depending on the error analysis. Finally, the metric field is defined at each node of the mesh as follows:

$$M^i = \left( \frac{1}{d} \sum_{j \in \Gamma(i)} s_{ij}^2 \mathbf{X}^{ij} \otimes \mathbf{X}^{ij} \right) \quad (3.42)$$

$$\text{where} \quad s_{ij} = \left( \frac{\lambda}{e_{ij}} \right)^{\frac{1}{p}} \quad \text{and} \quad \lambda = \left( \frac{\left( \sum_i \sum_{j \in \Gamma(i)} e_{ij}^{\frac{p}{p+2}} \right)^{\frac{p+2}{p}}}{A} \right)^{\frac{p+2}{p}}$$

( $p \in [1, d]$ ,  $p$  is a solution of  $n_{ij} = s_{ij}^{-p}$  and  $n_{ij}$  is the number of created edges)

## 3.5 Surface Tension

### 3.5.1 Surface Tension approximation

The equations describing the immiscible multiphase flow are the Navier-Stokes equations for incompressible flow. The contribution of the surface tension forces, denoted here by  $f$ , is in addition to the gravity forces and taken into account through a local volumetric source term [33]. The equation can be written:

$$\rho(\partial_t \mathbf{v} + \mathbf{v} \cdot \nabla \mathbf{v}) + \nabla p - \nabla \cdot (\mu (\nabla \mathbf{v} + (\nabla \mathbf{v})^T)) = \rho \mathbf{g} + \mathbf{f} \text{ in } \Omega \times [0, T] \quad (3.43)$$

$$\nabla \cdot \mathbf{v} = 0 \text{ in } \Omega \times [0, T] \quad (3.44)$$

where  $\rho$  and  $\mu$  are the density and the dynamic viscosity,  $\mathbf{v}$  and  $p$  denote the velocity field and the pressure field,  $\mathbf{g}$  is the gravity force, together with the boundary conditions:

$$\mathbf{v} = \mathbf{h}_1 \quad \text{on } \Gamma_1 \times [0, T] \quad (3.45)$$

$$\mathbf{n} \cdot \boldsymbol{\sigma} = \mathbf{h}_2 \quad \text{on } \Gamma_2 \times [0, T] \quad (3.46)$$

$\Gamma_1$  and  $\Gamma_2$  are complementary subsets of the domain boundary  $\Gamma$ . As initial condition, a divergence-free velocity field  $\mathbf{v}_0(\mathbf{x})$  is specified over the domain  $\Omega_t$  at  $t = 0$ :

$$\mathbf{v}(\mathbf{x}, 0) = \mathbf{v}_0(\mathbf{x}) \quad (3.47)$$

To account for the surface tension effects at the interface between two fluids, the localized surface tension force  $f$  is given by

$$f = \sigma \kappa \cdot \mathbf{n} \delta_\Gamma^e \quad (3.48)$$

Here,  $\delta_\Gamma^e$  is a measure of Dirac delta function type with support on  $\Gamma^e$ . Its action on any smooth test function  $\varphi$  is given by

$$\int_\Omega \delta_\Gamma^e \varphi d\Omega = \int_{\Gamma^e} \varphi d\Gamma^e \quad (3.49)$$

The last term denotes the line integral of  $\varphi$  along the interface  $\Gamma^e$ . This part of the expression determines the localization of the surface tension forces. Here  $\sigma \in \mathbb{R}$  is the surface tension coefficient,  $\kappa \in \mathbb{R}$  is the (local) curvature and  $\mathbf{n} \in \mathbb{R}^2$  is a normal vector to the interface  $\Gamma^e$ . At any point along an interface, the direction of this force is towards the local center of curvature. The continuum surface force (CSF) introduced in Brackbill ([34]) is used to compute the surface tension force. It depends on the location and the derivatives of the interface. The interfacial force is taken into account as a right hand side source term added to the momentum equation and the Laplace Beltrami operator is used to compute the curvature. This approach has been used before in several multiphase problems [35, 36]. The Laplace Beltrami operator  $\Delta_T$  is function of the tangential gradient  $\nabla_T$  and is defined for a given function  $g$  by:

$$\Delta_T g = \nabla_T \cdot \nabla_T g \quad \text{with} \quad \nabla_T g = \nabla g - \nabla g \cdot \mathbf{n} \cdot \mathbf{n} \quad (3.50)$$

This offers an advantage such as the superconvergent of the Laplace Beltrami operator in a triangular mesh as presented by Zhang [37]. Since the truncated LevelSet function  $u$  is used to predict the interface between the phases, then the normal vector and the curvature can be defined by:

$$\mathbf{n} = \frac{\nabla u}{\|\nabla u\|} \quad \text{and} \quad \kappa = -\Delta_T \mathbf{n} \quad (3.51)$$

However, the main challenge in this approach is still how to compute the curvature of the fluid interface as a second derivative of the LevelSet function in particular when using a linear finite element method. Here we propose to compute the normal and the curvature by using the recovered gradient at the nodal points, presented in the previous section:

$$\mathbf{n} = \frac{\mathbb{G}(u)}{\|\mathbb{G}(u)\|} \quad \text{and} \quad \kappa = -\Delta_T \mathbf{n} \quad (3.52)$$

$$\nabla_T \cdot g = \nabla g - \nabla g : \frac{\mathbb{G}(u) \otimes \mathbb{G}(u)}{\|\mathbb{G}(u)\|^2} \quad (3.53)$$

Once the normal and the curvature are evaluated, the new interfacial force  $f$  will be introduced as a volumetric term in the Navier-Stokes equations. Where the smoothed Dirac delta function  $\delta_\Gamma^e(u)$  is the same as the one used in the energy equation:

$$\delta_\Gamma^e(u) = \begin{cases} 0 & \text{if } |u| > e \\ \frac{1}{2e} \left[ 1 - \left(\frac{u}{e}\right)^2 \right] & \text{if } |u| < e \end{cases} \quad (3.54)$$

### 3.5.2 Time step restriction

The surface tension phenomenon in multiphase flow is characterized by the nondimensional capillary number expressed as

$$Ca = \frac{\mu \mathbf{v}_{cap}}{\sigma} \quad (3.55)$$

By defining  $\Delta t_h^{cap}$  as the typical time scale and  $L$  as the length scale of surface tension phenomenon, the velocity  $\mathbf{v}_{cap}$  is equal to  $\frac{L}{\Delta t_h^{cap}}$ . In the case of two-phase flows the capillary forces and the viscous term should counterbalance each other [38], then the characteristic time scale essential to reflect the dynamics of the physical process is given by

$$Ca = \frac{\mu L}{\Delta t_h^{cap} \sigma} \approx 1 \quad \implies \quad \Delta t_h^{cap} = \frac{\mu L}{\sigma} \quad (3.56)$$

Besides physical restriction on time step another numerical constraint appears during the explicit time discretization. The stability restriction is represented in a CFL condition form :

$$\frac{\mathbf{v}_{cap} \Delta t_h^{cap}}{h} < 1 \quad (3.57)$$

Where  $h$  denotes the mesh size.

The acceleration due to the curvature can be written as  $\frac{\delta_h \sigma \kappa_h}{\rho}$ . The surface tension force was multiplied by the discrete Dirac delta function  $\delta_h$  because it acts only at the interface. At the interface, the discrete Dirac delta function is equal to  $\frac{1}{h}$  and the curvature  $\kappa_h$  has a maximum value of  $\frac{1}{h}$ . Then the capillary velocity  $\mathbf{v}_{cap} = g \Delta t$  is upper bounded by  $\frac{\sigma}{h^2 \rho} \Delta t$ . By substituting this upper bound in the CFL condition, a new time step restriction condition is presented:

$$\Delta t_h^{cap} < \sqrt{\frac{\rho h^3}{\sigma}} \quad (3.58)$$

When using a grid adaptation, this condition presents a higher limitation on the time step.

### 3.5.3 Numerical Examples

In this section, several numerical tests have been achieved in the aim to validate the new surface tension model. Figure 3.15 presents the resolution algorithm that has been used in these simulations.

The algorithm presents a numerical method to simulate bubbles rising and coalescence. The method consists on solving the same set of momentum equation where the surface tension is added as a source term. The surface tension is modelled by coupling the CSF with the gradient computed at the nodes. The liquid-vapor interface is transported with the velocity field  $v$  by solving the Convection-Reinitialization equation (3.23). The simulation results of two and three-dimensional two-phase flow problems are shown. Results are compared with the literature and show that the flow solvers based on stabilized finite element method is able to exhibit good stability and accuracy

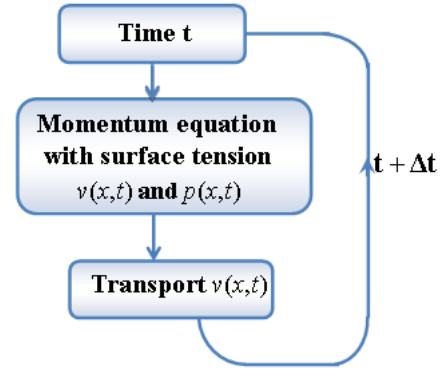


Figure 3.15: Resolution algorithm for bubbles rising

on anisotropic meshes with highly stretched elements. All the numerical implementations were carried out using CimLib based on a C++ parallel finite element library [39].

#### 3.5.3.1 Rising bubble shape in two-dimensional case

We investigate the rise and deformation of a two-dimensional gas bubble in liquid contained in a vertical, rectangular container. Due to the hydrostatic effects that increases the pressure towards the bottom of the domain, bubbles with lower density than the surrounding fluid rise and final shape is predicted. The computation domain is  $\Omega = [-0.01, 0.01] \times [-0.01, 0.02]$  m<sup>2</sup> and depicted in Figure 3.16. The air bubble is located initially at (0.01; 0.01) with a radius equal to  $1/300$  m. The fluid's surface tension is  $\sigma = 0.0728$  N.m<sup>-1</sup> and a constant gravity  $g = (0, -9.8)$  m.s<sup>2</sup> is used. At the interface, we set the thickness parameter  $E$  equal to 0.0005 m. The time step is  $\Delta t = 0.0001$  s. A no-slip boundary condition is applied on  $\partial\Omega$ .

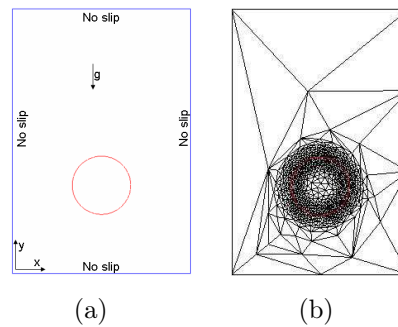


Figure 3.16: (a) Schematic domain and boundary conditions, (b) Mesh refinement at the interface of the level.

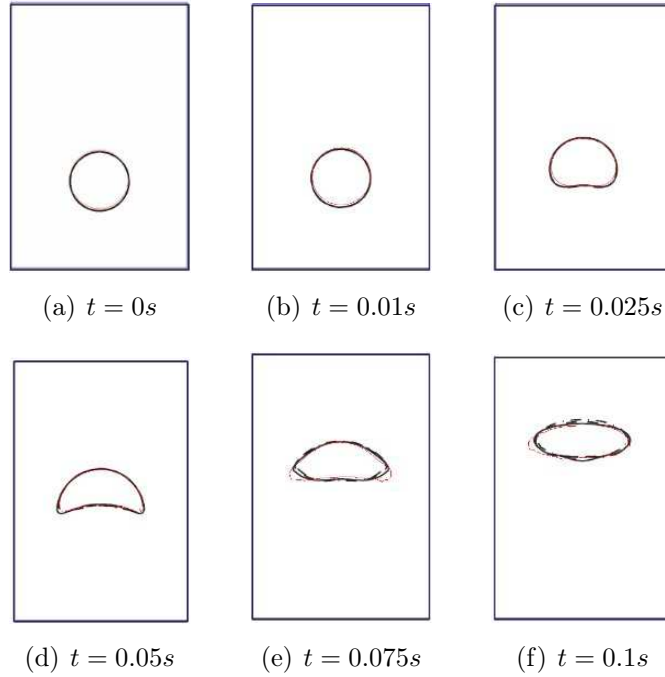


Figure 3.17: Time evolution of air bubble interface

Table 3.3 presents the fluid parameters. The evolution of the air bubble interface is shown in Figure 3.17 for different times  $t = 0.01 s$ ,  $t = 0.025 s$ ,  $t = 0.05 s$ , and  $t = 0.075 s$ . As time progresses, the bubble is severely distorted by the increase in the surface tension force. It can be seen that the bubble deforms during rising and an elliptical shape form is obtained due to viscous stress and surface tension forces. In this simulation, we fixed the number of nodes  $A$  equal to 2000 as illustrated in Figure 3.16(b). The adaptive process started from a uniform mesh and the anisotropic mesh adaptation algorithm is applied every five time step. Figure 3.17 presents a superposition between the computational results predict by CimLib (red line) and those found by Van der Pijl [40](black lines). Results show a very good agreement with the given reference using a fine structured meshes [40].

Table 3.3: Properties of fluid

|              |                                                 |                                             |
|--------------|-------------------------------------------------|---------------------------------------------|
| Vapor phase  | $\rho_v = 1.226 \text{ Kg} \cdot \text{m}^{-3}$ | $\mu_v = 1.78 \times 10^{-5} \text{ Pa.s}$  |
| Liquid phase | $\rho_l = 1000 \text{ Kg} \cdot \text{m}^{-3}$  | $\mu_l = 1.137 \times 10^{-3} \text{ Pa.s}$ |

### 3.5.3.2 Rising bubble shape in three-dimensional case

A classical example of multi phase flow with surface tension is to simulate the shape regimes indicate in Grace diagram. The aim of this example is to predict the final shape of a rising bubble. In the literature a large experimental work indicates that the bubble shape is characterized for

a range of dimensionless Morton, Eotvos and Reynolds number.

$$Mo = \frac{gu_l^4}{\rho_l \sigma^3} \quad Eo = \frac{\rho_l g D^2}{\sigma} \quad Re = \frac{\rho_l U_\infty D}{\mu_l} \quad (3.59)$$

For a single isolated very large bubble, surface tension effects and viscosity are neglected [41]. The characteristic rise velocity is given by  $U_\infty = 0.707\sqrt{gD}$  and the characteristic length  $L$  is equal to the diameter  $D$ .

The Reynolds number relates inertial forces to viscous forces. The Morton and Eotvos number relate inertial to surface tension effects and buoyancy forces to surface tension effects. Grace (1973) has made a bubble diagram for the shape of bubble rising in quiescent viscous liquid. The bubble has initially the spherical shape then it changes to different shapes as illustrated in Figure 3.18. In this work we simulate different cases that are indicated with capitals on Figure 3.18 and correspond to the parameters presented in Table 3.4.

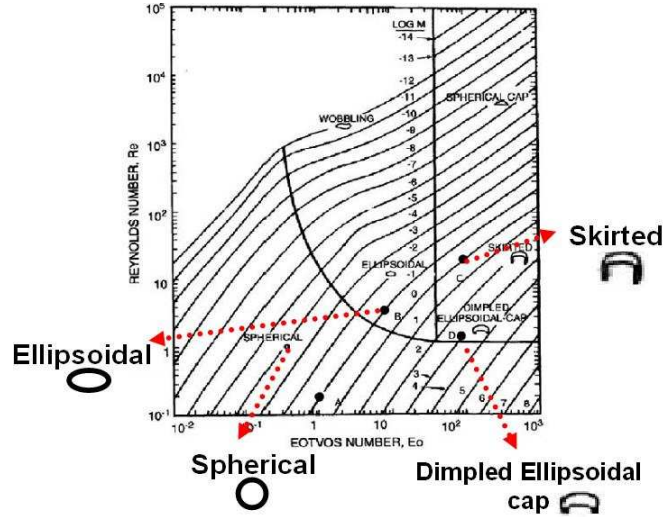


Figure 3.18: Bubble diagram of Grace reproduced from [3]: shape regimes for bubbles and drops

| Case | Shape              | Eo  | Mo   |
|------|--------------------|-----|------|
| A    | spherical          | 1   | 10   |
| B    | elipsoidal         | 10  | 0.1  |
| C    | skirted            | 100 | 1    |
| D    | dimpled elipsoidal | 100 | 1000 |

Table 3.4: Different shapes

The size of the computational domain has a large influence on the shape and terminal velocity of the bubble. To avoid this effect, the computational domain  $\Omega = [0, 3] \times [0, 3] \times [0, 6]$  m<sup>3</sup> is considered three times larger than the diameter of the bubble in each direction as in [13, 3]. The domain is discretized by using a homogenous mesh size equal to 0.05 m.



The bubble diameter is 1 m, located at (1.5; 1.5; 1.5) (Figure 3.19). The surface tension coefficient is equal to  $0.1 \text{ N.m}^{-1}$  and the constant gravity is equal to  $-10 \text{ m.s}^{-2}$ . For each case presented in table 3.4, the viscosity and density ratio were assumed equal to one hundred, then physical properties were computed from Morton and Eotvos number. Figure 3.20 presents the numerical results obtained for regimes indicated in table 3.4. Results agreed fairly well with the Grace diagram. To better visualize the shape of the bubble obtained in

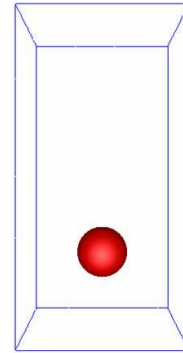


Figure 3.19: Initial bubble position

cases c and d, the intersection of the interface with the center plane of the computational domain is

presented in Figure 3.21. The surface tension model presented in this work predict a bubble shape that agree well with the experimental result.

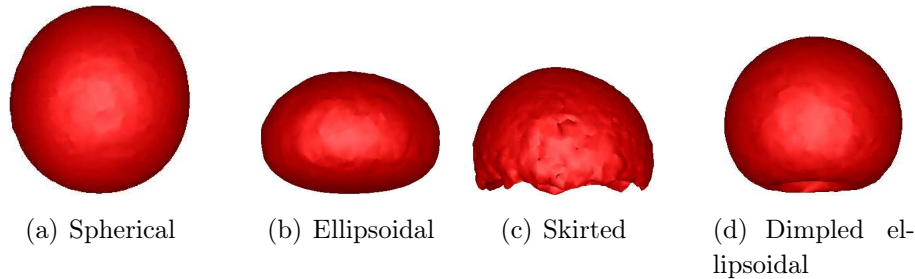


Figure 3.20: Bubble rising simulation results corresponding to the regimes indicated in table 3.4 respectively

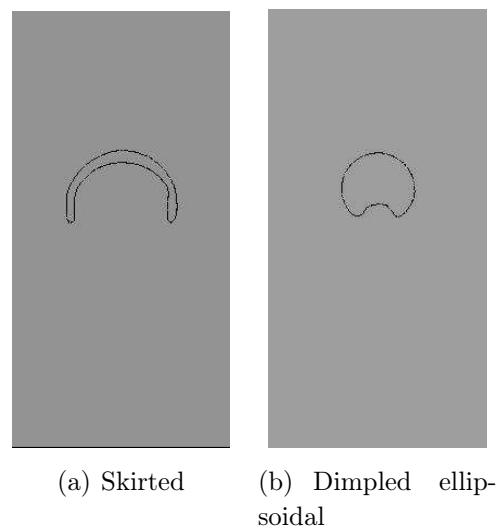


Figure 3.21: The intersection of the interface with the center plane of the computational domain

### 3.5.3.3 Coalescence of two bubble towards a free surface

In this simulation, two bubbles and a layer of fluid with properties noted by  $(\rho_2, \mu_2)$  are immersed in a heavier fluid with properties  $(\rho_1, \mu_1)$  as presented in Figure 3.22(a). The aim of this multi-phase flow is to simulate bubble coalescence with free surface. A slip condition is applied on the boundary off the domain  $\Omega = [-1.5, 1.5] \times [0, 6]$  m<sup>2</sup> as illustrated in Figure 3.22(b). The two bubbles are initially located at  $(0, 1)$  and  $(0, 2)$  with initial radius 0.4 m and 0.5 m. The layer is located on height of 3 m with surface tension coefficient  $\sigma = 0.1$  N.m<sup>-1</sup> and a constant gravity  $g = -10$  m.s<sup>-2</sup>. The fluids properties were deduced from the dimensionless number and properties ratios:

$$Mo = 0.1 \quad Eo = 10 \quad \frac{\rho_1}{\rho_2} = 100 \quad \frac{\mu_1}{\mu_2} = 2 \quad (3.60)$$

The anisotropic mesh shown in Figure 3.22(c) is obtained by using a grid adaptation with a

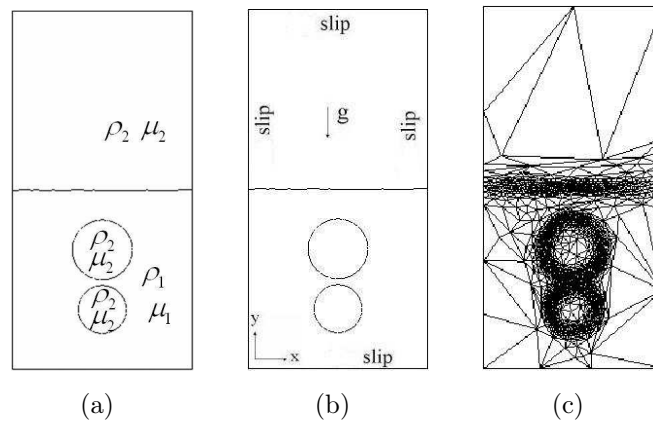


Figure 3.22: (a) Properties distribution, (b) Schematic domain and boundary conditions, (c) Mesh refinement at the interface

fixed number of edges of 4000. At the interface, the average mesh size is measured and then the characteristic time scale is computed 0.0014 s. In this simulation, the limitation on the time step is respected by choosing  $\Delta t = 0.001$  s. The numerical parameter  $E$  is set to 0.03 m. As time progresses, due to buoyancy forces the lighter bubbles rise in the surrounding fluids. During the rise the smaller bubble is deformed and the upper bubble shape changes from a sphere to a cap shape, then before reaching the surface the two bubbles at  $t = 1.05$  s merge together to become a single bubble. The filament between the bubble and the layer gets thinner which leads at  $t = 1.2$  s to a total merging of the bubble with the surface. Thanks to the grid adaptation a little drop of the lighter fluid is captured at  $t = 6$  s. Finally at  $t = 24$  s, the two fluids are separated by a flat surface located on a height of 2.58 m. This simulation shows that the use of a LevelSet function coupled to an anisotropic mesh adaptation is well suited for simulation including topological change. The mesh becomes locally refined around the zero isovalue of the LevelSet function which enables it to sharply define the interface and to save a great number of elements compared to classical isotropic refinement. The results presents in Figure 3.23 at times  $t = 0$  s,  $t = 0.5$  s,  $t = 1.05$  s,  $t = 1.2$  s,  $t = 6$  s, and  $t = 2.15$  s are similar to those found by Tornberg in [42].

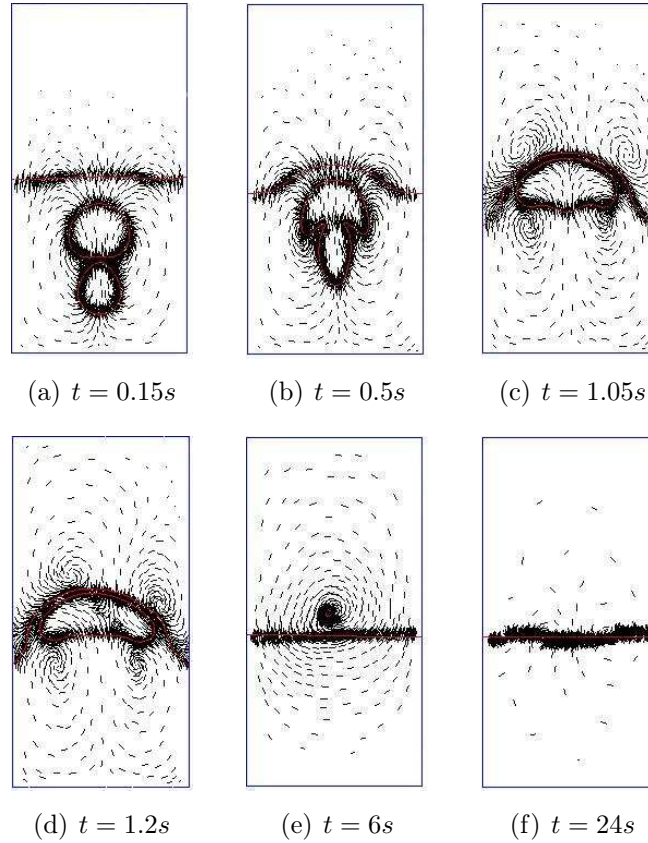


Figure 3.23: Time evolution of fluid interface and the velocity field

### 3.5.3.4 Bubble coalescence

The rise and deformation of a three-dimensional gas bubble in liquid contained in a vertical, rectangular container is presented in this paragraph. Two bubbles are initially located at  $(0.005; 0.005; 0.005)$  and  $(0.005; 0.005; 0.00797)$  inside a given domain  $\Omega = [0.01; 0.01; 0.02] \text{ m}^3$ . The bubbles have an initial diameter equal to  $D = 2.6 \text{ mm}$ . The domain is discretized by using a homogenous mesh size equal to  $0.0003 \text{ m}$ . The aim of this multi-phase flow is to simulate the bubble coalescence using the convected LevelSet method and the anisotropic mesh adaptation. The dynamic of the bubbles depends on two parameters: the first is the initial distance between bubbles and the second is the surface tension coefficient. In this numerical test, we follow the lines in [43], we set the distance to  $0.37 \text{ mm}$  and the surface tension coefficient to  $5.8 \times 10^{-4} \text{ N.m}^{-1}$ . The physical parameters for the surrounding fluid are  $\rho_1 = 880 \text{ Kg.m}^{-3}$  and  $\mu_1 = 0.0125 \text{ N.s.m}^2$ , whereas for the bubble we take  $\rho_2 = 440 \text{ Kg.m}^{-3}$  and  $\mu_2 = 0.00625 \text{ N.s.m}^2$ . As time progresses, the lower bubble is deformed and the upper bubble shape changes from a sphere to a cap shape (Figure 3.24 at times  $t = 0 \text{ s}$ ,  $t = 0.015 \text{ s}$ ,  $t = 0.045 \text{ s}$ ,  $t = 0.06 \text{ s}$ ,  $t = 0.075 \text{ s}$ , and  $t = 0.15 \text{ s}$ ). It can be noted that at time equal to  $0.15 \text{ s}$ , the two bubbles merge together to become a single bubble with a cap shape. These results are in very good agreement with those found in [43].

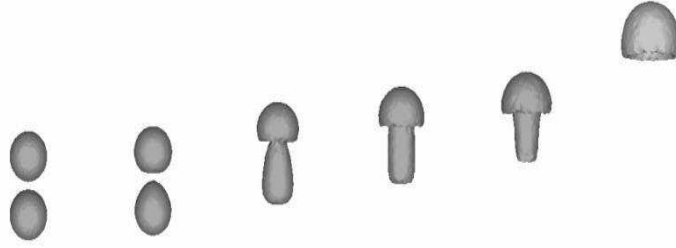


Figure 3.24: Isovalue zero of the LevelSet function for bubble coalescence

### 3.5.3.5 Ascension

When a single bubble rises in a stagnant liquid, the bubble terminal velocity can be used as a parameter of comparison between numerical and analytical result. The bubble rising reached a constant velocity (terminal velocity) when the forces acting on it are in equilibrium [44].

$$F_b + F_d = 0 \quad (3.61)$$

In fact these forces are the buoyancy  $F_b$  and the drag  $F_d$  forces. During the ascension, the pressure on the bottom of the bubble is higher than on its upper part, which induces a vertical force known as the buoyancy force. The fluid exerts a pressure and a tangential friction force that oppose to the bubble movement. This resistance force is carried by the axis of the bubble movement and represents the drag force. These forces can be expressed by:

$$F_b = \frac{4}{3}\Pi R^3 (\rho_l - \rho_g) g \quad , \quad F_d = \frac{1}{2}C_d A \rho_l u^2 \quad (3.62)$$

where  $R$  is the bubble radius,  $\rho_l$  is the density of the liquid,  $\rho_g$  is the density of the bubble,  $g$  is the gravity,  $C_d$  is a function of the Reynolds number and the bubble shape,  $A$  is the bubble area and  $u$  is the speed of the bubble.

#### Bubble size:

The bubble size can be predicted by the dimensionless Weber (ratio between inertia force and the surface tension force) and Reynolds number (ratio between inertia force and the viscous effect), defined respectively by:

$$We_b = \frac{u_\infty^2 d_e \rho_l}{\sigma} \quad , \quad Re_b = \frac{u_\infty d_e \rho_l}{\mu_l} \quad (3.63)$$

- a) If  $We_b \ll 1$  then the surface tension effect is dominant and the bubble will preserve the spherical form.
- b) If  $We_b \ll 1$  &  $Re_b \gg 1$  then the surface tension and the viscosity effects are negligible and the bubble is considered very large.

**Analytical terminal velocity:****a) Single isolated small bubble:**

Since the surface tension force is inversely proportionate to the radius  $2\sigma\kappa = \frac{2\sigma}{R}$ , when a small bubble rises this force becomes predominant and the bubble preserves the spherical form. The terminal velocity was deduced from the stokes solution as following [41]:

$$u_{\infty} = \frac{1}{18} \frac{gd_e^2 (\rho_l - \rho_g)}{\mu_l} \quad (3.64)$$

Here  $d_e$  is the equivalent bubble diameter (the diameter of a sphere with the same volume) and  $\mu_l$  is the liquid dynamic viscosity.

**b) Single isolated large bubble:**

For large bubbles, the surface tension and the viscosity effect are neglected, Talaia [41] presents the terminal rise velocity:

$$u_{\infty} = 0.707\sqrt{gd_e} \quad (3.65)$$

Here we present the numerical simulation of two different-sized bubbles rising in a liquid in order to test our numerical approach.

**Comparison numerical and analytical results:**

In this numerical example, we consider the same fluids properties as the one presented in section 3.6.3.1. Since the dimension of the computation domain affects the terminal bubble velocity and the bubble shape [45], we consider a domain size equal to ten times the bubble diameters in each spatial dimension. The computational domain  $\Omega = [-0.035; 0.035]^2 \text{ m}^2$  is discretized by using an unstructured grid and a mesh size  $h = 0.005 \text{ m}$ .

**a) Large bubble ascension:**

In this case, the Weber number is  $We = 3.651$  and the Reynolds number is  $Re = 117$ , since the two dimensionless numbers are superior to unit, a large bubble case is treated. The analytical velocity is given by (3.65)  $u_{\infty} = 0.18 \text{ m} \cdot \text{s}^{-1}$ . The time step is considered equal to  $\Delta t = 0.0005 \text{ s}$ . Figure 3.25 shows the bubble evolution at different time steps. The vapor bubble rises from its initial position  $(0; 0)$  with the corresponding numerical velocity:

$$u_{num} = \frac{y - y^-}{\Delta t} \approx 0.18 \text{ m} \cdot \text{s}^{-1} \quad (3.66)$$

**b) Small bubble ascension:**

In this numerical test, the liquid viscosity is increased to  $0.4 \text{ Pa} \cdot \text{s}$  so the Weber number becomes equal to 0.228. Since it is smaller than the unit number, the surface tension effect is dominant. The analytical terminal rise velocity is expressed by (3.64) and is equal to  $u_{\infty} \approx 0.06 \text{ m} \cdot \text{s}^{-1}$ . Figure 3.26 shows the bubble evolution at different time steps. The bubble rises and keeps the spherical form due to the surface tension dominance. The corresponding numerical velocity is given by:

$$u_{num} = \frac{y - y^-}{\Delta t} \approx 0.06 \text{ m} \cdot \text{s}^{-1} \quad (3.67)$$

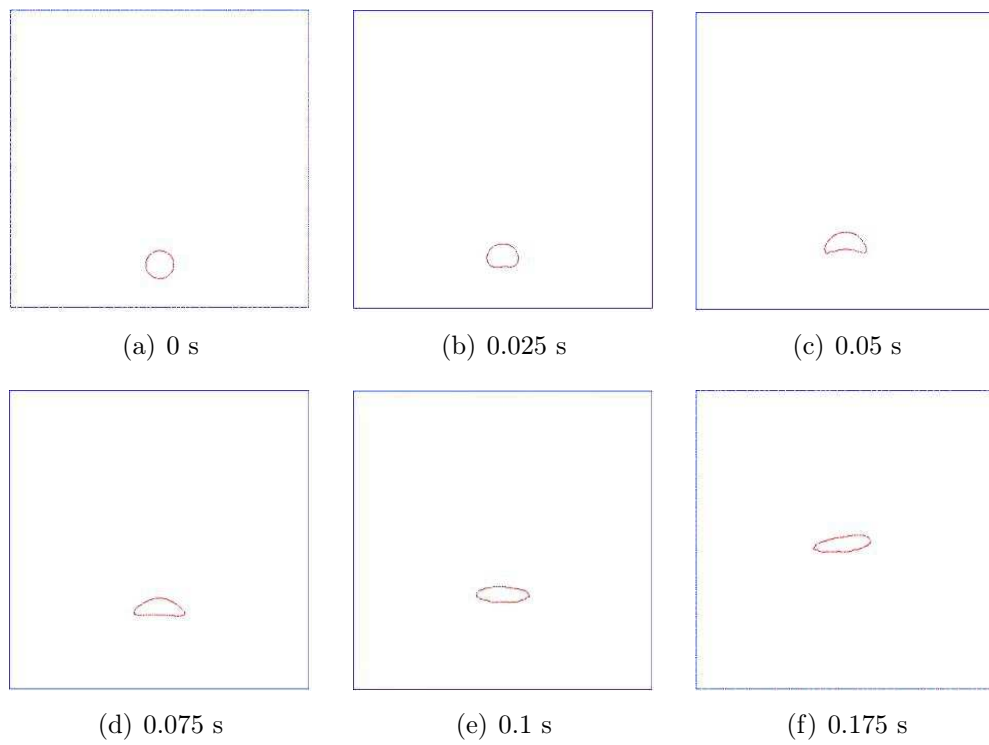


Figure 3.25: Large air bubble ascension

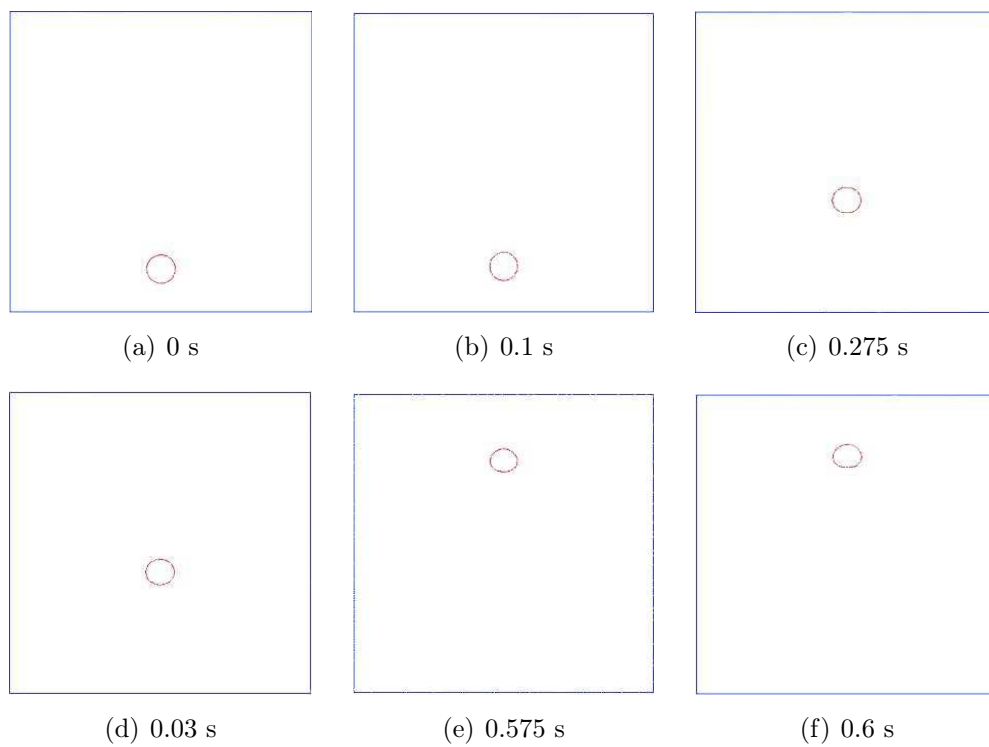


Figure 3.26: Small air bubble ascension

By using the numerical approach presented in this work, the numerical terminal velocities are in good agreement with the analytical ones in both cases.

### 3.5.3.6 Numerical & Experimental investigation of bubble rising

This paragraph reports experiment on the shape and detachment of air bubbles rising in water. We set up this experiment to validate our numerical approach. The bubbles images were recorded by a high speed CDD camera (Phantom Miro eX-series) Photonetics (125 to 2500 images/s) and coupled with a 110 macro photos objective. In this experience, the camera was configured to acquire images at a framing rate of 1800 frame/s with an image size of  $400 \times 800$  pixels. The experimental apparatus  $20 \times 10 \times 15$  cm<sup>3</sup> is a Plexiglas water tank, which is considered large enough to neglects the wall effects. At the center of the bottom plate, an air bubble is pushed out to the water tank through a Polyurethane tube. The outer diameter of the capillary tube is set to 4 mm. A schematic diagram of the experimental test used in this study is shown in Figure 3.27.

Figure 3.28 presents snapshots of bubbles at different times. As expected, the bubble generated

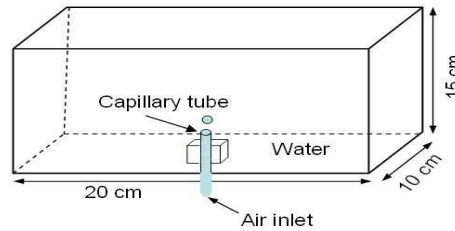


Figure 3.27: Set-up for air bubble generation method

by the capillary tube at  $t = 0$  s is ellipsoidal with a diameter of 5.8 mm. The detachment and the coalescence of bubbles depend on the surface tension force. As time progresses, the lower bubble is deformed and the upper bubble shape changes from an ellipsoidal to a cap shape. As the bubbles are merging together, a mushroom form can be observed.

We applied the same setup in a numerical context. Recall that the density and the viscosity of outer fluid are  $1000 \text{ Kg/m}^3$  and  $0.001137 \text{ N.s.m}^2$  respectively. For the bubble, density  $1.226 \text{ Kg/m}^3$  and viscosity  $0.0000178 \text{ N.s.m}^2$  are prescribed. Due to the small imposed pressure force, the bubble begins to rise and induces a jet of water that pushes the below bubble into the upper bubble. The gap between the formed bubble and the lower surface gets thinner and finally the first bubble detaches. The trailing edge of the detached bubble breaks of in a fast way and formes an ellipsoidal shape bubble as shown in the experimental results due to the surface tension. This is clearly highlighted in Figure 3.29. As expected, the anisotropic mesh adaptation captures accurately the vapor-liquid interface all along the simulation. An extremely refined mesh is well rendered in Figure 3.30 at the interfaces whereas far from the interfaces, the mesh is coarser. Again, this reflects and explains how, for a controlled number of nodes, the mesh is naturally and automatically coarsened in that region with the goal of reducing the mesh size at the interfaces of every new formed bubble. These numerical results are in good agreement with the experimental results presented above.

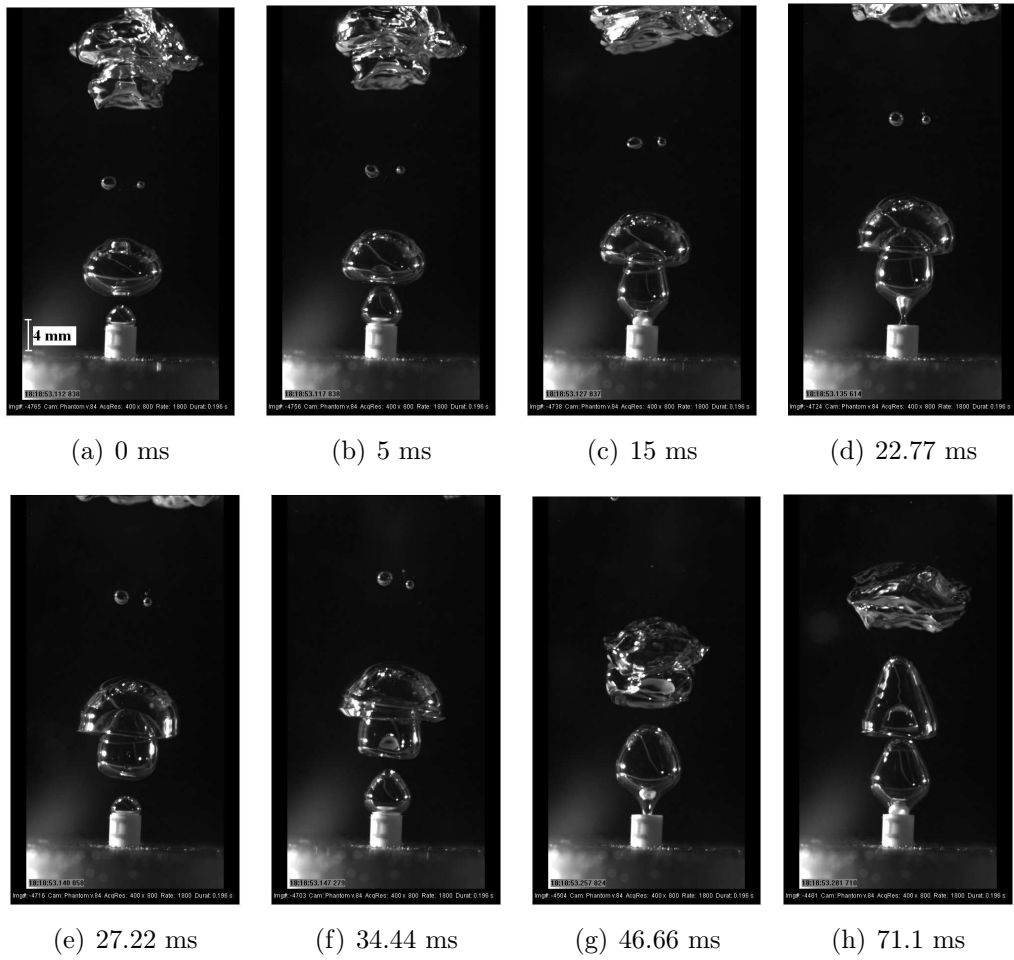


Figure 3.28: Experimental investigation of air bubble rising

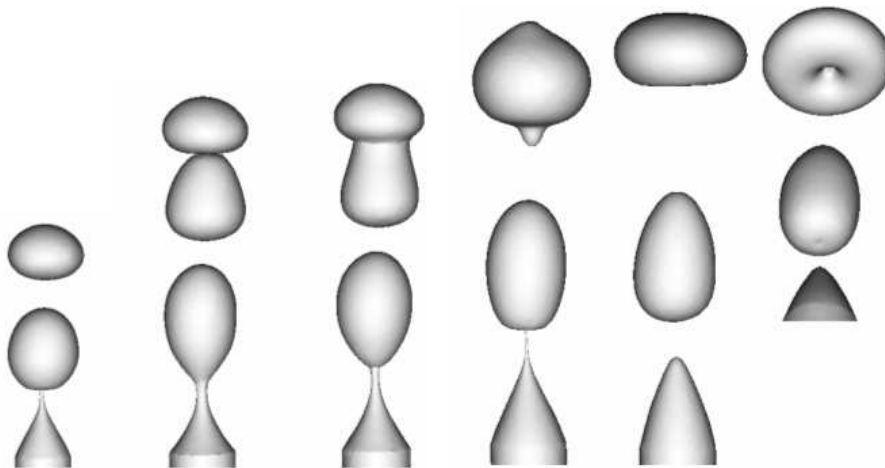


Figure 3.29: Flow rising of a 3D bubble with anisotropic mesh adaptation at the vapor-liquid interfaces



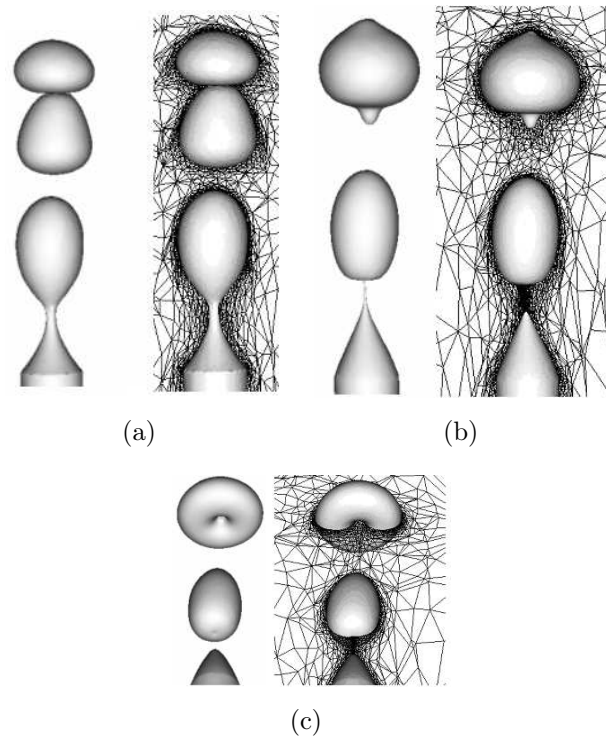


Figure 3.30: Anisotropic mesh adaptation at different time steps

## 3.6 Conclusion

A novel numerical approach is presented for the simulation of phase change using the LevelSet method to track the liquid-vapor interface and by solving one set of equations in both domains with different phase properties. The hyperbolic tangent function is used to truncate the interface and a convected reinitialization method is used to predict it at each time step. A new mathematical approach describing the bubble growth process was proposed and numerical simulation was performed. The surface tension was computed explicitly by combining the continuum surface force (CSF) and a continuous gradient computed directly at the nodes of the mesh. This new approach imposes a time step restriction but it is particularly suited for computing the curvature fields. The used approach takes advantage of the LevelSet method to capture the interface and to present the coalescence between bubbles. The performance of the new method was tested on different numerical examples in **2D** and **3D**. The surface tension model was validated. A benchmark of air bubble rising in water has also been achieved. It has shown a relatively good agreement between the numerical prediction and the experimental measurements. This method was also applied in Chapter 5 to simulate the generation of a film of vapor followed by its detachment.

## 3.7 Résumé français

Dans ce chapitre on présente la simulation de l'ébullition pas une approche multiphasique directe. En particulier, la simulation de l'évolution d'une ou quelques bulles de vapeur à partir d'un modèle unique de type germination croissance. La première partie est consacrée à la description de l'interface entre les deux phases par la méthode LevelSet. La méthode LevelSet permet de rendre compte de la croissance de la phase gazeuse dans le liquide en faisant intervenir une vitesse de croissance suivant la normale à l'interface et dont le module dépend de la température. Ce modèle de croissance, basé sur l'approche de Gibbs Thomson, est présentée dans la deuxième partie de ce chapitre. Différents tests numériques à températures homogène et hétérogène ont été réalisés, ainsi qu'une validation de cette approche par une comparaison avec la solution analytique. Les résultats de la troisième partie démontrent le rôle déterminant de la tension de surface sur le détachement, la coalescence et la prédiction de la forme des bulles. Les calculs de force de tension de surface nécessitent une très grande précision et l'adaptation de maillage s'avère un outil fondamental pour ce type de calcul. En particulier, pour le calcul de la courbure, on utilise une nouvelle approche de reconstruction du gradient basée sur une technique d'estimation d'erreur. Cette dernière étant le point délicat en termes de précision et de stabilité des calculs des forces interfaciales dans les écoulements multiphasiques. Les premières comparaisons numériques avec les résultats expérimentaux mettent en relief la combinaison d'une nouvelle méthode de capture d'interface dite " Convected LevelSet " et l'adaptation anisotrope de maillage.



# References

- [1] [http://darkwing.uoregon.edu/linke/papers/walker\\_leidenfrost\\_essay.pdf](http://darkwing.uoregon.edu/linke/papers/walker_leidenfrost_essay.pdf).
- [2] <http://www.thermopedia.com/content/602/>.
- [3] E. Marchandise, F. Geuzaine, N. Chevaugeon, and J. F. Remacle. A stabilized finite element method using a discontinuous level set approach for the computation of bubble dynamics. *Journal Of Computational Physics*, 225:949–974, 2007.
- [4] G. Yadigaroglu. Computational fluid dynamics for nuclear applications: from cfd to multi-scale cmfd. *Nuclear Engineering and Design*, 235:2–4, 2005.
- [5] M. G. Cooper. Saturation nucleate pool boiling—a simple correlation. *Institution of Chemical Engineers (IchemE) Symposium Series*, 86:786–793, 1984.
- [6] T. Bo. CFD homogeneous mixing flow modelling to simulate subcooled nucleate boiling flow. *SAE world congress, Ricardo Consulting Engineers, U.K.*, 01-1512, 2004.
- [7] F. Krause, S. Schüttenberg, and U. Fritshing. Modelling and simulation of flow boiling heat transfer. *International Journal of Numerical Methods for Heat and Fluid Flow*, 20(3):312–331, 2010.
- [8] K. Robinson, N. A. F. Campbell, J. G. H. Hawley, and M. J. Leathard. Predicting heat transfer in simulated ic engine cooling galleries. *Vehicle Thermal Management Systems, Brighton, United Kingdom*, 6(C599/038), 2003.
- [9] V. Srinivasan, K. M. Moon, D. Greif, D. M. Wang, and M. H. Kim. Numerical simulation of immersion quenching process of an engine cylinder head. *Applied Mathematical Modelling*, 34:2111–2128, 2010.
- [10] V. Srinivasan, K. M. Moon, D. Greif, D. M. Wang, and M. H. Kim. Numerical simulation of immersion quench cooling process using an eulerian multi-fluid approach. *Applied Thermal Engineering*, 30:499–509, 2010.
- [11] D. Turlajs, V. Grivcovs, and S. Yaundalders. Initial stage of vapor bubble growth in superheated liquids. *International Journal of Systems Applications, Engineering and Development*, 1, 2007.
- [12] J. J. Feng and C. A. Bertelo. Prediction of bubble growth and size distribution in polymer foaming based on a new heterogeneous nucleation model. *The Society of Rheology*, 48:439–462, 2004.

- [13] M. V. S. Annaland, N. G. Deen, and J. A. M. Kuipers. Numerical simulation of gas bubbles behaviour using a three-dimensional volume of fluid method. *Chemical Engineering Science*, 60:2999–3011, 2005.
- [14] A. Claisse, V. Ducrot, and P. Frey. Levelsets and anisotropic mesh adaptation. *Discrete and Continuous Dynamical Systems*, 23:165–183, 2009.
- [15] O. Basset. *Simulation numérique d'écoulements multi fluides sur grille de calcul*. PhD thesis, PhD thesis, Ecole Nationale Supérieure des Mines de Paris, 2006.
- [16] S. Osher H.K. Zhao D. Peng, B. Merriman and M. Kang. A pde based fast local level set method. *Journal of Computational Physics*, 155:410–438, 1999.
- [17] M. Sussman. *A Level Set Approach for Computing Solutions to Incompressible Two-Phase Flow*. PhD thesis, Ph.D. Thesis in Mathematics, University of California, Los Angeles, 1994.
- [18] S. Osher and R. fedkiw. *Level Set Methods and Dynamic Implicit Surfaces*. PhD thesis, Springer-Verlag, New York, 2003.
- [19] W. Zerguine. *Adaptation de maillage anisotrope et écoulements multifluides Applications en injection assistée eau*. PhD thesis, Ecole Nationale Supérieure des Mines de Paris, 2010.
- [20] T. Coupez. Réinitialisation convective et locale des fonctions level set pour le mouvement de surfaces et d'interfaces. *JournÉes ActivitÉs Universitaires De MÉcanique - La Rochelle*, 31 AoÛt Et 1Er Septembre, 2006.
- [21] L. Ville, L. Silva, and T. Coupez. Convected level set method for the numerical simulation of fluid buckling. *International Journal For Numerical Methods In Fluids*, 2010.
- [22] T. Coupez, N. Kosseifi, and E. Hachem. Direct computational methods for multiphase fluid dynamics of vapor-liquid flow. In *ECI 8th International Conference on Boiling and Condensation Heat Transfer Ecole Polytechnique Fédérale de Lausanne, Lausanne, Switzerland, 3-7 June 2012*, 2012.
- [23] R. N. Elias and A. L. G. A. Coutinho. Stabilized Edge-Based Finite Element Simulation Of Free-Surface Flows. *International Journal For Numerical Methods In Fluids*, 54(6-8):965–993, Jun-Jul 2007.
- [24] N. Zuber. The dynamics of vapour bubbles in nonuniform temperature field. *International Journal of Heat and Mass Transfer*, 2:83–98, 1961.
- [25] A. J. Robinson and R. J. Judd. Bubble growth in uniform and spatially distributed temperature field. *International Journal of Heat and Mass Transfer*, 44:2699–2710, 2001.
- [26] B. B. Mikic, W. M. Rohsenow, and P. Griffith. On bubble growth rates. *International Journal Heat Mass Transfer*, 13:657–666, 1970.
- [27] H. S. Lee and H. Jr. Merte. Explosive vapor bubble growth in uniformly superheated liquids: R-113 and mercury. *International Journal of Heat and Mass transfer*, 48:2593–2600, 2005.

- 
- [28] M. Barthès. *Ebullition sur site isolé : étude expérimentale de la dynamique de croissance d'une bulle et des transferts associés*. PhD thesis, Université De Provence, 2005.
- [29] G. Tryggvason, A. Esmaeelia, and N. Al-Rawahib. Direct numerical simulations of flows with phase change. *Computers and Structures*, 83:445–453, 2005.
- [30] L. Tan and N. Zabaras. A level set simulation of dendritic solidification with combined features of front-tracking and fixed-domain methods. *Journal of computed physics*, 211:36–63, 2006.
- [31] M. Rappaz, M. Bellet, and M. Deville. *Numerical Modeling in Materials Science and Engineering*. Springer-Verlag Berlin Heidelberg, 2002.
- [32] T. Coupez. Metric construction by length distribution tensor and edge based error for anisotropic adaptive meshing. *Journal of Computational Physics*, 230(7):2391–2405, 2011.
- [33] Y. C. Chang, T. Y. Hou, B. Merriman, and S. Osher. A level set formulation of eulerian interface capturing methods for incompressible fluid flows. *Journal Of Computational Physics*, 124:449–464, 1996.
- [34] J. U. Brackbill, D. B. Kothe, and C. Zemach. A continuum method for modeling surface tension. *Journal of Chemical Physics*, 100(2):335–383, 1992.
- [35] S. Groß, V. Reichelt, A. Reusken, and S. Osher. A finite element based level set method for two-phase incompressible flows. *Comput. Vis. Sci.*, 9:239–257, 2006.
- [36] S. Hysing. A new implicit surface tension implementation for interfacial flows. *Internet J. Numer. Methods Fluids*, 51:659–672, 2006.
- [37] Z. Zhang, H. D. Victory, Jr., and H. Dean. Mathematical analysis of zienkiewicz-zhu's derivative patch recovery technique. *Numerical Methods Partial Dierential Equations*, (4), 1996.
- [38] M. kang, R. P. Fedkiw, and X. D. Liu. A boundary condition capturing method for multi-phase incompressible flow. *CAM Report 99-27 UCLA*, 2000.
- [39] Y. Mesri, H. Digonnet, and T. Coupez. Advanced parallel computing in material forming with cimlib. *European Journal Of Computational Mechanics*, 18:669–694, 2009.
- [40] S. P. van der Pijl, A. Segal, C. Vuik, and P. Wesseling. A mass-conserving level-set method for modelling of multi-phase flows. *International journal for numerical methods in fluids*, 47:339–361, 2005.
- [41] M. A. R. Talaia. Terminal velocity of a bubble rise in a liquid column. *World Academy of Science, Engineering and Technology*, 28, 2007.
- [42] A. K. Tornberg and B. Engquist. A finite element based level set method for multiphase flow applications. *Computing Visualization in Science*, 3:39–101, 2000.

- [43] F. S. de Sousa, N. Mangiavacch, L. G. Nonato, A. Castelo, M. F. Tome, V. G. Ferreira, J. A. Cuminato, and S. McKee. A front-tracking/ front-capturing method for the simulation of 3d multi-fluid flows with free surfaces. *Journal of Computational Physics*, 198:469–499, 2004.
- [44] W. L. Haberman and R. K. Morton. An experimental investigation of the drag and shape of air bubbles rising in various liquids. *Navy department The David W. Taylor Model Basin Washington 7 D.C.*, Report 802, 1953.
- [45] J. Hua and J. Lou. Numerical simulation of bubble rising in viscous liquid. *Journal of Computational Physics*, 222:769–795, 2007.

# Chapter 4

## Temperature & velocity field measurement during nucleate boiling by PIV & LIF

### Contents

---

|            |                                                                  |            |
|------------|------------------------------------------------------------------|------------|
| <b>4.1</b> | <b>Experimental analysis of the bubble growth rate . . . . .</b> | <b>98</b>  |
| 4.1.1      | Experimental apparatus . . . . .                                 | 99         |
| 4.1.2      | Results and discussion . . . . .                                 | 99         |
| 4.1.3      | Results and analysis for a higher superheat . . . . .            | 102        |
| 4.1.4      | Conclusion & motivation for further experimental investigations  | 105        |
| <b>4.2</b> | <b>Particle Image Velocimetry . . . . .</b>                      | <b>106</b> |
| 4.2.1      | Principle of PIV . . . . .                                       | 106        |
| 4.2.2      | Results . . . . .                                                | 109        |
| <b>4.3</b> | <b>Laser Induced Fluorescence . . . . .</b>                      | <b>112</b> |
| 4.3.1      | Principle of two color LIF thermometry . . . . .                 | 112        |
| 4.3.2      | Fluorescence dyes selection and optical systems . . . . .        | 113        |
| 4.3.3      | Concentration choice . . . . .                                   | 116        |
| 4.3.4      | Camera calibration . . . . .                                     | 118        |
| 4.3.5      | Temperature calibration . . . . .                                | 119        |
| 4.3.6      | Results and discussion . . . . .                                 | 119        |
| <b>4.4</b> | <b>Conclusion &amp; Perspectives . . . . .</b>                   | <b>122</b> |
| <b>4.5</b> | <b>Résumé français . . . . .</b>                                 | <b>123</b> |

---



Fundamental comprehension of bubble growth on a heated surface is primordial to understand the heat transfer during boiling phenomenon. The behavior of a bubble growing at a heated surface has been studied by different authors using different numerical methods (e.g., [2, 6, 7, 8]). The bubble's shape, the growth rate, the local velocity and the temperature field around a bubble growing on a heated surface are not sufficiently known for detailed comparison with numerical simulations [9, 10, 11]. The purpose of the present chapter is first, to evaluate the bubble shape and the bubble growth rate by analyzing image captured by a high speed CDD camera; second, to measure the velocity around the bubble interface by applying the Particle Image Velocimetry (PIV). Finally, to measure the temperature distribution by applying the two-color Laser Induced Fluorescence (LIF) to the nucleate boiling problem. The application, of these optical techniques to nucleate boiling, poses an attractive test case for the PIV because of the flow turbulence and a specific challenge for the LIF because of the relatively high temperature range (60 °C - 70 °C).

## 4.1 Experimental analysis of the bubble growth rate

A lot of experimental researches are devoted for a complete understanding of the hemispherical vapor bubble growth on a superheated plan (Figure 4.1) [12, 13, 14, 15]. In this configuration, the timescale of the growth period is divided into inertia-controlled and thermal-controlled. The inertia growth period is controlled by the pressure difference and is a short interval of the growth period. The thermal growth is controlled by conduction through the liquid and is the largest part of the growth period. These two phases are distinguished by a change in the vapor bubble

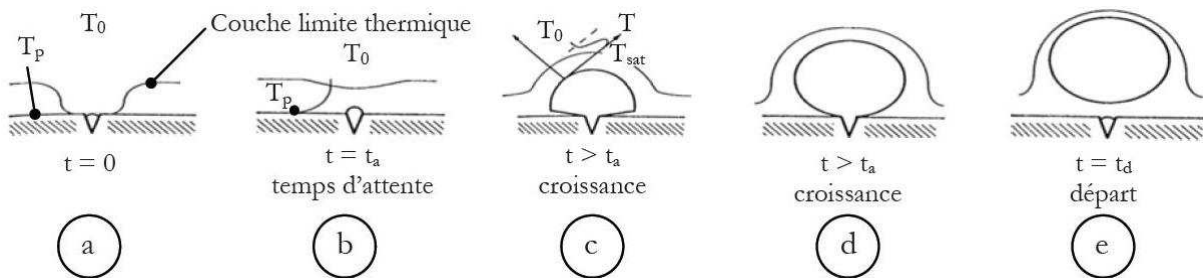


Figure 4.1: Schematic representation of the bubble growth on a heated wall [1]

shape from hemispherical to spherical. Figure 4.1 presents the bubble evolution, it can be noted that the thermal growth period starts at step d, where the surface tension gives the bubble a spherical shape. In Figure 4.2 the inertia-controlled is noted by IC and thermal-controlled by HT. Since HT is the largest part of the growth period as shown in (Figure 4.2), in this experimental investigation we treat the variation of the radius during it. In the present paragraph, we report a detailed study of a single bubble growing on a heated surface. The bubble shape was captured with a high speed CDD camera. The bubble growth rate is measured with an image analysis.

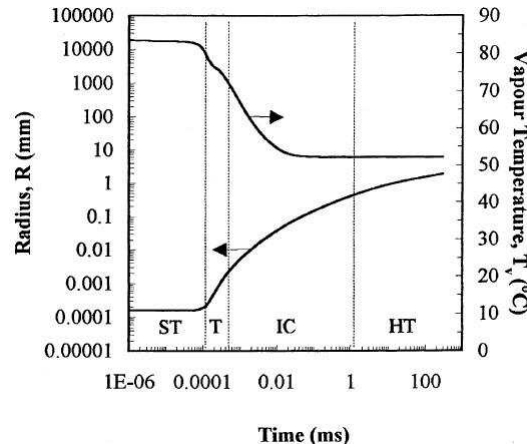


Figure 4.2: Variation of bubble radius and temperature for hemispherical bubble growing on a heated wall [2]

#### 4.1.1 Experimental apparatus

Nucleate boiling experiment is performed using distilled water. The aim of this experiment is to evaluate the bubble growth rate. A schematic diagram of the experimental apparatus used in this study is shown in (Figure 4.3). The apparatus consists mainly of a hot plate used to generate and maintain the heating surface of a beaker at a constant temperature. The beaker is made of a Pyrex glass; it has an inner diameter of 35.55 mm, a thickness of 6.2 mm and a height of 6 cm. The beaker is filled with 20 ml of distilled water. Images of bubble growth were captured using a high speed CDD camera (Phantom Miro eX-series) Photonics (125 to 2500 images/s) and coupled with a 110 macro photos objective. A halogen lamp was used as a lightening equipment to visualize better the bubble. Images were processed using software image analysis Visilog<sup>®</sup> 5 and the bubble radiuses were measured. This nucleate boiling experience is realized under the atmospheric pressure (1 atm). Near the edge of the beaker, the surface is not flat, then the cavity becomes a nucleation site where a single bubble can be generated.

#### 4.1.2 Results and discussion

In this experience, the camera was configured to acquire images at a framing rate of 1949 frame/s with an image size of  $256 \times 256$  pix<sup>2</sup>. The temperature was measured using K-type thermocouples as shown in table 4.1, and placed at the following positions:

1. Thermocouple welded on the hot plate.
2. Thermocouple fixed at level of the bubble.
3. Thermocouple fixed in 10 ml of water.
4. Thermocouple fixed in 10 ml on the beaker.

For this superheat a single nucleation site is activated and a vapor bubble is generated. Figure 4.4 presents the life cycle of the vapor bubble. The bubble has a hemispherical shape

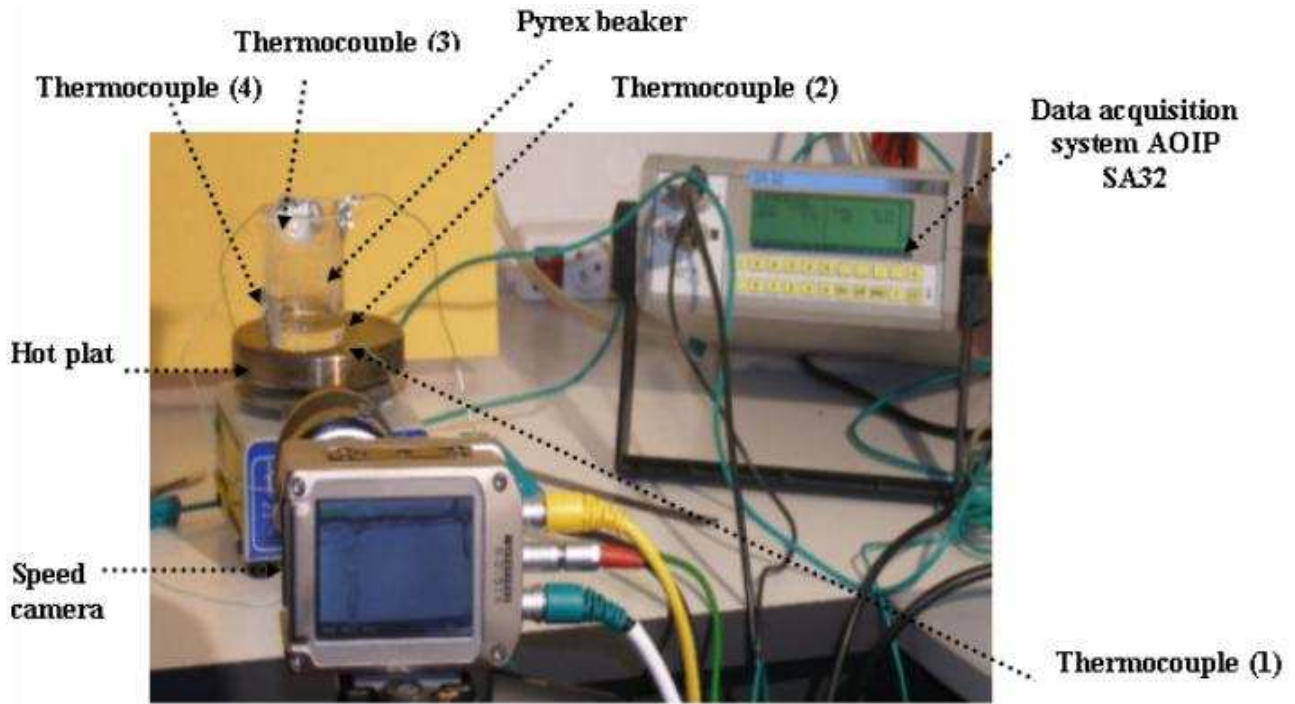


Figure 4.3: Experimental apparatus

| Thermocouple     | 1     | 2     | 3    | 4     |
|------------------|-------|-------|------|-------|
| Temperature (°C) | 297.7 | 103.5 | 95.5 | 102.5 |

Table 4.1: Temperature data from thermocouples

at the early growth stage then it changes to an elongated shape as it proceeds towards the detachment. The growth time is approximately 8 ms; it is divided into inertial growth noted by IC and heat transfer growth noted by HT as in Robinson [2] (Figure 4.6). These regimes are distinguished by a change in the vapor bubble shape from hemispherical to spherical, thanks to the surface tension the bubble becomes spherical at step (b) of Figure 4.4. Then at  $t = 0.5$  s the heat transfer period starts. Because the bubble didn't keep a spherical shape and changes to an elongated shape close to the moment of detachment. To calculate the bubble growth rate, in spite of using the equivalent radius  $R_{eq}$  as in Lee [15], we decide to calculate the evolution of the radius in both directions  $x$  and  $y$ . Let's denote  $R_x$  and  $R_y$  the radius in the  $x$  direction and the  $y$  direction, respectively. Figure 4.5 shows the change from a spherical form to a spheroidal shape where  $R_x = a'$  and  $R_y = b'$ . The experimental radiuses measured by Visilog<sup>®</sup> are compared to a function of time found by Qiu and Dhir [16]:

$$R = R_0 + Bt^n \quad (4.1)$$

In this equation,  $B$  and  $n$  are constants that depend on the experience configurations: the superheat, the inclination angle of the heated surface and the fluid nature. Figure 4.7 shows that by taking  $B = 0.3$  and the exponent equal to 0.5, both experimental radiuses vary with a function of time and are in good agreement with the one found by Qiu and Dhir.

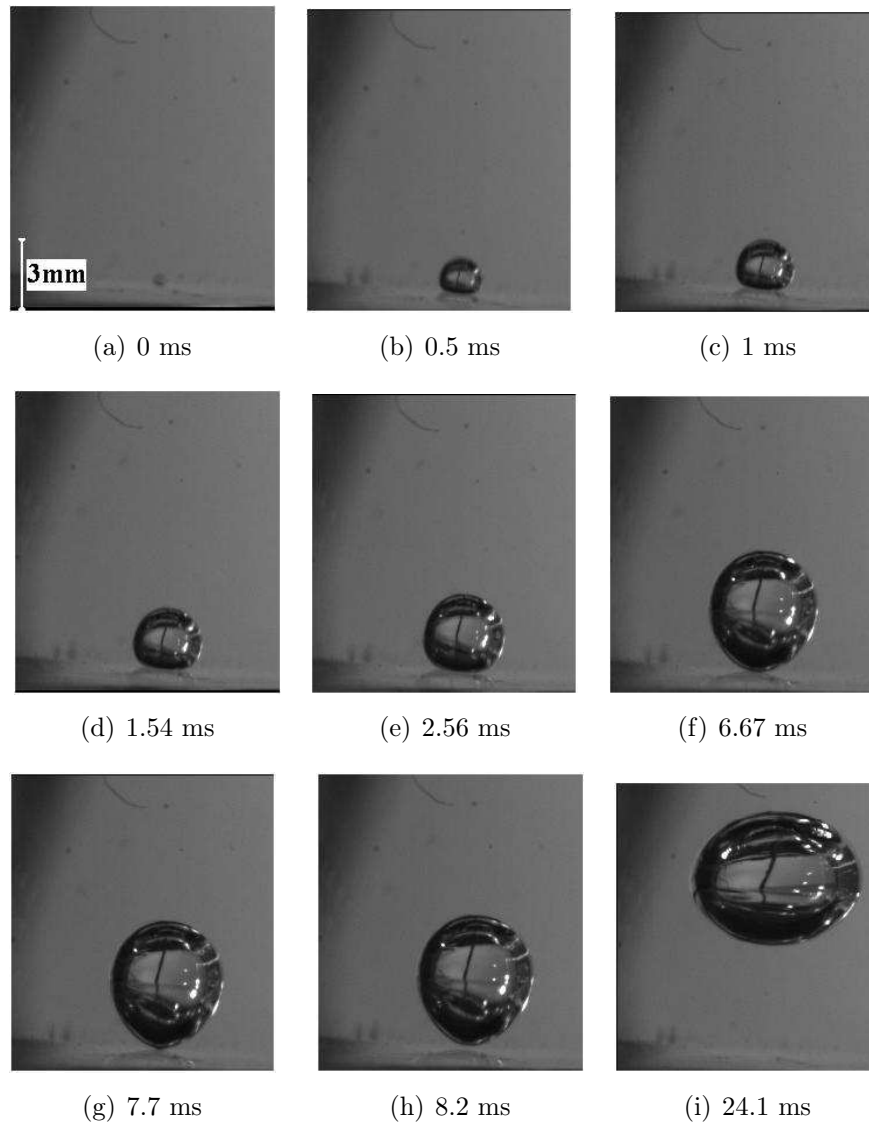


Figure 4.4: Bubble evolution

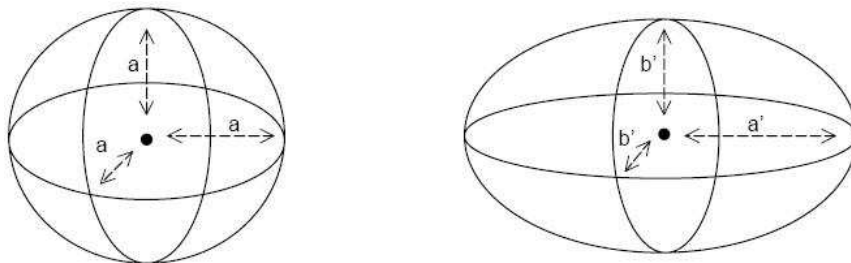


Figure 4.5: Bubble deformation [3]

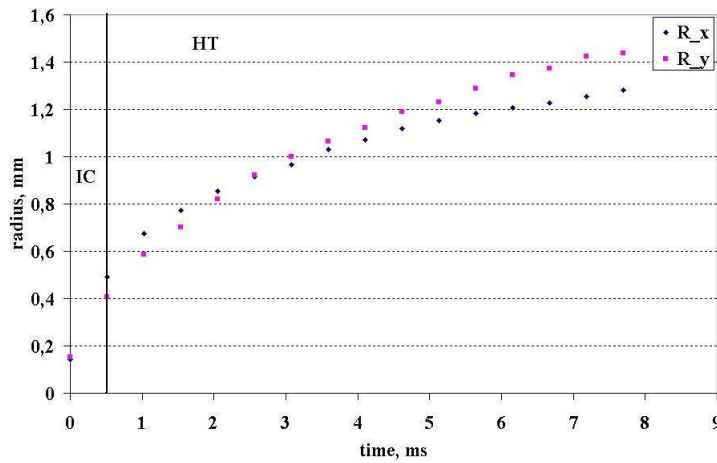


Figure 4.6: Evolution of  $R_x$  and  $R_y$  during the growth period

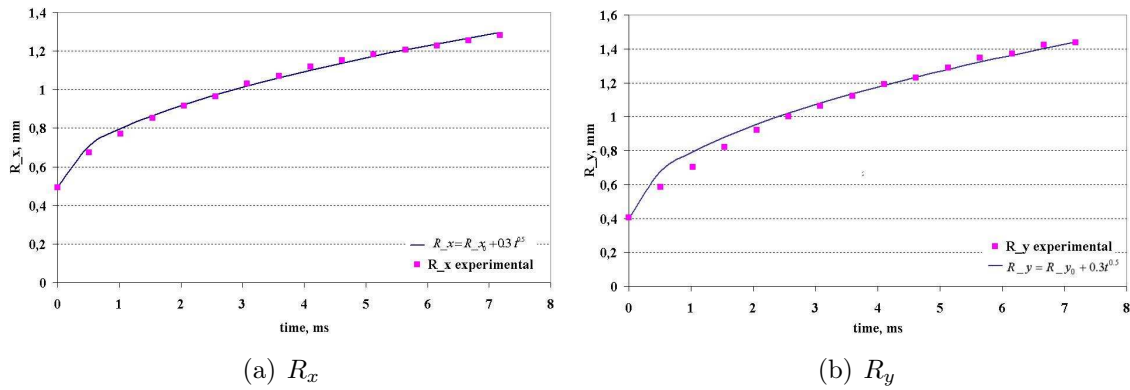


Figure 4.7: Variation of bubble radiuses before the detachment

### 4.1.3 Results and analysis for a higher superheat

When overheating with a temperature higher than the previous one, a nucleus is generated under the previous bubble (Figure 4.8). Then it grows up with a duration about 8 ms. As the bubble rises a new nucleus appears at  $t = 18.4$  ms. The waiting time corresponding to the period after bubble departure to the instance when a new nucleus appears [17] is about 9.6 ms. The bubble continues to rise and the new nucleus starts to grow. For higher superheats, vertical coalescence can occur. The bubble radiuses in each-direction and the vapor area were measured from the image using Visilog<sup>®</sup>.

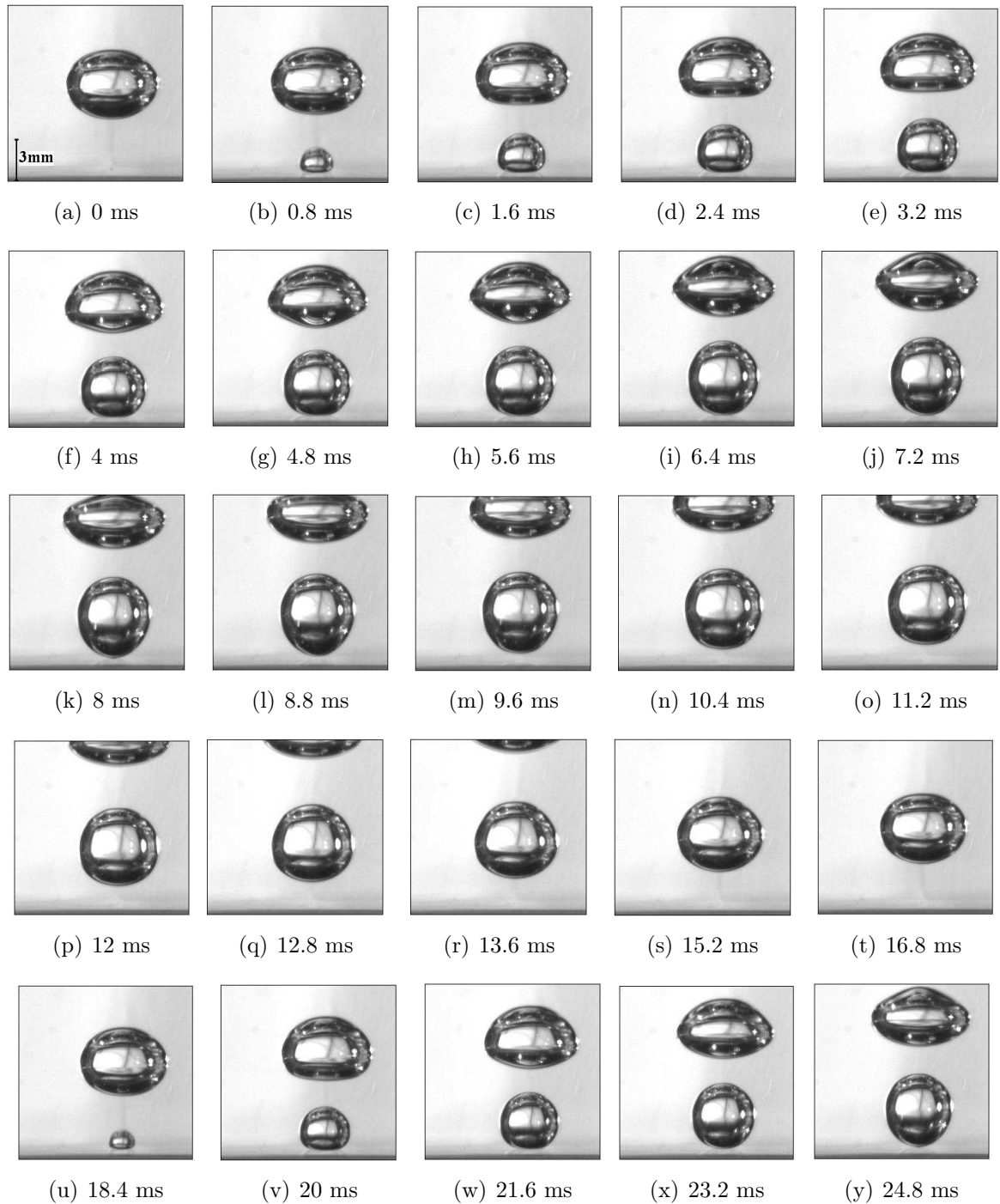


Figure 4.8: Cycle of events at the nucleation site

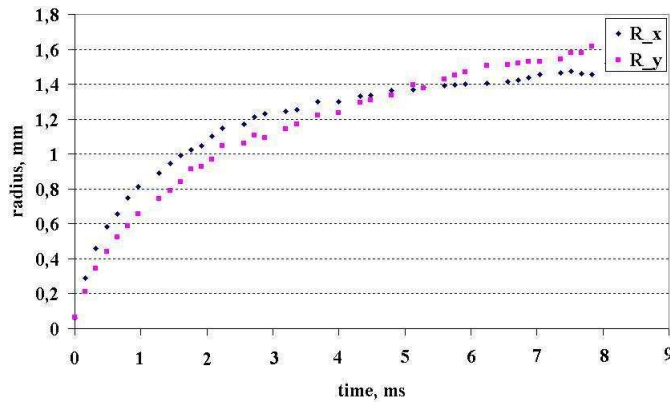


Figure 4.9: Variation of bubble radiuses during the growth

Figure 4.9 presents the measurement of radiuses during the bubble growth. Since the bubble radiuses are equal then the bubble has a spherical shape and the short period of growth was not captured. Figure 4.10 presents the comparison of the measured radiuses with polynomial forms  $R_x = R_{x_0} + 1.4t^{0.5}$  and  $R_y = R_{y_0} + 1.4t^{0.5}$ . As it can be seen these results are in good agreement with the function of time found by Qiu and Dhir [16]. In this experience, the exponent is 0.5 and the growth constant  $B$  is 1.4. Here we have the same exponent as above, but a different value of  $B$  which is due to the excess in the superheat. Figure 4.11(a) illustrates the radiuses

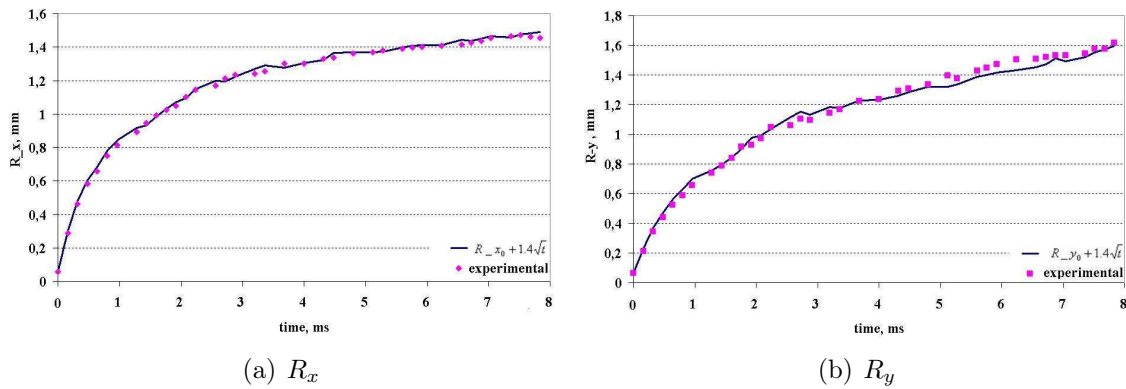


Figure 4.10: Comparison experimental and polynomial form for both radiuses

evolution versus time after the bubble detachment, it can be noted that  $R_x$  is increasing with the same rate as  $R_y$  is decreasing. Therefore after the detachment, the bubble stops growing and preserves a constant volume (Figure 4.11(b)).

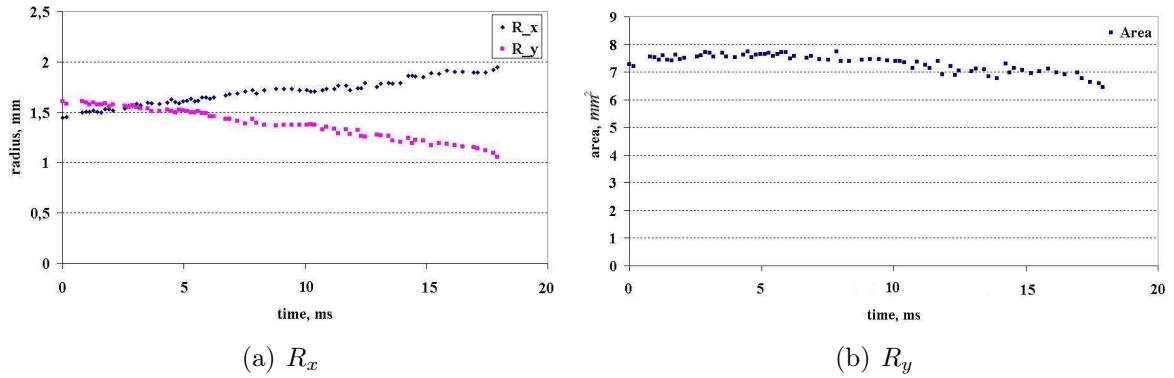


Figure 4.11: (a) Radiuses evolution after the bubble detachment, (b) Area evolution after the bubble detachment

#### 4.1.4 Conclusion & motivation for further experimental investigations

A high speed CDD camera was used to track the bubble's shape evolution. The bubble growth rates were analyzed and compared with a function of time from Qiu and Dhir [16]. Results are in good agreement with the previous work [16]. Different values of the constant  $B$  can be noticed, this difference is due to the thermal problem configuration.

A second objective of the present chapter is to measure the temperature and the velocity fields around a growing bubble. The intrusive methods such as thermocouple have poor spatial and temporal resolution [18]. Other categories of remote measurement suffers from some important limitation, for example the thermal infrared camera operates on a specific range of wavelength. Due to the rapid evolution of the optical techniques and the digital image processing techniques, the non-intrusive method becomes the most efficient in measuring the velocity and the temperature fields. These optical techniques offer a non-intrusive measurement with a high temperature resolution and provide information about the whole velocity field.

#### New test setup for further experimental investigations

Recently, Siedel[19] and Kowalewski [20] developed a new setup to generate bubble from an artificial site. Here to get an accurate study of the bubble growth, we developed a similar experimental apparatus as illustrated in Figure 4.12.

Bubbles are nucleated at an artificial cavity made at the center of a circular copper disk. The cavity is around 0.2 mm in mouth diameter. The disk is 20 mm in diameter and 0.2 mm in thickness. It is attached to the copper stem (see Figure 1(b)) that transmits heat generated by a cartridge heater (6 mm in diameter and 48 mm in height). The stem is equipped with four K-type thermocouples at distances 17 mm, 12 mm, 7 mm and 2 mm from the disk in order to deduce the disk temperature. The temperature of the heater is controlled by a PID. The whole heating system is installed in a thermal isolation cylinder made of Polytetrafluoroethylen (PTFE) and integrated to a cylindrical glass tube (50 mm in inner diameter) filled partially by a test liquid. In the present study, we chose ethanol as the test liquid because of its low boiling temperature



( $T_{sat} = 78.4\text{ }^{\circ}\text{C}$ ) under the atmospheric pressure and its compatibility with dyes used in the LIF thermometry. A typical volume of the test liquid is 100 ml. The tube is placed vertically, with the copper disk facing up, in a square tank of  $170 \times 170 \times 210\text{ mm}^3$  with transparent lateral walls made of Polymethyl Methacrylate (PMMA). The tank is filled by water and kept at a constant temperature by continuous water circulation from a thermostatic bath. It serves to condition the ambient temperature of the boiling and also to correct optical distortion due to the curvature of the tube's lateral wall. The temperature of the ethanol in the tube,  $T_e$ , and the temperature of the water in the square tank,  $T_w$ , are monitored by K-type thermocouples. Fluctuation of these temperatures during an experiment is typically of  $0.1\text{ }^{\circ}\text{C}$ . The difference  $T_e - T_w$  is typically  $-0.3\text{ }^{\circ}\text{C}$  without heating the copper disk and is around  $1\text{ }^{\circ}\text{C}$  with the heating.

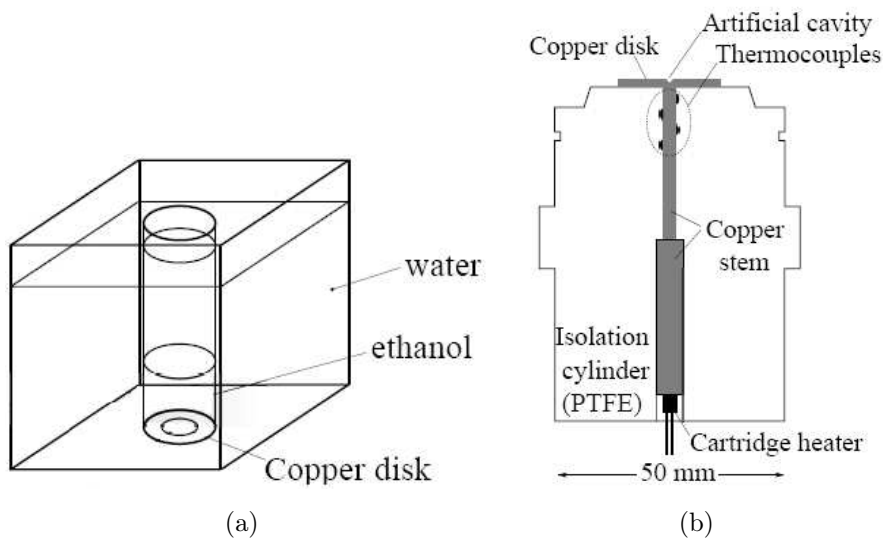


Figure 4.12: (a) Experimental device, (b) Heater element

## 4.2 Particle Image Velocimetry

The term of "Particle Image velocimetry" appeared in the literature 27 years ago [4], this technique is usually applied to measure the fluid flow velocity in a plane.

### 4.2.1 Principle of PIV

In fact, the local velocity was measured from the distance that a tracer particle has crossed during a certain time. Figure 4.13 illustrates the system components for PIV. It consists of a laser light sheet, a single camera and the flow where the tracer particles are added. The CCD camera (Image Pro X from Lavision) recorded images at 14 Hz. As it can be noticed in Figure 4.13, the camera is placed perpendicular to the illumination source. The laser in use is a dual cavity laser. It produces two sheets that have to be stacked. Actually a laser sheet illuminates the small particles added to the flow. Then two images were recorded at two time steps. If we denote  $\Delta x$

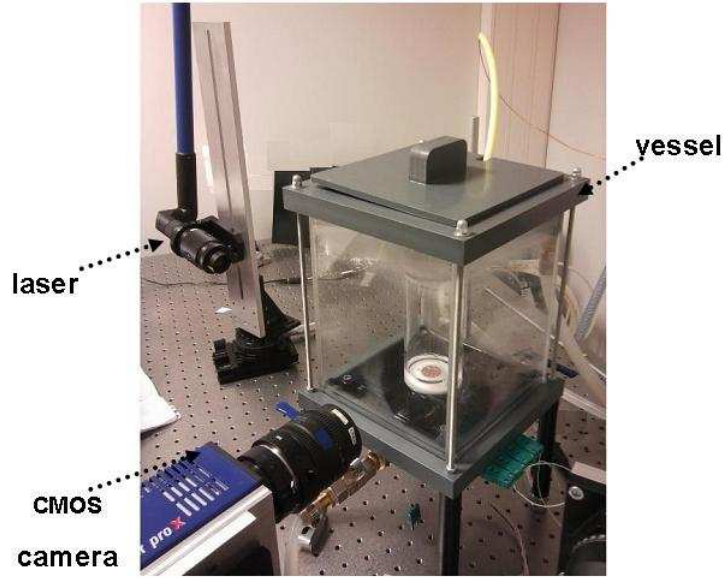


Figure 4.13: Apparatus of a Particle Image Velocimetry system

the distance travelled by the tracer particles during a time interval  $\Delta t$ . The local velocity of the liquid can be calculated by:

$$V = \frac{\Delta x}{\Delta t} \quad (4.2)$$

The particle displacement obtained by using an intercorrelation algorithm of images is predicted in Figure 4.14. We consider two images, one at time  $t$  and the other at time  $t + dt$ . Then we

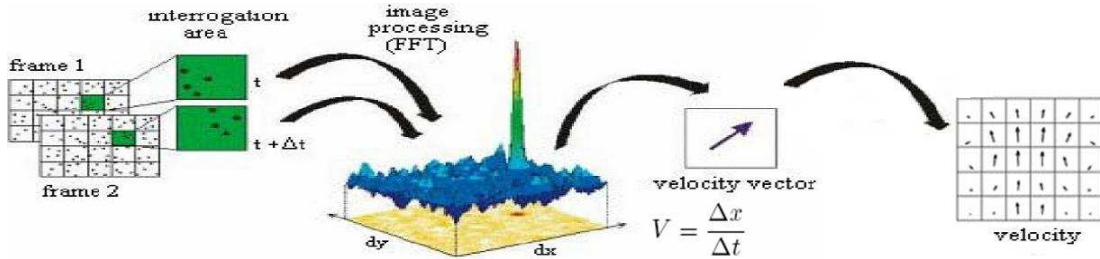


Figure 4.14: Intercorrelation algorithm of images (inspired from [4])

define a window called the interrogation area, in which the calculation is done. The correlation is performed from the intensity, the expression of direct intercorrelation is the following:

$$R_{N_1 N_2}(x, y) = \frac{\sum_i \sum_j N_1(i, j) N_2(i + x, j + y)}{\sum_i \sum_j N_1(i, j) \sum_i \sum_j N_2(i, j)} \quad (4.3)$$

where  $N$  denotes the dimension of the interrogation area. To reduce the computation time, it is more common to use the properties of the Fourier space in particular the algorithm of Fast Fourier Transforms (FFT). The result of the intercorrelation is graphically expressed by the cross-correlation diagram. The average displacement of particles in the interrogation area is equal to

the distance between the peak and the origin of the diagram. Once the displacement is measured, the velocity is obtained by dividing the displacement by the time step. This treatment, repeated over the entire image, allows the reconstruction of the velocity field in the measurement plane. Nevertheless, the cross-correlation can lead to the presence of some aberrant vectors which can be removed by different methods of post-treatment. By combining the local velocity, the velocity fields can be described on all the measurement plan.

### **Software:**

To analyze the images, we use the commercial particle image velocimetry (PIV) software Davis<sup>®</sup> from LaVision. It allows a lot of operations on the images and a synchronization between the laser and the camera. This software offers a control of the camera via LaVision's command language. The illumination source is a double cavity Nd:YAG laser from Litron Laser with a pulse energy of 600 mJ (max), at a wavelength of 532 nm. As the laser has a dual cavity, two kinds of frame can be done: a classic "single frame" and a dual cavity known as "double frame". Thanks to the dual cavity particle images can be obtained and the time separation between light pulses can be adjusted as an entry parameter.

### **Calibration:**

The first step before the measurement is known as the calibration. Several images of the calibration target (containing a number of dots) placed in the beaker parallel to the PIV light sheet and at a specific distance, were recorded. Then, the conversion between pixel and the real dimension, can be realized by measuring the real distance between two dots and from the image.

### **Preparation of the solution:**

The experimental work has been performed under atmospheric pressure for ethanol. This fluid is characterized by a low boiling temperature of 70 °C under atmospheric pressure. Several Fluorescent particles are available in various sizes. In the present experimental investigation, the flow is seeded with Fluorescent Nile Red Particles that have a size of 10-14  $\mu\text{m}$ . These particles are insoluble in ethanol and their fluorescence remains stable for a long period of time even under saturation conditions. As presented in Figure 4.15 the frame is first split into a set of correlation windows.

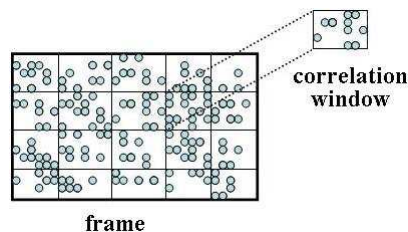


Figure 4.15: Frame and correlation windows

The size of the correlation window  $B$  plays an important role in predicting the number of tracers per correlation window. In fact, two criteria must be ascertained: the number of particles in the window has to be larger than typically 4 and the larger particle displacement should be

lower than  $B/3$  [21]. These two criteria are necessary to obtain a high peaked correlation function and to avoid the exiting of too many particles in the correlation window [22]. In this experiment, the size of the interrogation window is  $32 \times 32$  pixels<sup>2</sup> and contains at least 5 particles. The concentration of seeded particles has been maintained during the PIV measurement; it means that particles can be added if necessary. The seeding concentration must be accurate because the use of a large amount of tracers decreases the quality of the velocity measurement. Figure 4.16 presents the image intensity distribution of ethanol seeded with Fluorescent Nile Red Particles.

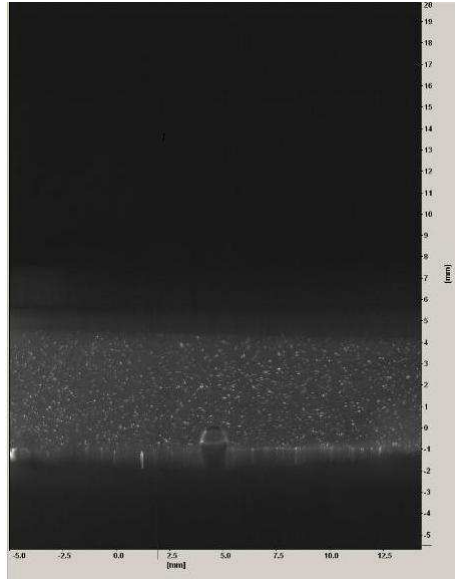


Figure 4.16: Particles distribution around the bubble

## 4.2.2 Results

By using the PIV technique to the phase flow, it is difficult to identify which velocity vectors correspond to which phase of flow [23]. Figure 4.17 shows the velocity field measurement for the growing vapor bubble. It can be noted that the growth rate of the bubble is not uniform. The highest speed reached at 72 ms is 0.075 m/s. After that the growth rates decreases, then the heat transfer growth periods starts at  $t=144$  ms. The last picture shows the bubble before the detachment, the velocity is nearly uniform and its magnitude is 0.075 m/s. The flow field surrounding the bubble is strongly dependent of the motion of the bubble interface [23]. In fact several forces act on the bubble interface which complicate the study of the bubble behavior and the measurement of the local interface velocity. The flow is not symmetric due to the fluid turbulence, more particularly to the vortex. Figure 4.18 shows the measured flow field in term of the velocity magnitude and the corresponding streamlines. It indicates the fluid turbulence due to the natural convection. Various vortices are seen near the bubble interface as presented in Figure 4.19.

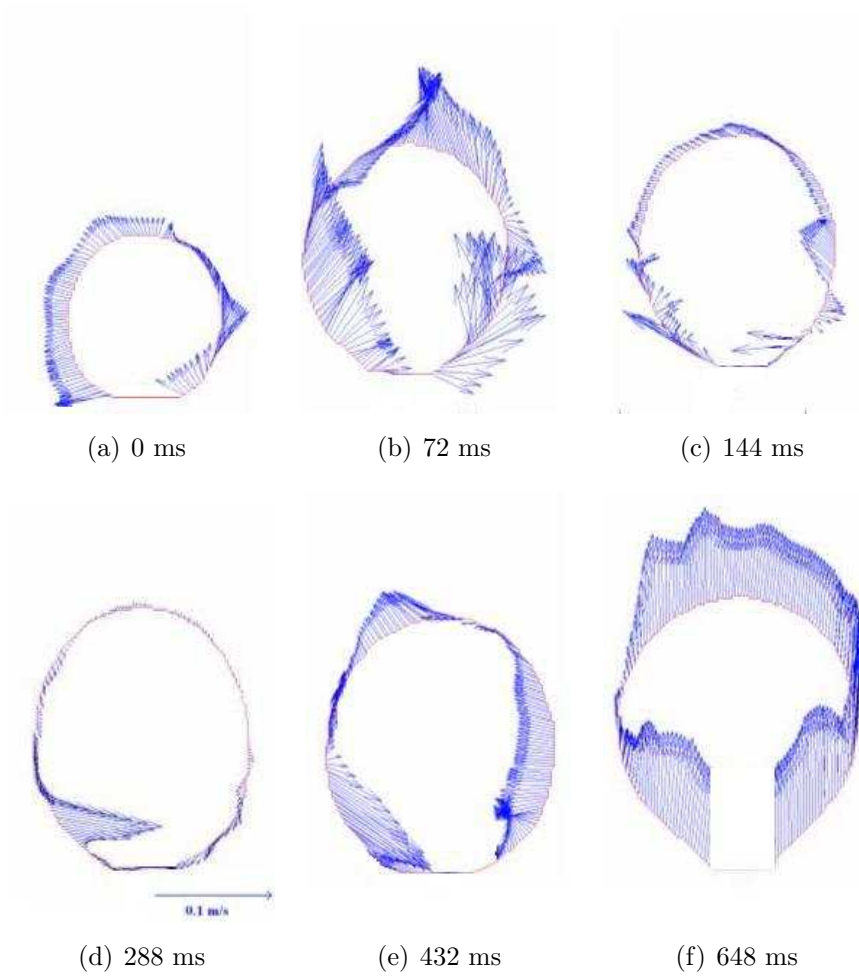


Figure 4.17: Velocity field PIV measurements at the bubble edge

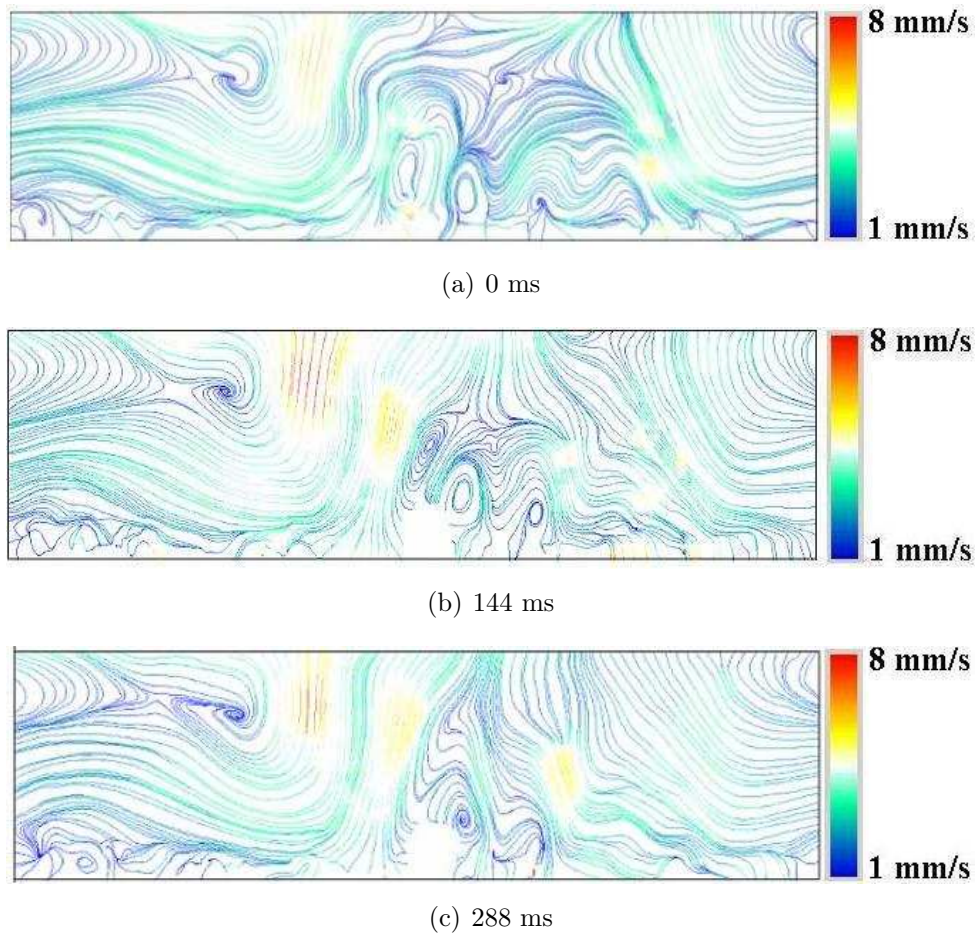


Figure 4.18: Experimental streamlines obtained by PIV measurements. The colors correspond to the modulus of the velocity

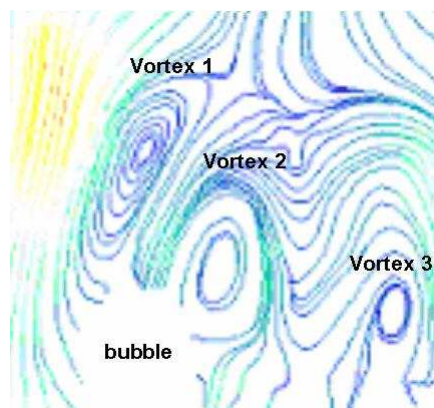


Figure 4.19: Location of the vortices near the bubble interface at  $t = 144$  ms

### 4.3 Laser Induced Fluorescence

The LIF is an optical measurement technique usually used to measure the concentration (Kück [24]) or the temperature fields in several engineering applications such as: turbulent mixing process (Hjertager [25]), heating and cooling system [26, 27] and biomedical engineering (Yuan [28]). In this work, this technique is applied to measure the temperature of ethanol in nucleate boiling condition. During boiling, a steep temperature gradient can be exhibited. This thermal gradient is accompanied by an optical index variation and the incident light is inevitably nonuniform. Sakakibara & Adrian [29] show that by using two dyes, one temperature sensitive and the other insensitive, the measurement error due to nonuniform lighting can be corrected. The use of two dyes is hence essential for an accurate measurement of the temperature field in boiling with a large subcooling.

#### 4.3.1 Principle of two color LIF thermometry

The two-color LIF thermometry has been applied to different problems such as: the thermal transport at the microscale (Natrajan & Christensen [30]), the thermal plume (Coppeta & Rogers [5]), but not to the boiling. In this investigation, experiments are performed at a relatively high temperature (60 °C - 70 °C) then the application of the two-color LIF thermometry technique becomes quite challenging. The LIF technique consists in temperature dependence of emission intensity of fluorescent dye molecules. These molecules are excited by a narrow spectrum of light and emit another spectrum of light with longer wavelengths due to the Stokes shift. Separating the source light out by optical filters, the emission intensity distribution of an area of interest is captured. For a dye whose emission intensity is temperature dependent, the pixel values  $V$  of the sensor of a camera reflect the temperature field of the viewed area. The two color LIF technique consists on using two dyes, one temperature sensitive and the other insensitive. The apparatus consists of two cameras,  $\alpha$  and  $\beta$ , equipped with optical filters with different ranges of wavelength. The pixel values of Cameras, Camera  $\alpha$  and Camera  $\beta$ , at sensor elements corresponding to a physical point  $(x, y)$  are given by, respectively:

$$V_{\alpha} = a_1 c_{\text{dye1}} I_0(x, y) + a_2 c_{\text{dye2}} I_0(x, y) + V_{\alpha,0} \quad (4.4)$$

$$V_{\beta} = b_1 c_{\text{dye1}} I_0(x, y) + b_2 c_{\text{dye2}} I_0(x, y) + V_{\beta,0} \quad (4.5)$$

Where  $c_{\text{dye1}}$  and  $c_{\text{dye2}}$  are the concentrations of the first and second dyes, respectively.  $V_{\alpha,0}$  and  $V_{\beta,0}$  are the sensor offset values. The coefficients  $a_1$ ,  $a_2$ ,  $b_1$  and  $b_2$  are functions of the temperature  $T$ , while they are independent from the incident laser intensity  $I_0$ . Taking the ratio of  $V_{\alpha}$  and  $V_{\beta}$  after subtracting the offsets, we have an  $I_0$ -independent function  $f$  of temperature:

$$f = \frac{V_{\alpha} - V_{\alpha,0}}{V_{\beta} - V_{\beta,0}} = \frac{a_1 c_{\text{dye1}} + a_2 c_{\text{dye2}}}{b_1 c_{\text{dye1}} + b_2 c_{\text{dye2}}} \quad (4.6)$$

Division of the pixel intensities of the cameras is made after mapping of Camera images  $\beta$  to Camera  $\alpha$  images. The mapping is performed based on the cameras geometrical parameters

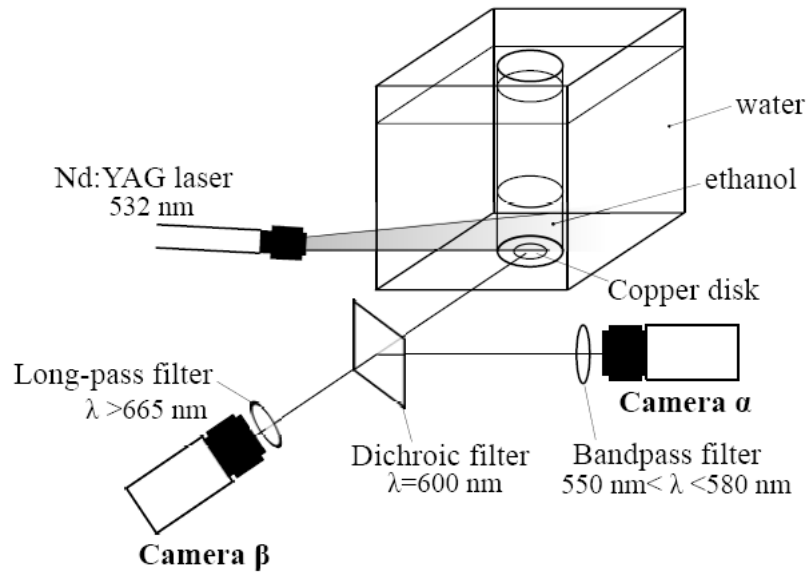


Figure 4.20: Schematic of the two color LIF experimental setup

determined through the camera calibration. The mapped image is used to calculate the  $f$ -function (4.6). The result is then converted into a temperature field by the use of a temperature calibration of the solution.

### 4.3.2 Fluorescence dyes selection and optical systems

The most important step is to choose the appropriate dyes. This experimental investigation is based on a combination between a temperature-dependent dye and a temperature-insensitive dye. During the selection several important factors have to be respected:

1. Dyes must be soluble in ethanol;
2. Since a single illumination source is used, dyes should have similar absorption spectra;
3. Appropriate filtering optics must be used to overcome the overlap between the emission spectra;
4. Since the experiments are performed under nucleate boiling condition, the dye fluorescence intensity must be visible in relatively high temperature.

**Rhodamine B (RhB):** There is a wide library of temperature sensitive dyes that can be used in the measurement of the temperature. For this specific application of nucleate boiling in ethanol, we chose the Rhodamine B. In fact this dye is soluble in ethanol. The absorption peak is located at 554 nm (Figure 4.21(a)). Then this dye can be excited by the laser diode 532 nm. Figure 4.21(b) presents the emission of Rhodamine B as a function of temperature. It can be noted that the Rhodamine B has a linear temperature dependence and the normal emission



intensity decrease to zero at 85 °C. For this reason the fluorescence is visible at the ethanol boiling temperature 70 °C. Therefore the Rhodamine B is well suited to be used as a temperature sensitive dye in ethanol boiling condition.

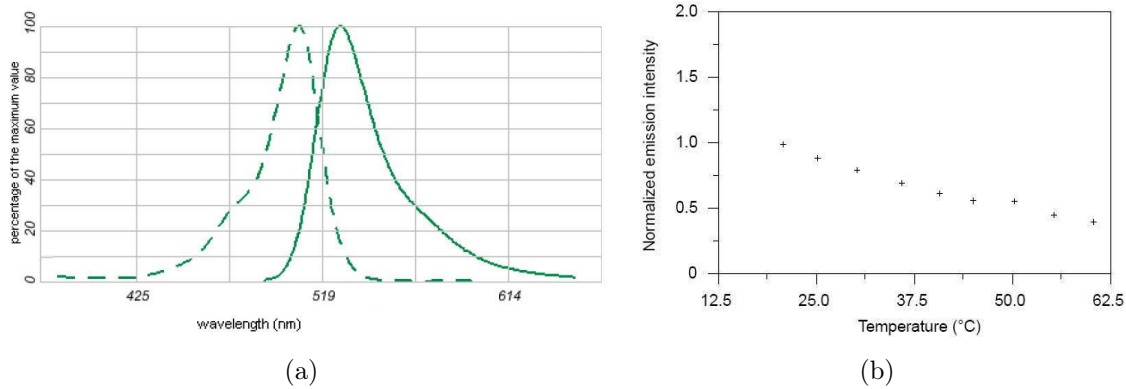


Figure 4.21: (a) Rhodamine B absorption (dotted line) and emission (full line) spectra, (b) Rhodamine B emission as a function of the temperature [5]

**Sulforhodamine-101 (SR101):** Natrajan [30] reported success in combining Rhodamine B with the temperature insensitive dye Sulforhodamine-101 (SR101) (Sulforhodamine-640). As shown in Figure 4.22(a), it's absorption peak is located at 580 nm and it can be excited by the same laser diode 532 nm. This dye exhibits little temperature depends in its fluorescence behavior (Figure 4.22(b)). The emission of these dyes excited by Nd: YAG laser light ( $\lambda = 532$  nm)

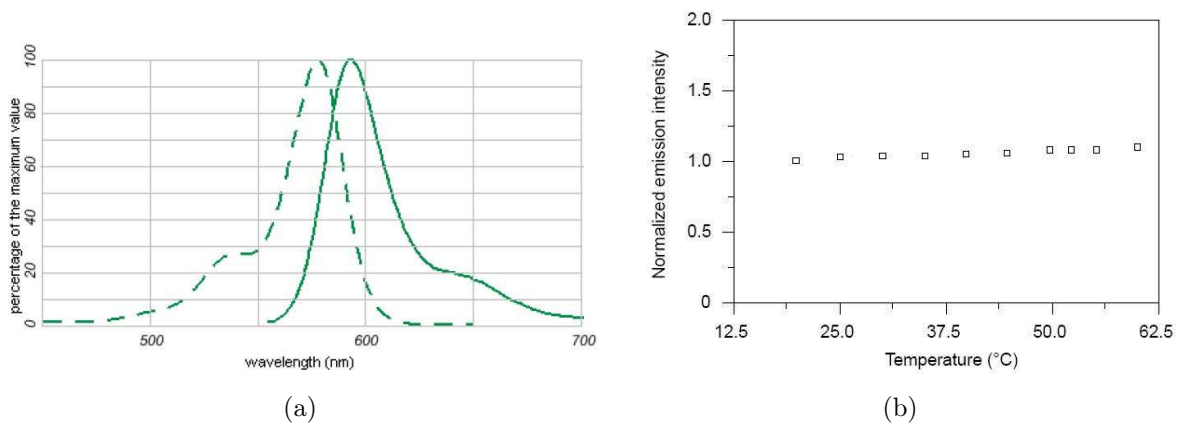


Figure 4.22: (a) Sulforhodamine absorption (dotted line) and emission (full line) spectra, (b) Sulforhodamine 101 emission as a function of the temperature [5]

can be separated effectively by optical filters (Figure 4.23) and behaves differently to a temperature variation of the solution. The emission of RhB decreases when increasing the temperature, while the emission of SR101 increases slightly [30]. Emission spectra of these dyes in ethanol at 20 °C and 40 °C are found in Natrajan & Christensen [30].

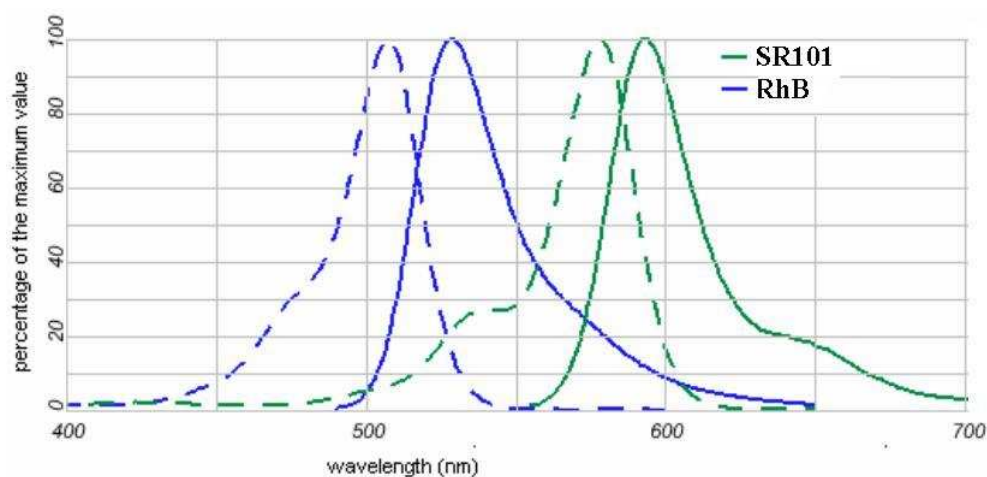


Figure 4.23: Rhodamine B and SR101 emission and absorption spectra when excited at 532 nm

#### Optical systems:

The glass tube is partially filled by a mixture of ethanol with RhB and SR101 and illuminated using successive laser pulses. The 0.5 mm laser sheet is placed perpendicular to the camera and passes through the artificial cavity created on the circular copper disk (Figure 4.24). In order to separate emitted light from different dyes, we used a dichroic filter with a transition wavelength value of 600 nm, a band-pass filter with a wavelength range of  $550 \text{ nm} < \lambda < 580 \text{ nm}$  and a long-pass filter  $\lambda > 665 \text{ nm}$ . The CCD cameras, Camera  $\alpha$  and Camera  $\beta$ , capture essentially light emitted by RhB and SR101, respectively. These cameras are configured as shown in Figure 4.24.

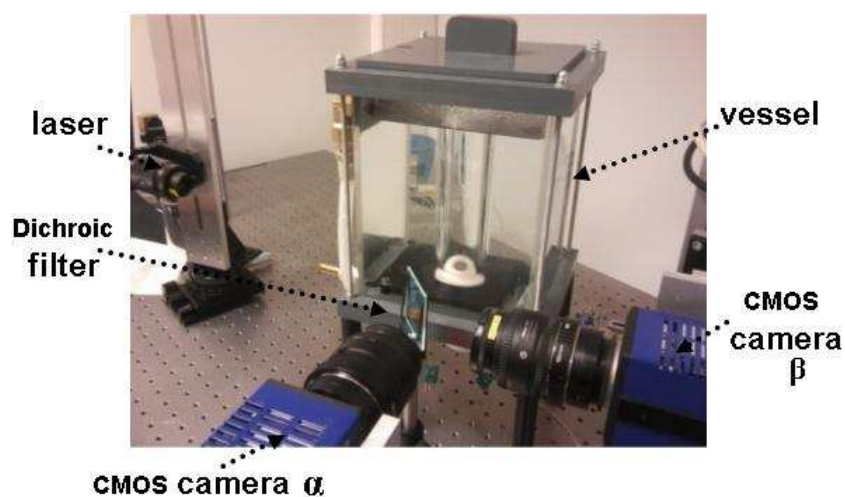


Figure 4.24: View of the PLIF experimental setup

### 4.3.3 Concentration choice

#### 4.3.3.1 First investigation

Since RhB is the temperature sensitive dye, it is important to find the concentration of Rhodamine B that allows the best variation of the fluorescence intensity. Inspired by the article of Natrajan and Christensen [30], we consider  $c_{RhB} = 0.01$  mg/l. As shown in Figure 4.25(a), by considering this RhB concentration, the variation of the fluorescence intensity is not visible. Therefore the concentration is risen up to 0.5 mg/l and the variation of the fluorescence intensity is better visualized in Figure 4.25(b). The variation of the fluorescence intensity is clearly visualized by considering  $c_{RhB} = 1$  mg/l and accurate measurement can be obtained by using this concentration (Figure 4.25(c)). In this first investigation, the SR101 is added with a con-

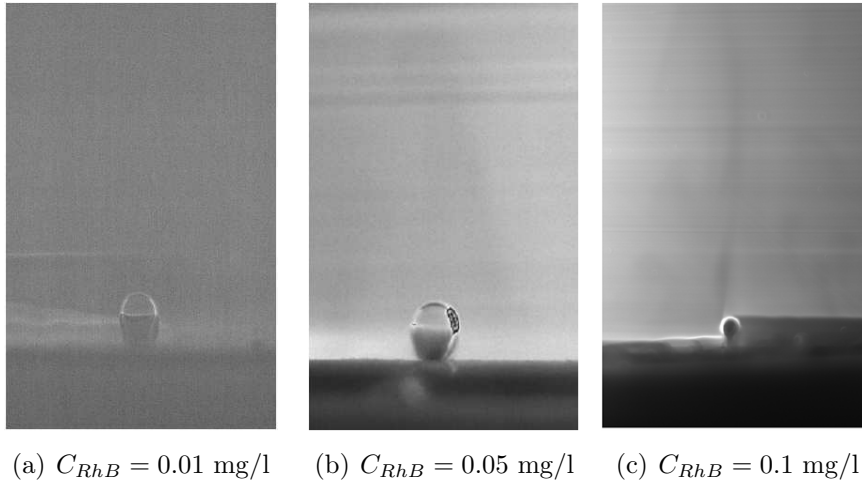


Figure 4.25: Visualization of RhB intensity for different RhB concentrations

centration of 0.05 mg/l. Since the Nd: YAG laser sheet enters the measurement area from the left (Figure 4.24), the reflection at the bubble surface gives rise to a dark area on the other side of the bubble (Figure 4.26). Comparing the images captured by Camera  $\alpha$  and Camera  $\beta$ , it can be noted that the fluorescence intensity of the RhB varies as a function of the temperature while the SR101 fluorescence intensity keeps constant. In the bulk, hot plumes rising from the disk surface and from the bubble can be distinguished as darker zones relatively to other areas of the left column of Figure 4.26 (representing images captured by Camera  $\alpha$ ). The plumes are not seen by Camera  $\beta$ , as shown in right column of Figure 4.26.

#### 4.3.3.2 Deeper investigation

The coefficients of the concentrations in (4.6) depend on the parameters of the optical system. In order to decide an optimal combination of  $c_{RhB}$  and  $c_{SR101}$  for our application, we investigated the behavior of the camera output voltages with varying the concentrations.

Figure 4.27(a) presents  $V_\alpha$  and  $V_\beta$  observed with different concentrations of RhB. No SR101 was mixed in these solutions. The values of the voltage were averaged over an area of  $230 \times 630$  pix<sup>2</sup> above the copper disk. It is seen that  $V_\beta$  is much lower than  $V_\alpha$ . The emission of RhB is

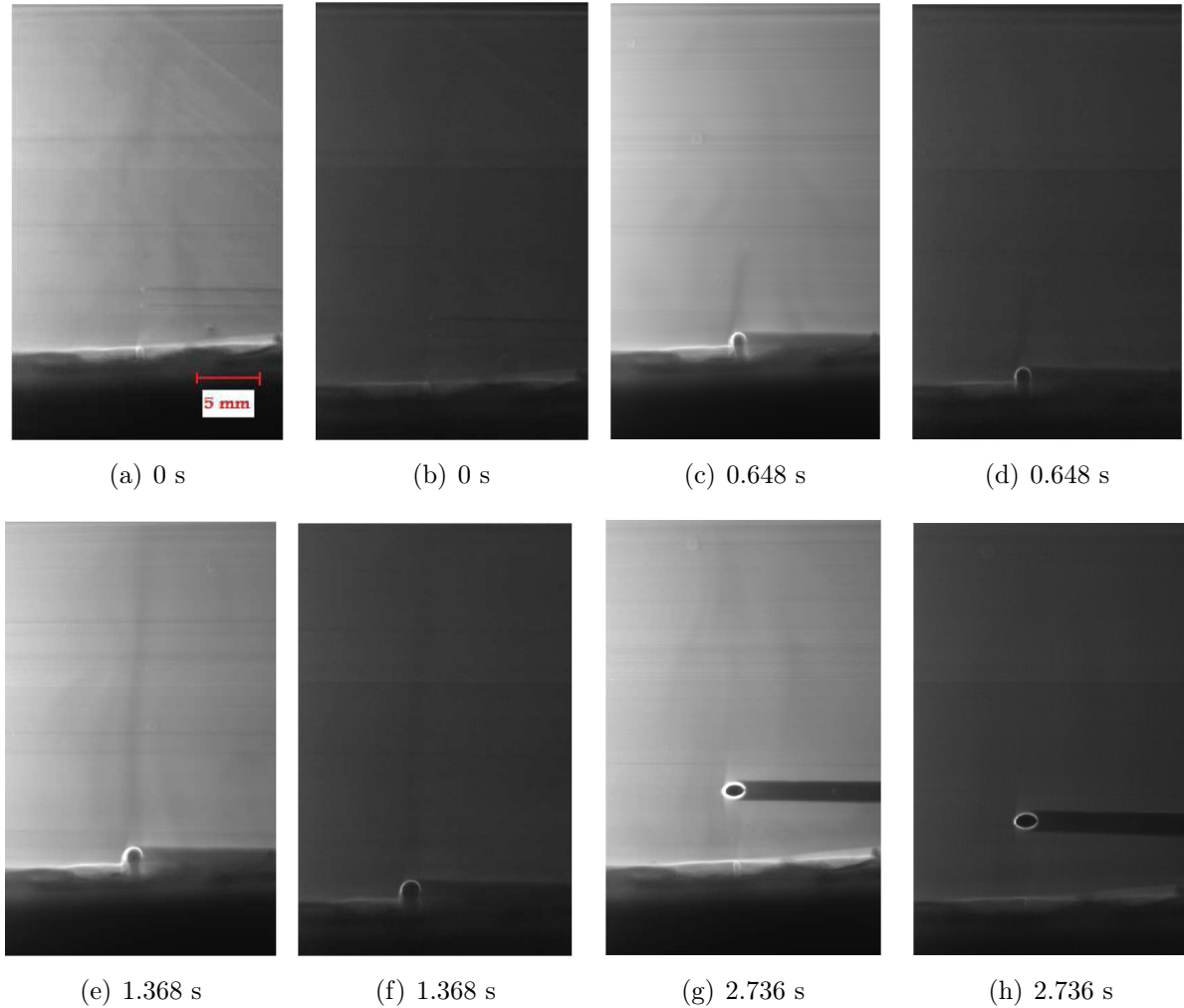


Figure 4.26: Two-color LIF images, RhB on the left and SR101 on the right

blocked effectively by the optical filters before entering Camera  $\beta$ . The voltage  $V_\alpha$  increases linearly with the concentration until  $c_{\text{RhB}} = 0.5$  mg/l. It reaches its maximum at 1 mg/l and then decreases. The latter decrease might be explained by the absorption of the emitted light over the optical path in the solution. The voltage  $V_\beta$  also increases linearly within the range  $0 \text{ mg/l} < c_{\text{RhB}} < 0.5$  mg/l and is saturated at a constant value for  $c_{\text{RhB}}$  larger than 1 mg/l. Figure 4.27(b) shows the results of a similar experiment with varying  $c_{\text{SR101}}$  ( $c_{\text{RhB}} = 0$ ). At concentrations lower than 1 mg/l, both voltages are of the same order of magnitude. The emission from SR101 is not effectively blocked by the filters of Camera  $\alpha$ .  $V_\alpha$  increases until  $c_{\text{SR101}} = 1$  mg/l with a linear behavior in  $0 < c_{\text{SR101}} < 0.5$  mg/l then decreases. In contrast,  $V_\beta$  always increases in the explored concentration range with a wider range of linear behavior ( $0 < c_{\text{SR101}} < 2.5$  mg/l).

For a simple application of the principle (4.6) of the two-color LIF thermometry, we decided to work in the linear regime of observed fluorescent intensities: our choice of  $(c_{\text{RhB}}, c_{\text{SR101}})$  is limited in the ranges of small concentrations:  $c_{\text{RhB}} < 0.5$  mg/l and  $c_{\text{SR101}} < 0.5$  mg/l. For the

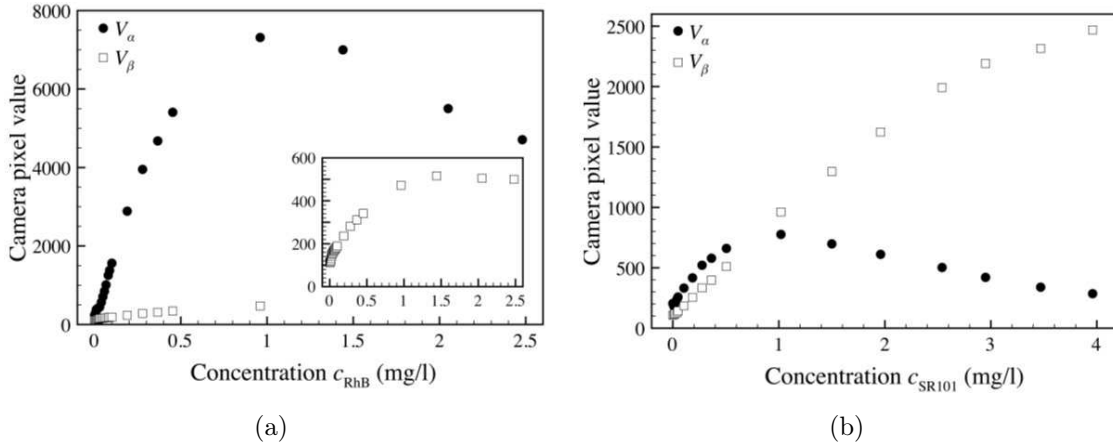


Figure 4.27: (a) Output voltages of Cameras  $\alpha$  and  $\beta$  as a versus of RhB concentration, the inset shows the same  $V_\beta$  behavior with a magnified scale, (b) Output voltages of Cameras  $\alpha$  and  $\beta$  as a versus of SR101 concentration

present experiment, we chose the concentrations 0.1 mg/l and 0.4 mg/l for RhB and SR101, respectively. The solution of these concentrations satisfies all the above requirements.

#### 4.3.4 Camera calibration

In the two-color LIF thermometry, the pixel intensity of a certain wavelength range is divided by the pixel intensity of another wavelength range for the same physical points in order to eliminate the inhomogeneities in the incident laser intensity distribution. When two cameras are used as in the present experimental setup, the output voltage  $V_\alpha(\mathbf{u}_1)$  of the sensor of Camera  $\alpha$  is divided by the output voltage  $V_\beta(\mathbf{u}_2)$  of the corresponding sensor of Camera  $\beta$  for all pairs of pixels  $\mathbf{u}_1 = [v_1, w_1]^T$  and  $\mathbf{u}_2 = [v_2, w_2]^T$  that point to the same physical point. The mapping  $\mathcal{G}$  that maps the two pixel coordinates,  $\mathbf{u}_2$  and  $\mathbf{u}_1$ , should be known accurately for an application of the thermometry. The multi-camera calibration technique used does not require a full **3D** calibration object but only a **2D** planar checkerboard which is moved on several locations. The method for the initial estimation of planar homographies and the final maximum likelihood estimation is the one proposed by Zhang [31]. The closed-form estimation of camera intrinsic parameters explicitly uses the orthogonality of vanishing points. Tangential distortion coefficients are also estimated following the camera model proposed by Heikkilä & Silvén [32]. Those methods were regrouped and automatized in the Camera Calibration Toolbox for Matlab (CCTM) developed by Bouguet [33]. The output of the calibration is the intrinsic and extrinsic parameters of each camera. Especially, the rotation matrices,  $\mathbf{R}_1$  and  $\mathbf{R}_2$ , and translation matrices,  $\mathbf{T}_1$  and  $\mathbf{T}_2$ , are obtained which relate pixels  $\mathbf{u}_1$  and  $\mathbf{u}_2$  with a physical point  $\mathbf{X} = [x, y]^T$  of the thermometry measurement plane:  $\mathbf{X} = \mathbf{R}_1\mathbf{u}_1 + \mathbf{T}_1$  and  $\mathbf{X} = \mathbf{R}_2\mathbf{u}_2 + \mathbf{T}_2$ . The mapping  $\mathcal{G}$  from  $\mathbf{u}_2$  to  $\mathbf{u}_1$  is then given by  $\mathbf{u}_1 = \mathbf{R}_1^{-1}\mathbf{R}_2\mathbf{u}_2 + \mathbf{R}_1^{-1}(\mathbf{T}_2 - \mathbf{T}_1)$ . Figure 4.28 presents the two cameras' views of a same object as well as a mapped image. Comparison of image a and image c indicates that the mapping is accurate with an error of the order of 0.05 mm.

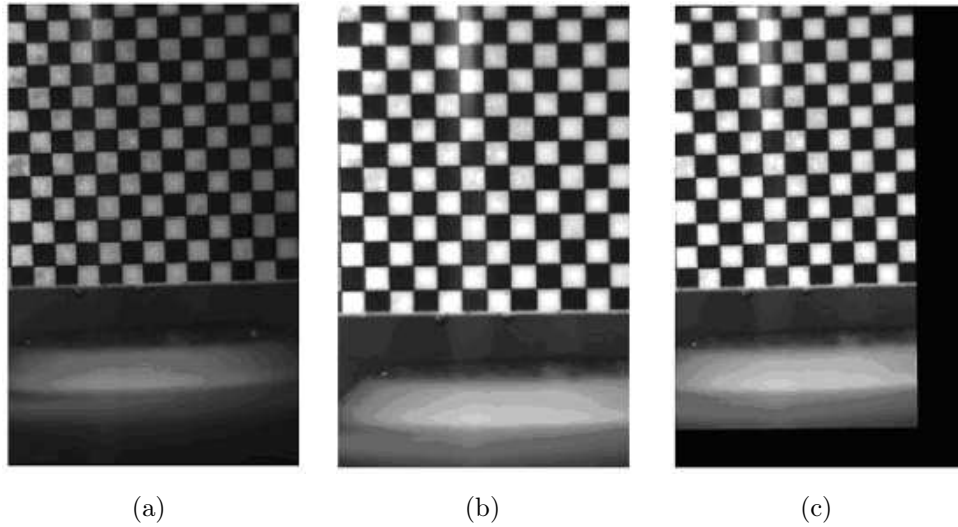


Figure 4.28: Views of cameras with a calibration plate: (a) Camera  $\alpha$  (b) Camera  $\beta$  and (c) Camera  $\beta$  after the mapping  $\mathcal{G}$ . The image size is  $1000 \times 1600 \text{ pix}^2$ . Each square pattern on the calibration plate has sides of 2 mm. The spatial resolution is 0.026 mm/pix

### 4.3.5 Temperature calibration

The noise level of the camera sensors gives rise to a further limitation. According to our examination of the sensor signals without any incident light, the output voltages  $V_\alpha$  and  $V_\beta$  have the same offset  $V_{\alpha,0} = V_{\beta,0} = 101$  with the Gaussian noise of magnitude around 30.  $V_\alpha$  and  $V_\beta$  should be much larger than the latter noise level for a precise measurement. The pixel values  $V_\alpha$  and  $V_\beta$  observed with this solution are shown in Figure 4.29(a) for a temperature range  $30 \text{ }^\circ\text{C} < T < 74 \text{ }^\circ\text{C}$ . The pixel values have been normalized by the values at  $40 \text{ }^\circ\text{C}$  (1415 and 423 for Cameras  $\alpha$  and  $\beta$ , respectively).  $V_\alpha$  decreases of 30 percent over , *i.e.*,  $44 \text{ }^\circ\text{C}$ , *i.e.*,  $0.7 \text{ } \%/^\circ\text{C}$ . This is comparable to the sensitivity  $1.4 \text{ } \%/^\circ\text{C}$  reported by Natrajan and Christensen [30]. While Camera  $\beta$  was solely intended to observe principally the emission from SR101, it reports a slight increase of the fluorescence intensity when increasing the temperature within  $10 \text{ }^\circ\text{C} < T < 44 \text{ }^\circ\text{C}$ . In the present experiment,  $V_\alpha$  decreases, in contrast, 10 percent over the entire temperature range, *i.e.*,  $0.2 \text{ } \%/^\circ\text{C}$ . Figure 4.29(b) shows the result of the temperature calibration predicting the variation of the temperature as a function of the ratio  $f$ . We adopted the latter fit, given analytically by equation  $T = -59.5 f + 265.0$ , as the temperature calibration curve. The sensitivity of  $f$  to the temperature is  $0.5 \text{ } \%/^\circ\text{C}$ , lower in magnitude than the one obtained by Natrajan and Christensen [30] ( $1.5 \text{ } \%/^\circ\text{C}$ ).

### 4.3.6 Results and discussion

Figure 4.30 shows a result of our preliminary experiment for measuring the temperature field in nucleate boiling. The temperature of surrounding ethanol is  $61.2 \text{ }^\circ\text{C}$ . Vapor bubbles nucleate on the copper disk under a subcooling  $\Delta T = T_{sat} - T_e = 17.2 \text{ }^\circ\text{C}$ . The left column of Figure 4.30 is captured by Camera  $\alpha$ . A vapor bubble of diameter 1 mm is growing at the artificial cavity

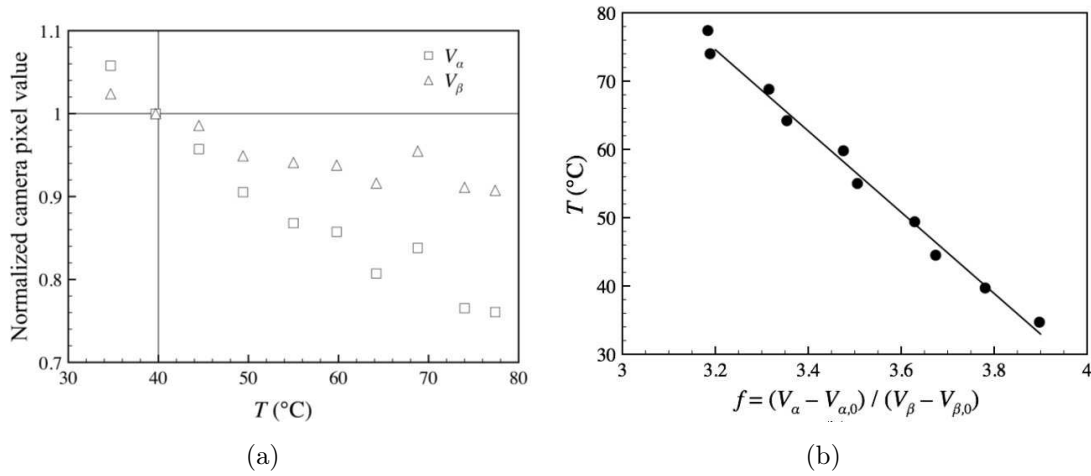


Figure 4.29: (a) Normalized output voltages for a solution of  $c_{\text{RhB}} = 0.4$  mg/l and  $c_{\text{SR101}} = 0.1$  mg/l, (b) the temperature calibration curve  $T = -59.5 f + 265.0$

site. Results are similar to the ones presented above: a dark area appears on the other side of the bubble because the laser sheet enters the measurement area from the left, hot plumes rising from the disk surface (at the left of the bubble) and from the bubble can be distinguished in Figure 4.30 showing the temperature distribution. This image has been mapped on the reference frame of Camera  $\alpha$  by the mapping  $\mathcal{G}$ . In both images, there are horizontal luminous and dark lines. These lines are result of optical imperfection of the setup. The roughness of the tank lateral walls and the tube wall can produce such inhomogeneous lighting. Fluctuation in temperature of the water in the tank and in the temperature of the ethanol mixture could also lead to non-uniform lighting. There is also non-uniform lighting due to the reflection of the laser light by the bubble surface. The nearly vertical luminous line is seen in both views above the bubble. These non-uniformities are inevitable in a boiling experiment and a single-color LIF thermometry will give erroneous thermal field. Use of a temperature insensitive dye is hence essential to obtain corrected information on the temperature distribution. The right column of Figure 4.30 shows a temperature field determined by calculating the  $f$ -function and converting them by the temperature calibration. Temperature values are shown by a color code indicated in Figure 4.30. The zones where unphysical temperatures (either lower than 50 °C or higher than 80 °C) are found are uncolored. At the right of the bubble, the temperature determination was failed due to the low pixel values (uncolored zone). Some other uncolored zones are found above the copper disk along the wavy luminous curve seen in Figure 4.30. The failure in these zones would be due to insufficient accuracy of the mapping  $\mathcal{G}$ . As estimated above, the order of magnitude of the mapping error is 0.05 mm, which is equivalent to half a wavelength of the wavy curve. In order to eliminate lighting non-uniformity with such a tiny scale, more accuracy of mapping is required. Except in those zones, the temperature field is successfully obtained over the whole zone of interest. According to Figure 4.30, the bulk liquid is at around 60 °C. This agrees well with the temperature measured by the thermocouple. The hot plumes are seen as higher temperature zones 70 ~ 73 °C. Furthermore, the inhomogeneous lighting due to the reflection at the bubble surface is successfully corrected. In the right column of Figure 4.30 there

is no color gradient corresponding to this reflection. The successful correction of the reflection underlines the significance of the two-color LIF thermometry in boiling experiments.

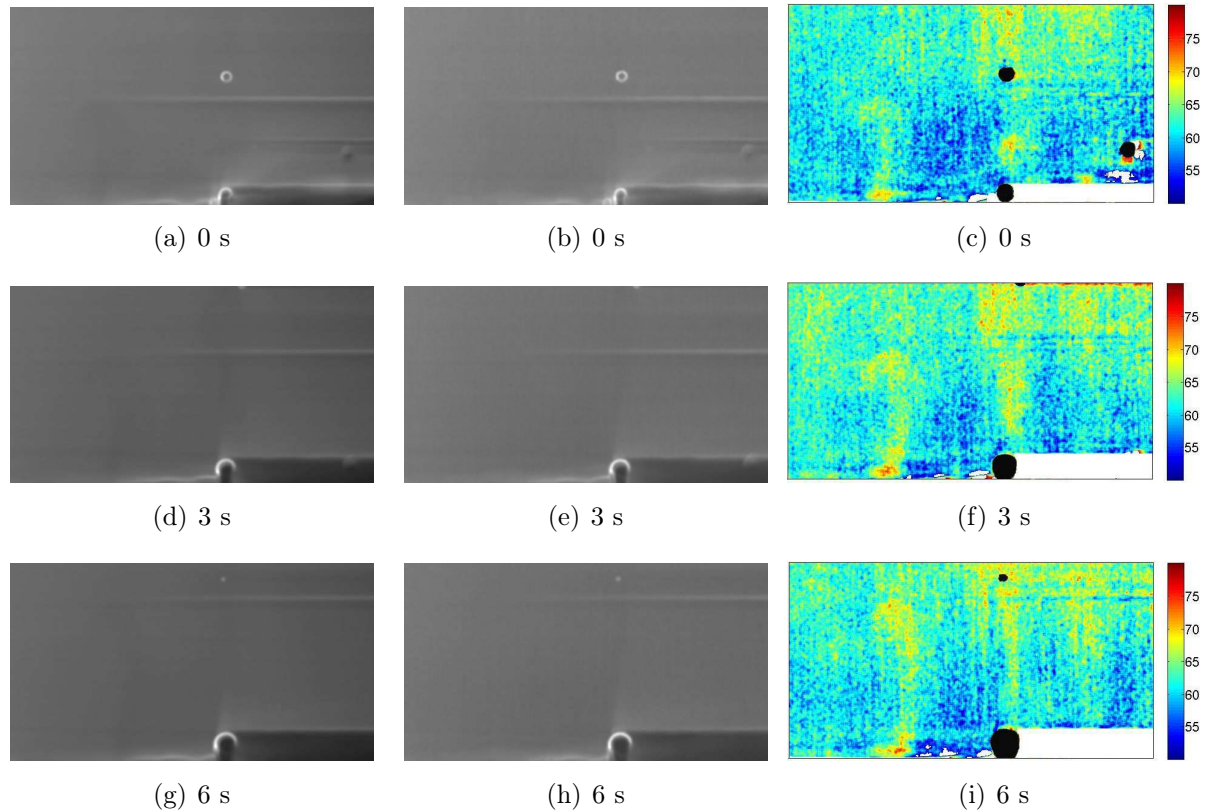


Figure 4.30: Nucleate boiling observed by Cameras  $\alpha$  and  $\beta$ , left and right, respectively, and the determined temperature ( $^{\circ}\text{C}$ ) field by calculating  $f$ -function

Figure 4.31 presents the same result as Figure 4.30 at  $t = 3\text{ s}$  with a different temperature scale. In Figure 4.31 a vapor bubble is growing on an artificial nucleation site in ethanol of  $T_e = 61.2\text{ }^{\circ}\text{C}$ . Considering this temperature scale, the hot plume are more visible than in Figure 4.30.

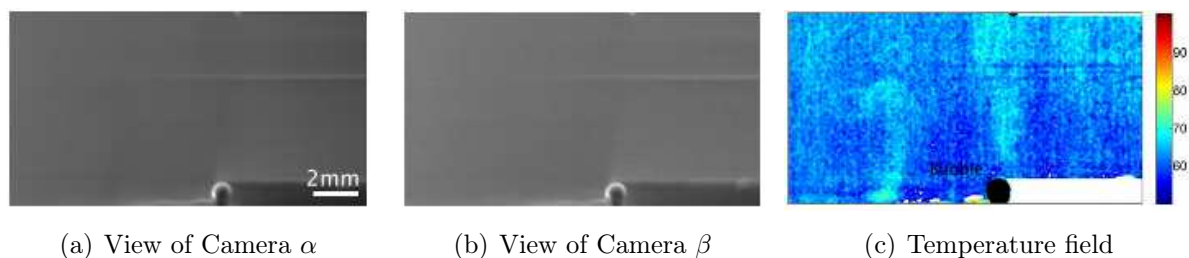


Figure 4.31: The same result as above ( $t = 3\text{ s}$ ) with a different temperature scale ( $^{\circ}\text{C}$ )



## 4.4 Conclusion & Perspectives

The bubble shape evolution and the bubble growth rate were carried out using a CCD high speed camera. The bubble interface changes through different shapes: hemispherical, spherical and ellipsoidal. This instrumentation offers a deep acquaintance of the bubble dynamics. Two superheat configurations were studied, in both cases the growth rates is in good agreement with the function of time found by Qiu and Dhir [16]. The velocity field has been determined at the bubble interface by applying the Particle Image velocimetry. The flow is turbulent and several vortexes are captured around the bubble. The two-color LIF thermometry has been applied to nucleate boiling investigation. The camera calibration procedure and the mapping necessary for practical application of this thermometry were presented. The choice of the concentration values of Rhodamine B and Sulforhodamine-101 was discussed. The fluorescence intensity was investigated in ethanol within a wide range of the concentrations of these dyes. The temperature calibration for a solution of 0.1 mg/l of Rhodamine B and 0.4 mg/l of Sulforhodamine-101 showed a sensitivity of 0.5 %/°C for the  $f$ -function. A temperature field around a vapor bubble for ethanol in nucleate boiling condition was successfully obtained, based on the thermometry principle. This preliminary result suggests that the thermometry is a promising method for the thermal field determination in boiling. Two-color LIF thermometry can correct inevitable lighting nonuniformity due to the reflection at vapor bubble surface and the temperature gradient in the path of incident laser light. Result show that the actual accuracy of the mapping is not sufficient to study in detail the thermal field around a vapor bubble of 1 mm in diameter. We are trying to improve our study by increasing the optical magnification. In fact, the zone of interest shown in Figure 4.30 is small compared with the entire CCD sensor size of the cameras. We are also developing an improved two-camera mapping procedure using the fundamental matrix method (Maas [34], Biwole [35]). Improvement of the temperature sensitivity of the  $f$ -function is also being carried out by optimizing the configuration of optical elements of the experimental setup and the dyes' concentrations. Further investigation can be done by synchronizing the PIV technique with the two color LIF technique.

## 4.5 Résumé français

Ce chapitre consiste à étudier les cinétiques de l'ébullition dont la connaissance est nécessaire à la modélisation. La première partie est consacrée à l'observation par une caméra rapide (type CDD - Phantom Miro eX-series, Photonetics 125-2500 images/s) la nucléation et la croissance d'une bulle de vapeur. La vitesse locale et les champs de température autour d'une bulle se formant sur une surface chauffée sont insuffisamment connus pour une comparaison détaillée avec des simulations numériques. Un des buts de ce chapitre est de combler en partie ce manque, par la thermométrie «two-color LIF» et par la vélocimétrie «PIV» appliquées au problème de «boiling pool». Ces techniques permettent une mesure non intrusive avec forte résolution spatiale et temporelle, bien que limitée à un plan **2D** du domaine de mesure. Le caractère novateur de l'étude vient de l'intervalle de température relativement élevé (60 °C - 70 °C) que l'on ne retrouve pas dans la littérature et de l'emploi de méthodes de stéréovision pour faire correspondre les zones vues par les deux caméras de LIF. L'emploi de deux caméras (chacune étant sensible à un seul colorant) est apparu crucial pour éliminer les non uniformités d'éclairage dues à la réflexion de la lumière laser sur la surface de la bulle, ces inhomogénéités pouvant fausser la mesure de température. Ainsi ces observations permettront de remonter aux paramètres clés nécessaires à la modélisation des «cinétiques de l'ébullition» des bulles de vapeur.



# References

- [1] M. Barthès. *Ebullition sur site isolé étude expérimentale de la dynamique de croissance d'une bulle et des transferts associés*. PhD thesis, Université De Provence, 2005.
- [2] A. J. Robinson and R. J. Judd. Bubble growth in uniform and spatially distributed temperature field. *International Journal of Heat and Mass Transfer*, 44:2699–2710, 2001.
- [3] T. Bonometti. *Développement d'une méthode de simulation d'écoulements à bulles et à gouttes*. PhD thesis, l'Institut National Polytechnique de Toulouse, 2005.
- [4] J. F. Torré. *Quenching runaway reactions: hydrodynamics and jet injection studies for agitated reactors with a deformed free surface*. PhD thesis, Polytechnique de Toulouse, 2007.
- [5] J. Coppeta and C. Rogers. Dual emission laser induced fluorescence for direct planar scalar behavior measurement. *Experiments in Fluids*, 1998.
- [6] Y. Chen and M. Groll. Dynamics and shape of bubbles on heating surfaces: A simulation study. *International Journal of Heat and mass transfer.*, 49:1115–1128, 2005.
- [7] Y. Fujita and Q. Bai. Numerical simulation of the growth for an isolated bubble in nucleate boiling. In 11<sup>th</sup> *International Heat transfer Conference*, 1998.
- [8] N. Kosseifi, E. Hachem, L. Silva, E. Massoni, and T. Coupez. Numerical simulation of boiling during the quenching process. *10e colloque national en calcul des structures, Giens, France*, <http://hal.archives-ouvertes.fr/hal-00592676/fr/>, 2011.
- [9] N. Zuber. The dynamics of vapor bubbles in nonuniform temperature fields. *International Journal of Heat and Mass Transfer*, 2:83–98, 1961.
- [10] S. Basic, L. Skerget, and J. Marn. Hydrodynamics of partial nucleate boiling by piv technique. *International Journal of Dynamics of Fluids*, 3(1):11–30, 2007.
- [11] T. A. Kowalewski, J. Paklezb, R. Trzciński, and A. Zachara. Experimental analysis of bubble growth on a heated surface. *archives of themodynamics*, 25(3):1–12, 2004.
- [12] M. S. Plesset and S. A. Zwick. The growth of vapor bubbles in superheated liquids. *Journal of applied physics*, 25:493–500, 1954.

- [13] S. Moghaddam, E. Pengwang, K. Lin, R. I. Masel, and M. A. Shannon. Millimeter-scale fuel cell with on-board fuel and passive control system. *Journal of Microelectromechanical Systems*, 17:1388–1395, 2008.
- [14] S. Moghaddam and K. Kiger. Physical mechanisms of heat transfer during single bubble nucleate boiling of fc-72 under saturation conditions-i. experimental investigation. *International Journal of Heat and Mass Transfer*, 52:1284–1294, 2009.
- [15] H. C. Lee, B. D. Oh, S. W. Bae, and M. H. Kim. Single bubble growth in saturated pool boiling on a constant wall temperature surface. *International Journal of Multiphase Flow*, 29:1857–1874, 2003.
- [16] D. Qiu and V. K. Dhir. Experimental study of flow pattern and heat transfer associated with a bubble sliding on downward facing inclined surfaces. *The Society of Rheology*, 26:605–616, 2002.
- [17] D. Euh, B. Ozar, T. Hibiki, M. Ishii, and C. H. Song. Characteristics of bubble departure frequency in a low-pressure subcooled boiling flow. *Journal of nuclear science and technology*, 47(7):608–617, 2010.
- [18] F. Mayinger, W. Gabler, G. Kappler, R. Hönig, and R. Laghner. Spectroscopic techniques for ram-combustors. *Space Course*, pages 11–22, 1993.
- [19] S. Siedel, S. Cioulachtjian, and J. Bonjour. Experimental analysis of bubble growth, departure and interactions during pool boiling on artificial nucleation sites. *Experimental Thermal and Fluid Science*, 32(8):1504–1511, 2008.
- [20] T. A. Kowalewski, J. Pakleza, and A. Cybulski. Particle image velocimetry for vapour bubble growth analysis. In *8<sup>th</sup> International Conference Laser Anemometry Advanced and Applications*, 1999.
- [21] P. Meunier and T. Leweke. Analysis and treatment of errors due to high velocity gradients in particle image velocimetry. *Experiments in Fluids*, 35(5):408–421, 2003.
- [22] F. Blanc, F. Peters, and E. Lemaire. Particle image velocimetry in concentrated suspensions: Application to local rheometry. *Applied Rheology*, 21, 2011.
- [23] M. Honkanen. *Turbulent Multiphase flow Measurements with Digital Particle Image Velocimetry: Application to bubbly flows*. PhD thesis, Tampere University of Technology, 2002.
- [24] U. D. Kück, M. Schlüter, and N. Rübiger. Investigation on reactive mass transfer at freely rising gas bubbles. In *7<sup>th</sup> international conference on multiphase flow*, 2010.
- [25] L. K. Hjertager, B. H. Hjertager, N. G. Deen, and T. Solberg. Measurement of turbulent mixing in a confined wake flow using combined piv and plif. *Canadian Journal of Chemical Engineering*, 2003.

- 
- [26] L. Shi, X. Mao, and A. J. Jaworski. Application of planar laser-induced fluorescence measurement techniques to study the heat transfer characteristics of parallel-plate heat exchangers in thermoacoustic devices. *Meas. Sci. Technol.*, 21:115405, 2010.
- [27] F. Guillard, R. Fritzon, J. Revstedt, C. Trägårdh, M. Aldén, and L. Fuchs. Application of planar laser-induced fluorescence measurement techniques to study the heat transfer characteristics of parallel-plate heat exchangers in thermoacoustic devices. *Experiments in Fluids*, 25:143–150, 1998.
- [28] Y. Yuan. *Mass transfer process analysis near phase boundary with combined PIV-PLIF method, a single-camera single-laser approach*. Purdue University. Civil Engineering. 2008.
- [29] J. Sakakibara and R.J. Adrian. Measurement of temperature field of rayleigh-bénard convection using two-color laser-induced fluorescence. *Experiments in Fluids*, 2004.
- [30] V. K. Natrajan and K. T. Christensen. Two-color laser-induced fluorescent thermometry for microfluidic systems. *Measurement Science and Technology*, 20, 2009.
- [31] Z. Zhengyou. Flexible camera calibration by viewing a plane from unknown orientations. In *Proceedings of the International Conference on Computer Vision (ICCV'99), Corfu, Greece, September 1999, IEEE 0-7695-0164-8/99*, 1999.
- [32] J. Heikkilä and O. Silvén. A four step camera calibration procedure with implicit image correction. In *Conference on Computer Vision and Pattern Recognition (CVPR'97), San Juan, Puerto Rico*, 1997.
- [33] J. Y. Bouguet. Camera calibration toolbox for matlab. In *available on website [http://www.vision.caltech.edu/bouguetj/calib\\_doc/](http://www.vision.caltech.edu/bouguetj/calib_doc/)*, 2002.
- [34] H. G. Maas. Complexity analysis for the establishment of image correspondences of dense spatial target fields. *International Advances of Photogrammetry and Remote Sensing, XXIX (B5)*, 1992.
- [35] P. H. Biwole, W. Yan, Y. Zhang, and J. Roux. A complete 3d particle tracking algorithm and its applications to indoor airflow study. *Measurement Science and Technology*, 20:015401–015412, 2009.



# Chapter 5

## Integrating boiling model to the quenching process

### Contents

---

|            |                                                                                 |            |
|------------|---------------------------------------------------------------------------------|------------|
| <b>5.1</b> | <b>Micro-quenching</b> . . . . .                                                | <b>130</b> |
| 5.1.1      | Experimental setup . . . . .                                                    | 130        |
| 5.1.2      | Experimental results . . . . .                                                  | 131        |
| <b>5.2</b> | <b>Numerical simulation</b> . . . . .                                           | <b>133</b> |
| 5.2.1      | Resolution algorithm . . . . .                                                  | 134        |
| 5.2.2      | Two dimensional film boiling . . . . .                                          | 135        |
| 5.2.3      | Three dimensional film boiling-Micro Scale . . . . .                            | 138        |
| 5.2.4      | Three dimensional film boiling-Meso Scale . . . . .                             | 140        |
| 5.2.5      | Numerical simulation of film boiling during industrial quenching case . . . . . | 142        |
| 5.2.6      | Conclusion . . . . .                                                            | 143        |
| <b>5.3</b> | <b>Résumé français</b> . . . . .                                                | <b>144</b> |

---



From Chapters 1-4 it is clear that the boiling phenomena is the most efficient mode of heat transfer. However, it is a complex matter involving several regimes such as nucleate boiling, transition boiling and film boiling. The existence and the duration of each regime depend on different parameters: the solid temperature, the bath temperature, the solid roughness, the orientation of the steel and the agitation . . . . In fact if the solid temperature is above the Leidenfrost temperature, a vapor film covers the solid and the boiling mode corresponds to film boiling (Figure 5.1(b)). Once the solid temperature becomes less than the Leidenfrost temperature the film boiling breaks and a population of bubbles covers the solid (Figure 5.1(a)). This chapter is divided in two parts: the first part is devoted to an experimental investigation during the micro quenching process, the second part is devoted to develop a general model for boiling. This model allows the modelling of different regimes: nucleate boiling and film boiling. The main idea is to consider the population of bubbles as a film vapor with specific physical properties. Then the numerical simulation of both regimes consists on modelling the film vapor behavior: from the generation to the growth and the detachment.

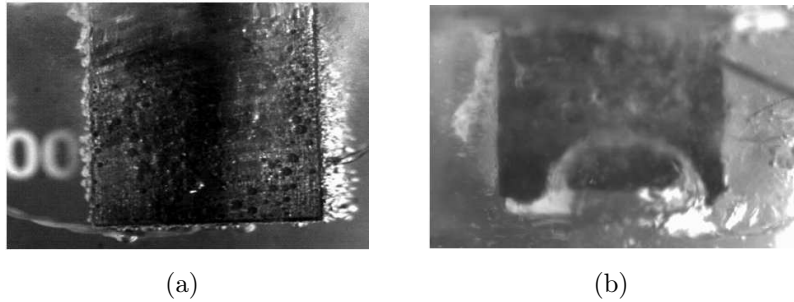


Figure 5.1: (a) Nucleate boiling, (b) Film boiling

## 5.1 Micro-quenching

The micro quenching setup was carried out to investigate the effect of surface and water temperature on the boiling regime and the film vapor stability. The observation of these phenomena was done by means of a high speed camera.

### 5.1.1 Experimental setup

The micro quenching machine (Figure 5.2) was designed and performed by the design department of Cemef. This machine allows a descent at a constant speed between 1 and 10 mm/s over a distance exceeding 300 mm. The quench tank is made of a Pyrex glass; it has a diameter and a height of 125 mm and 200 mm, respectively. The tank is filled with water. The quenching was carried out without any agitation. Images were captured using a high speed CDD camera (Phantom Miro eX-series) Photonetics (125 to 2500 images/s) as in [1, 2] and coupled with a 110 macro photos objective. A halogen lamp was used as a lightening equipment to better visualize the boiling regimes and the rewetting phenomenon. The ingot is made of steel; its dimensions are  $L = 8 \text{ cm}$  and  $l = 2 \text{ cm}$ . The boiling regimes and the stability of the film vapor depend on

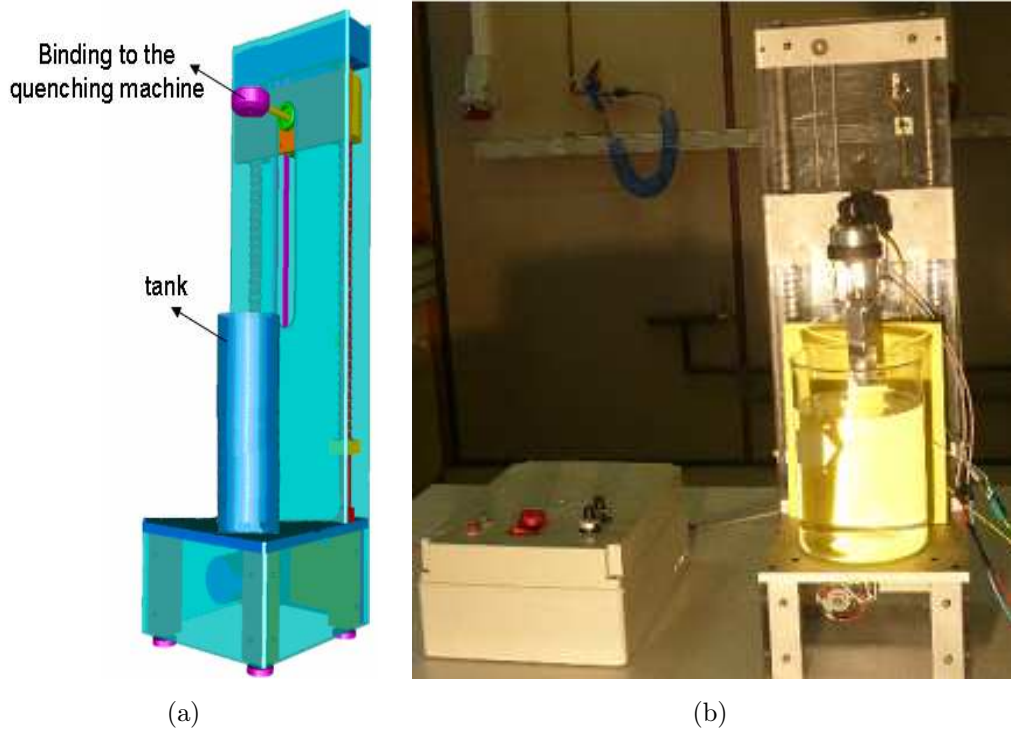


Figure 5.2: (a) Schema of the Micro quenching setup, (b) Photograph of the Micro quenching setup

several parameters such as the kind of fluid, fluid temperature, solid nature, solid temperature and roughness. In the next paragraph we point out the influence of the solid and the fluid temperature on the stability of the film vapor.

### 5.1.2 Experimental results

The duration of the film boiling during quenching is systematically influenced by varying the initial temperature of the solid or by varying the water temperature. Figure 5.3 presents the boiling regimes that occurs during the quenching process on the downward-facing of the solid surface for different initial solid temperatures (200 °C, 350 °C, 500 °C and 700 °C) where the water temperature is constant (20 °C). When the solid temperature is less than 350 °C, small bubbles were observed to emerge on the solid surface. The boiling mode captured in Figure 5.3(a)-5.3(b) corresponds to nucleate boiling at the high heat flux condition near the critical heat flux (CHF). Figure 5.3(c) shows that a vapor film covers the solid, this vapor film can be a heat transfer insulator between the solid and the liquid if the bath was not agitated. When the solid temperature increases, large vapor film is vigorously generated from the heated surface (Figure 5.3(d)). From these observations, we can deduce that the Leidenfrost temperature (the temperature above which a vapor film covers the solid) is greater than 350 °C and the film vapor becomes more stable by increasing the initial temperature of the solid. Figure 5.4 compares the boiling regimes that occurs during the quenching process on the downward-facing of the solid surface for different water temperatures (30 °C, 70 °C and 80 °C) where the initial solid

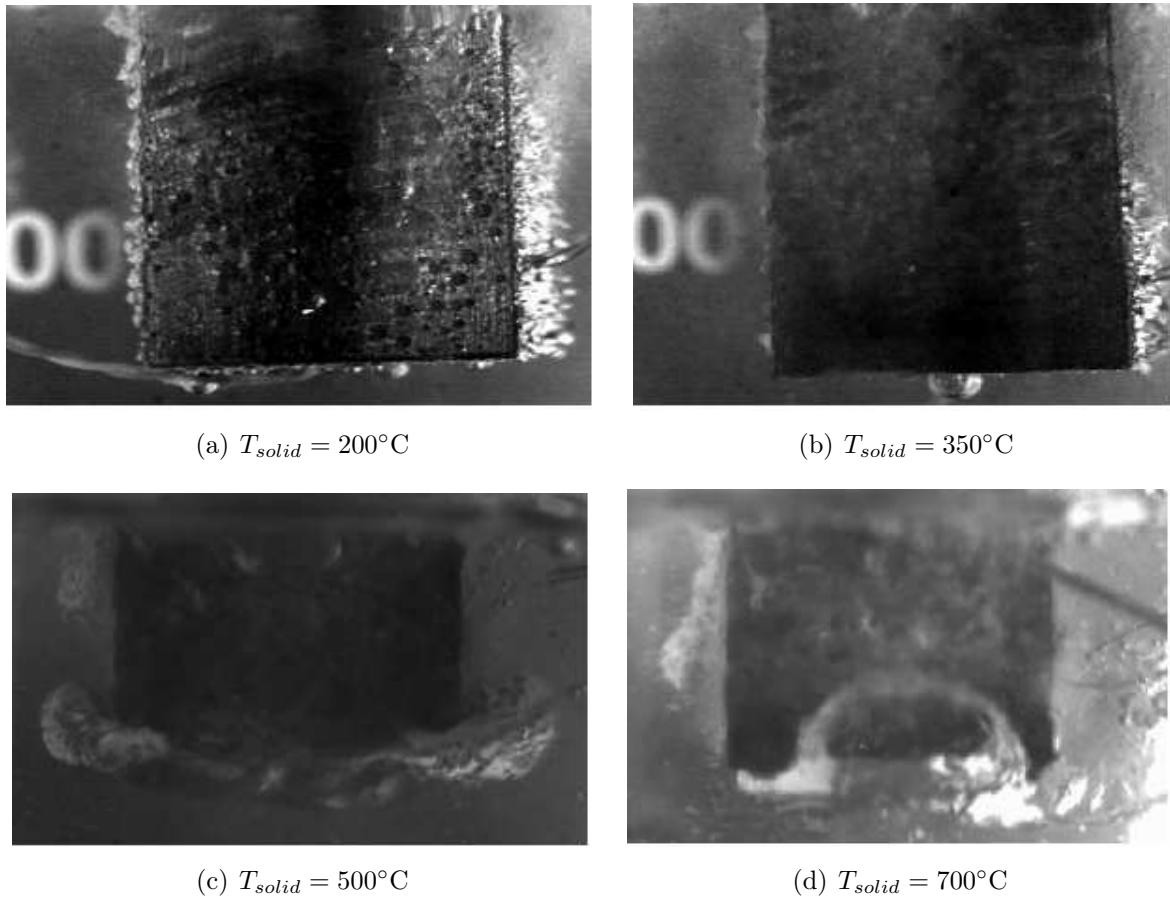


Figure 5.3: Boiling regimes for a ingot quenched in water at 20 °C

temperature is constant (700 °C). Figure 5.4(a) shows an unstable vapor film at the top of the solid. Figure 5.4(b) demonstrates that the vapor film propagates on the solid surface and the surface rewetting is kept at the lower position. By increasing the tank temperature the solid surface was covered with a thin vapor film (Figure 5.4(c)). From these observations, it can be noticed that the film vapor occurs when the water temperature is greater than 70 °C and becomes more stable by increasing the bath temperature. Measuring the temperature at different locations of the solid in different conditions will be the subject of the future work experimental because it requires an accurate instrumentation technique. These results show that different boiling regimes (nucleate boiling, film boiling) occur in the solid surface and they depend on the solid and water temperature. The stability of the vapor film is also depending on those parameters. In the following section, numerical tests were performed in liquid saturation condition or with a very high heated solid (985 °C), thus the treated and the simulated regime corresponds to the film boiling.

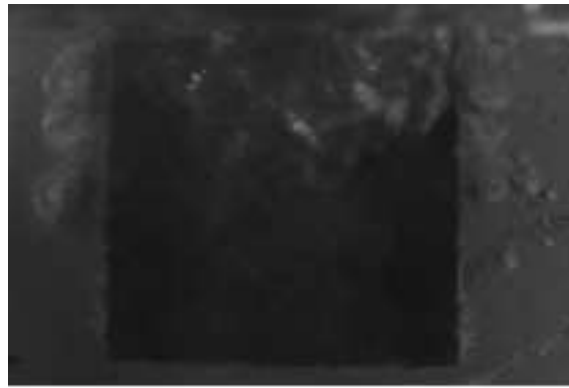
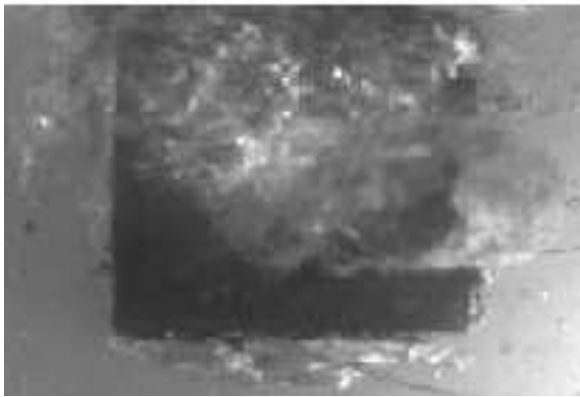
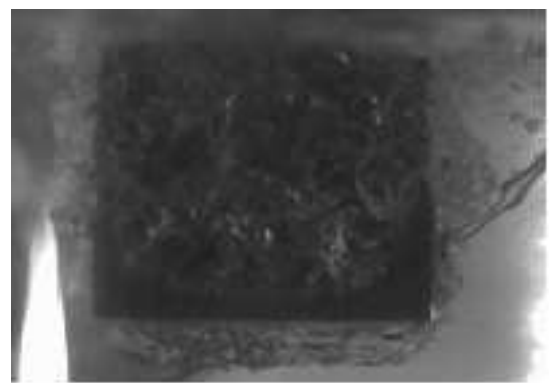
(a)  $T_{bath} = 30^{\circ}\text{C}$ (b)  $T_{bath} = 70^{\circ}\text{C}$ (c)  $T_{bath} = 80^{\circ}\text{C}$ 

Figure 5.4: Boiling regimes for a ingot at  $700^{\circ}\text{C}$  quenched in water at  $30^{\circ}\text{C}$ ,  $70^{\circ}\text{C}$  and  $80^{\circ}\text{C}$

## 5.2 Numerical simulation

The objective of this thesis is to develop a numerical tools able to model the quenching process. In the literature, many mathematical models have been proposed over the past years. Recently these numerical methods begun to integrate boiling model in this engineering application. Typically, the general idea of these techniques consists in solving separately two sets of governing equations and the solution is matched through jump conditions across the interface. This method offers good qualitative results but it requires a high computational cost [3]. Other alternative approaches have been applied for multi-phase flows problems during quenching process by using a boiling mass transfer between phases. Different modes of boiling (film boiling and transition boiling) have been covered but not nucleate boiling and natural convection modes [4, 5]. Wang [6, 7] used the commercial CFD code AVL-FIRE, in which the computations were performed by solving two momentum equations for each phase, a mixture energy equation for both phases and a conduction equation for the solid part. This paragraph provides details about a new developed method of integrating boiling model to the quenching process.

### 5.2.1 Resolution algorithm

The integration of boiling phenomenon to the quenching model is achieved by modifying the computational fluid dynamics **CFD** solver introduced in Chapter 2. As predicted in Chapter 3, the formation and the evolution of a film vapor will be modelled via a germination and a growth approach. During the modelling of bubble evolution, the bubble formation was not simulated because the main goal of this thesis is to model the boiling phenomena during the quenching process, in this case the film vapor generation can be automatically done by assuming that the film vapor interface is coincident to the steel surface. The behavior of the vapor film is highly dependent on simultaneous effects such as the surface tension and the latent heat, none of them can be ignored. All numerical models (interface tracking, growth, surface tension) that were developed and applied to nucleate boiling benchmarks tests are used in this chapter to create a software tool that integrates the boiling phenomenon to the quenching process. This model is given by the following resolution algorithm (Figure 5.5):

1. The film vapor interface is assumed to be coincident with the heat source boundary;
2. The energy equation is solved to obtain the temperature;
3. The growth velocity  $v_{\Gamma}$  is deduced from Gibbs Thomson relation (3.31);
4. The Navier Stokes equations are solved to determine the fluid velocity field;
5. The transport velocity is calculated as the sum of the fluid velocity and the growth velocity;
6. The Convection Reinitialization equation is used to advance the liquid vapor interface;
7. Steps (1) to (6) are repeated until the final time is reached.

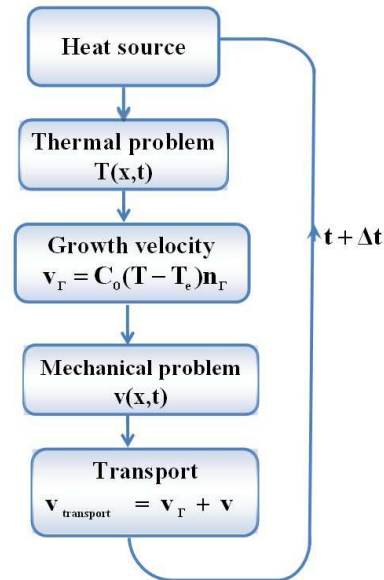


Figure 5.5: Resolution algorithm for boiling model during quenching

This algorithm (Figure 5.5) presents a numerical method to simulate liquid-vapor phase change during quenching process. The method consists on solving the same set of momentum and energy equation over the entire domain including both phases and solid region with variable properties. The surface tension and the latent heat are added as interfacial source terms. The interfaces are tracked by LevelSet formulation, the liquid-vapor interface is transported by using a Convection Reinitialization equation (for more details see Chapter 3). The numerical difficulty due to the

large properties (density, viscosity ...) difference between the phases, is overcome using the proposed method. In this chapter, this algorithm is applied to simulate the vapor film behavior during quenching, where vapor bubbles are generated from a film vapor covering the hot solid. The numerical simulation of boiling during quenching represents a big challenge because it must be capable to handle with large **3D** problems (industrial equipment of tens meter scale).

### 5.2.2 Two dimensional film boiling

The aims of this test is to bring out the generation of a vapor film around a solid object (close to the quenching problem) and to analyze the behavior of a thin vapor film generated on a solid surface (Figure 5.7). Since industrial quenching process is usually performed on large parts of dimensions as illustrated in Chapter 1. We present in this section the simulation of film boiling generated from a heated solid of width 0.3 m and height 0.15 m located at (1.412; 0.7) inside a **2D** domain  $\Omega = [4.6; 2.3]$  m<sup>2</sup>. The duration and the stability of the film boiling mode increase linearly with the growth of the bath temperature [8]. The film boiling mode is the most noted for a bath having a temperature above 70 °C as shown in the previous experimental investigation. Here we consider, initially, the liquid at a temperature (95 °C ) close to the saturation temperature and the solid at a temperature of 985 °C. The top surface of the domain was defined as a free slip surface and for the other surfaces a no slip condition is applied. The time step is equal to 0.00125 s. The vapor interface is coincident with the solid boundary. In this test, the constant growth velocity is  $c_0 = 0.000075$ . Table 5.1 presents mechanical and physical properties of the solid and the fluids. These properties are assumed to be constant in each phase (the temperature dependence of properties is not included). The heat source warms the surrounding liquid. As the growth velocity is proportional to the temperature difference, the vapor will appear when the liquid temperature is higher than the boiling temperature (Figure 5.6).



Figure 5.6: Two dimensional film boiling interface profile computed on a large scale grid

Figure 5.7 shows results of film boiling calculation at four different times (6.25 s, 8.75 s, 10 s, 12 s). The top of Figure 5.7 shows the liquid vapor interface, where in each frame the liquid vapor interface is plotted as a blue line. The liquid vapor interface begins to exhibit a Rayleigh-Taylor

instability with the formation of vortices (Figure 5.8(a)). The water goes in the vapor film and two vapor bubbles are released from the vapor blanket (Figure 5.7(b)-(Figure 5.7(f)). As time progress, bubbles rise releasing large amount of energy (Figure 5.7(f)-(Figure 5.7(g)). As shown in Figure 5.7(d) more vapor bubbles are generated and pulled away from the film vapor more quickly due to the upward motion of the first bubbles (Figure 5.8(d)). The bottom of Figure 5.7 shows the temperature field (to better illustrate the temperature field, the temperatures above 170 °C are shown as red). The temperature for this calculation actually range from 95 °C to 985 °C with the highest temperature being in the solid. The solid and the liquid vapor interfaces are plotted as a white and a black line, respectively. Figure 5.7 shows the ability of boiling to liberate large amounts of energy. These results are similar to those found in the literature by Juric [9], where the author simulate the liquid-vapor phase change more particularly the evolution of a vapor film resting on a vertical plane.

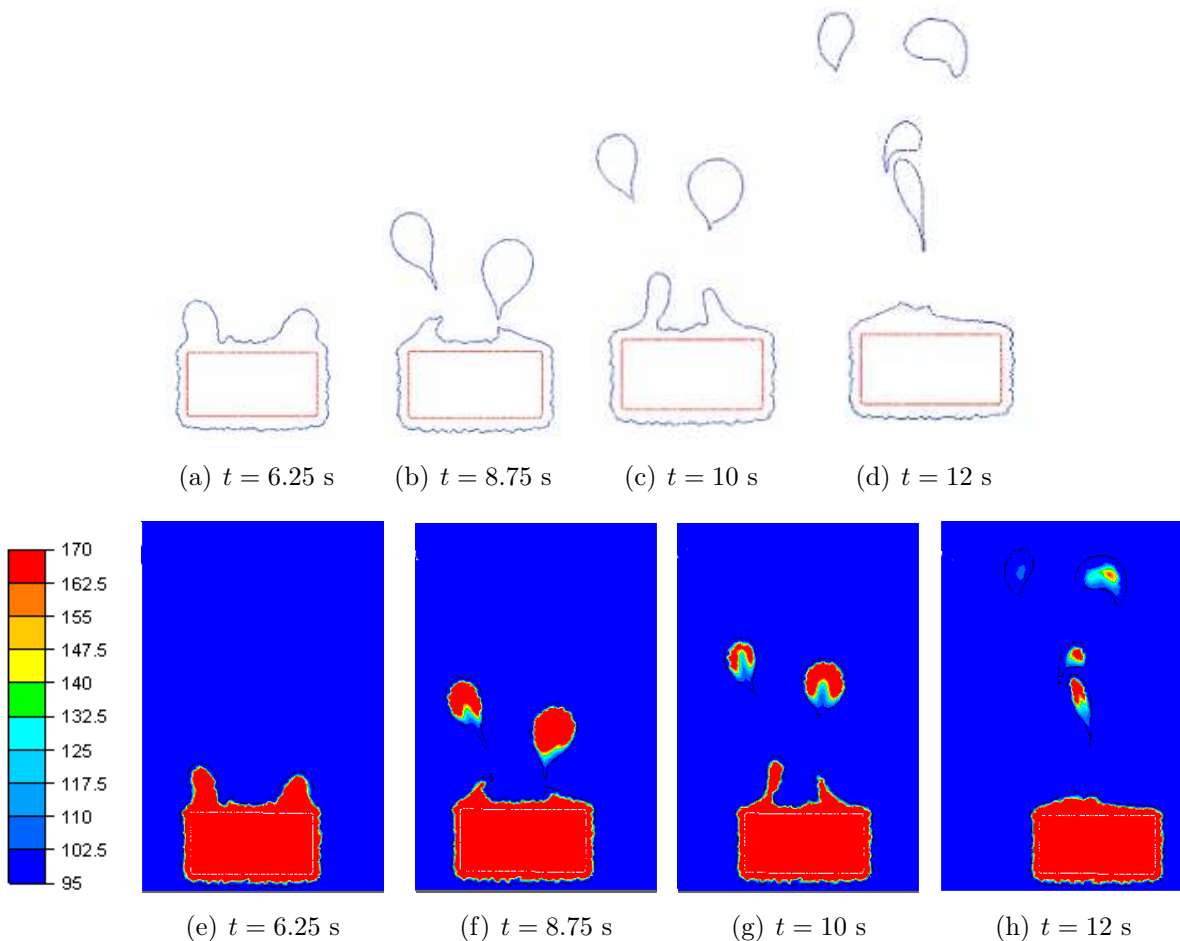


Figure 5.7: Top: close-up on the film boiling interface profile. Bottom: close-up on the temperature ( $^{\circ}\text{C}$ ) field

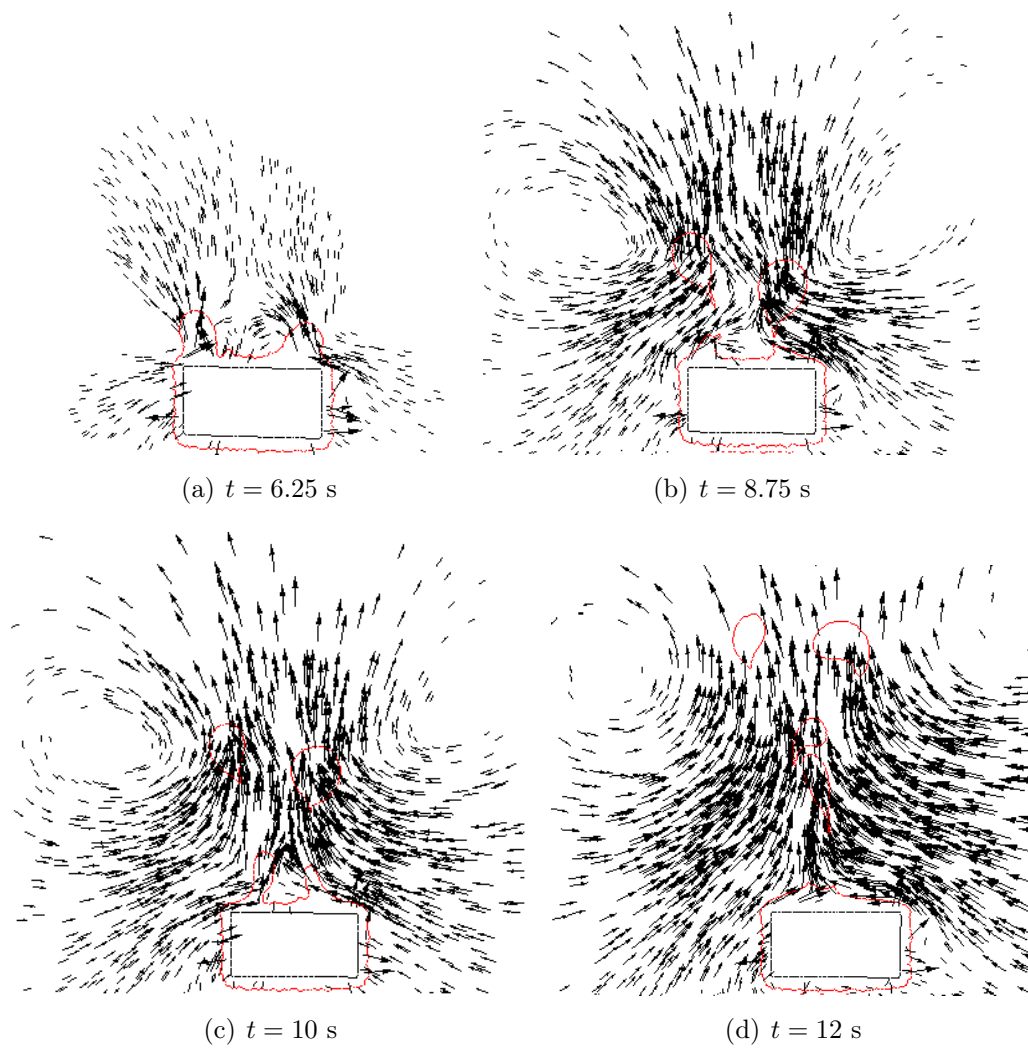


Figure 5.8: Velocity (m/s) vectors, the liquid vapor and the solid interface are plotted as red and black line, respectively

| Domain             | Density<br>( $kg/m^3$ ) | Specific heat<br>capacity ( $J/Kg^{\circ}C$ ) | Thermal<br>conductivity ( $W/mK$ ) | Viscosity<br>( $Pa \cdot s$ ) |
|--------------------|-------------------------|-----------------------------------------------|------------------------------------|-------------------------------|
| Water              | 965                     | 4210                                          | 0.67                               | $10^{-3}$                     |
| Vapor              | 0.597                   | 2054                                          | 0.037                              | $10^{-5}$                     |
| Nickel based alloy | 8200                    | 617.42                                        | 274                                |                               |

Table 5.1: Fluids and material properties



### 5.2.3 Three dimensional film boiling-Micro Scale

The aim of this test is to simulate the **3D** film boiling problem and to show the ability of this approach to naturally and automatically handle the interface breakup in **3D** flows. We first simulate the film boiling behavior generated along a heated cylinder of 4 mm diameter and 2 mm long. The temperatures of the liquid and the solid are  $95\text{ }^\circ\text{C} < T_{sat}$  and  $300\text{ }^\circ\text{C}$ , respectively. To study this problem, we used a domain  $\Omega = [20; 10; 45]\text{ mm}^3$ . The fluid and the solid properties are the same as above (Table 5.1). The domain is discretized by using a homogenous mesh size  $h = 0.6\text{ mm}$ . As presented in the resolution algorithm (Figure 5.5), the transport velocity is the sum of the fluid velocity and the growth velocity. In this computation, the constant growth velocity is  $c_0 = 0.00025$ . The top surface of the domain was considered as a free slip surface and for the other surfaces a no slip condition is applied. At  $t = 1\text{ s}$  the solid is blanketed by a vapor film (Figure 5.9(a)). The vapor interface is transformed to a rising mushroom-shaped bubble that pinches off from the vapor layer to continue rising. In the literature, several authors [10, 11] have performed similar computations and similar film vapor behavior were observed. The top of

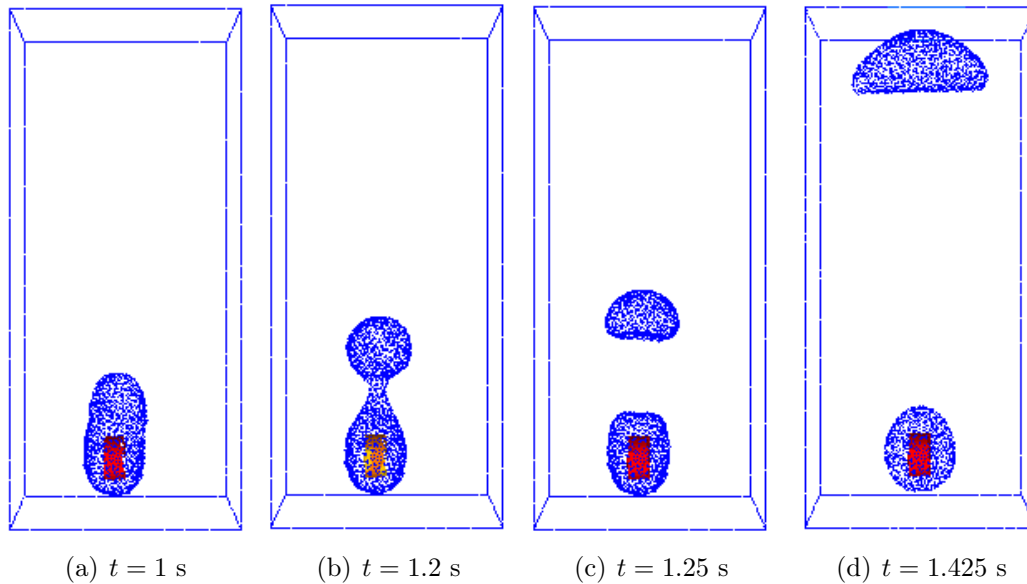


Figure 5.9: The film boiling interface profile. Isobar contour for the solid is plotted with red color, the liquid vapor is plotted with blue at every grid point

Figure 5.10 shows the interface as well as the temperature profile through a vertical center plane (the temperatures above  $170\text{ }^\circ\text{C}$  are shown as red). The bottom of Figure 5.10 shows the velocity field at different time steps through a vertical center plane. The growing bubble pushes the hot vapor upward while the colder liquid descends toward the solid. This numerical method overcome the difficulty due to the sharp discontinuity of the fluids properties. The density evolution across the liquid-vapor interface is presented in the bottom right of Figure 5.10. Circulations appear in the vicinity of the film vapor (Figure 5.10). This film boiling generation is repeated periodically and bubble formation occurs alternatively until the solid temperature becomes lesser then the Leidenfrost temperature. As shown in these two and three dimensional tests, the vapor film

plays an important role in evacuating the energy from the heated solid. Therefore by integrating the boiling model to the simulation of the quenching process, the boiling heat transfer will be considered and the new version of the software **ThosT** will be capable to simulate accurately the quenching process.

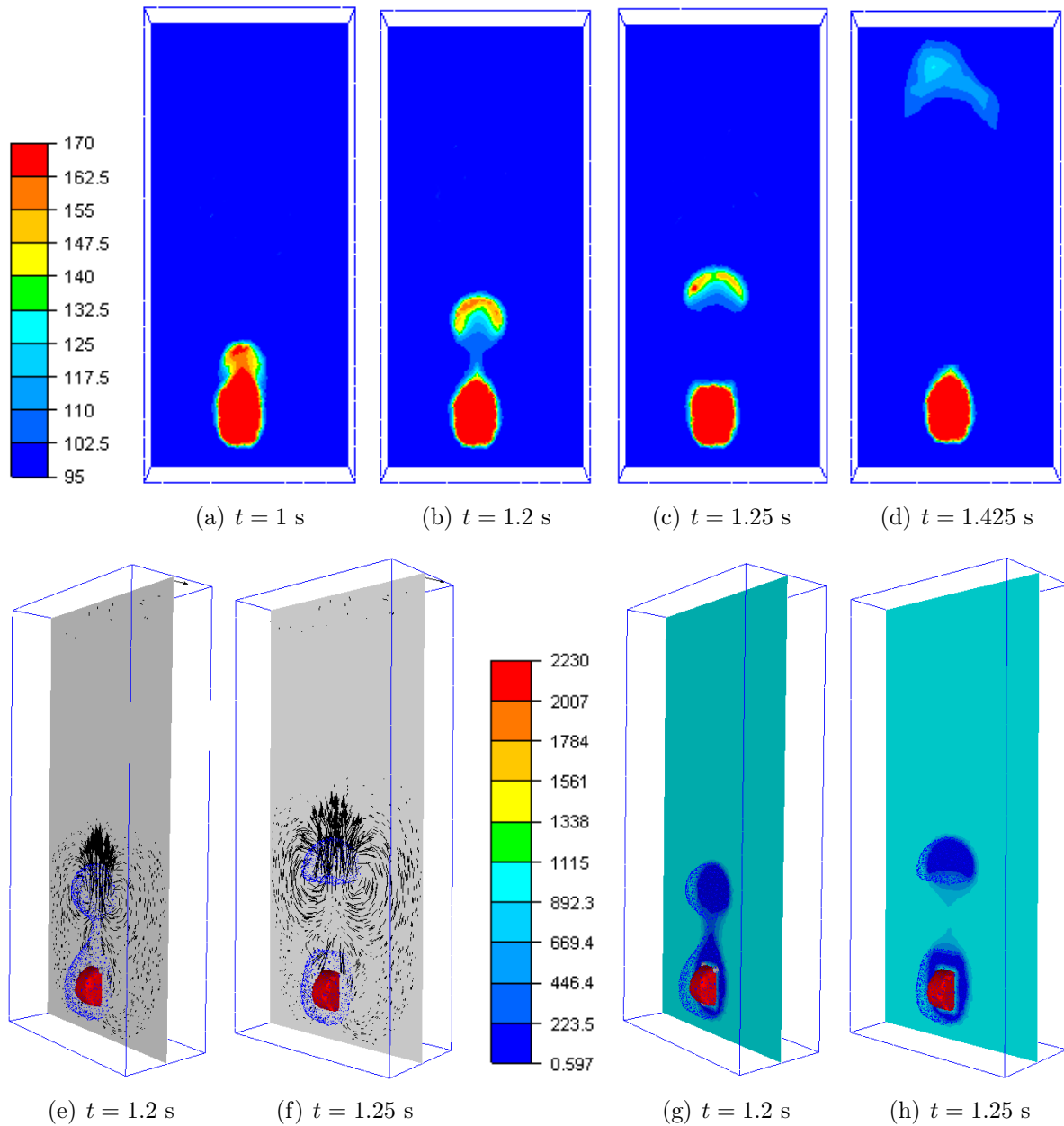


Figure 5.10: Top: The temperature ( $^{\circ}\text{C}$ ) field. Bottom: Evolution of the velocity (m/s) field on the left and the density (Kg/m<sup>3</sup>) distribution across the liquid-vapor interface on the right, through a vertical center plane for the solid

### 5.2.4 Three dimensional film boiling-Meso Scale

This computation is performed in a three-dimensional hexahedral domain with a heat source (Figure 5.11). Using the immersed volume method and a stabilized finite element method for solving conjugate heat transfer, a hot solid is immersed inside a filled-water tank as shown in (Figure 5.11). The heat source is at a temperature of  $700\text{ }^{\circ}\text{C}$  and is made of a nickel-based alloy (inconel718). The water is at a temperature ( $90\text{ }^{\circ}\text{C}$ ) close to the saturation temperature. The time step is equal to  $0.0005\text{ s}$ . The vapor interface is initially coincident with the solid boundary. The evolution of the interface during film boiling is plotted in Figure 5.12. At  $t = 0.2\text{ s}$ , a continuous vapor layer forms between the heated solid and the surrounding liquid. In contrast to the results for small geometry workpieces, where a vapor bubble is periodically detached from the vapor film, the results for a heated solid (with width  $2\text{ cm}$ , length  $2\text{ cm}$  and height  $8\text{ cm}$ ) shows the interfacial disturbance growing along the upper surface of the solid, as seen at  $t = 0.25\text{ s}$  and  $t = 0.375\text{ s}$ . Then a population of bubbles are released along the upper surface of the solid Figure 5.12(c)-5.12(d). Figure 5.13 shows the evolution of the velocity field on a vertical center plane. From this test we can deduce that in the quenching process, the dipped metal provides a natural generator of vapor. This **3D** computation has required 10 days on 16 cores. The numerical results are similar to the one performed by Son in [12], where the author simulates the liquid-vapor phase change, and more particularly, the evolution of a vapor film on a horizontal cylinder. These numerical results indicate without doubts that the proposed approach is suitable for parallel numerical simulation of industrial quenching process with different loads and complex geometries. At a lower solid temperature, wall contact should occur but the study of this effect and the modelling of the nucleate boiling regimes will be the subject of future work.

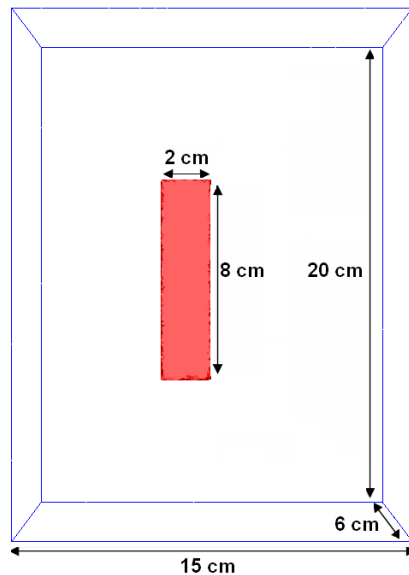


Figure 5.11: Computational domain meso scale

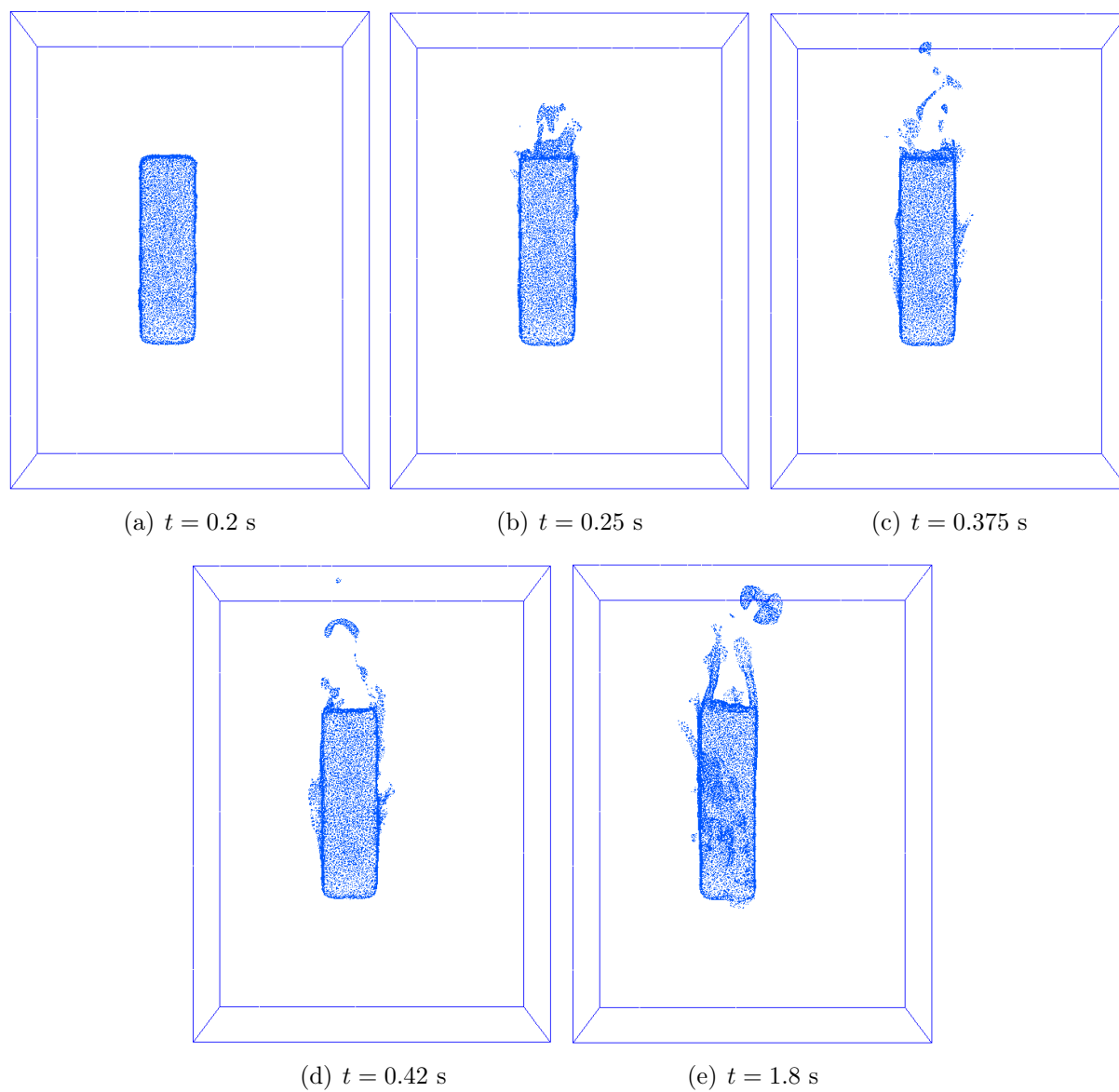


Figure 5.12: Interface plot for a three-dimensional vapor film generation test

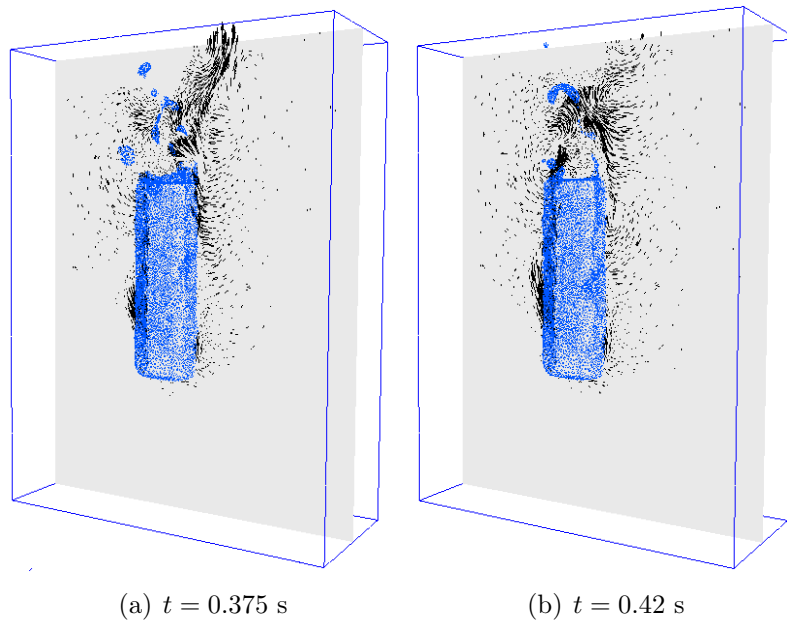


Figure 5.13: Evolution of the velocity (m/s) field through a vertical center plane for the solid

### 5.2.5 Numerical simulation of film boiling during industrial quenching case

In this paragraph, we carry on the industrial case that was simulated without integrating the boiling model in section 2.5.2 of Chapter 2 (Figure 5.14). Here, the calculations were performed with activating the boiling model. The simulation of the boiling model was achieved by using the resolution algorithm presented in Figure 5.5. In Chapter 2, the cylinder was instrumented with several thermal sensors at different locations, as it was shown for thermal sensors fixed inside the solid part, numerical and experimental results were in good agreement despite the fact that the boiling model was not integrated. This agreement is due to the fact that the heat transfer within the solid is provided by conduction. For the thermal sensors fixed on the solid surface, since the boiling model were not integrated, our numerical and experimental results were in discrepancy. In this paragraph, we measure the temperature in two different locations of the solid interface. The time step is equal to 0.0001 s. Figure 5.15 shows the comparison between numerical and experimental results obtained with and without integrating the boiling model. Figure 5.15(b) shows the temperature distribution during the first 50 s of the simulation, it is clear that when boiling occurs, the temperature distribution is significantly modified and

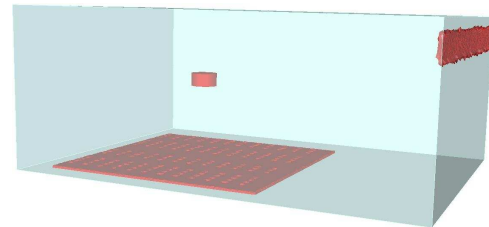
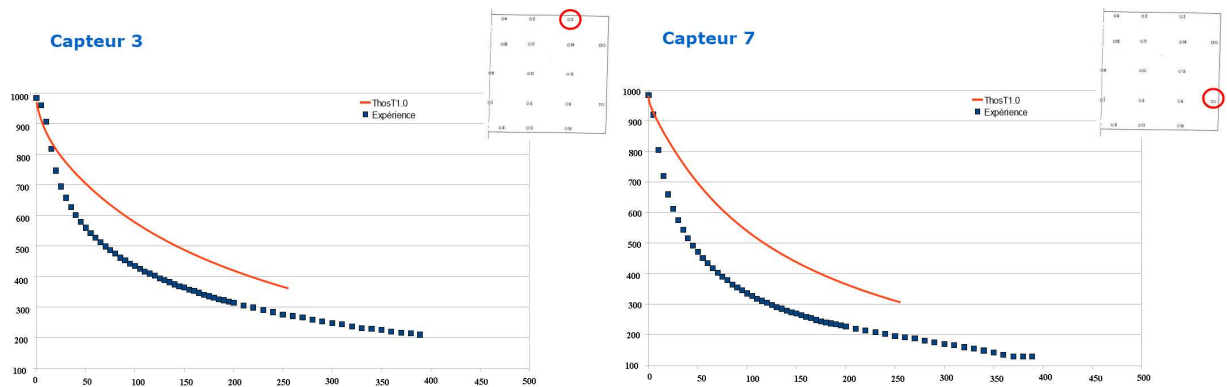
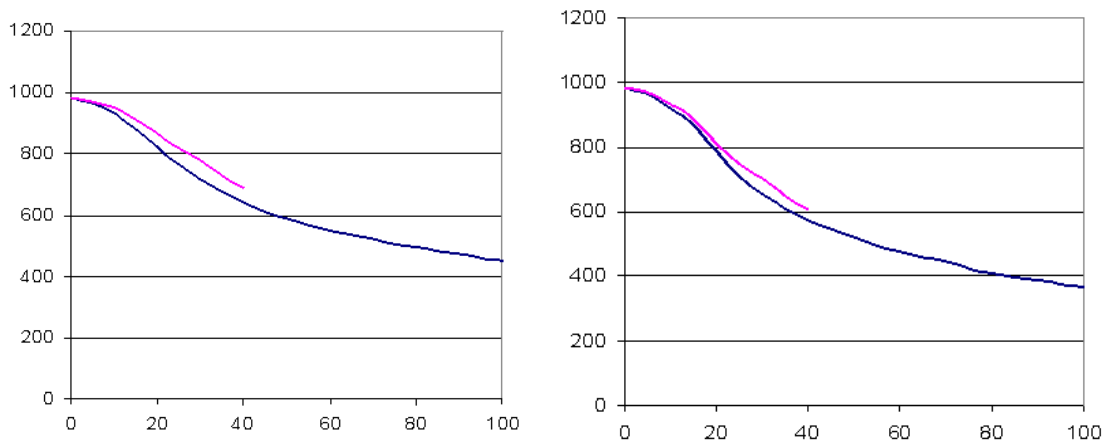


Figure 5.14: Computational domain after anisotropic mesh adaptation around the workpiece interface and an isotropic refinement near the agitation system

the numerical and the experimental results are in better agreement. Definitely a great effort



(a) Without boiling



(b) With boiling

Figure 5.15: Comparison of temperature ( $^{\circ}\text{C}$ ) profiles between experimental and numerical results with/without boiling calculation. From left to right: sensors 3, 7

is still necessary to reduce the computational time, this can be realized by using an adaptive time step. By integrating the boiling model to the computational fluid dynamics **CFD** solver introduced in Chapter 2, the quenching process can be optimized. Then the industrial partners are able to optimize better the heat treatment processes and improve the mechanical and metallurgical properties of the final metallic parts.

## 5.2.6 Conclusion

A boiling model has been developed to simulate the phenomenon of boiling which occurs during the quenching process. The numerical technique adopted in this model is based on the single field formulation where one set of equations is applied for the entire flow field. This method involves an anisotropic mesh adaptation, growth & germination model, surface tension model coupled with the LevelSet method. The simulation results of film vapor evolution are compared

with the literature, they show a good agreement. The integration of the boiling model to the quenching process accelerates the solid cooling since a large amounts of energy is liberated by this phenomenon. The simulation of quenching without modelling the boiling phenomenon is insufficient. As a first implementation, the agreement between the present and the experimental results can be considered satisfactory.

### **5.3 Résumé français**

La première partie de ce chapitre porte sur le développement d'un outil de micro-trempe d'une pièce portée à haute température. Grâce à une caméra rapide, une observation réelle de différents régimes d'ébullition et une étude de l'influence de la température du bain et de la température initial du solide sur la stabilité d'un film de vapeur ont été réalisées. La deuxième partie de ce chapitre est consacrée aux développements numériques du modèle d'ébullition film. Ces développements permettent le calcul couplé de la température des pièces avec l'environnement du bac de trempe afin de contrôler la métallurgie via le chemin de refroidissement et de diminuer les distorsions et les risques de fissuration dus à la sévérité de la trempe. Plusieurs tests numériques à différentes échelles (macro et méso) ont été réalisés, ainsi qu'une validation de cette approche par une comparaison avec les résultats expérimentaux fournis par nos partenaires industriels. Les résultats montrent le rôle déterminant du film de vapeur sur l'évacuation et le transfert de chaleur.

# References

- [1] Th. Lubben, F. Frerichs, F. Hoffiman, and H. W. Zoch. Rewetting behaviour during immersion quenching. *New challenges in heat treatment and surface rewetting*, 09-12 June 2009, Croatia.
- [2] C. S. Kim, K. Y. Suh, J. L. Rempe, F. B. Cheung, and S. B. Kim. Effect of interfacial wavy motion on film boiling heat transfer from isothermal downward-facing hemispheres. *Nuclear Engineering and Design*, 235:2141–2154, 2005.
- [3] T. Bo. CFD homogeneous mixing flow modelling to simulate subcooled nucleate boiling flow. *SAE world congress, Ricardo Consulting Engineers, U.K.*, 01-1512, 2004.
- [4] V. Srinivasan, K. M. Moon, D. Greif, D. M. Wang, and M. H. Kim. Numerical simulation of immersion quench cooling process using an eulerian multi-fluid approach. *Applied Thermal Engineering*, 30:499–509, 2010.
- [5] V. Srinivasan, K. M. Moon, D. Greif, D. M. Wang, and M. H. Kim. Numerical simulation of immersion quenching process of an engine cylinder head. *Applied Mathematical Modelling*, 34:2111–2128, 2010.
- [6] D. M. Wang, A. Alajbegovic, X. M. Su, and J. Jan. Numerical modeling of quenching cooling using eulerian two-fluid method, in: Proceedings of asme. *International Mechanical Engineering Congress and Exposition, New Orleans, Louisiana*, November 17-22, 2002.
- [7] D. M. Wang, A. Alajbegovic, X. M. Su, and J. Jan. Numerical simulation of water quenching process of an engine cylinder head, in: Proceedings of asme. *FEDSM 2003, 4th ASME JSME Joint Fluids Engineering Conference, Honolulu, Hawaii, USA*, 24, July 6-10, 2003.
- [8] G. Jérôme. *Etude Expérimentale des Aspects Thermiques lies à une Opération de Trempe*. PhD thesis, Ph.D. Thesis, Ecole Doctorale de Nantes., 2004.
- [9] D. Juric and G. Tryggvason. Computations of boiling flows. *International Journal Multi-phase Flow*, 24:387–410, 1998.
- [10] G. Tryggvason A. Esmaeeli. Computations of film boiling. part i: numerical method. *International Journal of Heat and Mass Transfer*, 47:5451–5461, 2004.
- [11] D. Juric S. Shin. Modeling three-dimensional multiphase flow using a level contour reconstruction method for front tracking without connectivity. *Journal of Computational Physics*, 180:427–470, 2002.



- [12] G. Son and V. K. Dhir. Three-dimensional simulation of saturated film boiling on a horizontal cylinder. *International Journal of Heat and Mass Transfer*, 51:1156–1167, 2007.

# Chapter 6

## Conclusion & perspectives

The present work aimed at developing a numerical model in the CimLib library in order to simulate the boiling phenomenon for industrial quenching processes. Such study involves numerical developments as well as experimental investigations and it was achieved at different scales: meso-scale (bubble scale) and macro scale (workpiece scale). At the meso scale, a physical mathematical model was developed to model the bubble evolution; it includes interface tracking, growth model and surface tension. To validate this numerical model an experimental investigation is performed by using a high speed camera to capture the bubble shape evolution and non-intrusive methods "Particle Image Velocimetry & Laser Induced Fluorescence" to measure the temperature and the velocity fields. The same mathematical model has been used to simulate the boiling during quenching process at the macro scale. The tools used in this thesis are the Finite Element Method (FEM) and Computational Fluid Dynamics (CFD). This method is shown as an attractive way to develop a boiling model for quenching process and it can be applied for a variety of workpieces, bath geometries and boundary conditions.

- The first part of the thesis consisted in identifying the need of a software tool integrating the boiling to the quenching model. The stabilization methods in the case of unsteady diffusion problems have been revisited accompanied with a study of the influence of several parameters on the thermal shocks. To deal with convection dominated problems (in case of agitated bath), the Navier-Stokes equations with a variational multiscale method were presented in Chapter 2.
- The first step of this work is to develop several numerical tools for modelling the bubble evolution that was achieved by an improvement of the existing numerical techniques.
  - To track the liquid vapor interface: 1) a hyperbolic tangent function is used to truncate the interface (predicted by the LevelSet method); and 2) a convected reinitialization method is used to predict it at each time step.
  - The bubble growth velocity has been defined from the Gibbs Thomson relation.
  - The momentum and the energy equation are modified to account for the surface tension and the latent heat acting along the interface, respectively by adding source terms to the right hand side. The main challenge in creating the surface tension

model is to compute the curvature of the fluid interface as a second derivative of the LevelSet function since a linear finite element method is used. While constructing a metric field directly at the nodes of the mesh, T. Coupez proposed a continuous gradient operator, known as the recovered gradient, based on the length distribution tensor and the projection of the gradient along the edges. In this work, the normal and the curvature are calculated based on the continuous gradient operator. The surface tension was computed explicitly by combining the continuum surface force (CSF) and the continuous gradient computed directly at the nodes of the mesh.

These developments provide an accurate model of boiling capable to simulate bubbles growth, detachment and coalescence. The performance of this approach was tested on different numerical examples in **2D** and **3D**. The first tests involved modelling for the isothermal and non-isothermal bubbles growth and collapse, the numerical bubble growth rate is in good agreement with the literature. The next numerical tests involved modelling for the bubbles rise and coalescence. Results obtained by this approach agreed fairly well with the literature. The final test involved modelling an air bubble rising in water, it has shown a relatively good agreement between the numerical prediction and the experimental measurements. This new multiphase approach offers a simple way to model bubbles evolution and nucleate boiling phenomenon.

- The second part of this research is to achieve an experimental investigation on the meso-scale as proposed in Chapter 4. The purpose of this task is to measure the fields that are not sufficiently known to ensure a detailed comparison with numerical results.
  - A high speed camera was used to capture the bubble shape and to measure the bubble growth rate. The bubble growth rate obtained in this study agrees with the one found in the literature by Qiu and Dhir.
  - The Particle Image Velocimetry (PIV) technique was used to measure the velocity field at the bubble interface.
  - The two color Laser Induced Fluorescence (LIF) was used to measure the temperature in nucleate boiling condition. The lightening nonuniformity due to the reflection at the vapour surface and the temperature gradient in the path of the incident laser light can be corrected by using the two colour LIF technique. The preliminary results show that the LIF technique is a promising method for the thermal field in nucleate boiling condition.
- The last part of this research focuses on the integration of boiling to the modelling of quenching process. Chapter 5 is divided in two parts: the first is devoted to an experimental investigation during a micro quenching, the second is devoted to develop a general model of boiling. In the first portion, a high speed camera is used to bring useful information about the influence of the bath and the solid temperature on boiling regimes and film vapor stability. The numerical models (interface tracking, growth, surface tension) developed and applied at the meso scale, are extended to the macro scale to create a software tool that integrates the boiling to the modelling of quenching process. During quenching, the

---

solid temperature is higher than the Leindenfrost point then the film boiling mode occurs on the solid surface. The formation and the evolution of a film vapor will be modelled via a germination and a growth approach. The film vapor generation is automatically done by assuming that the film vapor interface is coincident to the solid surface, this gives the advantage that the approach can be applied to a variety of workpiece geometries. Several numerical tests are performed at different scales with several geometries. The results demonstrate that:

1. The proposed method overcomes the numerical difficulty due to the large properties (density, viscosity ....) difference between the phases;
2. The film boiling behavior agrees fairly well with the literature;
3. The boiling model has been integrated successfully to industrial quenching configuration of large scales;
4. By integrating the boiling model to the quenching, the large amount of energy liberated by this phenomenon is modelled and the quenching process is optimized.

The proposed approach is suitable for parallel numerical simulations of industrial quenching process. This work offers numerical tools for the industrial partners to model the quenching, then they will be able to optimize the heat transfer and to improve the metallurgical properties of their metallic parts.

## **PERSPECTIVES**

At the current stage, improvements in the numerical methods as well as in the experimental measurements can be proposed. From the point of view of numerical computation, the following points remain to be developed:

- Reduction of the computational time. For the current boiling model, the surface tension was computed explicitly which induces a limitation on time step. Moreover even if we use the anisotropic mesh adaptation to reduce the computational time, the limitation on the time step becomes more important. Then the development of an implicit surface tension model is necessary. In order to simulate full cooling process in reasonable computational time, the adaptive time step is recommended.
- Higher treatment efficiency test. The focus of this work is on developing a new concept for numerical methods to model boiling in quenching process. However, the test cases showing the efficiency of integrating the boiling model on accelerating the heat transfer are not in the scope of this work. Therefore, in future works with the proposed approach it is important to prove the usefulness of the proposed quenching model with a number of tests at the level of industrial parts. These tests should be achieved by considering vapor films or a phase of liquid vapor mixture. The results of such simulations should be assessed and compared with experiments conducted by the industrial partners.

- Modelling of turbulence induced by boiling. The numerical models proposed in this work should be extended to model the turbulence induced by boiling in a CFD approach. This represents a challenging issue.

From the point of experimental investigations, the following points affecting bubble evolution should be considered in a future work in order to optimize the heat transfer due to boiling in industrial cooling process:

- Nucleation of one or a few bubbles. The experimental observations should be performed to control, in the volume or at surface, the nucleation of one or a few bubbles of vapor using a high speed camera.
- Thermal field around a vapor bubble. In fact, the zone of interest is too small compared to the entire CCD sensor. The LIF study should be improved to measure in detail the thermal field around a vapor bubble by increasing the optical magnification. This allows a comparison between numerical and experimental growth dynamics.
- Image mapping. An improved two-camera mapping procedure using the fundamental matrix method needs to be developed. Improvement of the temperature sensitivity of the  $f$ -function can be carried out by optimizing the configuration of optical elements of the experimental setup and the dyes concentrations.
- Synchronization between PIV and two color LIF technique.

## Simulation numérique de l'ébullition pour les procédés de trempe industrielle

**RESUME :** Cette thèse porte sur la modélisation de l'ébullition qui joue un rôle important dans les vitesses de refroidissement lors de la trempe des pièces métalliques. Elle possède un volet numérique et un volet expérimental. Les simulations et les expériences envisagées se situent à deux échelles. A l'échelle d'une ou quelques bulles de vapeur, il s'agit de faire des simulations multiphasiques très précises en prenant en compte la tension de surface, les calculs directs d'écoulement à grand nombre de Reynolds, et en rendant compte du détachement et de la coalescences des bulles. Des observations expérimentales sont réalisées à la même échelle en capturant en surface la croissance d'une bulle de vapeur à l'aide d'une caméra rapide. Des mesures de champs de vitesse par PIV et de température par "two color LIF thermometry" sont réalisées dans les mêmes conditions. Ceci a permis de confronter la croissance, la dynamique et les formes des bulles observées et calculées. Les techniques numériques les plus avancées sont utilisées : Eléments finis stabilisés VMS, LevelSet, adaptation anisotrope et calcul intensif. Les modèles numériques proposés dans cette thèse permettent de passer à l'échelle macroscopique des pièces industrielles en considérant un film de vapeur ou une phase de mélange liquide vapeur. L'enjeu supplémentaire sera de modéliser la turbulence induite par l'ébullition dans une approche de type CFD.

**Mots clés :** Ebullition, Trempe, Germination, Croissance, Bulle et film de vapeur, Tension de surface, Convected LevelSet, Maillage adaptatif anisotrope, PIV, Two color LIF

## Numerical Simulation of Boiling for Industrial Quenching Processes

**ABSTRACT :** This thesis focuses on the modelling of boiling that plays an important role on the cooling and heat treatment in quenching processes, it has two components: numerical simulations and experimental measurements. Both simulations and experiments are envisaged for two scales. The first one concerns small scales: the scale of one or few bubbles. In this case, the focus is put on very precise numerical simulations for multiphase flows taking into account the surface tension, the direct computations of flows at high Reynolds number in order to model the detachment and coalescence of bubbles. On that same scale, experimental observations are performed to control, in the volume or at surface, the nucleation of a vapour bubble using a high speed camera. Measurements of velocity fields by PIV and the temperature by PLIF are realized under the same conditions. This will allow us to compare the growth dynamics and shapes of bubbles observed and calculated. Advanced numerical methods are used to fulfil this task: VMS stabilized finite elements, LevelSet, anisotropic adaptation and parallel computing. The numerical models proposed in this work are extended and also used to deal with macroscopic scales: at the level of industrial parts considering the vapor films or a phase of liquid vapor mixture. The additional challenge resides in the modelling of turbulence induced by boiling in a CFD approach.

**Keywords :** Boiling, Quenching, Germination, Growth, Bubble and film vapor, Surface tension, Convected LevelSet, Anisotropic mesh adaptation, PIV, Two color LIF

